Perspectives from the Juno Microwave Radiometer: Probing Jupiter's Deep Rock Clouds, Thermochemistry and High-Energy Electron Precipitation over Northern Aurora

by

Ananyo Bhattacharya

A dissertation submitted in partial fulfillment
of the requirements for the degree of
Doctor of Philosophy
(Climate and Space Sciences and Engineering)
in the University of Michigan
2025

Doctoral Committee:

- Professor Emeritus Sushil Atreya, Co-Chair
- Assistant Professor Cheng Li, Co-Chair
- Professor Xianzhe Jia
- Associate Professor Emily Rauscher
- Professor Nilton Renno
- Research Professor Jack Hunter Waite Jr., University of Alabama

Ananyo Bhattacharya
ananyo@umich.edu
ORCID iD: 0000-0003-1898-8080

© Ananyo Bhattacharya 2025

DEDICATION

I dedicate it to the eternal charioteer and to those who persist in keeping this world running through their hard work and random acts of kindness. You and I are beneficiaries of their work.

”Āmār mukti sarbajanēr manēr mājhē,
duḥkhabipad-tuccha-karā kaṭhina kājē.
Biśwadhātāra yajñaśālā ātmahōmēr bahni jwālā
jīban jēno di'i āhuti mukti-āśē.”

translates to

Within the hearts of one and all
In tasks that mock peril and pain
Alight is the sacrificial fire
At the altar of creation
May I offer my life as oblation
In the hope of liberation

- Rabindranath Tagore

ACKNOWLEDGEMENTS

The list is going to be long. As they say, it takes a village to raise a man. I would firstly thank my advisors Prof. Sushil K. Atreya, and Prof. Cheng Li for their mentorship and guidance throughout the program. They have acquainted me with the breadths and depths of scientific research in planetary science and space exploration.

I will always remain grateful to my parents, Mr. Arup Bhattacharya, and Mrs. Sanjukta Bhattacharya. They have made a lot of sacrifices for my dreams since my early childhood. My father has always pushed me to work hard for my dreams and never stopped believing in them. I received unwavering support from them and my grandmother, Mrs. Suprava Bhattacharjee throughout my academic journey. They invested in my education, and my positive qualities are largely shaped by the good quality of education that I have received over the years.

I thank Dr. Steven Levin and Dr. Scott Bolton for welcoming me to be a part of the Juno meetings. My experience with Juno and the science team has fulfilled my dream of working with a space mission. Being associated with the Juno science team has played a crucial role in my professional development. On 31st December 2023, Juno made a close flyby of Jupiter's moon Io. We watched the mountains of another moon on New Year's Eve. A senior scientist compared the mountains of Io to the ones on Earth and that moment expanded my horizon. The similarities between planetary bodies, and the existence of life are not just important to science, they are equally important for philosophical understanding of our universe. I was fortunate to spend a summer working at JPL where Steve offered me a summer job to study Jupiter's aurora.

I express my deepest gratitude to Dr. Jack Hunter Waite Jr. for his exceptional mentorship and support throughout my project and dissertation. His guidance helped me to overcome many challenges and he introduced me to a host of methods to study gas giant aurorae. I would also like to extend my sincere appreciation to Dr. Tom Nordheim, Dr. James Sinclair, Dr. Michael H. Wong, and Dr. Glenn Orton for their collaborative support and for providing a supportive environment for graduate students in planetary science.

Thanks to Prof. Nilton O. Renno and Dr. Mojtaba Akhvan Tafti for encouraging and supporting my interest in engineering. Interacting with the Space Engineering students and working with them improved my understanding of space systems and the design process. Many thanks to Dr. David Sweeney and Mr. Dillan McDonald for their commitment and support to the cause of mentoring graduate students.

I am deeply grateful to the CLaSP faculty members for guiding me through the fundamentals. As an engineering undergraduate, I had a lot to cover to bridge my knowledge gaps. Special mention to Prof. Mike Liemohn, Prof. Mark Moldwin, and Prof. Enrico Landi.

Thanks to Dr. Nick Moroz, Mrs. Grace Hsia Haberl, and Dr. Scott Merz for introducing me to the world of entrepreneurial practice and technical innovation. The Entrepreneurs Leadership Program helped me with goal setting and identification of real-world problems that can be solved by technology.

Dr. Jeff Masters, you have been a constant source of encouragement for my learning about science and society. Your efforts have been a major boost to my reading habits. Representing the University at United Nations Climate Change Conference COP 28 was an eye-opener for me. There is a lot that needs to be done for the environment keeping the humane connections in perspective.

A big shout-out to the people in CLaSP: Timothy Keebler, Erika Hathaway, Talha Arshad, Tyler Eddy, Shirsh Soni, Andrew Bahlmann, Jennifer Seth, Dauda Kashim, Onyinye Gift Nwanko, Sandra Pytlinski, Martha Moon, Connor Metz, Linfeng Li, Xiantong Wang, Nishtha Sachdeva, Gabor Toth, Alexander Cushen, Mitchell Indek, Yinsi Shou, Daniel Muccio, Yury Aglyamov, Jiheng Hu, Yan Xie, Sunanda Suresh, Nelvin Vincent, Nathan Smith, and Remi Free. The GUStO community brought us together, and I'm glad that I made some wonderful memories with them. I would like to especially acknowledge Tim who has been my mentor since the first year. The department coffee hour has been a space for me to bond with colleagues and senior researchers.

The University introduced me to talented people from very diverse backgrounds who share my curiosity for understanding the world: Akshay Kumar Verma, Anirudh Aatresh, Kavita Rani, Shunshuke Saito, Dwiky Putra, Manasa Jagadeesh, Trupti Khade, and Harmeet Kaur.

Special thanks to my support system outside Michigan: Swastik Bhattacharya, Swastik Bhattacharya, Abhishek Kumar, Gulshan Rana, Gourav Namta, Gagandeep Gill, Siddarth Chechani, Abhijit Ghosh, Ipshita Biswas, Ankita Talukdar and Stuti Chowdhury. It wouldn't be possible without you all. Moving to a new country and adjusting to a new environment was a challenge for me. You made the transition easy for me.

Lastly, I would like to mention my colleagues for supporting me, and fostering a healthy community for the future of astronomy and space sciences: Arthur Chadwick, Adrienne Rudolph, Sourabh Shubham, Sihe Chen, Dr. Ali Hyder, Dr. Mohammed Afzal Shadab, Dr. Emma Dahl, Dr. Ramannakumar Sankar, and Dr. Huazhi Ge.

TABLE OF CONTENTS

CHAPTER

LIST OF FIGURES

FIGURE

LIST OF TABLES

TABLE

LIST OF APPENDICES

LIST OF ACRONYMS

MWR MicroWave Radiometer

NASA National Aeronautics and Space Administration

CERN European Organization for Nuclear Research

ESA European Space Agency

JUICE Jupiter Icy Moons Explorer

UOP Uranus Orbiter and Probe

TVAC Thermal Vacuum

MCS Microwave Calibration System

GPMS Galileo Probe Mass Spectrometer

ADEOS Advanced Earth Observing Satellite

SMAP Soil Moisture Active Passive

RADAR Radio Detection and Ranging

JOI Jupiter Orbit Insertion

JEDI Jupiter Energetic Particle Detector Instrument

JADE Jovian Auroral Distributions Experiment

JIRAM Jovian Infrared Auroral Mapper

SRU Stellar Reference Unit

ASC Advanced Stellar Compasses

IMF Interplanetary Magnetic Field

MAE Main Auroral Emission

VLA Very Large Array

ALMA Atacama Large Millimeter/submillimeter Array

IRTF Infrared Telescope Facility

TEXES Texas Echelon Cross Echelle Spectrograph

JSE Jovian Synchrotron Emission

HARP High performance Atmospheric Radiation Package

DISORT Discrete-Ordinate-Method Radiative Transfer

JAMRT Juno Atmospheric Microwave Radiative Transfer

JTGCM Jupiter Thermosphere Global Circulation Model

JGITM Jupiter Global Ionosphere Thermosphere Model

UVS Ultraviolet Imaging Spectrograph

CIA Collision Induced Absorption

C^{3}M Comprehensive Coupled Chemistry Model

CFL Courant–Friedrichs–Lewy

GGChem Gleicht-Gewichts-Chemie

TOA Top of the Atmosphere

CANOE Comprehensive Atmosphere N’ Ocean Engine

NIST National Institute of Standards and Technology

HST Hubble Space Telescope

JWST James Webb Space Telescope

ABSTRACT

Microwave remote sensing from Earth and space-borne instruments have been crucial to understanding the atmospheric dynamics of Jupiter and monitoring its space environment. Probing Jupiter's atmosphere below the water cloud region offers valuable insights into Jupiter's deep convective-diffusive transport and overall energy balance. The inventory of heavy elements in the Jovian envelope, including condensable volatile species, provides us with inference about the origin and evolution of Jupiter. Jupiter's magnetic field interacts with its upper atmosphere through precipitation of energetic electrons and ions. The contribution of high-energy electrons to auroral heating, ionization, and chemical kinetic processes serves to couple the Jovian magnetosphere to its upper atmosphere.

The Juno Microwave Radiometer instrument measures the thermal radiation emitted by Jupiter's atmosphere at six different frequency bands. It is sensitive to changes in the microwave opacity of the Jovian atmosphere. The 600 MHz channel is sensitive to microwave opacity sources originating between 100–1000 bar deep into the atmosphere. Rock cloud-forming alkali metals such as sodium and potassium, are expected to undergo thermal ionization at pressures exceeding 100 bar, providing free electrons opaque to microwave radiation. Measurement of Jovian thermal emission and its angular dependence constrains the free-electron density of the deep atmosphere. Free electrons produced by the thermal ionization of alkali vapors can be leveraged to constrain the abundance of sodium and potassium, revealed to be 10^{-2} to 10^{-5} times their solar photospheric abundances. This result contrasts with the enrichment of heavy elements at pressures above 20 bar measured by the Galileo Probe Mass Spectrometer, hinting at a potential compositional gradient. It has implications for heat and mass transport within the Jovian envelope.

Deep below the water clouds, the alkali metals react with other constituents in the Jovian atmosphere. The thermochemistry of alkali metals with other condensable volatile affects the concentration of charge carriers and alkali salt-cloud thickness. Numerical modeling of Jovian thermochemical equilibrium reveals the formation of stable anions such as HS^- and Cl^- driven by partial decomposition of atmospheric H_2S and HCl, and consequent electron attachment process. These high-temperature chemical reactions remove a proportion of free electrons, elevating the alkali metal abundances ~ 0.1 times their solar abundance. Alternatively, enrichment of either Na or K partially matches with MWR observations, contingent on the existence of alkali metals sequestered at levels deeper than pressure regimes sensitive to the MWR instrument. This analysis negates the possibility of a deep radiative layer on the basis of contemporary estimations of Jupiter's atmospheric opacity. Knowledge of atmospheric chemistry improves the understanding of heavy-element reservoirs in Jupiter's envelope.

The MWR measurements within the main auroral oval show low brightness temperatures compared to the deep thermal emission. Electron precipitation-driven ionization is expected to cause an increase in ionospheric electron density that leads to the absorption of microwaves near 1 GHz in a highly collisional medium. Electron energies with 1 MeV or higher penetrate below the methane homopause to increase microwave opacity, exhibiting a strong variation over tens of seconds. The microwave data provides a complementary perspective to understand magnetosphere-ionosphere-atmosphere coupling in addition to the in-situ electron flux and ultraviolet auroral emissions observed by Juno. Atmospheric models of microwave radiative transfer, chemical kinetics, and electron precipitation are applied to present a comprehensive theory of Jupiter's deep atmosphere and polar aurorae, informed by synergistic observations from Juno.

CHAPTER 1

Introduction

1.1 Jupiter — A giant among other worlds

Jupiter is the largest planet in the solar system, comprising about two-thirds of the total mass of the solar system. Its presence in the night sky has inspired many generations to search for other worlds in the cosmic ocean. It possesses characteristics that are similar to and distinct from our Earth. Physical processes on Earth can be found on Jupiter, with their strengths amplified by orders of magnitude. For example, similar to Jupiter, the water vapor and cloud formation processes control the distribution of energy in Earth's atmosphere [262].

Jupiter's troposphere manifests clouds of water of ice and liquid droplets and gives rise to mesoscale weather phenomena and long-lasting storms on the gas giant [149] [113]. The Great Red Spot (GRS), one of the most prominent features found in Jupiter, is a storm that has existed for centuries [96]. Thus, one might say that both Earth and Jupiter are natural laboratories for meteorology.

1.1.1 In mythology and modern times

Jupiter is the third brightest object in the night sky after the Moon and Venus. It has been the subject of folklore and mythologies. In Roman mythology, Jupiter is the king of the gods,

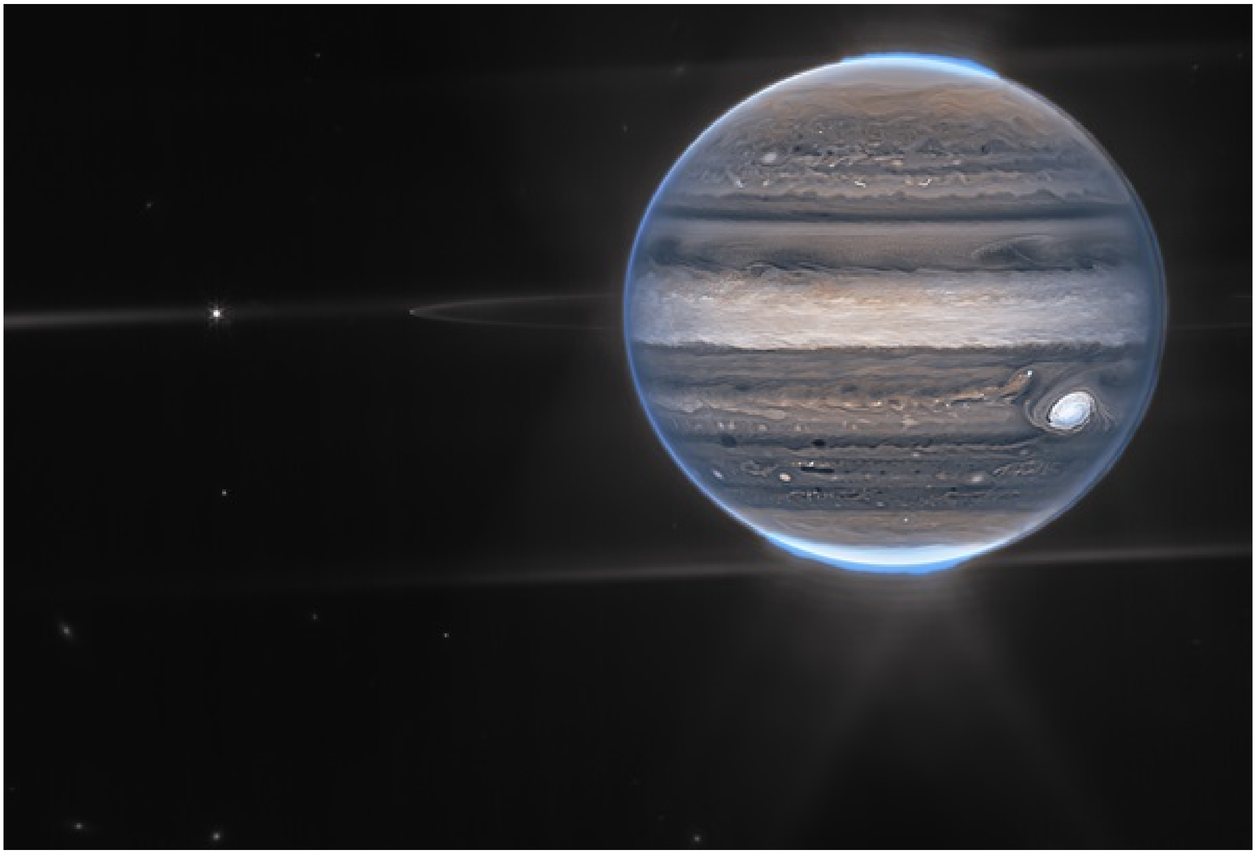

Figure 1.1: Jupiter and its space environment as captured by James Webb Space Telescope NIR-Cam instrument. Image credit: NASA/ESA/Jupiter ERS Team; image processing by Ricardo Hueso (UPV/EHU) and Judy Schmidt

possessing powers to govern the sky and thunder (Fig. 1.2 (a)). Likewise, in Greek mythology, Zeus has powers identical to Jupiter's. Interestingly, Jupiter's clouds are also characterized by lightning phenomena first discovered by Voyager 1 [129]. In Hindu mythology, the planet Jupiter is known as Guru or Brihaspati (Fig. 1.2 (b)). Brihaspati is a deity and counselor to gods and goddesses. Brihaspati happens to be one of the nine celestial objects (Navagraha) that affect human life on Earth. The planet has also been a harbinger of scientific renaissance in medieval Europe. In 1610, Galileo discovered the four moons of Jupiter by pointing a telescope at the night sky. These moons namely Io, Ganymede, Europa, and Callisto orbit around the planet and represent a harmonic motion when seen from Earth. Some of these moons are currently known to possess a subsurface reservoir of liquid water. The habitability of these "ocean worlds" is one of the most important modern science questions. In the next decade, two spacecraft missions JUICE

[120] and Europa Clipper [217] will unveil the mysteries of two of these ocean worlds: Ganymede and Europa.

1.1.2 Jupiter: Origin and Evolution

The origin and evolution of solar system bodies is one of the most fundamental questions of planetary science. The formation of gas giants in our solar system can be explained by two major theories, i.e., the gas instability [48, 49] and the core accretion model [173, 223]. In the gas instability model, the protoplanetary disk undergoes a magnetohydrodynamic instability to form clumps of highly dense protoplanets,, which eventually cool down to form gas giants. However, the core-accretion model poses the existence of massive bodies made up of accreted rock and ice that constitute the planetary core. As the core orbits around the Sun, it collects the inventory of gas and condensate surrounding itself to make up gas giant planets composed of gaseous hydrogen and helium. Additionally, the distance from the Sun causes temperatures to drop, leading to the formation of astrochemical ices like H_2O, NH_3 and CH_4 ice that feed into the gas giant cores.

Jupiter is not expected to have a solid core, unlike Earth. The gravitational acceleration of spacecraft orbiters has been closely investigated to determine its internal structure [127, 263]. Recent observations of Jupiter's gravity hint at a possibility of a dilute core in Jupiter's interior which slowly diffuses out radially [196, 142]. Reservoirs of heavy elements influence Jupiter's gravitational field. However, it is difficult to distinguish the contribution of each element to the overall mass.

Over the years of gravitational accretion, and mixing processes throughout the planet's history caused heavy elements to be uniformly mixed throughout Jupiter's envelope [264]. In Jupiter's troposphere, the elements C, N, O, and S form condensable volatiles with spatial variability attributed to regional-scale atmospheric dynamics [18, 19]. The abundance of heavy elements

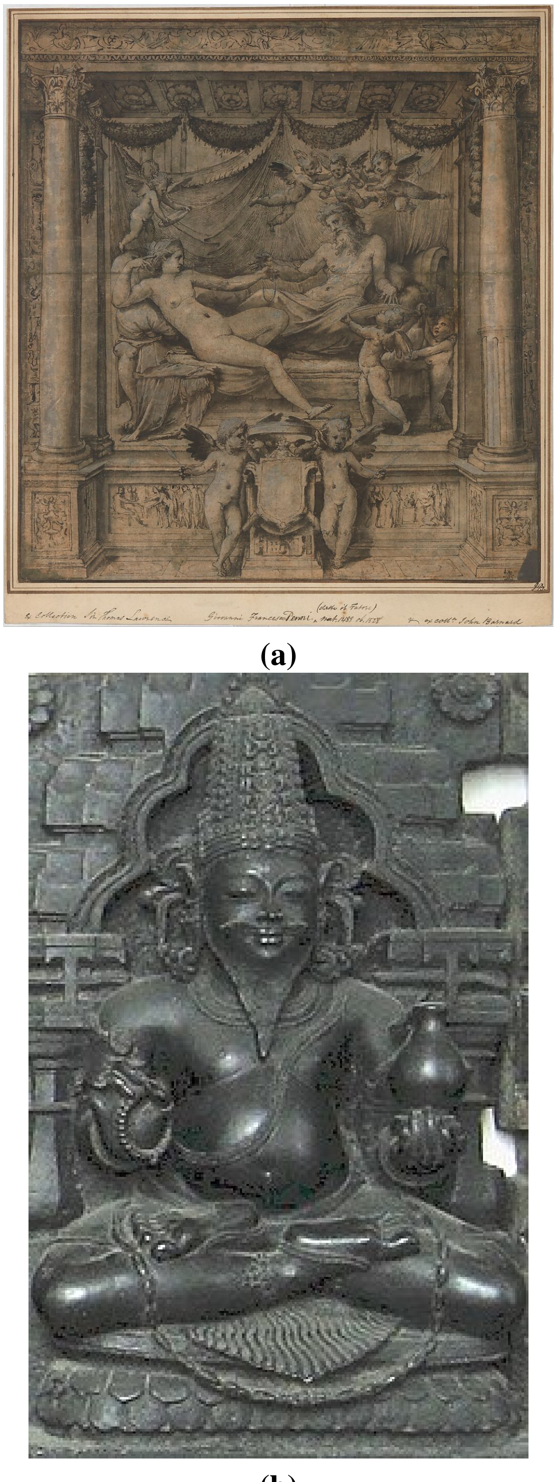

(a)

(b)

Figure 1.2: (a) Jupiter and Juno: Study for the ”Furti di Giove” Tapestries. Artist: Perino del Vaga (Pietro Buonaccorsi) (Italian, Florence 1501–1547 Rome). (b) Brihaspati, British Museum sculpture: 13th century, Konark, India.

is represented in terms of metallicity, i.e., the ratio of elemental abundance to their protosolar values. The solar photospheric abundances are correlated with the abundance of heavy elements in the protoplanetary disk. Aspund et al., (2009) [16] provides a review of solar photospheric abundances of all chemical elements up to Tungsten (W). In astronomy, stellar metallicity refers to the abundance of Fe in stars. Fe is important to understand the evolution of nuclear fusion processes inside the stellar interior. However, detection of Fe is difficult in planetary atmospheres, due to their reactivity and sequestration in gas giants.

Planetary bodies have been discovered around other stars, and advances in optical technology and data processing techniques have improved detection techniques over the last few decades. To date more than 5000 exoplanet candidates have been detected [191, 72]. A large proportion of these exoplanets are gas giants belonging to the class of hot Jupiters or sub-Neptunes [22]. Neither of these classes has a representation in our solar system. However, understanding Jupiter and other gas giants provides us with a baseline to understand the planetary evolution in other stellar systems.

1.1.3 Jupiter: Atmosphere

Jupiter's atmosphere consists of a series of gaseous layers present in the envelope of the gas giant above more than 95 percent of planetary radius [127]. The thin envelope is composed of hydrogen, helium, and several cloud and haze forming volatiles like CH_4, NH_3, H_2S, and H_2O. Like Earth's atmosphere, Jupiter has a stratosphere consisting of hydrocarbon ice and hazes with an inversion in temperature structure between 0.1-0.01 bar [205]. Its chemical composition is actively shaped by photochemical processes due to solar EUV radiation causing dissociation and ionization of major constituents like hydrogen, helium, and methane [204] [257] [101].

Just below the stratosphere, a weather layer is formed between 0.7-10 bar pressure levels. This region forms the Jovian troposphere, constituted by clouds of NH_3, NH_4SH, and H_2O (Fig.

1.3). Jupiter emits more heat than the solar insolation it receives, which controls the atmospheric convection [170]. Phase change processes, and latent heat exchange due to water vapor combined with a fast planetary rotation cause various dynamical processes in this region. Mean meridional and vertical transport cause long-term changes exhibited by changes in vapor concentration, and thermal radiation [110].

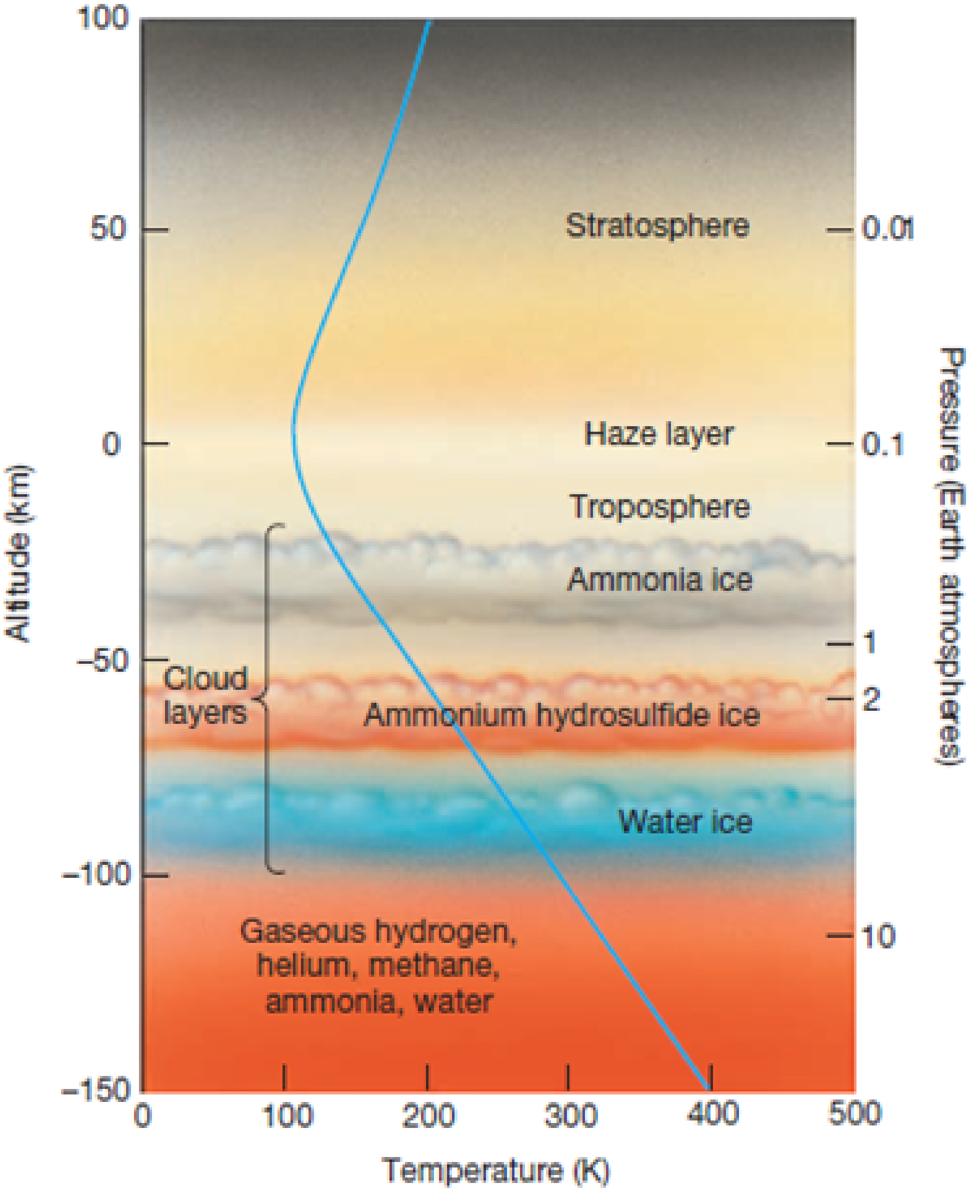

Figure 1.3: Illustration depicting pressure and temperature conditions for Jupiter's cloud decks. Image credit: GAPT/IAA

The Galileo Probe mass spectrometer (GPMS) provided the first and only direct measurement of Jupiter's atmospheric composition between 1 and 22 bar pressure level [211, 19, 290]. The abundances of volatile condensates suggest them to be $\sim 3 \times$ solar except for He, Ne, and O. The noble gases He and Ne were found to be depleted in Jupiter's troposphere. One explanation is given by the sequestration of noble gases in Jupiter's interior due to lower miscibility in hydrogen. Helium is expected to form liquid droplets, trapping some amount of Ne in them [178, 286]. The story of Oxygen is described in the next section. It is connected to the dynamics of the Jovian atmosphere.

Under high-pressure conditions of the Jovian deep atmosphere, chemical constituents are expected to be in thermochemical equilibrium [105] except for species like PH_3, CO, GeH_4 and SiH_4. The tropospheric abundances of CO and PH_3 appear to be much higher than their equilibrium concentrations [36, 97]. The timescale associated with their chemical quenching is expected to be much larger than the dynamic mixing timescale. Thus, atmospheric updrafts cause mass transport of disequilibrium species to the tropopause level. As convection and mixing processes are largely controlled by water clouds, their diffusion is connected with the atmospheric oxygen inventory. Wang et al., (2015, 2016) applied one-dimensional chemical kinetic models to study the effects of eddy mixing on CO and PH_3 [279, 280]. Hyder et al. (2024) extended the analysis by simulating moist convection-dominated tracer transport [146]. The latter highlighted the role of convective inhibition due to H_2O condensation and constrained the oxygen abundance to be super-solar.

At pressures exceeding 100 bar, clouds of alkali metals, alkaline earth metals, iron, and silicates are expected to form, sequestering heavy element inventories at deeper levels [27, 105]. The inventory of these metallic elements governs the cooling rate of Jupiter's released internal heat. There is no direct measurement of metallic elements. Guillot et al., (1994 a,b) [125, 124] predicted alkali metals to undergo thermal ionization in high-temperature conditions deep below the water clouds [125, 124]. Thermal ionization provides a significant contribution to the Rosseland mean opacity, defined as the weighted mean of all opacity sources over the entire range of the electromagnetic spectrum. Mathematically, it is expressed as:

$$\frac{1}{k_R} = \frac{\int_0^\infty \frac{1}{k_\lambda}\frac{dB}{dT}d\lambda}{\int_0^\infty \frac{dB}{dT}d\lambda} \tag{1.1}$$

Here, k_λ is monochromatic absorption, B is the Planck function and T refers to atmospheric temperature. The limits of integral signify coverage of the entire electromagnetic spectrum. Due to the characteristic shape of the Planck function, opacity sources ranging from visible to near-infrared wavelengths are generally considered. Based on the Rosseland mean opacity, and atmospheric temperature structure, one can determine the radiative and adiabatic gradients. If the adiabatic gradient is smaller than the radiative gradient, there is an onset of convection, also known as the Schwarzchild criterion [243].

The absence of alkali metals hints at the presence of a radiative layer between 1 and 9 kbar [127]. Cavalie et al., (2023) pointed out that the presence of a radiative layer is also expected to directly influence the interpretation of disequilibrium species in the context of the deep oxygen inventory [66]. The presence of a radiative layer inhibits large-scale convection and causes Jupiter to lose its internal heat much faster. The inclusion of a radiative layer in planetary evolution models predicts Jupiter to be younger by a timescale of a few Myrs based on present values of temperature and luminosity [126]. Thus, the abundance of alkali metals is closely tied to the origin and evolution of Jupiter.

For our study, we defined Jupiter's deep atmosphere as between 100 bar and 10 kbar. Juno MWR is not sensitive to pressure levels deeper than 10 kbar. At higher pressure levels, the EoS diverges from the ideal gas law and eventually transitions towards a region of H_2-He immiscibility. Figure 1.4 shows a four-layer model of Jupiter's internal structure [195].

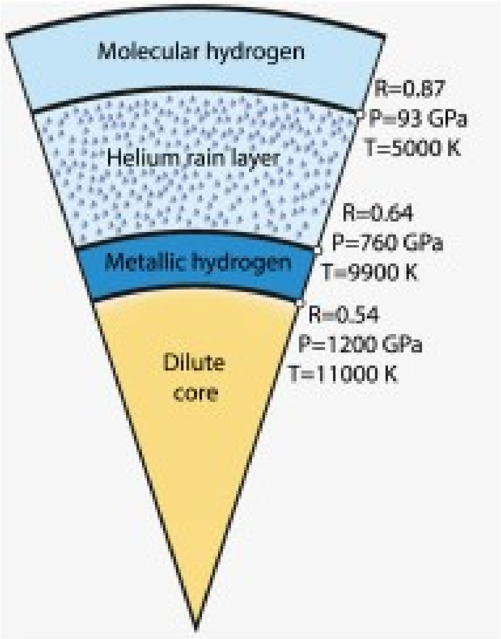

Figure 1.4: Four-layer model of Jupiter's atmosphere. The helium rain boundary lies at 87 percent of the Jovian radius, while the deep atmosphere sensitive to MWR lies beyond 90 percent of the Jovian radius [195].

1.1.4 Jupiter: Space environment

Jupiter has the strongest intrinsic magnetic field among all planets in the solar system. The interaction of Jupiter's internal magnetic field with the solar-wind-driven interplanetary magnetic field (IMF) shapes the magnetosphere. It is different from that of Earth's magnetosphere and its space environment. The difference is that the angular momentum and energy of the Jovian magnetosphere are largely driven by its internal rotation. Jupiter has a faster rotation rate, currently evaluated to be 9 hours 50 minutes, and 28 seconds. The fast rotation of the planet causes the magnetospheric plasma to co-rotate with the field itself. A large supply of charged particles is provided by the volcanic activity on the Jovian satellite Io, known to be one of the most volcanically active bodies in the solar system. The massive amount of volcanic injections and consequent ionization processes, provide a high concentration of energetic electrons and ions within the magnetosphere. A typical volcanic eruption causes injection of 100–1000 m^3/s into Jupiter's magnetosphere [82]. It largely provides a large supply of S, O, and Na atoms.

Unlike Earth's magnetosphere, Jupiter's magnetospheric dynamics are driven by planetary rotation described by Vasyliunas cycle [271]. The formation of polar aurorae is caused by the failure of plasma co-rotation. Electrons and ions precipitate along field-aligned currents in closed magnetic field lines. Recent studies from Juno have highlighted the role of Alfven waves in charged particle scattering and acceleration, evident by the presence of broadband electron distribution. The polar aurorae of Jupiter are the most powerful auroral emissions in our solar system, exhibiting its signature over a broad spectral range, i.e., radio to X-rays [275, 266]. It has a main oval co-rotating with the planet, with diffuse structures within the main oval [122]. Precipitation of electrons, protons, O, and S ions primarily contribute to these signatures at various atmospheric levels [81] [141]. It is important to understand the processes driving these polar aurorae as they provide a strong contribution to thermal structure, dynamics, and chemical transport in the upper atmosphere. Temperatures of Jupiter's upper atmosphere are observed to be larger than the contribution due to solar heating. One of the proposed solutions of the "*giant planet energy crisis*" comes from atmospheric heating due to energetic particle precipitation at the poles. Equatorward traveling thermal waves have been observed to distribute heat and increase atmospheric temperature at lower latitudes [215].

The three moons of Jupiter: Io, Europa, and Ganymede interact with the Jovian magnetic field. Io and Europa react to the magnetic field due to the presence of subsurface magma, and subsurface ocean, while Ganymede is the only moon in our solar system to possess an intrinsic magnetic field. The rotation of the Jovian satellites relative to magnetospheric plasma causes impingement of charged particles on the trailing end. Surface particle interactions influence the degree of space weathering and ion implantation in the subsurface. The Jovian satellites act as a sink of radially drifting charged particles from the outer magnetosphere.

Surrounding the main oval, one can find distinct emissions from footprints of Jovian moons: Io, Ganymede, and Europa [122]. All of these moons interact with the magnetosphere as they travel through it and act as sources of energetic electrons and ions for precipitation at the poles. Io is the most volcanically active body in the solar system. It ejects sulphur compounds like SO_2 which undergo ionization due to solar EUV and electron impact processes [207, 258]. Ejected gas escaping its tenuous atmosphere forms a toroidal cloud around Jupiter along Io's orbit. Both Europa and Ganymede interact with the Jovian magnetosphere and there is poleward transport of ions [24].

At infrared wavelengths, H_3^+ and CH_4 contribute to polar emissions [277]. H_3^+ is formed from reaction of H_2^+ and H_2 above $\sim$ 400 km above 1 bar level. Methane homopause has been observed to show a strong variation from mid-latitude (380 km above 1 bar) to main auroral oval (461 km) [63, 254]. This region of photochemically active hydrocarbon compounds shows a local increase in temperature of the lower stratosphere [206, 255]. Thereby, remote sensing of polar aurorae provides a comprehensive picture of radiative and chemical processes occurring in different regions of the upper atmosphere.

1.2 Exploring Jupiter

In the past 50 years, nations across the world have collaborated to formulate, launch, and operate scientific missions to all the outer planets: Jupiter, Saturn, Uranus, and Neptune. Jupiter's massive structure and gravitational field act in favor of outer solar system exploration efforts. It is a primary candidate for spacecraft flyby to provide a natural delta-V to reach outer orbits. A list of all flyby and missions to Jupiter is provided in Table 1.1.

Both the Pioneer and Voyager series of spacecraft have provided crucial information on Jupiter's atmosphere, gravity field, and mechanical properties of its moons. Leveraging the wealth of knowledge from satellite flyby, Galileo mission was designed to conduct detailed investigations of Jupiter and its satellites. It consisted of an orbiter and atmospheric probe

Table 1.1: List of missions and flyby to Jupiter including the upcoming planned missions

Mission	**Launch date**	**Date of orbit insertion/flyby**
Pioneer 10	March 2, 1972	December 4, 1973
Pioneer 11	April 5, 1973	December 3, 1974
Voyager 1	September 5, 1977	March 5, 1979
Voyager 2	August 20, 1977	July 9, 1979
Ulysses	October 6, 1990	February 8, 1992
Galileo	October 18, 1989	December 7, 1995
Cassini Huygens	October 15, 1997	Dec. 30, 2000
New Horizons	January 19, 2006	February 28, 2007
Juno	August 5, 2011	July 5, 2016
JUICE	April 14, 2023	July 2031
Europa Clipper	October 14, 2024	April 11, 2030

designed to provide in-situ measurements of isotopic abundances of elements constituting volatiles. It reached Jupiter in 1995 almost 350 years after the demise of Galileo. Galileo probe entered into Jupiter's atmosphere and provided measurements of atmospheric composition to a depth of 22 bars, much below ammonia (0.7 bar) and water (6 bar) cloud base levels. The Galileo probe mass spectrometer measurements indicated almost all elemental abundances to be near 2-3 × solar magnitude, indicating an enrichment in Jupiter's envelope [210] [211]. However, the oxygen abundance was found to be depleted due to the descent of the Galileo probe into a relatively cloudless region [290] [249]. These regions being relatively cloudless appear to be locally bright at infrared wavelengths, also referred to as "five-micron hot spots". The existence of these hot spots is a testament to Jupiter's dynamic atmospheric conditions.

Determining the oxygen abundance is crucial to understanding the exact location of Jupiter's origin. Given the trend in the enrichment of heavy elements like C, N, S, and P; one can expect oxygen in the envelope to be enriched. In the case of Saturn, elements are expected to be 10 times enriched compared to solar values. For ice giants like Uranus and Neptune, the enrichment values are expected to be around 80–100 times solar values [20, 22]. As the atmospheres of giant planets exhibit a strong dynamic variation, a regional or global perspective is required to estimate the variation in heavy element abundances. They could be inferred from concentrations of cloud-forming volatiles like H_2O, and NH_3. Changes in vapor concentration of H_2O, and NH_3 exhibit changes in thermal radiation emitted by the planet from deeper levels. In particular, microwave frequencies can probe Jupiter's troposphere and water cloud regions [84, 87].

For this purpose, the Juno mission was proposed to study Jupiter's oxygen inventory through passive microwave remote sensing. Juno is a spin-stabilized spacecraft in polar orbit around Jupiter. This provides an extensive survey of Jupiter's atmosphere and space environment. It carries the Juno MicroWave Radiometer (MWR) instrument, which senses thermal radiation emitted by Jupiter's atmosphere at centimeter wavelengths corresponding to six different pressure levels ranging from 0.7 to 100 bar [151]. Spectral inversion of microwave thermal radiation, and limb darkening, has provided some unique insights about the meridional distribution of NH_3 vapor. Both H_2O and NH_3 vapors are enriched relative to solar abundance. NH_3 abundance is 2.7 $\times$ solar abundance [168] while recent studies have estimated H_2O abundance of deep atmosphere in range of 4-8 $\times$ solar value [164].

The orbit of Juno spacecraft provides several advantages to probe the composition of energetic particles, and survey radio and microwave emission sources from Jupiter's inner magnetosphere. Juno's energetic particle and plasma wave instrument suite provide complementary capabilities to explore the wave-particle interactions in the inner magnetosphere. Global scale magnetohydrodynamic simulations conducted on the Jovian system reveal complex magnetic field line topology due to solar wind interactions [241, 296, 89]. These structures are also evident from the morphology of auroral emissions at the poles [122]. The combination of in-situ plasma and auroral emission data provides a means to map sources of charged particle precipitation.

1.3 Motivation

Here I introduce the processes that motivate the studies contained within this body of work.

The atmospheric composition of Jupiter has been explored by combined analysis of remote sensing and in-situ measurements. The technique of passive microwave remote sensing provides an additional capability to study the deep atmosphere of Jupiter below water clouds. This region consists of metal and silicate clouds that control the inventory of heavy elements in the Jovian envelope, and yet it has remained unexplored. Given that Jupiter's envelope is found to be enriched in volatiles and the interior is expected to be depleted in heavy elements: "**What inferences do Jupiter's deep atmosphere provide about its compositional gradient and its effects on the evolution of the planet ?**"

Jupiter's rotationally driven magnetic field is coupled to its upper atmosphere through the precipitation of energetic ions and electrons. Its interaction in the hydrogen-dominated atmosphere causes polar auroral emissions that govern atmospheric dynamics and temperature changes in the thermosphere and upper stratosphere. Given that Juno has detected highly energetic electron fluxes in Jupiter's space environment: "**How do high-energy electron fluxes and their variability influence the state of Jupiter's high-latitude ionosphere ?**"

Answers to the proposed questions will provide a clear understanding of Jupiter's atmosphere and its connection with the deep interior and space environment. In recent years, there has been a growing focus on understanding the effects of the deep atmosphere reservoir and space environment of exo-worlds belonging to the class of gas giants. Therefore, an understanding of Jupiter serves as a fundamental basis for comparative planetology.

Here is a breakdown of the following chapters: **Chapter 2** provides a detailed description of the Juno MicroWave Radiometer (MWR) instrument, and its observations of Jupiter's thermal radiation from the deep atmosphere. Sources of microwave opacity in the deep atmosphere are used to constrain the abundance of prominent alkali metals sodium and potassium. **Chapter 3** discusses the thermochemistry and cloud condensation processes in the deep atmosphere. We investigate the sources and sinks of free electrons and their effects on microwave opacity and chemical composition at shallow pressure levels. **Chapter 4** summarizes the Juno MWR observations of Jupiter's polar aurorae. High-energy electron precipitation processes are investigated to understand electron impact processes and energy deposition in Jupiter's upper atmosphere. A comprehensive theory of electron precipitation-driven changes, and passive microwave radiometry are applied to constrain the electron density of Jupiter's polar aurorae. In **Chapter 5**, we provide a synthesis of the works covered in previous chapters and a discussion about future possibilities of multi-instrument investigations of Jupiter's northern aurora.

CHAPTER 2

Juno Microwave Observations of Jupiter's Deep Atmosphere

2.1 Introduction

In remote sensing, microwave frequencies are of fundamental importance to understanding atmospheric and subsurface processes on Earth. A near-continuous monitoring of Earth's environment has provided a huge corpus of well-maintained data products to advance data-driven prediction systems for weather and climate applications. These techniques have been adopted for planetary applications over the previous decades. In particular, the techniques of ground and space-borne passive radiometry [94] and radio occultation have been applied to the Jovian planets.

The microwave radiometer is a passive microwave remote sensing instrument that measures the amount emitted or reflected by the target body. The instrument has a history dating back to the 1930-50 period [94]. It was primarily designed to retrieve the concentration of water vapor in Earth's atmosphere. Water vapor is a strong source of microwave absorption at centimeter wavelengths which allowed for continuous development in Earth observation and climate monitoring with extended applications to soil moisture, ice sheets, and clouds [242, 208, 152, 77]. The current state-of-the-art microwave radiometers have flight heritage in many space missions such as Aqua [156], Nimbus 5 [283], ADEOS-II [200], Aquarius [221], and SMAP [220]. Satellite-borne radiometers have a flight heritage for planetary missions like Mariner II [26], Magellan [219], and

Cassini [102]. Surface radiometric measurements of Venus have been crucial in understanding the characteristics of near-surface water vapor, emissivity, and potential sites of active volcanism. In the case of Titan, the Cassini RADAR instrument was operated in a passive radiometer mode to obtain information about surface composition and bathymetry.

Juno MWR observations of atmospheric thermal radiation are sensitive to ionization/conductivity at high atmospheric pressures. Thus, Juno provides a unique window for probing Jupiter's deep atmosphere. The analysis of MWR data at 0.6 GHz and 1.2 GHz frequencies indicates that high-temperature thermal ionization of alkali metals explains the trends in brightness temperature and its angular dependence. In this chapter, we apply microwave radiative transfer modeling to constrain the abundance of sodium and potassium in Jupiter's atmosphere at pressures exceeding 100 bars. The synergy between atmospheric chemistry and laboratory measurements of microwave opacity provides us with unique insights into the nature of rock cloud-forming alkali metals in Jupiter's atmosphere.

2.2 Microwave remote sensing of Jupiter

The microwave emission spectrum of Jupiter consists of sources from thermal and nonthermal emission features. The primary nonthermal radiation source refers to synchrotron radiation due to the acceleration of high-speed electrons in the energy belts [240] [239]. The intensity of these nonthermal sources dominates over thermal radiation at low frequencies. The field of view of Jupiter as seen from Earth will therefore explicitly capture the synchrotron radiation at such frequencies. Several Earth-based radio astronomy facilities like the Very Large Array (VLA) [86], Giant Metrewave Radio Telescope (GMRT) [37, 160], and the Goldstone Apple Valley Radio Telescope (GAVRT) [272, 183] monitor the spatio-temporal variations in the belt of radiation around Jupiter. It is a proxy for understanding the interactions within Jupiter's magnetosphere [44] [132].

Major volatiles in Jupiter's atmosphere i.e., H_2O, NH_3, and PH_3 are all active contributors to line absorption at microwave frequencies in addition to the collision-induced absorption produced by H_2 and He. The sensitivity of microwave thermal radiation to atmospheric temperature and composition is determined by the shape of its weighting function. The weighting function peak shifts radially inward with a decrease in microwave frequency. Thus, low-frequency thermal radiation provides a tool to probe atmospheric composition and structure at levels deeper than the Galileo probe, which made measurements to 22 bars. However, it is found that Earth-based observations at frequencies below 5 GHz are generally dominated (or contaminated) by nonthermal radiation sources [85]. This imposes a limit on Earth-based remote sensing of Jupiter's weather layer and deep atmosphere [85, 88]. Another caveat of Earth-based remote sensing is that the measurements have limited spatial resolution and do not resolve limb darkening [151].

Despite these caveats, VLA and ALMA have provided important measurements to capture changes in meridional and vertical structure in the Jovian weather layer corresponding to NH_3 and H_2O clouds. Spectral inversion of thermal radiation revealed changes in NH_3 vapor concentration around the north equatorial belt and mid-latitude, consistent with findings of Galileo Probe [88, 201]. In the case of Saturn, VLA provided measurements of the troposphere during a giant storm [166]. Earth-based remote sensing has been used to probe Saturn's tropospheric cloud structure and properties of ring particles in A, B, and C rings [298, 297]. Fig. 2.1 shows the HST visible images and VLA radio frequency maps for Jupiter and Saturn.

Radio occultation of Jupiter and Saturn has measured the atmospheric pressure and temperature based on the refraction of microwave signals during transmission from a spacecraft to a receiver antenna on Earth. During transmission through the neutral atmosphere, the bending of waves provides information about variations in atmospheric density and temperature [171, 128]. Current state-of-the-art atmospheric models assume a 1 bar pressure level as a datum for referencing. The temperature at 1 bar is a crucial input to these models, and uncertainties in 1 bar temperature contribute to errors in the interior structure and gravitational field. Galileo probe measured T_{1bar} to be at 166.1 K. Gupta et al., (2022) [128] provided a reanalysis of Voyager radio occultations to show an increasing T_{1bar} with latitude. Voyager radio occultations constrain T_{1bar} in the range of 167.3 to 170.3 K with 3.8 K uncertainty. In passive microwave remote sensing, atmospheric temperature and absorber concentration are degenerate terms. A reference temperature bound provides a good resolution for separating the effect of temperature and concentration. Radio occultations conducted at Saturn measured T_{1bar} to be 134.8 K, revealing Saturn's atmosphere to be colder compared to Jupiter [270]. Saturn is also expected to be enriched in volatile and heavy elements compared to Jupiter [20] [22]. Therefore, for a given microwave frequency, Saturn's atmosphere is relatively opaque to Jupiter due to the enrichment of volatile acting as microwave opacity sources. The weighting function peak shifts to shallow pressure levels in the case of Saturn. Thus, for a given range of microwave frequencies/frequency bands, measurement of thermal radiation allows us to probe Jupiter at much deeper levels compared to Saturn [166].

The ionosphere of gas giants also exhibits its effects on microwave signals during radio occultation. An Abelian transform is used to infer the total electron content and local electron density. Radio occultation experiments conducted by Pioneer 10 and 11, Voyager 1 and 2, and the Galileo orbiter have provided a detailed structure of Jupiter's equatorial and high-latitude ionosphere [193]. These electron density layers are shaped by photoionization, multipath propagation, and metallic ion layers due to meteorite ablation [206, 209].

The atmospheric cloud structure predicted by Equilibrium Cloud Condensation Models (ECCM) consists of H_2S, NH_4SH and H_2O clouds between 1 bar—1 kbar pressure [284, 105, 227]. Table 2.1 provides a summary of giant planet solar insolation and effective heat fluxes.

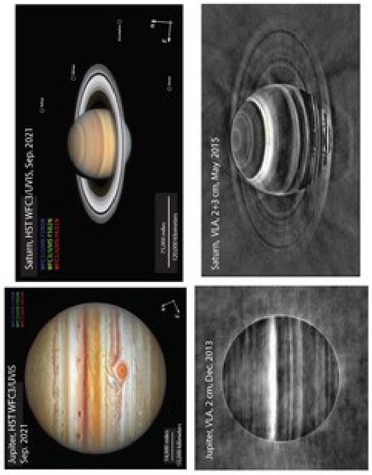

Figure 2.1: Hubble Space Telescope images and radio frequency maps constructed from VLA observations of Jupiter and Saturn [289]

Table 2.1: List of total solar insolation and heat flux emission by gas giant atmospheres

Planet	**Distance from Sun**	**Absorbed power**	**Emitted power**	**T_{1bar}**
Jupiter	5.2 AU	6.613 Wm^{-2}	14.098 Wm^{-2}	169 K
Saturn	9.5 AU	1.8-2.37 Wm^{-2}	4.83-5.01 Wm^{-2}	134.8 K
Uranus	19 AU	0.64 Wm^{-2}	0.042 Wm^{-2}	76.4 K
Neptune	30 AU	0.27 Wm^{-2}	0.43 Wm^{-2}	71.5 K

2.3 Juno

2.3.1 Orbit and instrument suite

The Juno spacecraft orbits around Jupiter in a highly elliptical orbit with a perijove centered around Jupiter's North Pole. It carries a suite of 11 instruments for scientific research and public outreach (Table 2.2). The brief description of instruments along with their names is indicated in the following table. Throughout this work, MWR measurements provide a significant contribution to extend our understanding of Jupiter's atmosphere.

The JADE, JEDI, Waves, UVS and SRU instruments provide significant contributions to our understanding of Jupiter's magnetospheric electron distribution. Data from these instruments complement the MWR observations of northern aurora, which will be discussed later in Chapter 4.

Table 2.2: List of instruments onboard Juno spacecraft

Acronym	Instrument
MWR	MicroWave Radiometer
JIRAM	Juno InfraRed Auroral Mapper
JADE	Jovian Auroral Distributions Experiment
JEDI	Jupiter Energetic Particle Detector Instrument
Waves	-
UVS	UltraViolet Imaging Spectrograph
Radio and Gravity science	-
Magnetometer	-
JunoCam	-
SRU	Stellar Reference Unit
ASC	Advanced Stellar Compass

The Juno spacecraft was launched in 2011 and inserted into Jupiter's orbit on 5th July 2016. Following JOI, the spacecraft started collecting data from its instrument suite during perijove passes. The perijove provides a closer look at Jupiter's atmosphere to resolve regional scale dynamic features and their vertical structure. Measurements of microwave thermal radiation emitted by Jupiter are important to understand the atmospheric dynamics in water and ammonia clouds. For Jupiter, Earth-based measurements are limited by synchrotron radiation that dominates over thermal emissions at frequencies below 5 GHz. Juno overcomes this limitation by passing between the planet and its surrounding radiation belts. Its unique orbital geometry provides a window to probe Jupiter's atmosphere at greater depths compared to VLA observations.

2.3.2 Juno Microwave Radiometer Instrument

The MWR instrument senses thermal and nonthermal radiations emitted by its atmosphere and plasma environment [151]. The Juno spacecraft is spin-stabilized around Jupiter in a polar orbit, with perijove near the North Pole. Its orbit provides a significant advantage for the MWR instrument in observing both the atmosphere and synchrotron radiation. MWR provides the capability to probe deeper than Jupiter's water clouds, inaccessible from Earth-based microwave observations. Thermochemical models of Jupiter's atmosphere predict the formation of exotic alkali salt clouds in addition to the presence of gas-phase NH_3 and H_2O. Thus, MWR can probe the thermal structure and composition deeper than Jupiter's weather layer to understand the heat transport in the Jovian envelope up to 1 kbar level [125, 127]. It provides support to the findings of Jovian gravity science data to infer the presence of non-adiabatic temperature profile and compositional gradients in Jupiter [142].

MWR senses the thermal radiation emitted by Jupiter's atmosphere at six different frequency channels: 0.600 GHz (50 cm), 1.248 GHz (24 cm), 2.597 GHz (11.55 cm), 5.215 GHz (5.75 cm), 10.004 GHz (3 cm), and 21.9 GHz (1.37 cm). They were chosen to target the composition and dynamics of the Jovian atmosphere, from ammonia clouds to the deep atmosphere (beyond 100 bar). These six channels together probe the temperature and concentration of major microwave absorbers like ammonia and water. Each frequency channel is sensitive in a given pressure/temperature range, determined by the peak of the weighting function (W) of the atmosphere. The weighting function (W) of the Jovian atmosphere at a given frequency can be expressed as the gradient of microwave opacity w.r.t. pressure or altitude scale. In the Rayleigh-Jeans limit, the intensity of radiation (I_λ) emitted by a blackbody is proportional to its physical temperature. MWR senses the intensity of microwave radiation with an equivalent temperature known as brightness temperature (T_b). It can be expressed as the integral of physical temperature (T) weighted over the weighting function along the depth.

$$W(z) = \frac{dt(z)}{dz} \tag{2.1}$$

$$I_\lambda = \frac{2k_B T_b}{\lambda^2} \tag{2.2}$$

$$T_b = \int_{-\infty}^{\infty} W(P)T(P)dlnP \tag{2.3}$$

Where T is atmospheric temperature, W is the weighting function k_B is the Boltzmann constant, and λ refers to the wavelength of radiation. The effective contribution of an atmospheric region to the observed brightness temperature or outgoing radiation can also be expressed in terms of a weighting function along the pressure scale. If the integral is expressed in terms of net radiance at the TOA, the integrand is referred to as the contribution function. The last two channels, i.e., channels 5 and 6 are sensitive to the NH_3 cloud region, and channels 3-4 are sensitive to the H_2O cloud regions. Channels 1-2 are sensitive to the deep atmosphere, and they are expected to be sensitive to both NH_3 and H_2O vapor absorption (Fig. 2.2).

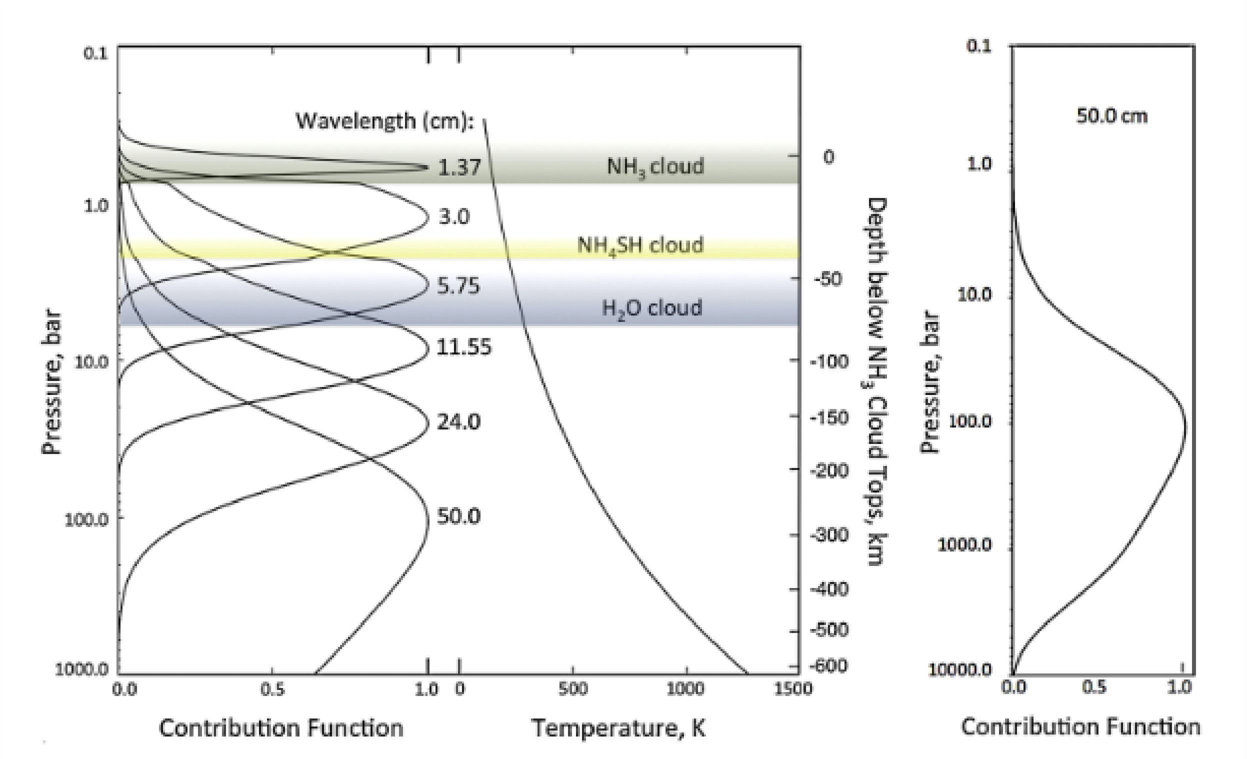

Figure 2.2: Contribution functions corresponding to the six channels Juno MWR instrument in Jupiter's atmosphere. The contribution function is the integrand of the net outgoing spectral radiance while the brightness temperature is connected to the product of atmospheric temperature and the weighting function integrated over the atmospheric column.

A spaceborne microwave radiometer provides a good spatial distribution of atmospheric thermal radiation, spanning over a range of latitudes and longitudes. The polar orbit of Juno aids in measurements of Jupiter's thermal radiation from the North to the South Pole with an adequate resolution to investigate the dynamics. It provides a unique advantage to probe the major dynamic features such as polar vortices or the great red spot at different depths to get a comprehensive three-dimensional picture of atmospheric circulation. The emission angle dependence of thermal radiation has been proposed as a physical quantity to discriminate the effects of various microwave absorbers. It complements the spectral brightness temperature measurements, and MWR can provide highly accurate measurements of the emission angle dependence. It is a derivative of the measured brightness temperature and can be expressed in terms of limb darkening ($L_d(\theta)$) such that:

$$L_d(\theta) = \frac{T_b(0) - T_b(\theta)}{T_b(0)} \tag{2.4}$$

Where $T_b(0)$ refers to the brightness temperature at the nadir and $T_b(\theta)$ is the brightness temperature of the atmosphere viewed from the spacecraft viewed at an angle θ concerning the nadir.

The MWR instrument consists of three subsystems: Antenna, Receiver, and Electronics subsystem. The antennas are located on two different external panels of the spacecraft. As the antenna size is inversely proportional to its frequency, the low-frequency channels (A1 and A2) have a larger size than the other four channels. In particular, A1 is placed on a separate panel opposite other antennas, as shown in Fig. 2.3. Therefore, channels 2-6 observe the target at the same time, and there is a time difference of about half of the spacecraft rotation time between A1 and other antennas. The design of these antennas was driven by the least surface mass density. A patch antenna array system provides the optimal surface mass density for channels 1 and 2. These channels also have two output channels for low and high gain to accommodate atmospheric and synchrotron emissions (Fig. 2.4). Their beam width is restricted to 20.6^o and 21^o following instrument design requirements. Antennas A3-A5 have a slotted array antenna design with beam width $\sim 12^o$. The largest frequency antenna A6 is designed as a corrugated horn antenna. Table 2.3 provides a summary of MWR channels, antenna design, and corresponding contribution function peak

Table 2.3: Antenna characteristics and the corresponding contribution functions

Antenna	**Center frequency**	**Bandwidth**	**Design**	**Contribution function peak**
A1	0.6 GHz	5.0	patch array	$\geq$ 100 bar
A2	1.25 GHz	5.0	patch array	20 bar
A3	2.6 GHz	4.6	slot array	7 bar
A4	5.2 GHz	6.0	slot array	3 bar
A5	10.0 GHz	4.6	slot array	1.5 bar
A6	22.0 GHz	$\geq$ 5.0	Corrugated horn	0.6 bar

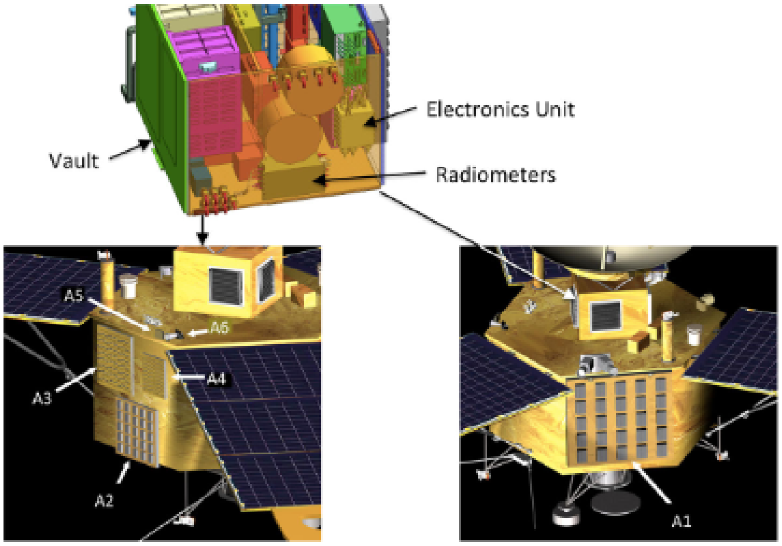

Figure 2.3: Juno MWR instrument subsystem and placement of antennae (A1-A6) on spacecraft body panels

The receiver subsystem consists of six direct-detection Dicke-switched radiometer receivers. They are placed with integral noise diodes for short-term gain calibration. The upper end of the dynamic range for each channel was set to be at least twice the expected maximum antenna temperature. The antennas are connected to the receivers using two sets of transmission lines. Both the receiver and electronics subsystem have been placed in the vault to protect them from Jupiter's ionizing radiation. A full description of the MWR subsystems is provided in the detailed engineering block diagram in Fig. 2.3.

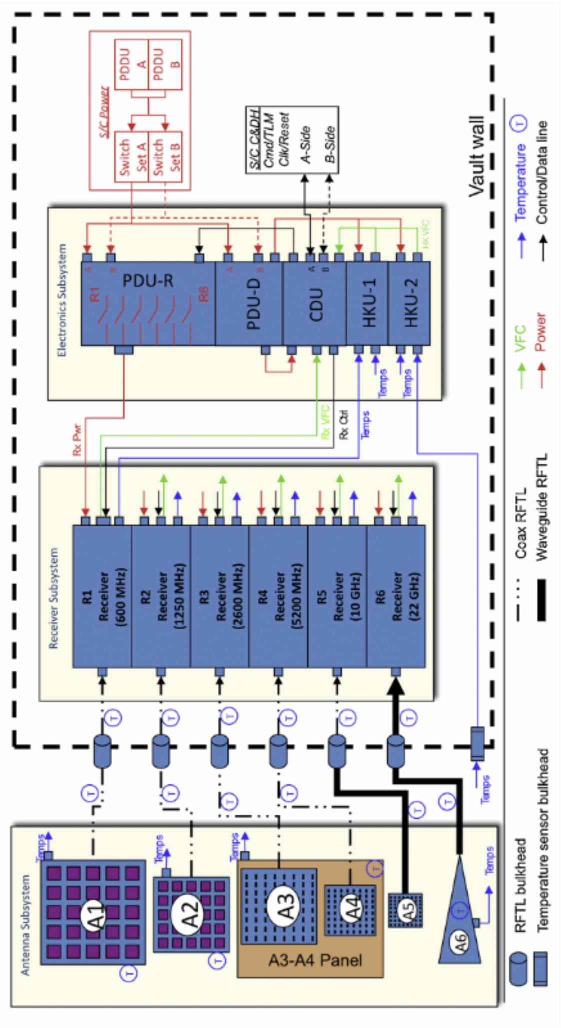

Figure 2.4: Engineering block diagram of Juno MWR instrument [151]

2.3.3 Brief review of Juno MWR results

The primary objective of Juno MWR was focused on determining the abundance of oxygen in Jupiter's atmosphere. Most of Jupiter's oxygen is contained in water vapor. Water vapor in Jupiter's atmosphere drives moist convection, cloud lightning, and the transport of disequilibrium trace species to shallower levels. In the microwave spectrum between 0.6-22 GHz, ammonia and water vapor are known to be the dominant microwave absorbers in Jupiter. Ammonia vapor exhibits a strong absorption relative to water vapor and exhibits a strong effect on the thermal emission of Jupiter at those frequencies. Juno MWR provides a highly accurate measurement of brightness temperature and limb darkening from the equator to the poles. These physical quantities have been used in synergy to perform spectral inversions of MWR observations during each perijove. A Monte Carlo-based spectral inversion was used to derive the vertical distribution of ammonia vapor assuming a hydrostatic adiabat at the T_{1bar} measurement. The inversion of MWR observations revealed a coherent variation in ammonia distribution from the equator to the pole. Near the equatorial belt at 6 deg. N ammonia vapor was found to be depleted, consistent with measurements of nitrogen abundance from GPMS [290, 168]. Furthermore, a peak was observed near the equator with an omnipresent trend of increase in ammonia concentration along the vertical direction as shown in Fig. 2.5. Overall, the nitrogen abundance from Juno MWR was found to be 2.7 times solar abundance [168, 147].

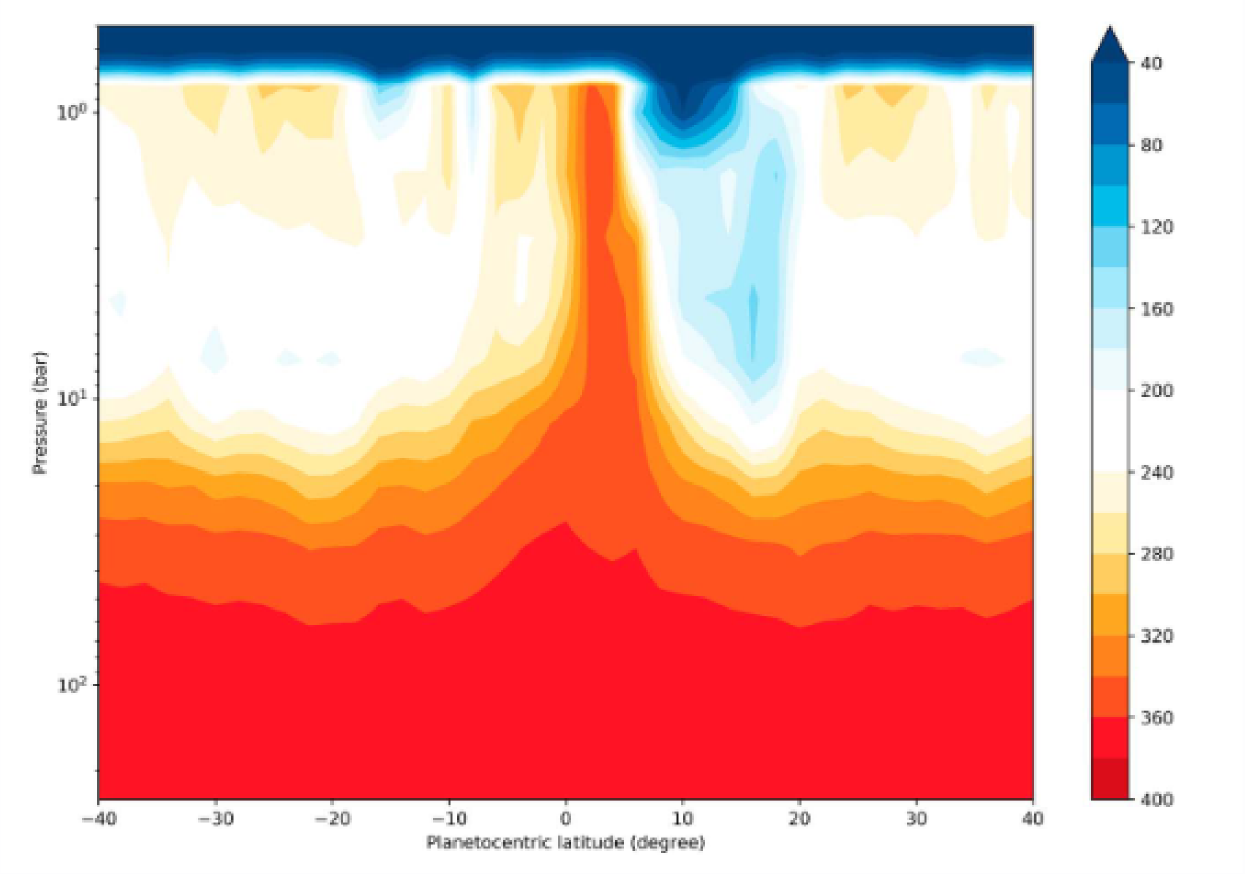

Figure 2.5: Distribution of ammonia vapor mixing ratio as inferred from inversion of MWR observations [168]

The lowest frequency channels i.e., channels 1 and 2 have detected bursts of nonthermal emissions due to lightning [56]. Lightning is expected to originate from shallow ammonia clouds and deep water clouds [30, 6]. A theoretical estimation of water cloud lightning provides a lower bound of oxygen abundance. Phase transformations and latent heat release have been found to control the mixing of trace species. A super-adiabatic temperature gradient was found by MWR measurements at the Jovian equator, which indicated oxygen abundance to lie between 1.5-8.3 times solar value [164].

Jupiter's synchrotron environment has been observed from ground-based telescopes to model its radiation environment [85, 240]. Juno MWR provides a comprehensive map of Jupiter's synchrotron radiation [239]. The new set of observations is found to have some discrepancies with previous models of Jovian synchrotron radiation due to uncertainties in knowledge of the electron energy spectra and magnetic field. Juno continues to provide measurements of energetic particles in the plasma environment of Jupiter and its satellites. Energetic electrons and ions ($\geq$ 1 keV) can enter the loss cone at the poles, causing precipitation of electrons in the Jovian ionosphere [276]. MWR channels 1-3 have observed cold antenna temperatures that can be attributed to high-energy electron precipitation process [140, 40]. Chapter 4 will discuss the physical mechanisms governing the presence of cold spots at microwave frequencies.

2.4 Jupiter's Deep Atmosphere

Phase change processes due to ongoing condensation and evaporation cause moist convection and mixing of chemical reactive trace species. At shallow pressure levels $\sim$ 0.7 bar, NH_3 undergoes condensation to form ice particles. As we go deeper, NH_3 reacts with atmospheric H_2S to form clouds of NH_4SH [267]. H_2O clouds dominate the moist convection activity driving atmospheric circulation and heat transport [148]. Understanding the cloud condensation processes is valuable for understanding the reservoirs of heavy elements at deeper levels. However, Jupiter's thick clouds provide challenges to explore the chemical abundances of heavy elements in its deep atmosphere. A knowledge of the chemical concentrations of trace species provides information about the opacity governing radiative cooling and convective inhibition. Sunlight is scattered by the aerosols consisting of NH_3, NH_4SH, H_2O clouds and stratospheric hazes made up of hydrocarbons. Thus, visible and infrared wavelengths are not sensitive to clouds below the water condensation level. Low-frequency microwave radiation provides a way of probing the atmosphere much deeper than 20 bar.

For our context, we refer to the deep atmosphere as the region of Jupiter's envelope between 20-10,000 bar. In this regime, chemical kinetic processes consist of thermochemical reactions accompanied by phase change processes. Under high-pressure conditions, these processes are expected to be under thermochemical equilibrium. Therefore, the abundances of chemical species can be estimated using thermochemical equilibrium models. Equilibrium cloud condensation models predict the condensation levels and cloud densities of Jovian clouds. Metallic elements like Li, Na, K, Mg, and Ca are expected to condense at pressure levels exceeding 100 bar [105] [227]. They react with non-metals and semimetallic elements like O, S, Cl, and Si to form clouds of their respective oxides, sulphides, chlorides, and silicates [274] [202]. The formation of these exotic clouds is expected to be responsible for the sequestration of heavy elements in the deep atmosphere [105].

Out of all metallic elements, the alkali metals Na and K have been prominently studied and detected in many exoplanetary atmospheres. They are expected to form stable clouds of Na_2S and KCl. In the case of Jupiter, we estimate the cloud condensation level of Na_2S and KCl by comparing the partial pressure of alkali metals to their saturation vapor pressures [202]. Fig. 2.6 shows the condensation curves of alkali metal clouds and their relative positions to the NH_3, NH_4SH, H_2O condensation levels.

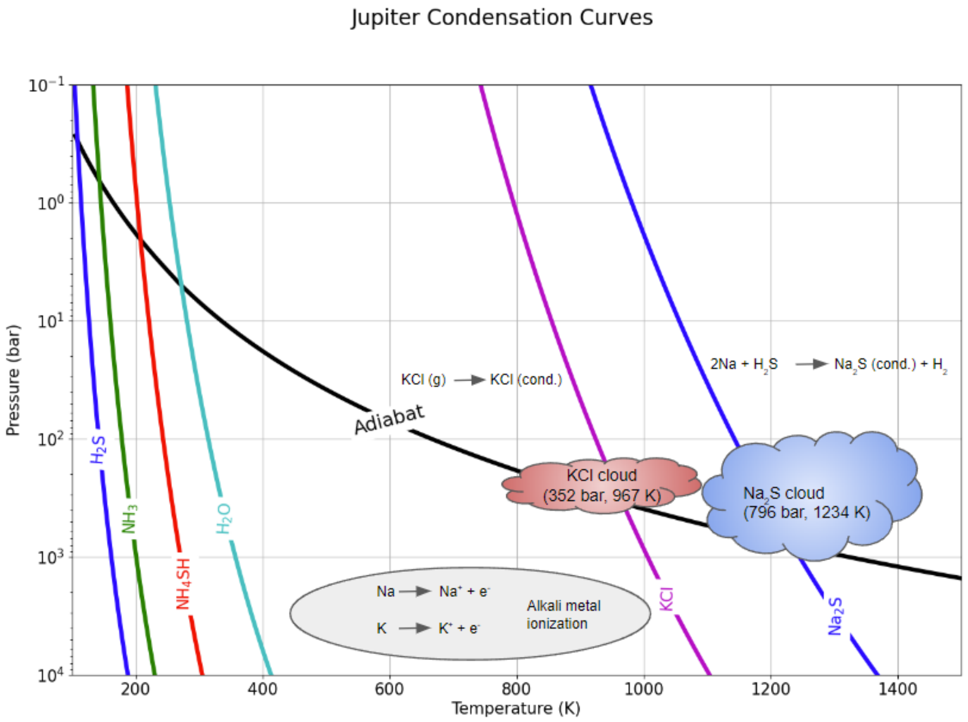

Figure 2.6: Condensation curves of NH_3, H_2O, H_2S and alkali metals Na_2S and KCl at solar abundance.Calculations are based on the equilibrium cloud condensation model [19], and saturation vapor pressure corresponding to Na_2S and KCl [274, 202]. The cloud bases are at the levels where the condensation curves cross the adiabat considering T_{1bar} = 166.1 K. Calculations in the figure were done by Pranika Gupta and Sushil Atreya

$$log(p'_{Na_2S}) = 8.55 - \frac{13889}{T} - 0.5[Fe/H] \tag{2.5}$$

$$log(p'_{KCl}) = 7.611 - \frac{11382}{T} \tag{2.6}$$

Where p'_{Na_2S} and p'_{KCl} are saturation vapor pressures corresponding to Na_2S and KCl expressed in bar. T is atmospheric temperature and [Fe/H] corresponds to metallicity. The species will undergo condensation when partial pressure is greater than the saturation vapor pressure. It is found that the alkali salt clouds will condense between 100-1000 bar.

Na and K have low ionization potentials. Under high-temperature conditions of the deep atmosphere, they will undergo thermal ionization and recombination processes [124] [125]. These processes will act in a dynamic equilibrium to provide a source of free electrons. They undergo a free-free absorption process and contribute to radiative opacity source across all wavelengths, including the microwave spectrum [124] [60].

Therefore, the lowest frequency channels of Juno MWR could be sensitive to multiple microwave opacity sources: NH_3 vapor, H_2O vapor, and free electrons from alkali metal ionization.

2.5 Microwave radiation model of Jupiter's atmosphere

Theoretical models provide a tool to test various hypotheses with the help of observations. To make a comparison between the MWR observations and theoretical knowledge of Jupiter's atmosphere, we developed a benchmark model of Jupiter's ideal atmosphere. The list of assumptions in Jupiter's ideal atmosphere is as follows:

- The atmosphere is in a hydrostatic balance
- The temperature of the Jovian atmosphere corresponds to a moist adiabatic atmosphere. T_{1bar} is used as a reference temperature to construct the adiabatic temperature profile.
- The specific heat of an atmosphere consists of a linear mixture of specific heats of its major constituents (H_2 and He) and vapors (NH_3 and H_2O). Note: CH_4, an important trace gas in gas giant planets is transparent in the microwave [32]. However, it influences the NH_3 opacity due to the pressure-broadening effect.
- Ortho and Para hydrogen are assumed to be in a state of thermal equilibrium. The specific heat of hydrogen is estimated from the mixing ratios of Ortho and Para states.
- The concentration of ammonia and water vapors is controlled by the cloud condensation process by forcing the partial pressures to be equal to their saturation vapor pressures.

We develop a one-dimensional radiative transfer model using the High-Performance Atmospheric Radiation Package (HARP) [169] [38]. HARP is written in C++ and uses the DISORT solver [260]. We solve the equation for microwave radiative transfer in a one-dimensional plane-parallel atmosphere. The Brightness temperature is calculated in terms of physical temperature, and the atmospheric weighting function as discussed previously. HARP in its present form is contained within the Comprehensive Atmosphere N' Ocean Engine (CANOE) framework, publicly available on GitHub.

Collision-induced absorption (CIA) by H_2-H_2 and H_2-He collisions are important sources of atmospheric opacity in gas giants. Collision-induced dipoles of H_2 and He are major sources of opacity at infrared wavelengths. They also contribute to opacity at microwave frequencies. We adopt the model from the HITRAN database [235] that provides high-temperature values of CIA relevant to Jupiter's deep atmosphere. Their magnitude is well constrained due to the invariance of hydrogen and helium abundances in Jupiter's deep atmosphere. Jupiter's atmosphere is also characterized by depletion in He and Ne abundance due to the sequestration of noble gases at much higher pressures. Thus, such gradients are not relevant to pressure levels sensitive to microwave wavelengths.

The microwave absorption behavior of water and ammonia vapor has been investigated by laboratory experiments that show the pressure and temperature dependence of mass absorption coefficients (Fig. 2.7(b)) [154, 93, 32]. In addition, hydrogen, methane, and water vapor contribute to line broadening in the ammonia vapor absorption. The models based on laboratory experiments show significant divergent behavior when extrapolated to pressures greater than 50 bar and 550 K [32].

For water vapor absorption at microwave frequencies, the previous laboratory models from Karpowicz (2011) [154], Devaraj et al., (2014) [93], and Bellotti et al., (2016) [32] show divergence

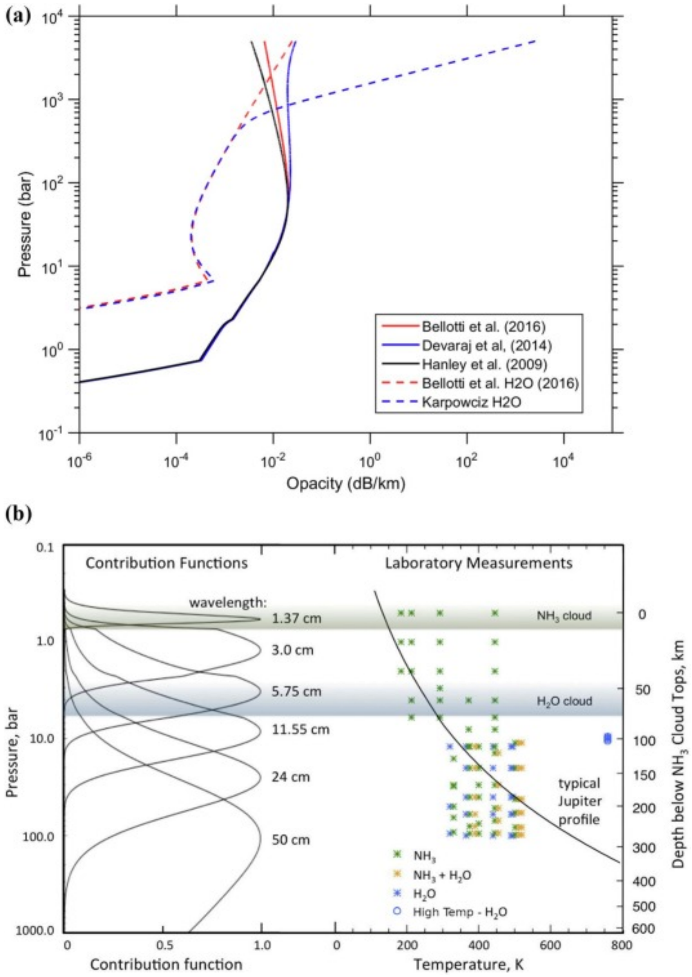

Figure 2.7: (a) Discrepancies between water vapor microwave opacity models, (b) laboratory environment physical conditions compared to MWR contribution function in the context of NH_3 and H_2O microwave opacity measurements.

in microwave opacity of H_2O vapor (Fig. 2.7(a), 2.8). However, recent laboratory measurements [261] at high pressure show that water vapor absorption can be explained by the Bellotti et al., (2016) [32] model. Therefore, the Bellotti et al., (2016) [32] model is chosen to compute the water vapor opacity, which incorporates water opacity measurements at high temperatures above 500 K.

2.6 Data preprocessing

The atmospheric thermal emission at microwave frequencies is measured by Juno MWR at different emission angles from pole to pole. From Chapter 1, we infer that Jupiter has a strong magnetic

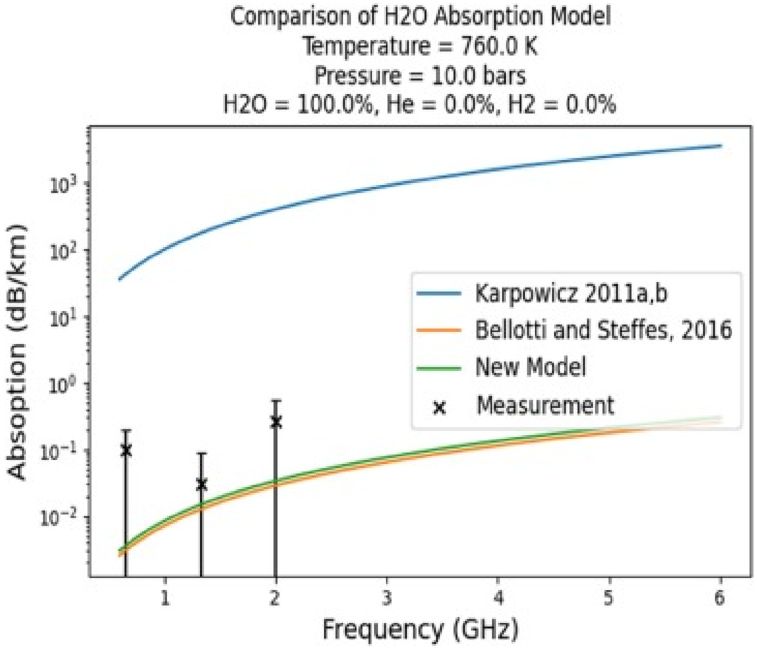

Figure 2.8: Comparison of water vapor microwave opacity model performance at high-temperature and high-pressure conditions

field, and its magnetospheric electrons achieve relativistic speeds to emit synchrotron radiation at microwave frequencies. At frequencies lower than 5 GHz, the contribution of synchrotron radiation dominates over atmospheric thermal radiation [85]. At higher latitudes above 55 deg., Jupiter's poles have an omnipresent aurora extending down to mid-latitudes at several longitudes [140, 214, 40]. Polar auroras exhibit regions of cold T_b at the lowest frequencies of Juno MWR.

Jupiter has an oblate shape caused by its planetary rotation. The planetary radii at the equator and poles are 71,492 km and 66,854 km respectively. The bulging at the equator introduces a change in the gravity field owing to the distribution of its mass. It is evident from the acceleration due to gravity at its equator (23.12 ms^{-2}) and poles (27.01 ms^{-2}). A change of 4 ms^{-2} can introduce large changes in depth between two pressure levels, thereby causing variations in observed T_b. Lower values of acceleration due to gravity would cause equatorial temperatures to be lower than the poles at the same pressure levels. Therefore, T_b is expected to increase with latitude. Additionally, the MWR instrument occasionally observes T_b showing a large deviation from longitudinal mean variation. It could be attributed to sudden changes in the local atmosphere or unknown anomalies associated with instrument data.

Thus, we summarize the sources of error for thermal emission in four categories: i) synchrotron [4], ii) polar aurorae [140, 40], iii) change in gravitational field, and iv) anomalies in T_b. These sources are due to various physical processes in the Jovian atmosphere and space environment. The latitudinal variation of T_b for channel 1 and channel 2 for PJ 1-9 are illustrated in Fig. 2.9 and 2.10.

The channel 1 and 2 T_b exhibits some variability over the PJ orbits, and planetocentric latitudes. The north equatorial belt (NEB) shows a local maximum in T_b followed by a minimum southward. This feature corresponds to variation in local NH_3 concentration as inferred from the multispectral inversion of MWR data. A generic trend is observed between the equator to mid-latitude, where T_b increases with latitude. This effect can be attributed to latitudinal changes in local acceleration due to gravity.

High latitudes above 60 deg. show a large variation in T_b. This effect is a combination of two factors i.e. Jovian synchrotron, and polar aurorae. The synchrotron emission comes in the field of view of MWR instruments at high emission angles, and high latitudes. It causes the observed T_b at 600 MHz to increase $\sim$ 1000 K. In contrast, the polar aurorae are expected to show a strong reflection of the cosmic microwave background, owing to absorption in the thermal emission from higher electron densities in the Jovian ionosphere.

The contribution of synchrotron emission can be filtered by restricting the emission angles to 50 deg. At lower emission angles, MWR measurements are solely caused by the thermal emission from the deep atmosphere. The Jovian aurora consists of the main auroral oval and surrounding magnetospheric footprints of its satellites: Io, Europa, and Ganymede. These features can extend up to 55 deg. latitude. PJ 5 is an example where T_b drops down to 550 K between 50-60 deg.

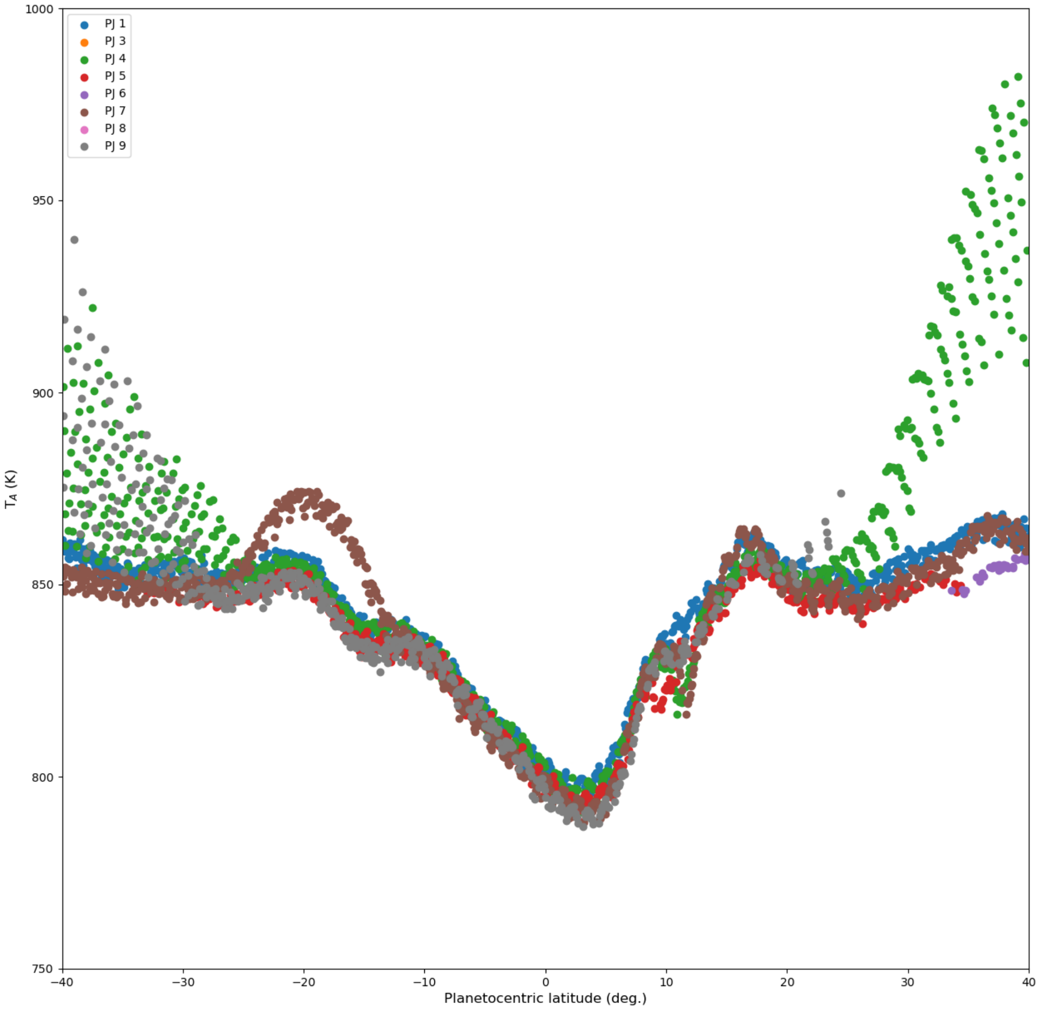

Figure 2.9: MWR antenna temperatures (0.6 GHz) for the Northern and Southern Hemisphere at planetocentric latitudes up to 40 deg.

latitude [140]. Channel 1 antenna temperatures can decrease anywhere between 100 - 300 K relative to brightness temperatures at the equator and mid-latitude values (∼ 850 K). A correlation analysis with auroral emission from Juno Ultraviolet Spectrograph (UVS) found these features to be related to the main aurora. Contributions from the polar aurorae can be minimized by restricting the MWR observations from -40 to 40 deg. latitude.

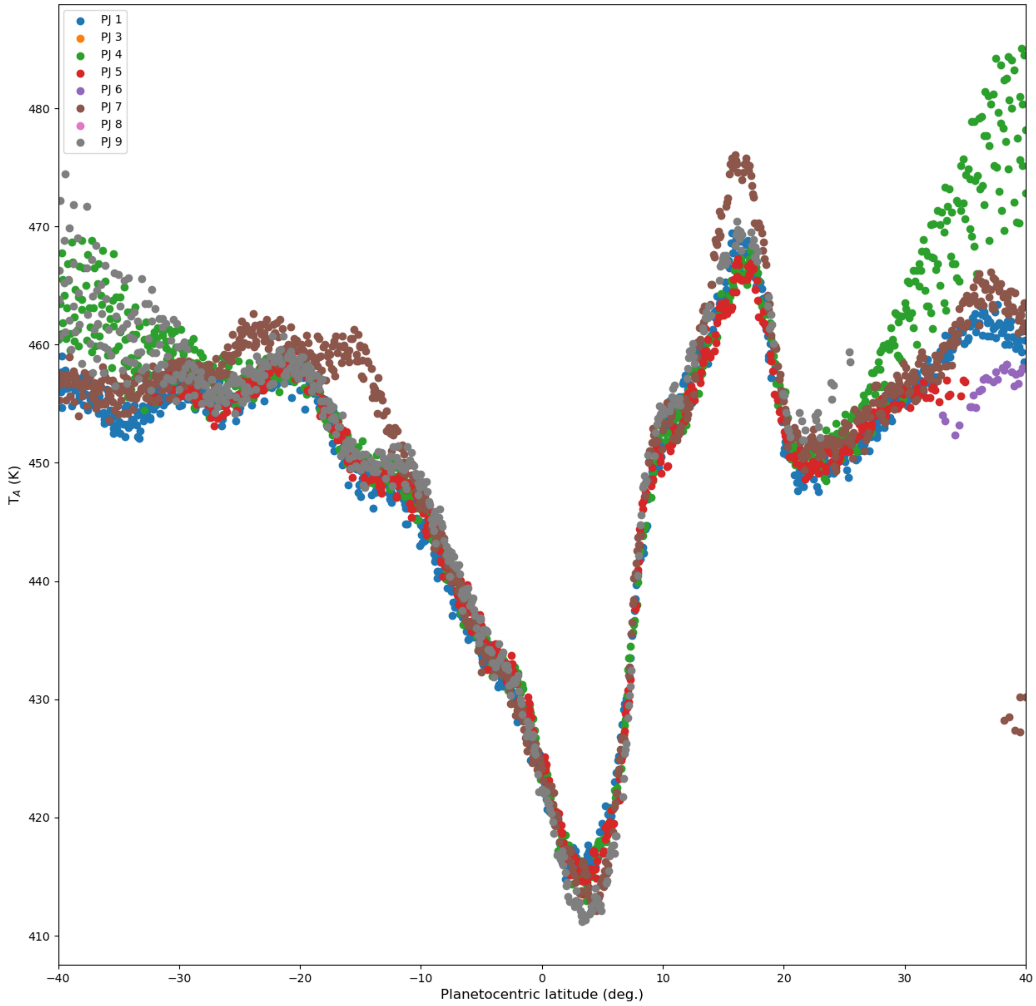

Figure 2.10: MWR antenna temperatures (1.2 GHz) for Northern and Southern Hemisphere at planetocentric latitude up to 40 deg.

The latitudinal variation in T_b can be removed by normalizing it to its equatorial value. We apply HARP to generate synthetic T_b values for each latitude at 1 deg. resolution. A correction factor is generated by dividing the equatorial T_b by its value, a given latitude. We perform a linear interpolation for the correction factor as a function of planetocentric latitude. This factor is multiplied by the MWR data to normalize the gravity to the equator. This filter removes the general variation of T_b over latitudes.

The anomalies in MWR data are eliminated using a ranking algorithm. The gravity-corrected data are analyzed for mean values and deviations. A threshold of 5 K is chosen as a filter to remove anomalies from MWR data. Thus, anomalous data points showing T_b deviations greater than the threshold are removed. The choice of threshold is determined from the local variations in T_b. The series of filters and corrections mentioned above provide us with accurate observations of Jovian thermal emission.

2.7 Juno MWR observations

2.7.1 Comparison with Juno Observations

We compare the Juno MWR observations with an ideal model of Jupiter's atmosphere as described in section 2.5. The temperature profile of Jupiter's atmosphere is constructed for two cases of reference temperatures: (i) T = 166.1 K at the 1-bar pressure level from the Galileo probe [244] and (ii) T = 168.8 K at the 1-bar pressure level based on the reanalysis of the Voyager radio occultation experiment at Jupiter [128]. The abundances of ammonia and water vapor have been assumed to be 2.7 and 5 times the solar abundance [168, 167]. Because there is no a priori information on the alkali metal abundance in Jupiter, we do not include alkali metals in the baseline case (ideal atmosphere model).

Ammonia and water vapor are considered vapors for the moist adiabat and their partial pressure is controlled by the cloud condensation process by forcing the partial pressures to be equal to their saturation vapor pressures. In the deep atmosphere of Jupiter, water and ammonia are not expected to form clouds; however, alkali metals are expected to undergo condensation. Therefore, a similar approach is applied to alkali metals to estimate the concentration of alkali metals.

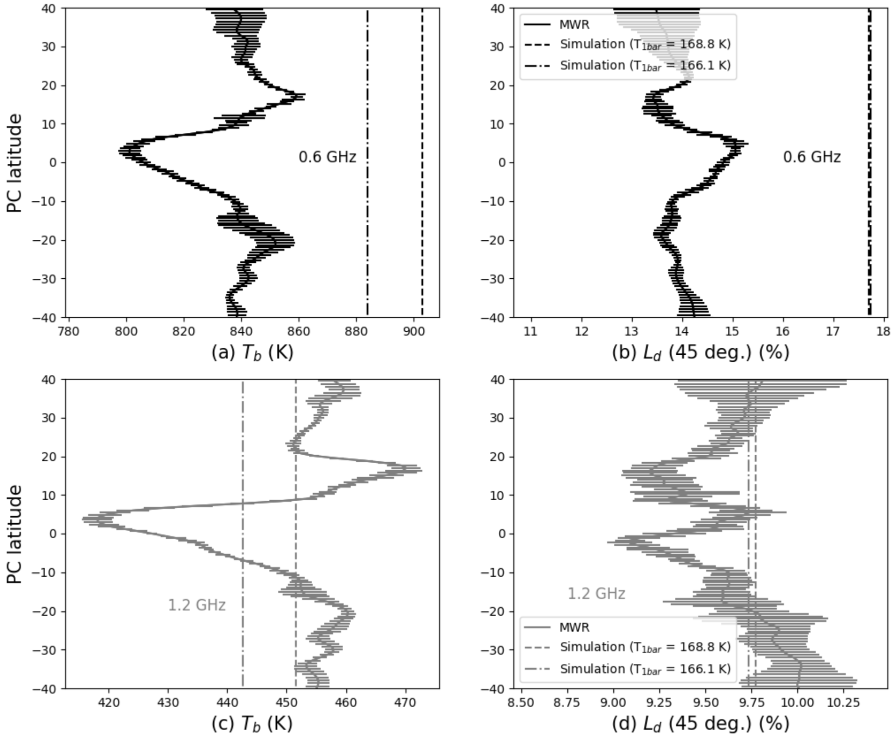

Figure 2.11: Limb darkening and brightness temperature MWR observations compared with simulation results at 0.6 GHz and 1.2 GHz corresponding to Jovian adiabats at (i) T_{1bar} = 166.1 K and (ii) T_{1bar} = 168.8 K, (a) T_b vs. latitude at 0.6 GHz, (b) L_d vs. latitude at 0.6 GHz, (c) T_b vs. latitude at 1.2 GHz, (d) L_d vs. latitude at 1.2 GHz.

A latitudinal variation in brightness temperatures is observed at both 0.6 and 1.2 GHz (Fig. 2.11, panels (a) and (c)). The small-scale variations in T_b and L_d in all the panels can be attributed to variations in the atmospheric temperature structure and composition. It is important to note that the baseline case (without alkali metals) corresponds to two different temperature profiles of Jupiter's atmosphere for two different T_{1bar}. There is an agreement between the baseline case and observations at 1.2 GHz in the equatorial region (panel (c)). On the other hand, brightness temperatures at 0.6 GHz are lower than the baseline case by 40-60 K at all latitudes (panel (a)) indicating the possibility of an additional source of opacity. Such a source is also supported by a depressed L_d observed by MWR; it is 4 percent less than the L_d magnitude of the ideal Jupiter atmosphere across all latitudes (panel (b)).

The latitudinal distribution of brightness temperatures and limb darkening from the forward model indicates the decrease in limb darkening from the equator to the pole at 0.6 GHz. It is opposite to the variation of limb darkening at 1.2 GHz across the same latitudes.

The mismatch between the baseline and observations at 0.6 GHz is much greater than the uncertainty in measurements and variations in T_b and L_d. Since the brightness temperatures correspond to different pressure regions in the atmosphere, the anomalous observations at 0.6 GHz must be attributed to the presence of an additional opacity source in the deep atmosphere or to a different opacity source that absorbs more effectively at 0.6 GHz than at 1.2 GHz. We test four confounding factors: (1) the distribution of ammonia, (2) the ammonia opacity at temperatures exceeding the range of laboratory measurements, (3) the opacity of water at high temperatures, and (4) the contribution of alkali metals.

2.7.2 Effect of water vapor and ammonia

Brightness temperature variations with latitude and the spectral inversion of brightness temperatures show a non-uniform distribution of ammonia vapor in Jupiter's atmosphere in the deep atmosphere region [168, 147]. Therefore, the non-uniform distribution of NH_3 could contribute to variations in microwave opacity of the deep atmosphere.

To estimate the effect of NH_3 concentration variations, we perturb the NH_3 profile from a homogeneous mixing condition as prescribed in the baseline model. These perturbations are based on the MWR inversion-based vertical profiles of NH_3 concentration. A scaling factor is used to vary the magnitude of ammonia vapor concentration in the model, as described in the equation below.

$$q_{NH_3}(P) = q_{NH_3,0}(P) - (q_{NH_3,0}(P) - q_{NH_3,MWR}(P))s \tag{2.7}$$

Here, q_{NH_3} is the ammonia mass mixing ratio at a given pressure *P*, $q_{NH_3,0}(P)$ is the homogeneous ammonia mixing ratio which is set to 2.7 times solar abundance for $NH_3 \sim 360$ ppm [168] from the deep atmosphere up to the NH_3 vapor saturation point. Above the saturation point, the mixing ratio follows the NH_3 saturation vapor pressure curve. $q_{NH_3,MWR}$*(P)*is the mixing ratio retrieved from MWR inversion. We use a scaling factor to vary the ammonia mixing ratio between the homogeneous case to MWR derived profiles. The scaling factor, s ranges from 0 to 1.5 where 0 is the case for homogeneous mixing ratio. Increasing s to 1 will change the ammonia profile to the MWR inversion case for the equator and mid-latitude regions. We also extend the scaling factor to 1.5, to take into account the low ammonia mixing ratio observed at the NEB of Jupiter [168].

NH_3 opacity measurements are currently not available for high temperatures ($\sim$ 550 K-3000 K) corresponding to Jupiter's deep atmosphere and there is a decrease in the magnitude of absorption of NH_3 at high pressures. Thereby, we invoke a scaling factor to the NH_3 absorption coefficient to provide an estimation of the opacity at high temperatures. The mass absorption coefficient of ammonia is estimated by multiplying the temperature-scaling law by the absorption coefficient based on [134].

$$\alpha(NH_3) \sim \left(\frac{T_c}{T}\right)^h \tag{2.8}$$

In this equation, α is the absorption coefficient of NH_3, h is the opacity factor, *T* is temperature and T_c is reference temperature equal to 750 K. The NH_3 opacity models show that the absorption coefficient peaks at 750 K and decreases at temperatures beyond 750 K. In the simulations, the scaling factor is multiplied by the NH_3 opacity at temperatures higher than T_c. The power law index (h) is varied from 1 to 5 keeping the ammonia concentration constant, i.e., 2.7 times solar abundance.

We keep the water vapor constant at 5 times solar abundance, as the laboratory measurements demonstrate that water vapor absorption does not show a significant increase with pressure and can be said to be relatively transparent when compared to the previous models of microwave absorption [261].

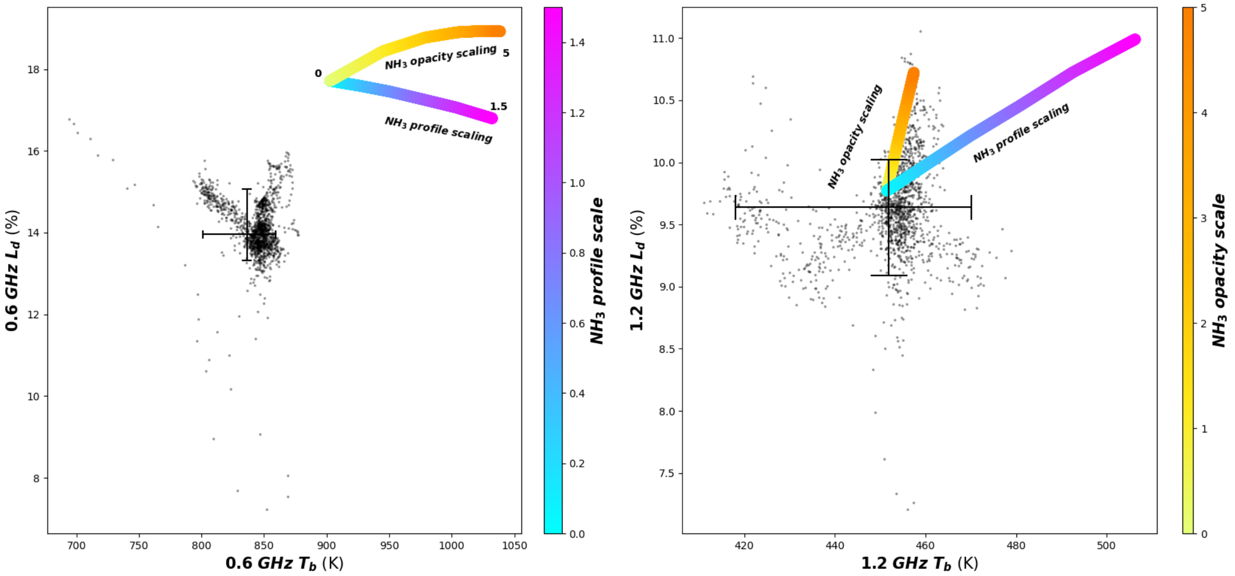

Figure 2.12: Comparison is drawn between the Juno MWR observations and the results of the radiative transfer model for T_b and L_d at 0.6 GHz and 1.2 GHz, keeping the water abundance constant $\sim$ 5 times solar abundance. Jupiter's atmosphere in the absence of alkali metals, with only variations in the NH_3 vapor profile and the NH_3 opacity

Changing the ammonia profile and introducing the additional temperature-dependent scaling factor produce brightness temperature and limb darkening divergent from MWR data at 0.6 GHz as shown in Fig. 2.12. The difference between T_b from the model and observations is in the range of 50-200 K at 0.6 GHz. Reducing the ammonia concentration causes a monotonic increase in T_b and a decrease in L_d. Further, reducing the ammonia opacity shows a similar trend in T_b, while a saturation in L_d is expected at a power law factor of 5. Changing the ammonia profile and ammonia opacity has a similar effect on T_b and L_d at 1.2 GHz.

The 1.2 GHz observations correspond to $\sim$ 20 bar (Fig. 2.12), much above the cloud base of alkali metals and at relatively lower pressure levels. By changing the ammonia concentration profile, and opacity values, we determine the projected range of T_b and L_d values at 0.6 GHz. However, the MWR T_b and L_d data is found to be lower than the forward model simulation of ammonia scaling. Despite scaling the vertical profile and microwave opacity, it can be established that variation in ammonia vapor opacity cannot solely explain the anomalous observations at the 0.6 GHz channel (Fig. 2.12).

2.7.3 High-temperature thermal ionization

At high pressures of 100 bar and beyond, alkali metals would undergo ionization to form a cold plasma, and the electrons generated in the process would act as an additional source of opacity at microwave frequencies. The number density of free electrons due to the ionization of alkali metal atoms in the gas phase is calculated using the Saha ionization [236] (Eq. 2) equation assuming Jupiter's atmosphere to be in a state of thermal equilibrium. The ionization equation itself assumes a single-component gas phase system. Thereby, we add the electron densities from the ionization of sodium and potassium to determine the total number density of free electrons. Here, N_e is the electron density, N is number density, ϵ is ionization energy, λ is De Broglie wavelength, g_0 and g_1 are statistical weights, k_B is Boltzmann constant, m_e is mass of the electron and h is Planck's constant.

$$
\begin{aligned}
\frac{N_e^2}{N - N_e} &= \frac{2}{\lambda^3}\frac{g_1}{g_0}e^{-\epsilon/k_BT} && (2.9)\\
\lambda &= \sqrt{\frac{h^2}{2\pi m_e k_B T}} && (2.10)
\end{aligned}
$$

The brightness temperatures correspond to electromagnetic radiation traveling from the interior of Jupiter radially outwards through the atmospheric layers. Thus, the transmission through the deep atmosphere is similar to the transmission through a cold plasma medium. The refractive index of microwaves propagating through a cold plasma media can be described by the Appleton-Hartree equation [139]. The formulation applies to low-temperature plasma medium, both in the presence or absence of magnetic fields. At 100-1000 bar pressure levels, the contribution of the magnetic field is insignificant in the Appleton-Hartree formulation [139]. Therefore, a simplified version of the Appleton-Hartree equation (Eq. 4) is used to calculate the complex refractive index of the deep atmosphere using the electron number density calculated from the Saha ionization equation. For an unmagnetized cold plasma medium, i.e. Jupiter's deep atmosphere, the Appleton-Hartree equation is simplified to:

$$
\begin{aligned}
n^2 &= 1 - \frac{X}{1 - iZ} && (2.11)\\
\alpha &= \frac{2\pi}{\lambda_{ch} Q} && (2.12)
\end{aligned}
$$

Here, $X = \frac{\omega_0^2}{\omega^2}$, $Z = \frac{\nu}{\omega}$, ω_0 is electron plasma frequency, ω is the angular frequency of microwave radiation, ω_h is electron gyro frequency, ν is electron-neutral collision frequency, λ_{ch} is the frequency of a given MWR channel, n is the refractive index, α is the extinction coefficient and Q is the quality factor i.e. the ratio of squares of real and imaginary parts of the refractive index.

We run a matrix of simulations by keeping Na and K metallicities fixed. The metallicity is varied from solar value to 10^{-7} times solar value. For each value of alkali metallicity, the NH_3 profile and absorption coefficients are scaled according to the previous set of simulations. It provides complete coverage of variations in NH_3 and free electron contributions.

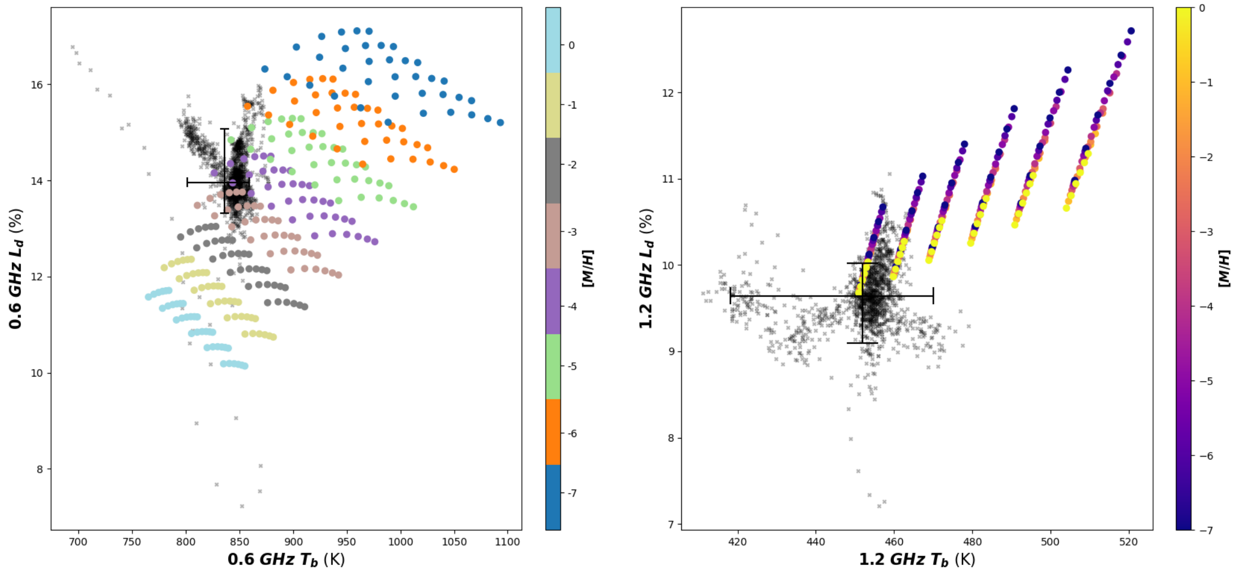

Figure 2.13: Jupiter's atmosphere in the presence of alkali metals with variations in the NH_3 vapor profile and the NH_3 opacity. The NH_3 profile of Jupiter's atmosphere is varied using a scale from 0 to 1.5 to take into account the contribution of non-uniform distribution of NH_3 vapor observed by MWR [168]. NH_3 opacity at temperatures above 750 K undergoes power law scaling as a function of atmospheric temperature (Eq. 7). In the absence of alkali metals, the changes in NH_3 vapor profile and the scaling in NH_3 vapor opacity deviate significantly from Juno MWR observations at 0.6 GHz. However, in the presence of alkali metals of low metallicity, i.e., in the range of -2 to -5, there is an agreement between model results and MWR observations. Observations at 1.2 GHz can be explained by variations in the NH_3 vapor profile and the NH_3 opacity independent of opacity contributions from alkali metals.

When we compare the new model result with MWR observations (Fig. 2.13), we observe that the model matches with observations at 0.6 GHz for free electrons corresponding to alkali metal metallicities in the range of -2 to -5 (chocolate-colored patches), i.e. 10^{-2} to 10^{-5} times the solar abundance. There is an agreement between the model and observations at 1.2 GHz for the same range of metallicities.

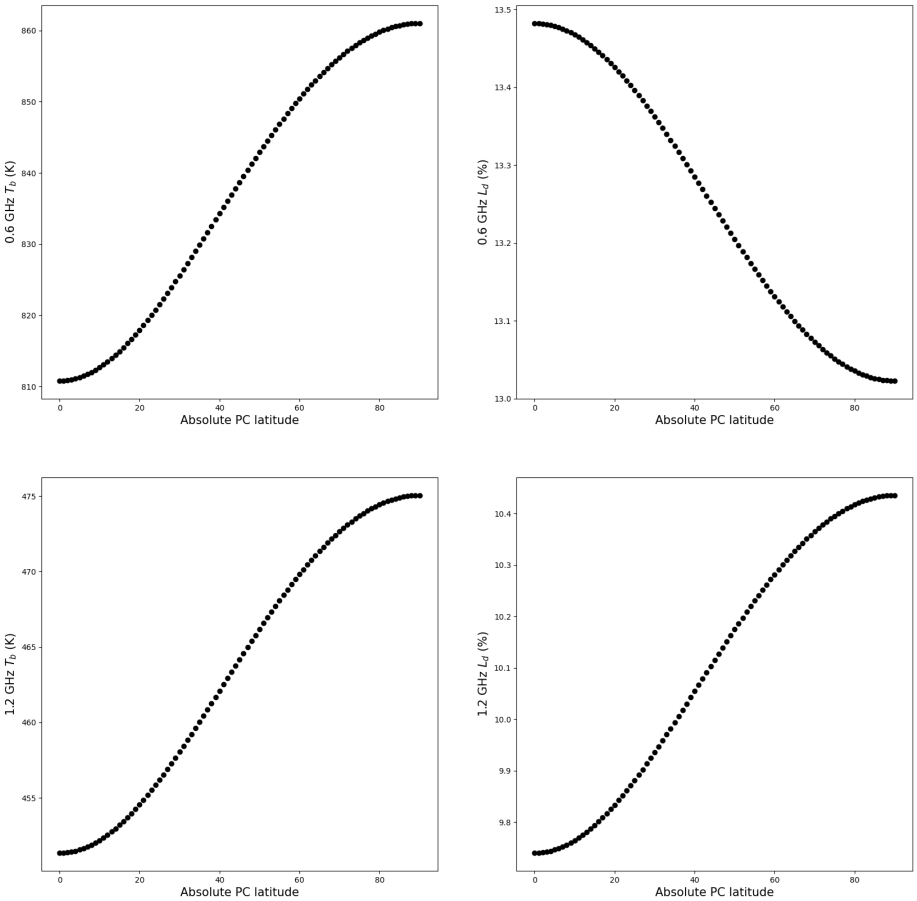

Figure 2.14: Latitudinal variation of brightness temperature and limb darkening of Jupiter's atmosphere at 0.6 GHz and 1.2 GHz at [M/H] = -3

The latitudinal distribution of brightness temperatures and limb darkening from the forward model indicates the decrease in limb darkening from the equator to the pole at 0.6 GHz. It is opposite to the variation of limb darkening at 1.2 GHz across the latitudes. This effect could be attributed to the free electrons in the deep atmosphere, which could be inferred from the shift in the contribution functions toward higher pressures in the presence of alkali metals (Fig. 2.14). Alkali metals greatly affect the absorption behavior at 0.6 GHz, which dominates the effect of gravitation on limb darkening. We expect the limb darkening to decrease from the equator to the poles assuming a uniform mixing ratio of water and ammonia vapor. It serves as a baseline to understand the sole effect of free electrons on the latitudinal variation of microwave radiation from Jupiter's deep atmosphere.

One might also expect microwave opacity contributions to ionospheric electron density layers. However, the formation of the day-side ionosphere due to photoionization does not provide significant opacity to MWR channel 1. Likewise, low energy electrons ($\leq$ 1 keV) may not provide opacity sensitive to MWR. Microwave opacity is dependent on neutral electron collision interactions. Therefore, only the high-energy electrons capable of penetrating down to lower stratospheric levels (0.01 to 1 mbar) generate sufficient microwave opacity to cause changes in MWR antenna temperatures. Radiation belt losses at high latitudes are sporadic, and therefore their contribution is not expected to be uniform across the Jovian latitudes. The topic will be extensively discussed in Chapter 4.

2.8 Sources of error and uncertainty

A continuous monitoring of antenna temperature, and its calibration, is essential to establish the uncertainties in measurements of brightness temperature. Calibration measurements are strategically conducted at both pre-launch and post-launch phases. The antenna temperature (T_a) represents the power from the antenna that is effectively transmitted to the receivers. It is a function of brightness temperature (T_b) and antenna gain (G) in different viewing directions.

$$T_a(\theta, \phi) = \int_0^{2\pi} \int_0^{\pi} T_b(\theta', \phi') G(\theta' - \theta, \phi' - \phi) sin\theta' d\theta' d\phi' \quad (2.13)$$

$$\int_0^{2\pi} \int_0^{\pi} G(\theta, \phi) sin\theta d\theta d\phi = 1 \quad (2.14)$$

Where T$_b(\theta', \phi')$ is brightness temperature from the direction of solid angle $sin\theta' d\theta' d\phi'$ and $G(\theta' - \theta, \phi' - \phi)$ is the antenna gain pointed in the direction (θ, ϕ). The calibration has two important objectives: conversion of raw count in receivers to brightness temperature values and accounting for temporal variations in the output. An instrument model is developed to relate antenna temperature to the raw counts. The first objective of calibration is also referred to as absolute calibration. Absolute calibration of the radiometer is achieved with the help of hot and cold targets of different blackbody temperatures. These targets are observed through the antenna to determine the absolute gain. Tests are performed at both component and system integration levels.

Instrument thermal-vacuum test (TVAC) and end-to-end calibration tests were conducted on the instrument. Instrument temperature was controlled at the receiver and antenna ends to introduce thermal gradients in the system. A microwave calibration system (MCS) developed at the University of Michigan was used as a stable cold load for the radiometer. With the help of a reference load and additional noise from a noise diode, four stable calibration points are obtained. A calibration end-to-end test was performed to check the calibration of the integrated system. The absolute calibration was verified using a 2 x 2 m temperature-controlled target and the uncertainty was found to be about 2 percent.

The uncertainty associated with limb darkening is primarily due to three factors: i) antenna beam side lobe levels, ii) uncertainties with the side lobe levels, and iii) observation geometry and global brightness temperature of the background sky. An antenna pattern correction was devised based on the overall antenna gain, and gain associated with the mean beam. Central lobes of MWR antennas are approximated using Gaussian distribution with half-power bandwidths. The uncertainty in limb darkening is estimated using a Monte Carlo method for temperature perturbation. A standard radiative transfer program JAMRT is used as a thermal emission model to compare it with antenna perturbation. It provides a quantification of limb darkening uncertainty as a function of emission angles and latitudes. Uncertainties are minimal at low emission angles and eventually reach a peak at ~ 45 deg.

Brightness temperatures of Jupiter's atmosphere are measured relative to the background sky. The contribution of all-sky brightness temperature is taken into account by adding it to foreground measurements. The baseline for brightness is the Cosmic Microwave Background Radiation, approximately equal to 2.7 K. However, there are contributions from discrete emission sources from energetic electrons, especially near the galactic center. To measure these discrete sources of emission, Juno MWR was turned on during most of the cruise phase. It produced a map of all-sky brightness temperature and Cosmic Microwave Background at the MWR microwave frequencies. The sky observations collected for varying instrument temperatures were used to adjust the instrument model temperature coefficients to maintain absolute calibration. Additionally, the continuous operation of MWR during the cruise phase provided a detailed analysis of the performance characteristics of the radiometers and strategies for optimum calibration. Tests were also conducted to check the presence of electromagnetic interference and thermally induced effects. However, the instrument performance was found to be normal. The uncertainties in antenna temperature and limb darkening for all channels are summarized in Table 2.4.

Table 2.4: A breakdown of prelaunch calibration error for limb darkening measurements MWR channels

	Ch 1	**Ch 2**	**Ch 3**	**Ch 4**	**Ch 5**	**Ch 6**
Measurement noise (5 s avg.)	0.031	0.027	0.026	0.032	0.023	0.029
Antenna temperature calibration (ATC)	0.054	0.054	0.042	0.063	0.069	0.075
Antenna pattern correction (APC)	0.070	0.050	0.010	0.010	0.008	0.003
Net error in R (percent)	0.094	0.078	0.05	0.071	0.073	0.081

2.9 Sensitivity tests

2.9.1 Electron density and conductivity

The electron density of Jupiter's atmosphere is governed by two fundamental processes: (i) condensation of alkali metal condensates i.e. Na_2S and KCl, and (ii) ionization of alkali metals in thermal equilibrium. Fig. 2.6 shows the pressure levels corresponding to the cloud base of Na_2S and KCl based on their saturation vapor pressures. Cloud condensation reduces the amount of alkali metals available in the gas phase that act as a source of free electrons, and restricts the abundance of Na and K corresponding to their respective saturation vapor pressure. In the cloud region, the electron density is controlled by the saturation vapor pressure of alkali metals whereas, below the cloud base, electron densities are governed by the metallicity of alkali metals. Thereby, it is evident that condensation controls the electron density and, thereby, conductivity at low-pressure levels. Condensation-limited ionization is observed at low pressure (below 1 kbar) irrespective of the alkali metal abundance as the electron density lines converge (Fig. 2.15 (a)). Fig. 2.15 (a) and (b) show the presence of a kink in electron density and their respective conductivity at the cloud base, corresponding to different alkali metal abundances. However, condensation does not play a significant role in governing the electron densities at $\sim$ 1 kbar pressure level, corresponding to the global maxima in the weighting function at 0.6 GHz (Figure 1).

The electron density of the deep atmosphere is much lower than in the case of alkali metals at solar abundance. It is the true representation of the electron density of the deep atmosphere. At greater pressures, hydrogen behaves as a semiconductor and becomes the major contributor to the electron density [174]. The electrical conductivity of the atmosphere is calculated using Drude's equation. It provides an estimate of the conductivity due to the free electrons provided by alkali metal ionization.

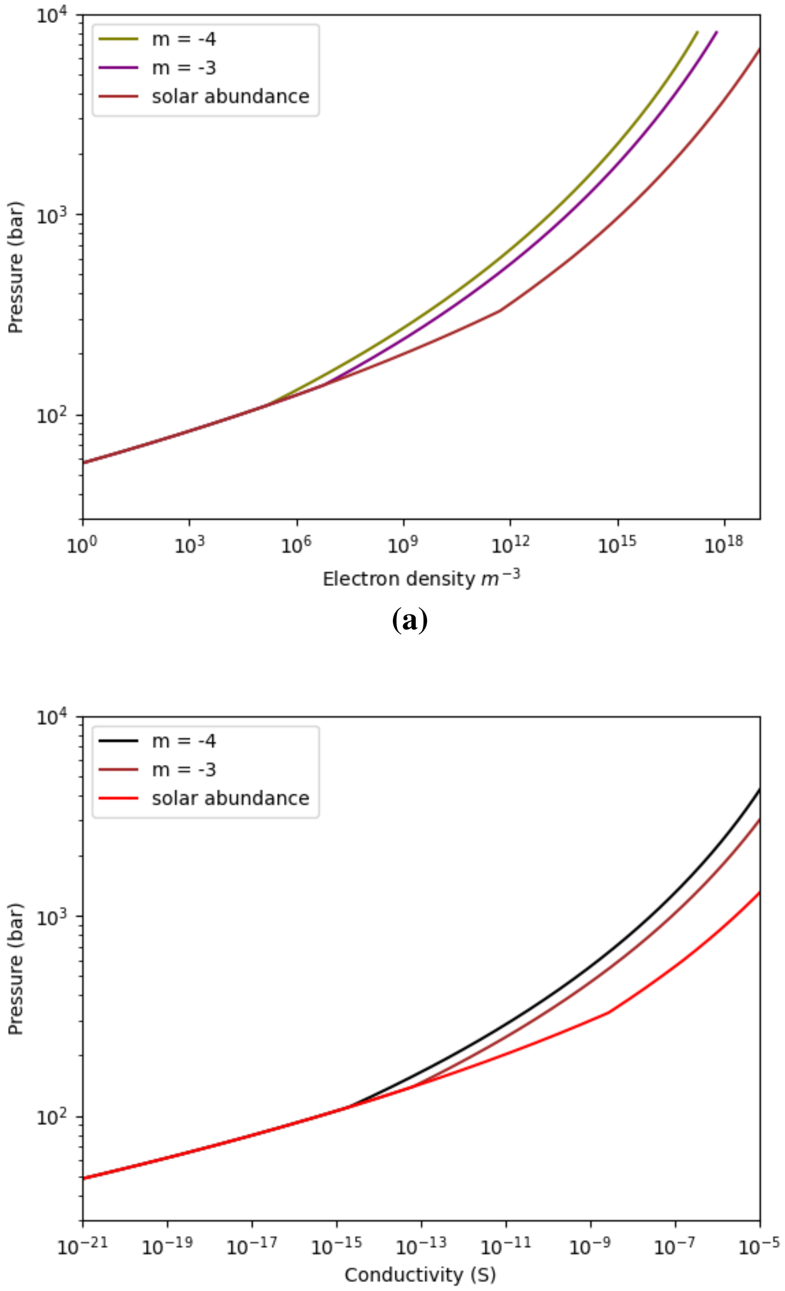

(a)

(b)

Figure 2.15: (a) Electron density of Jupiter's deep atmosphere at the solar abundance and *[M/H]* = -3 and -4, (b) electrical conductivity of Jupiter's deep atmosphere at the solar abundance and [M/H] = -3 and -4.

2.9.2 Complete sequestration of K

Even though Na_2S has a deeper condensation level compared to KCl, cloud condensation is governed by atmospheric temperature and does not reflect the chemical reactivity of alkali metals. K is more electropositive than Na and, thereby, is expected to be more reactive as compared to Na. Therefore, there may be a chemical mechanism that could selectively deplete K into other compounds, leaving Na as the only source of free electrons in Jupiter. Under such conditions, we find that Na metallicity should be in the range of 0 to -3 to match the MWR observations. The increase in alkali metal metallicities can be attributed to two factors: (i) low ionization energy of K, and (ii) Na_2S condenses much below KCl (Figure 2.6). Thereby, a larger amount of Na is required to produce enough free electrons to match the MWR brightness temperatures and limb darkening.

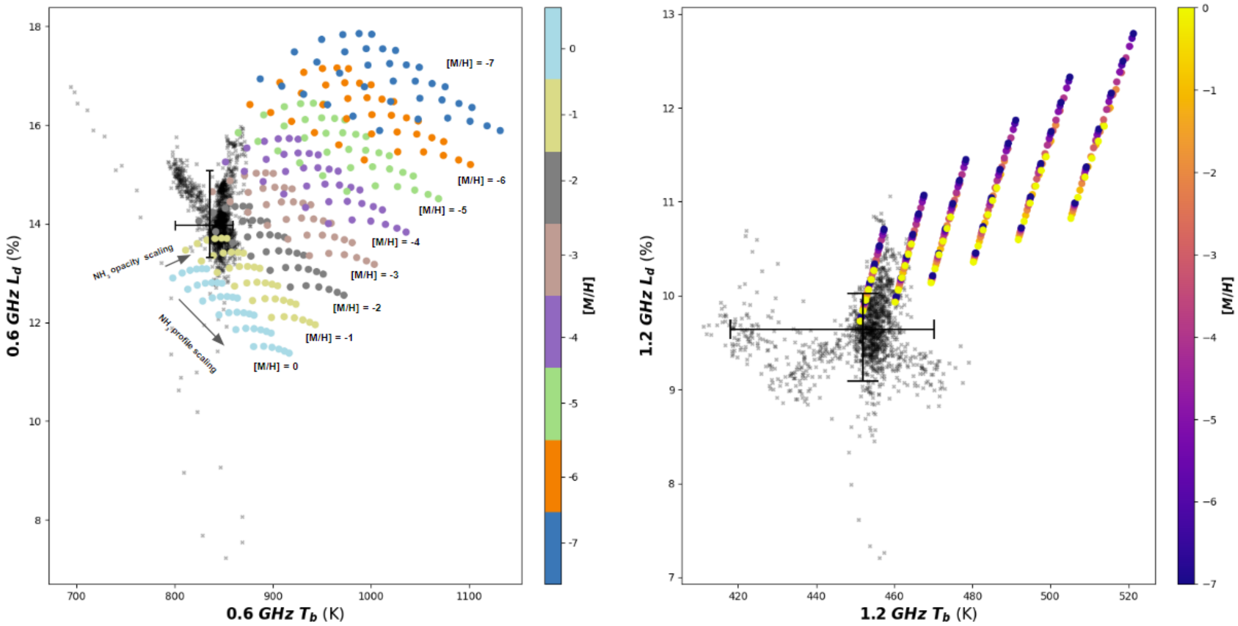

Figure 2.16: Limb darkening and brightness temperature comparison of MWR observations and forward model results at 600 MHz and 1.2 GHz for metallicities ranging from 0 to -7 at different ammonia vapor concentration profiles and opacities. It showcases the sole effect of free electrons due to the ionization of Na, without considering any contribution from K.

The elimination of K from the atmosphere highlights the role of the elemental abundance of Na required to match the MWR observations. The results of the forward model in Fig. 2.16 indicate the possible solutions of Na metallicity under different conditions of ammonia vapor concentration profiles and microwave opacities. It is observed that the range of Na metallicity is expected to be from 0 to -3 i.e. solar abundance to highly sub-solar abundance. Thus, the metallicity of Na required is expected to be higher than those considering both Na and K to be sources of free electrons.

2.9.3 Sensitivity to changes in deep atmosphere temperature

The relative weighting function for the adiabats is that of the ideal Jupiter's atmosphere without the inclusion of opacity due to free electrons from alkali metals. It shows a peak at $\sim$ 100 bar. From the difference in physical temperature of the atmosphere of the two adiabats, it is seen that the difference reaches $\sim$ 10-15 K at 100 bar level (Fig. 2.17). The weighting function at 600 MHz also extends below 100 bar which could explain the difference in brightness temperatures. An interesting observation is that the difference in adiabat temperatures increases with an increase in atmospheric pressure. This increase can be attributed to the temperature-dependent specific heat of the atmospheric constituents.

The interior models of Jupiter generally use a high temperature in the range of 170-180 K at the outer boundary (1 bar pressure level) [128, 194]. These temperatures are about 10-15 K higher than the measurements from the Galileo probe (166.1 K) [244] and Voyager radio occultation reanalysis (168.8 K) [128]. A simulation of brightness temperatures and limb darkening at 0.6 GHz and 1.2 GHz is carried out for all cases of alkali metal metallicities, ammonia concentration, and opacity variation assuming T_{1bar} = 175 K. It can be seen in Fig. 2.18 that the high temperature at 1 bar doesn't match with the entire range of MWR observations for both the frequencies. Some alternate possibilities could be the presence of a non-adiabatic gradient or a radiative layer in Jupiter's deep atmosphere that can account for a higher temperature at 1 bar level. However, the mismatch with MWR at 1.2 GHz poses a serious question on the assumption. The current

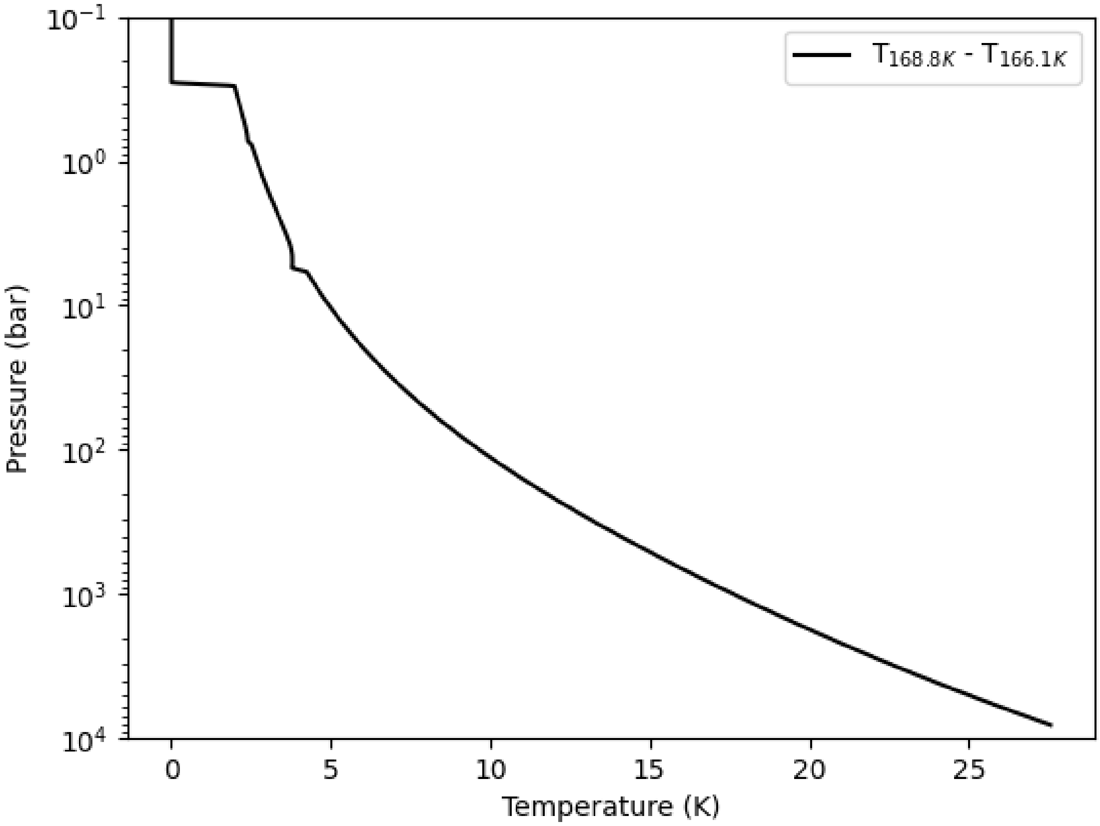

Figure 2.17: Pressure v. temperature difference in temperatures of Jovian adiabats constructed using T_{1bar} = 168.8 K and T_{1bar} = 166.1 K

measurements of temperature at 1 bar level are from limited radio occultation experiments. There is a need for radio science experiments from the equator to the poles, to estimate the true variability in temperatures at 1 bar.

2.10 Discussion

We infer the metallicity of the alkali metals in Jupiter to be much lower than the solar value. It is instructive to compare the abundance of alkali metals in Jupiter from this work with the abundance of the other heavy elements. While the opacity contribution from alkali metals suggests that Na

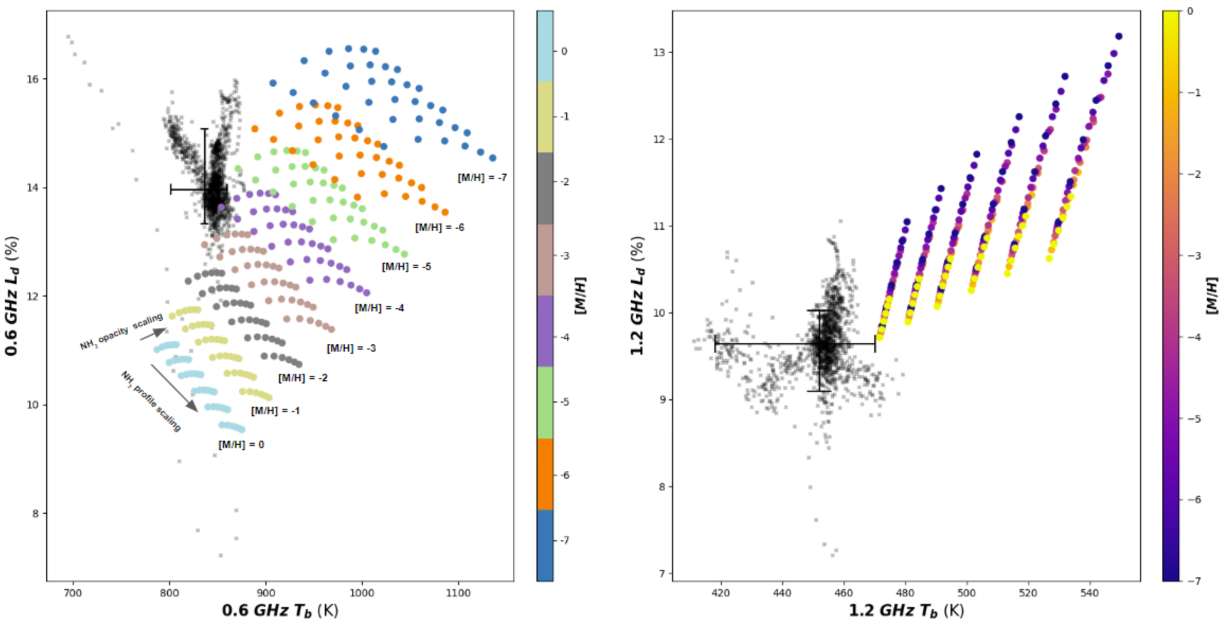

Figure 2.18: Limb darkening and brightness temperature comparison of MWR observations and forward model results at 600 MHz and 1.2 GHz for metallicities ranging from 0 to -7 at different ammonia vapor concentration profiles and opacities considering T_{1bar} = 175 K

and K are strongly depleted relative to solar at the level probed by MWR at 0.6 GHz, all other heavy elements are enriched by a factor of approximately three to five; while nitrogen is highly variable but enriched, and the water abundance remains uncertain [20], [167], [168], [181]. The comparison to other heavy metal measurements from the Galileo probe corresponds to much lower pressures, i.e. < 22 bars. The estimation of alkali metal metallicity from MWR implies lower metallicity at much higher pressures. The results (Fig. 2.13) provide an important constraint on alkali metal abundance at pressures sensitive to 0.6 GHz channel. A [M/H] = -1 for alkali metals provides too much opacity, while too little abundance or absence of alkali metals does not provide sufficient opacity to match the MWR observations at 0.6 GHz.

The low abundance of alkali metals indicated by MWR observations could be attributed to any of the following scenarios. (i) Initially enriched alkali metals, consistent with the other heavy elements in the atmosphere, are depleted by chemical reactions with other constituents deep in the atmosphere, resulting in a low abundance of Na and K at $\sim$ 1 kilobar level sufficient to provide the free electrons to explain the MWR data at 0.6 GHz. Fegley and Lodders [105] predict, for example, the formation of gas-phase species of Na and K in the atmosphere i.e. NaCl, NaOH, and KOH. Should there be chemical mechanisms that could selectively deplete K in the atmosphere, leaving Na to be the most significant contributor to free electrons in the deep atmosphere, the metallicity of Na would be expected to be in the range of 0 to -2 i.e. solar to highly sub-solar abundance (Appendix B). (ii) Unconventional planet formation processes, whereby Jupiter did not accrete a solar complement of alkali metals, or that the alkali metals are not well mixed at greater depths. This view is consistent with gravity science, GPMS, and MWR. However, if the depletion of alkali metals at $\sim$ 1 kbar inferred in this paper is representative of their bulk abundance, it could be indicative of the depletion of all rock-forming elements, with significant implications for the formation and evolution of Jupiter. Our conclusion of depletion is based on the data of the 0.6 GHz channel, whose weighting function peaks at 1 kilobar level with the inclusion of alkali metals. Thus, we are confident about the result only at this level. Alkali metals could well be more abundant deeper in the atmosphere, and they could have been depleted by some as yet unknown mechanism before reaching the 1-kilobar level, though the degree of depletion would have to be huge. The enrichment of envelope in volatile elements would require a significant amount of late infall from comets, asteroids, and meteorites. [27] considered one such possibility, where silicates were found to be a way of sequestration of gas phase alkali metals. However, a later study by [105] found it to be an ineffective mechanism. Further modeling and laboratory studies are needed to cover the full parameter space of combined thermochemistry of alkali metal and rock cloud-forming species corresponding to the very high temperature and high-pressure conditions of the deep atmosphere of Jupiter, together with any dynamical effects, before drawing any firm conclusions about the depletion of alkali metals in bulk Jupiter below the level to which the MWR data of this paper are sensitive.

The new constraints on the abundance of alkalis are linked to their low ionization potential, and the fact that the electrons that they provide directly affect opacities at 0.6 and 1.2 GHz (see Eq. 4). But when present, they are strong absorbers at visible wavelengths (e.g., [60]) and therefore directly affect the planetary radiative flux. The low abundances that we derive imply that a radiative zone may be present in Jupiter [124] [127]. Interestingly, this could explain at the same time the relatively low abundance of CO observed in Jupiter's atmosphere compared to expectations for a fully convective deep atmosphere [66].

2.11 Conclusion

In this work, we analyze the 0.6 GHz observations of low-latitude brightness temperature and limb darkening as measured by the Juno MWR instrument. The atmospheric thermal emission was found to be colder than previous models of Jupiter's atmosphere developed from GPMS tropospheric measurements. At temperatures relevant to Jupiter's deep atmosphere, water vapor appears relatively transparent at 0.6 GHz. Thus, MWR the lowest frequency channel is not sensitive to the water vapor at pressures exceeding 20-50 bar. It poses a limitation on the capability of the MWR instrument to directly determine the deep oxygen abundance.

We included an updated adiabat based on Voyager radio occultation T_{1bar} reanalysis. Microwave radiative transfer modeling of brightness temperature and limb darkening test the sensitivity to ammonia variation in Jupiter's atmosphere. The 0.6 GHz measurements are not found to be strongly sensitive to ammonia vapor variations. Ammonia is generally well mixed below 20 bar and cannot solely explain the additional opacity at deeper levels. Thermochemical models predict the formation of alkali metal clouds at regions sensitive to the 0.6 GHz channels. The inclusion of high-temperature ionization based on Saha ionization equations projects the abundance of Na and K to be sub-solar abundance. Sensitivity tests in microwave radiative transfer provide insights into the contribution of deep atmosphere temperature and alkali metal chemistry. The contribution

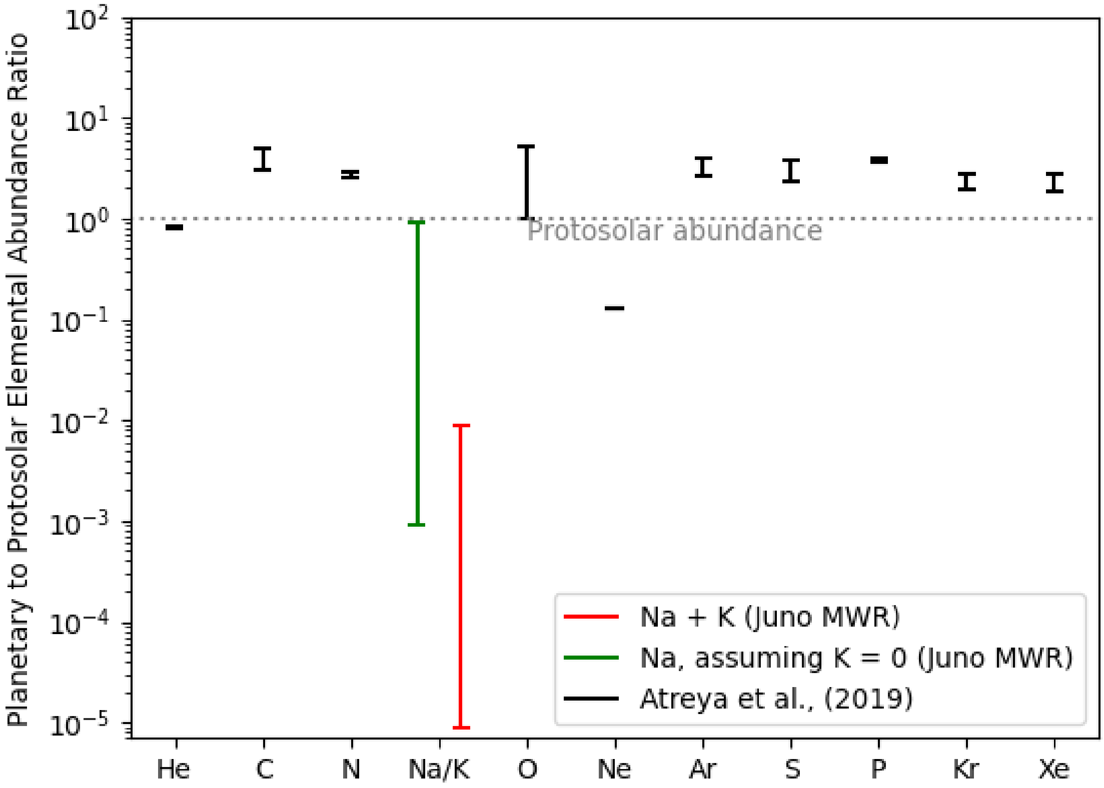

Figure 2.19: The ratio of Jupiter's heavy element abundance to their protosolar values. Juno MWR measurements hint at sub-solar abundance of alkali metals i.e. Na and K. This result is found to be inconsistent with heavy element measurements from Galileo Probe. However, the inclusion of gravity science, MWR, and GPMS hints at the possibility of a stable compositional gradient.

of additional sinks of free electrons or alkali metals can significantly contribute to elevating their abundance in Jupiter. The metallicity of alkali metals between 100 bar—1 kbar is found to contrast the enrichment of condensable volatile measured by GPMS (Fig. 2.19). Too low an abundance of alkali metals could lead to the formation of a radiative zone between 1 – 9 kbar levels.

CHAPTER 3

Thermochemistry of Deep Atmosphere and Effect of Anions on Thermal Emission at Microwave Frequencies

3.1 Introduction

In the previous chapter, we inferred that free electrons act as a major microwave absorber at the lowest frequency channel of the MWR instrument. Brightness temperature and limb darkening measurements were used to constrain electron concentration that would correspond to alkali metal metallicity ([M/H]) between -2 and -5. There is a significant contrast in the abundance of Na and K relative to other heavy elements like C, N, O, and S which are all enriched relative to their solar values (He and Ne are subsolar due to their removal in the interior, as discussed in previous chapters). In the case of alkali metals, MWR identifies the contribution of free electron density to microwave opacity to constrain Na and K from prior knowledge of atmospheric chemistry. Therefore, it is important to understand the budget of sources and sinks of alkali metals and free electrons in the deep atmosphere for a clear interpretation of Juno MWR data.

In this chapter, we analyze the role of various chemical processes in cloud formation and production of free electrons at pressures between 100 bar - 10 kbar. The principles of thermochemistry are applied to estimate the equilibrium concentrations of charge carriers and alkali salt clouds under different scenarios of deep oxygen and alkali metal abundance. Leveraging the MWR 0.6

GHz brightness temperature and limb darkening data, we provide an updated interpretation of the ongoing processes in Jupiter's deep atmosphere and the inventory of alkali metals.

3.2 Equilibrium thermochemistry of Jupiter's deep atmosphere

Equilibrium Cloud Condensation Model (ECCM) predictions show deep condensation of exotic clouds made up of alkali salts, which may store a significant reservoir of Na and K, effectively reducing the amount of alkali atoms available for thermal ionization. Both Na and K being electropositive are reactive to other atmospheric constituents containing O, S, and Cl. Gas phase thermochemical reactions can deplete the amount of alkali metals available for providing free electrons. Therefore, a significant proportion of alkali metals may be present in the form of cloud particles or stable reaction products of gas-phase reactions.

Free electrons can potentially combine with electronegative species to form anions. Major electronegative species like O, S, and Cl are generally in the form of H_2O, H_2S, and HCl. These species are stable at the Jovian troposphere but under conditions of high temperature, they may undergo thermal decomposition and reactions with metallic elements. A holistic picture of these sinks and their stability requires a full-scale modeling of atmospheric thermochemistry.

The deep atmosphere of Jupiter is an interesting region of the planetary envelope in the context of cloud formation. For pressure levels much deeper than the visible clouds, environmental conditions are suitable for the formation of exotic clouds formed from semimetallic and metallic elements i.e. Mg, Al, Si, Ca, Ti, Cr, Mn, Fe, Co, Ni, Na, K, etc. At pressures that exceed the respective cloud bases, temperatures are high enough to cause complete evaporation and thermal dissociation of complex cloud-forming compounds. However, the upper part of the planetary envelope exhibits temperatures just cold enough for condensation of elements important in rocky planets i.e. Fe, Si, and Mg. These species condense out in the deeper cloud decks, effectively getting sequestered in the local atmosphere. Table 3.1 provides the condensation pressure and temperature points for important clouds in Jupiter's atmosphere corresponding to solar elemental abundances.

Table 3.1: Important clouds and corresponding condensation at solar abundance

Cloud type	**Condensation pressure (bar)**	**Condensation temperature (K)**
NH_3	0.654	143.260
NH_4SH	2.053	208.030
H_2O	5.016	272.270
ZnS	276.038	900.240
Na_2S	796.345	1234.320
KCl	351.618	967.330
MnS	1965.960	1623.610
$MgSiO_3$	3773.872	1991.190
Mg_2SiO_4	5202.326	2207.700
Fe	11339.055	2862.210

The Jovian atmosphere is expected to have multiple cloud decks of metallic and silicate clouds. Thermochemical models of Jupiter and Saturn's deep atmosphere predict the formation of alkali metal clouds consisting of their sulphides (Na_2S, K_2S) and chlorides (LiCl, NaCl, KCl) (Fig. 3.2). These cloud particles constitute the upper deck of metallic clouds at several hundred bars consisting of many overlapping alkali salt clouds like NaCl, KCl, Na_2S and NaF. The primary alkali metals also react with atmospheric water and hydrogen to form gas-phase hydrides, oxides, and hydroxides.

Chemical reactions for alkali salt clouds:

$$H_2S + 2\,Na \rightleftharpoons Na_2S\ (s) + H_2$$

$$2\,HCl + 2\,K \rightleftharpoons 2\,KCl + H_2$$

$$2\,HCl + 2\,Na \rightleftharpoons 2\,NaCl + H_2$$

$$2\,HCl + 2\,Li \rightleftharpoons 2\,LiCl + H_2$$

Just below the primary alkali salt clouds, we expect cloud layers of ZnS, MnS, and Cu At pressure levels below, we expect high-temperature reactions to drive reactions toward the formation of two thick layers: i) Fe-Ni alloy and ii) silicate lava cloud. The silicate clouds might react with alkalis and cause additional removal of Na and K from deeper levels. However, Juno MWR is not sensitive to pressure levels much below 1000 bar even in the presence of low metallicity Na and K. Therefore, we exclude the possibility of alkali silicate reactions in the context of microwave thermal emission observations.

Chemical reactions for other metal sulphide and metal silicate clouds:

$$\mathrm{H_2S + Mn \rightleftharpoons MnS\ (s) + H_2}$$

$$\mathrm{H_2S + Zn \rightleftharpoons ZnS\ (s) + H_2}$$

$$\mathrm{Cu \rightleftharpoons Cu\ (s, l)}$$

$$\mathrm{Fe \rightleftharpoons Fe\ (s, l)}$$

$$\mathrm{Mg + 2\ H_2O + SiO \rightleftharpoons MgSiO_3\ (s,l) + 2\ H_2}$$

$$\mathrm{2\ Mg + 3\ H_2O + SiO \rightleftharpoons Mg_2SiO_4\ (s,l) + 3\ H_2}$$

3.2.1 Theory

Thermochemical equilibrium corresponds to a state of dynamic equilibrium where the rates of forward and backward reaction balance out each other for a given concentration of chemical species at a specific temperature and pressure. The exact state of the equilibrium concentrations can be numerically determined using two methods:

- Chemical kinetic evolution to steady state
- Free energy minimization

Numerical models of atmospheric chemistry use the former technique to evolve the chemical concentration using reaction rate expressions derived from ab initio or laboratory experiments.

These models are evolved over long time scales to achieve a steady state with prescribed diffusion conditions. In the case of the Jovian atmosphere, chemical kinetic models have helped provide insight into the transport of disequilibrium species like CO, PH_3, and GeH_4 [280, 146].

On the other hand, the minimization of the Gibbs free energy of a reaction corresponds to its equilibrium state without giving information on how that state may be reached. The Gibbs free energy of a reaction can be expressed in terms of enthalpy and entropy changes associated with it. One can also determine the Gibbs free energy change from the free energies associated with reactants and products. Given an initial condition for elemental abundances, the equilibrium state of other chemicals in the reaction network can be determined by the minimization of total free energy associated with all the reactions and physical transitions. The free energy minimization problem is solved numerically, analogous to mathematical optimization.

One of the caveats in the application of chemical kinetic models to the formation of alkali metals is the lack of laboratory experiments to determine the kinetic rate constants of the reactions. On the other hand, there are public databases of the thermochemical properties of metallic elements and their salts. These databases have accurate measurements of enthalpy and entropy values associated with the stable state, and their variation with temperature. Hence, the Gibbs free energy minimization method is preferred over chemical kinetic models.

For calculating the ion assemblage, we use the GGChem model. Its name stands for *Gleicht-Gewichts-Chemie*, meaning equilibrium chemistry in German. It is a code that calculates an equilibrium assemblage of chemical species, including ions, for a set of elemental abundances and temperature-pressure conditions, using free energy minimization. The code is based on the work of Gail and Sedlmayr (1986) [109] and exists in its current form in Woitke et al. (2018) [287].

Free energy minimization has been previously applied to the Jupiter and Saturn atmospheres.

However, the numerical codes are generally proprietary and do not provide a pathway for reproducing the scientific results. GGChem in its current form was rewritten in the modern Fortran 90 architecture as described in Woitke et al. (2018) [287]. It is open-source software, available on GitHub. It derives its thermochemical data from several accredited sources like NIST-JANAF [69, 68] and BURCAT [58]. The database supports all elements from hydrogen to zirconium (Z = 40) along with a special case of tungsten (Z = 74), including major ionic species. We assume Jupiter's atmosphere to be an ideal gas throughout the domain. This assumption is valid till 10 kbar pressures and diverges from other non-ideal equations of state (EOS) at higher pressures [142]. Please refer to Appendix B for standard mathematical formulations of the thermochemical data.

Let's consider a system of gaseous molecules made up of elements A, B, and C with stoichiometric coefficients a, b, and c respectively. According to Guldberg's law of mass action [34] the partial pressure of the molecule and its atomic elements can be expressed in terms of free energy:

$$\frac{p_{A_aB_bC_c}}{p^0} = (\frac{p_A}{p^0})^a(\frac{p_B}{p^0})^b(\frac{p_C}{p^0})^c exp(-\frac{\Delta G_f^0}{RT}) \tag{3.1}$$

$$p_{A_aB_bC_c} = k_p(A_aB_bC_c, T)p_A^a p_B^b p_C^c \tag{3.2}$$

$$k_p(A_aB_bC_c, T) = (p^0)^{1-a-b-c} exp(-\frac{\Delta G_f^0}{RT}) \tag{3.3}$$

$$\epsilon_k n_H = \Sigma_i s_{i,k} n_i \tag{3.4}$$

$$\rho = \Sigma_i m_i n_i = \Sigma_k m_k \epsilon_k \tag{3.5}$$

$$p = \Sigma_i n_i kT = n(\rho, T)kT = \frac{\rho kT}{\mu(\rho, T)} \tag{3.6}$$

Where p_A, p_B, p_C are the partial pressure of the atomic species. $p_{A_aB_bC_c}$ is the partial pressure of $A_aB_bC_c$. p^0 is the standard pressure. ΔG_f^0 is the free energy of formation, k is the Boltzmann constant and T is atmospheric temperature. ϵ_k are elemental abundances normalized to the hydrogen atom, n_H is total hydrogen atom density, n_i are the density of gas species, $s_{i,k}$ is the stoichiometric coefficient of element k in gas species i. In the case of charged particles, a stoichiometric coefficient for charge $s_{i,el}$ is included. For neutral species $s_{i,el}$ = 0 it equals 1 for anions and -1 for cations.

In the case of condensable species, the partial pressure is expressed in terms of a saturation ratio. If the saturation ratio is greater than unity, the species undergoes condensation, and the excess amount is removed from the gas phase by invoking saturation vapor pressure.

$$
\begin{aligned}
S_j &= \frac{p_j}{p_j^{vap}(T)} && (3.7)\\
p_j^{vap} &= p^0 exp(\frac{G^0(j[cond],T) - G^0(j,T)}{RT}) && (3.8)\\
s_{A_aB_bC_c} &= (\frac{p_A}{p^0})^a(\frac{p_B}{p^0})^b(\frac{p_C}{p^0})^c exp(-\frac{\Delta G_f^0}{RT}) && (3.9)\\
\Delta G_f^0 &= G^0(A_aB_bC_c[cond.],T) - aG^0(A,T) - bG^0(B,T) - cG^0(C,T) && (3.10)
\end{aligned}
$$

Where S_j is the saturation ratio and pj^{vap} is the saturation vapor pressure.

The solution of the system of equations is challenging due to degenerate numerical solutions at low temperatures. Using traditional numerical methods like Newton-Raphson leads to a large condition number for the Jacobian matrix at low temperatures. Moreover, the inclusion of phase change processes adds a new layer of complexity to the system of equations.

GGChem uses an adaptive method to update the network of chemical reactions by their elemental abundances. A sorting process arranges elements in order of their abundance based on user input. For each iteration, GGChem solves a small network of major chemical elements to update the concentrations of their compounds using a Newton-Raphson method. Output from this step is used as the initial condition for the next iteration (Fig. 3.1). This process goes on until the equations are solved for all chemical elements within the system.

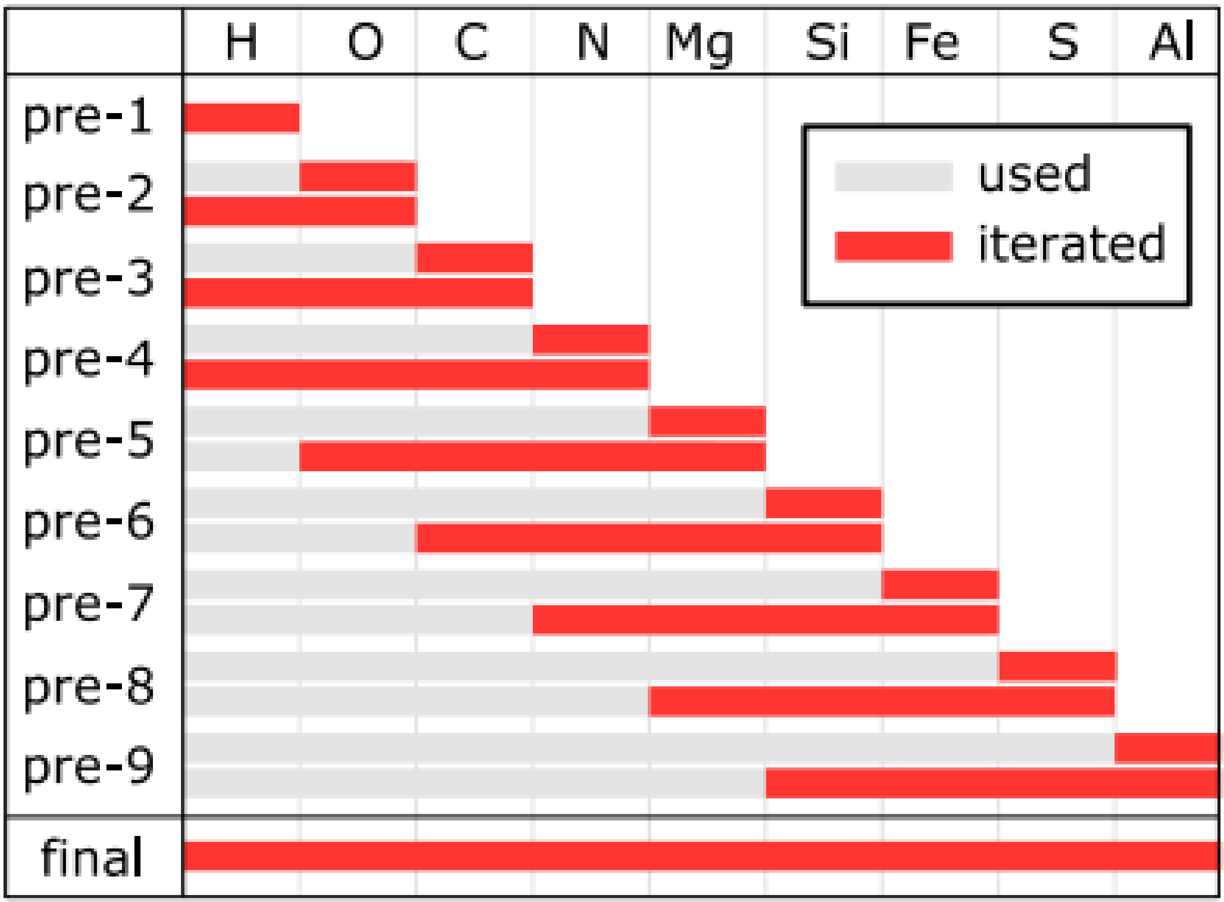

Figure 3.1: Illustration of GGChem algorithm applied to equilibrium chemistry for the total number of elements, K = 9 and number of elements taken into account during the iteration, N = 4 [287]

In the case of condensates, a compound can affect the concentration of more than one element. Changes in elemental abundances due to condensed species are expressed in a transition matrix. The concentration of dependent variables is updated over multiple iterations of applications of equilibrium chemistry and the conversion matrix. At each Newton-Raphson iteration, the algorithm makes sure that the abundances do not reach negative values. The formulation of conservation equations in the presence of condensates is expressed as follows:

$$\epsilon_k^0 = \epsilon_k + \Sigma_{j=1}^{N} s_{j,k} c_j \tag{3.11}$$

$$y_j = \Sigma_i^{N_{ind}} A_{j,i} x_i \tag{3.12}$$

$$\epsilon_k \rightarrow \epsilon_k + \delta\epsilon_k \tag{3.13}$$

$$c_j \rightarrow c_j + \delta c_j \tag{3.14}$$

Where N_{ind} refers to the number of independent variables, k is the element number and c_j refers to the concentration of condensed species j per hydrogen nucleus. N is the number of condensates and $s_{j,k}$ is the stoichiometric coefficient of element k in condensate j.

3.3 Cloud formation at high pressures: Metal and silicate cloud formation

From the list of chemical reactions corresponding to both cloud groups mentioned in previous sections, it can be concluded that cloud densities change under different assumptions of the heavy element inventory. Atreya et al. (2019) [20] used a representative value of 3 x solar for all heavy elements. However, the sub-solar abundance of Na and K as inferred from Juno MWR poses a question on the fundamental assumption of abundance relative to solar. In the case of alkali metals, their relative abundance and availability of S and Cl affect the thickness of clouds. Additionally, the inventory of oxygen and condensation of silicate contributes to sinks at deeper levels. Therefore, we study three different scenarios of heavy element inventories driving cloud formation processes:

- Low, medium, and high values of deep water abundance
- Relative depletion of Na and K reservoirs

- Effect of alkali and silicate cloud condensation

In their atomic states, electronegative species capture free electrons to form stable anions. In Jupiter's atmosphere, the primary electronegative elements are O, S, and Cl. These anions effectively act as sinks of free electrons in the atmospheric medium. Thereby, reducing the microwave opacity in the presence of a larger proportion of anions. At shallow pressure levels, O, S, and Cl are primarily stored in the form of neutral compounds like H_2O, H_2S, NH_4SH, and HCl. H_2O is stable in vapor form even at high temperatures. On the other hand, H_2S and HCl are known to be reactive with metallic species. Their inventory is distributed among gaseous and cloud-forming condensates throughout the deep atmosphere (Fig. 3.2). Therefore, we study three different scenarios of thermochemical equilibrium driving free electron and ion concentrations.

Free electrons act as a source of absorption at all microwave frequencies. Free-free absorption applies to mobile electrons due to their low masses relative to other nucleons. Anions on the other hand carry at least 1000 times more mass than electrons. Therefore, their contribution to microwave opacity can be neglected compared to that of free electrons. Molecular hydrogen has a high first ionization potential, and the fraction of ionization continuously increases with pressure [175]. However, in the pressure range between 100 bar and 10 kbar, alkali metals are the major source of free electrons.

We determine the equilibrium concentrations of free electrons and ions from the thermochemical equilibrium model of Jupiter's atmosphere under different conditions of heavy element inventory. We adopt the temperature profile from Rensen et al., (2023) [227] corresponding to pressure levels ranging from millibar to kbar. The total electron concentration from equilibrium chemistry models is used to calculate the microwave opacity using the HARP radiative transfer model. HARP simulates the brightness temperature and limb darkening for different conditions of NH_3 opacity and NH_3 concentration, as described in Chapter 2.

3.3.1 Role of anions on microwave opacity

In the gas phase, a variety of species are predicted, but the primary interest for this work lies in the ions. The formation of anions acts as a sink for free electrons in Jovian atmosphere, reducing the effective microwave opacity. We evaluate the concentration of neutrals, ions, and condensable using GGChem for a range of alkali metal abundances between 3 and 10^{-7} x solar value. All other elements are kept at 3 x solar abundance, with solar abundance values adopted from Asplund et al. (2009) [16]. Concentrations of free ions and electrons as shown in Fig. 3.3 exhibit a monotonically increasing trend with temperature which directly correlates with pressures, consistent with our intuition of thermal ionization processes.

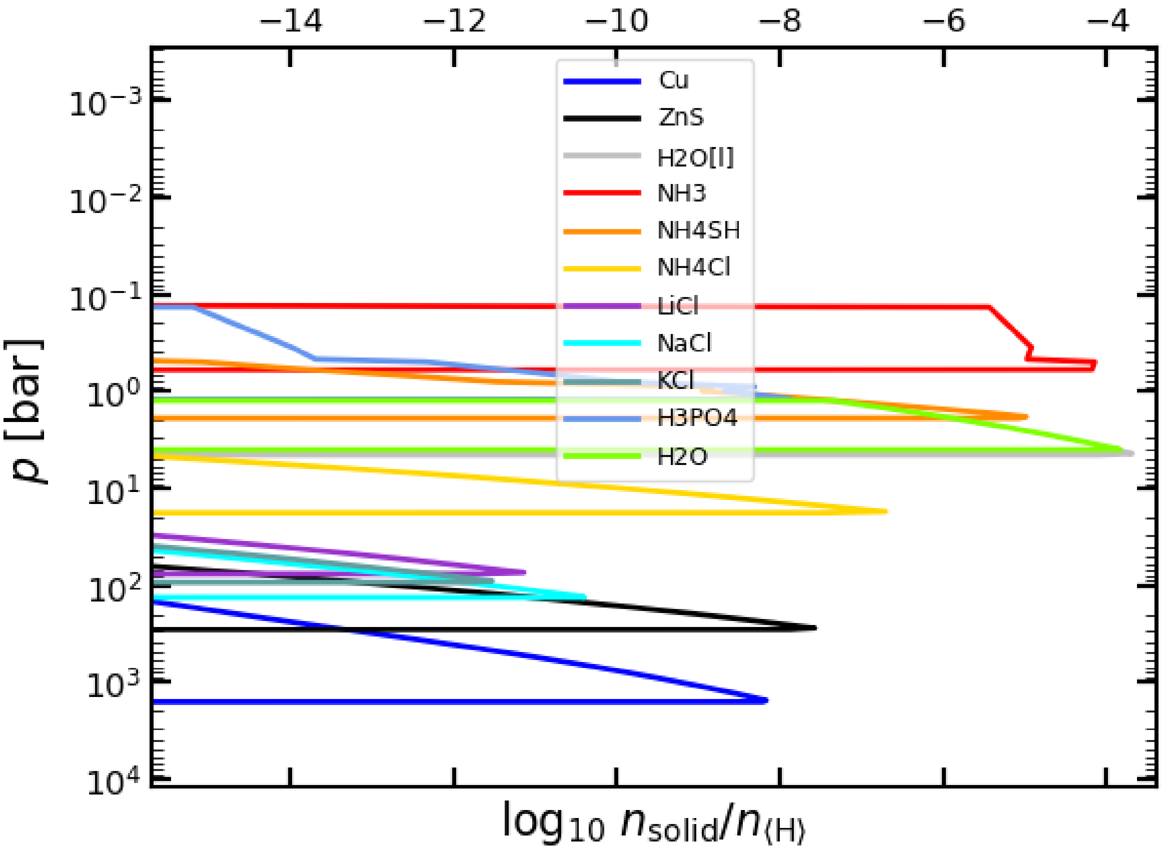

Figure 3.2: Modeled cloud decks for Jupiter's deep atmosphere with C, N, O, P, S set to 3 x solar abundance with [M/H] = -4 for alkalis: Na and K [5]

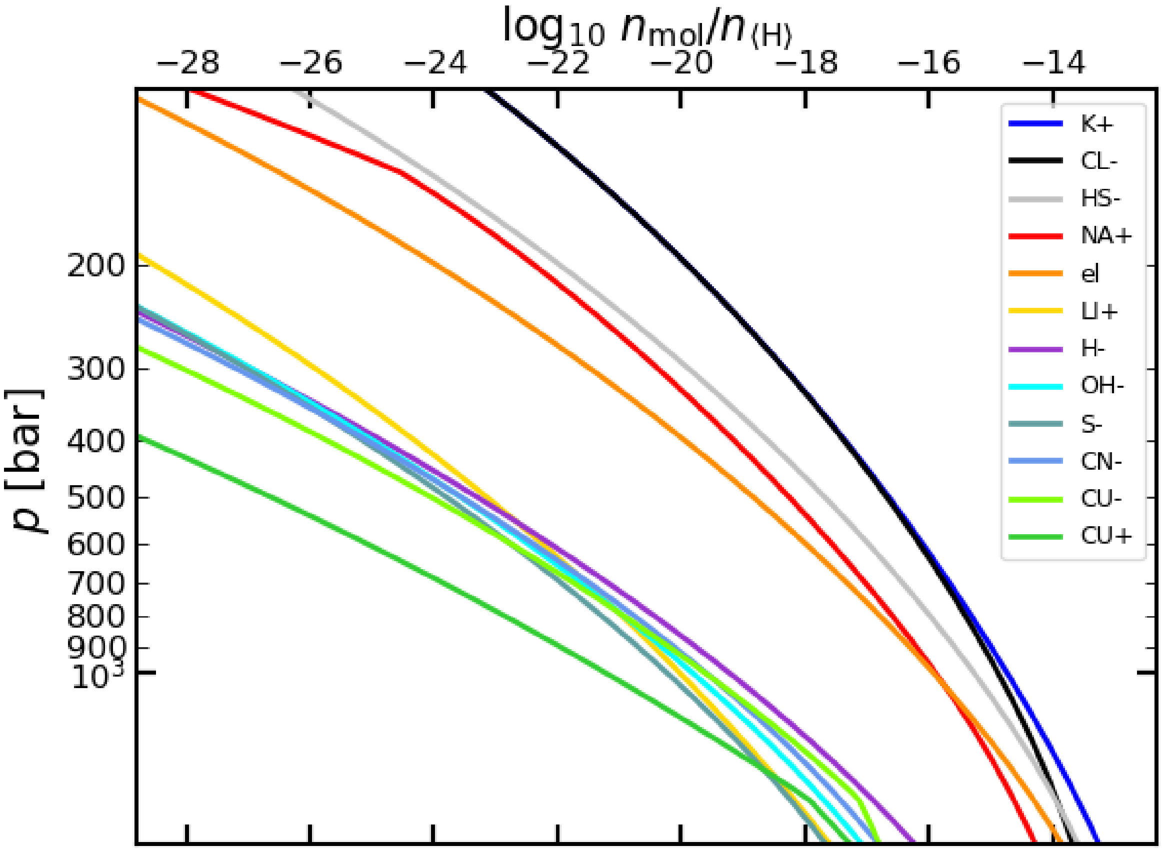

Figure 3.3: Charge carrier concentrations for Jupiter's deep atmosphere with C, N, O, P, S set to 3 x solar abundance with [M/H] = -4 for alkalis: Na and K [5]

Under equilibrium conditions, the primary carriers of positive charge in the 100-2000 bar region are expected to be K^+ and Na^+ respectively. The primary negative carriers would be expected to be free electrons from thermal ionization. However, it is inferred that most negative charge is carried by anions, primarily HS^- and Cl^-. The formation of these anions is thermodynamically more favored compared to a state of solely free electrons released by thermal ionization at such temperatures. Their formation is likely due to an electron attachment process, and it is highly dependent on the relative abundance of HS and Cl radicals. These radicals are a product of high-temperature decomposition of H_2S and HCl, which also act as important reagents of alkali salt formation.

Thermochemical decomposition, thermal ionization, and recombination processes attain a state of dynamic equilibrium. The production of HS^- and Cl^- can be summarized by the following reactions:

$$\mathrm{Na} \rightleftharpoons \mathrm{Na}^+ + e^-$$

$$\mathrm{K} \rightleftharpoons \mathrm{K}^+ + e^-$$

$$\mathrm{HCl} + \mathrm{H} \rightleftharpoons \mathrm{H_2} + \mathrm{Cl}$$

$$\mathrm{Cl} + e^- \rightleftharpoons \mathrm{Cl}^-$$

$$\mathrm{H_2S} + \mathrm{M} \rightleftharpoons \mathrm{H_2} + \mathrm{S} + \mathrm{M}$$

$$\mathrm{H_2S} + \mathrm{H} \rightleftharpoons \mathrm{HS} + \mathrm{H_2}$$

$$\mathrm{H_2} + \mathrm{S} \rightleftharpoons \mathrm{HS} + \mathrm{H}$$

$$\mathrm{HS} + e^- \rightleftharpoons \mathrm{HS}^-$$

Free electron concentration, on the other hand, is found to be depleted by at least an order of magnitude relative to total anion abundance. Therefore, even though the anions do not exhibit any microwave opacity, they act as a major sink of free electrons in the atmosphere. A comparison of the GGChem-based free electron concentrations finds them to be depleted relative to the Saha ionization-derived concentrations (Fig. 3.4). The discrepancy arises from the exclusion of electronegative ions and important reactions of alkalis with atmospheric volatiles at high temperatures [39]. The gap between the simulations is found to be consistent for [M/H] = -3 and [M/H] = -4. As MWR is directly sensitive to free electron concentration, a larger amount of alkali metals is required to fit the same electron concentration.

Without accounting for electron attachment, analysis of MWR observations as described in Chapter 2 indicated that alkali abundances [M/H] may range between -2 to -5. The decrease in electron concentration affects the brightness temperature and limb darkening values. We run a matrix of radiative transfer simulations to compare the T_b and L_d with the 600 MHz channel. If we assume Na and K to have the same metallicity, then [M/H] = -1 or 0.1 x solar

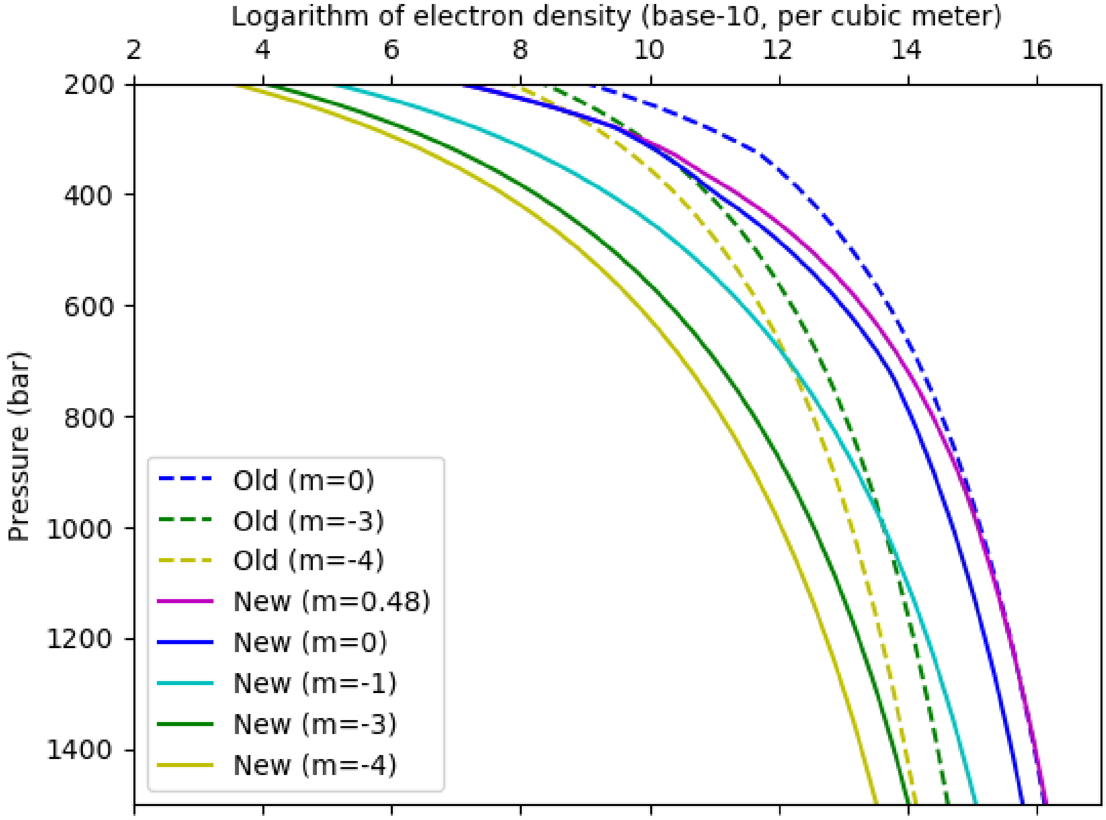

Figure 3.4: Comparison of electron concentration profiles from GGChem thermochemical equilibrium (new) compared to Saha equation based alkali metal thermal ionization (old) from Bhattacharya et al., (2023) [39].

abundance, at the 1 kilobar level best fits the MWR observations (Fig. 3.5). Alkali metals are found to be almost an order of magnitude less abundant than other heavy elements. Therefore, the inclusion of thermochemical reactions and ionization processes hints at the abundance of Na and K to be depleted relative to their solar values. A large dynamic range for alkali abundance still exists due to the variability of NH_3 vertical concentration, and corresponding molecular absorption.

It is largely established that alkali salt clouds, and the formation of anions, act as major sinks of free electrons from alkali metals. As the formation of lower deck clouds is dependent on the deep abundance of heavy elements, we investigate the response of cloud thickness to variability in

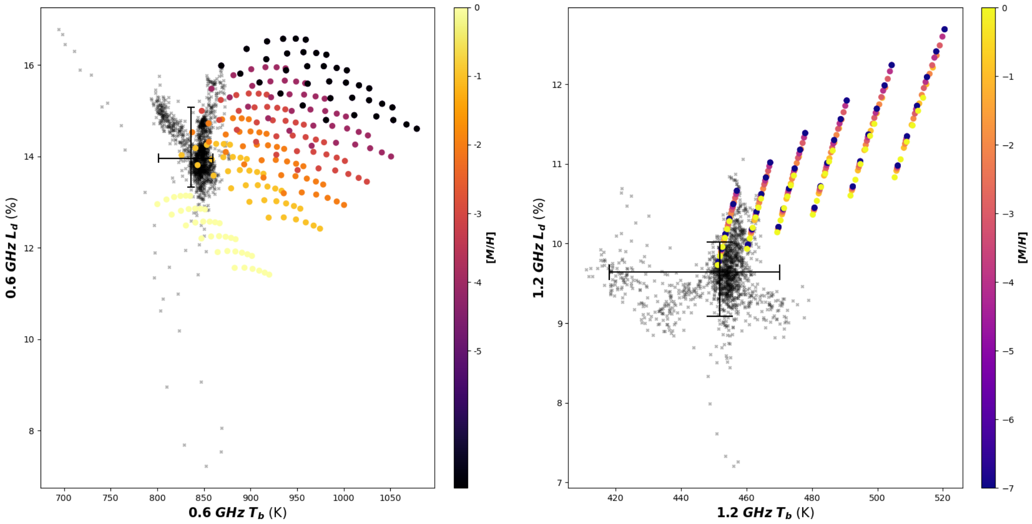

Figure 3.5: Limb darkening and brightness temperature comparison of MWR observations and forward model results at 600 MHz and 1.2 GHz for alkali metal [M/H] 0 to -7 at different ammonia vapor concentration profiles and opacities. Assuming Na and K to have the same metallicity, [M/H] = -1 matches with Juno MWR measurements at 0.6 GHz [5].

oxygen, alkali, and other metallic elements.

3.3.2 Effects of deep water abundance

The value of equatorial deep oxygen abundance from Juno MWR exhibits a large range from 1.5 to 8.3 [164], while the GPMS found 0.5 x solar oxygen abundance in a 5 μm hot spot. The global abundance of deep oxygen abundance is still an unresolved question due to the observed variability in atmospheric mixing. Therefore, we test two extreme cases of oxygen abundance i.e., 0.5 x solar and 5 x solar following the expected range indicated by Juno and GPMS.

For each case of oxygen abundance, we keep the abundance of C, N, P, S, and Cl at 3 times their solar abundances i.e., [M/H] = 0.48. The variation in oxygen abundance affects the condensation level of H_2O liquid and ice clouds. No significant change is observed in the cloud thickness of alkali salt clouds (Fig. 3.6, 3.7).

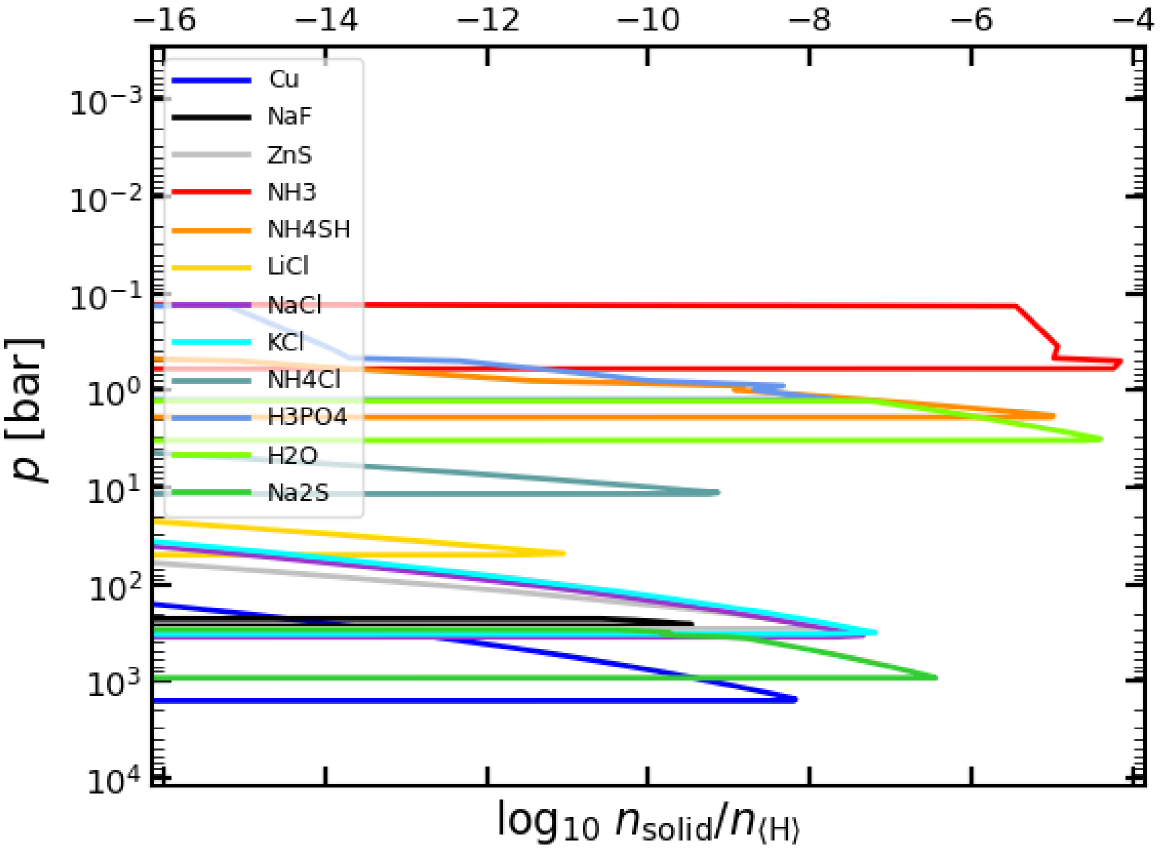

Figure 3.6: Modeled cloud decks for Jupiter's deep atmosphere with observed C, N, P, S abundances (GPMS) and 0.5x solar oxygen [5]

Any change in oxygen abundance between 0.5 to 5 times solar value doesn't affect the concentration of dominant charge carriers (Fig. 3.8, 3.9). We have exhausted a large database of thermochemical reactions in GGChem to show that the thermochemistry of oxygen is not strongly coupled to alkali cloud formation. However, oxygen abundance can play an important role in the formation of silicate clouds at deeper levels. Radiative transfer simulations do not show any major changes compared to the standard case (Fig. 3.10, 3.11). Oxygen abundance affects the temperature structure only around water cloud lifting condensation level, which exhibits changes in higher frequency channels of Juno MWR [164].

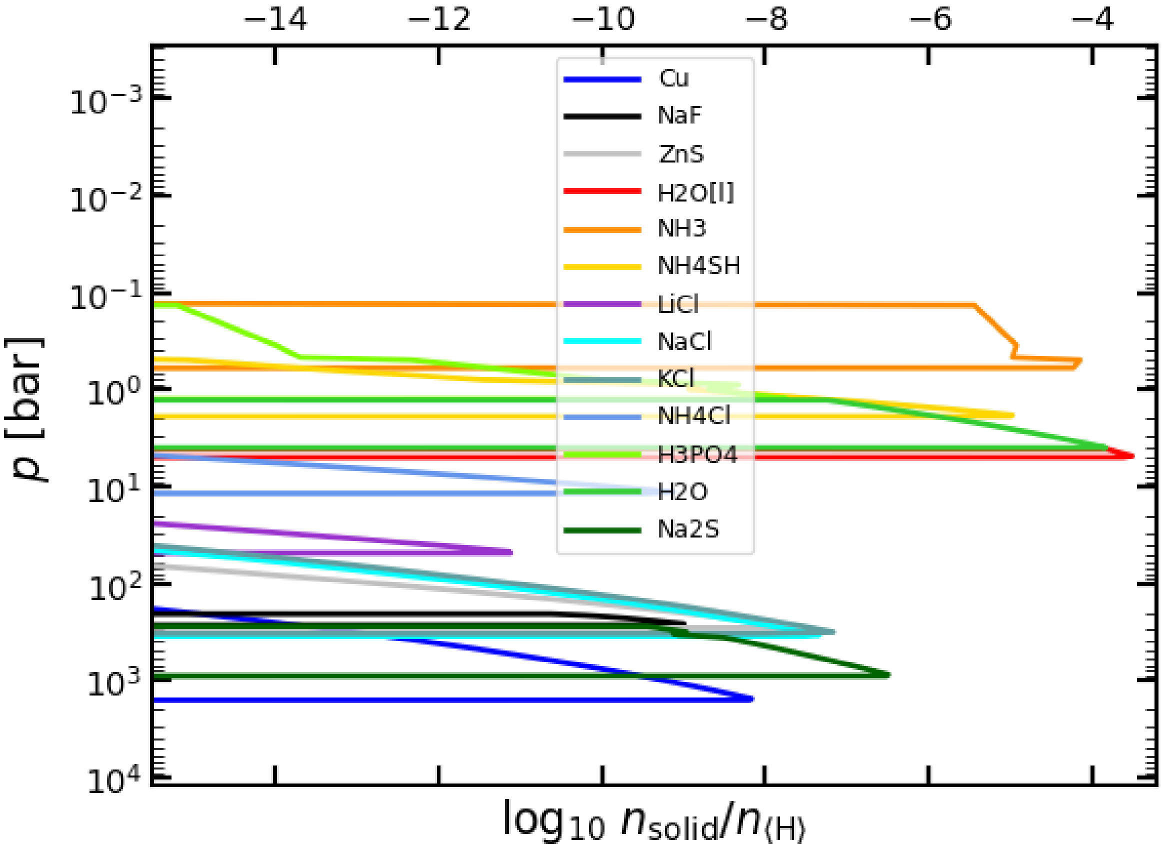

Figure 3.7: Modeled cloud decks for Jupiter's deep atmosphere with observed C, N, P, S abundances (GPMS) and 5 x solar oxygen [5]

3.3.3 Effects of alkali metal depletion

In Chapter 2, we show that the complete removal of K from Jupiter's atmosphere would require elevated amounts of Na abundance to fit the MWR 600 MHz observations. Both Na and K have similar effects on the observed microwave radiation and its angular dependence. Depletion of either Na or K would affect the cloud densities of alkali salt clouds. In an alternate possibility, one out of the two elements could have an enriched abundance, and the other could be depleted.

We use GGChem to simulate the thermochemical equilibrium concentrations of charge carriers and densities of alkali salt clouds. The abundances of C, N, S, P, and Cl are kept at 3 times

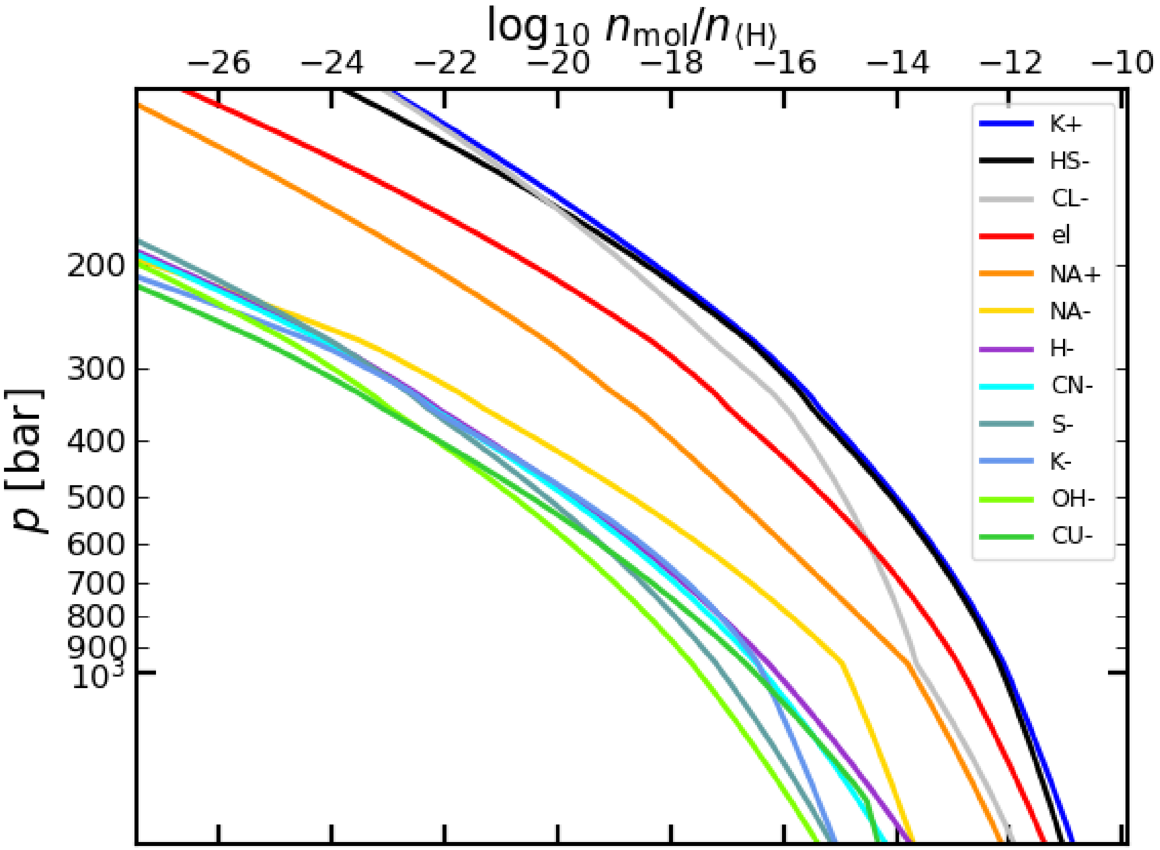

Figure 3.8: Charge carrier concentrations for Jupiter's deep atmosphere with observed C, N, P, S abundances (GPMS) and 0.5x solar oxygen

solar abundance as described in the previous section. The depletion of alkali metals at deeper levels causes atmospheric Cl to increase in concentration and react with NH_3 at shallow levels to form NH_4Cl clouds. These clouds are extremely thin and highly sensitive to alkali abundance. Therefore, we test two different scenarios of alkali element inventory where one of the elements (Na or K) is assumed to be enriched (3 x solar). We simulate the charge carrier by varying the abundance of the other element from [M/H] = -7 to [M/H] = 0.48.

First, we assume the Na abundance to be fixed while varying the atmospheric [K/H] (Fig. 3.12). GGChem simulations of charge carrier concentrations reveal Na^+ to be the dominant positive ion beyond 300 bar due to the higher concentration of Na atoms available for thermal ionization. K dominates over Na at pressures less than 200 bar due to the lower ionization energy of the former.

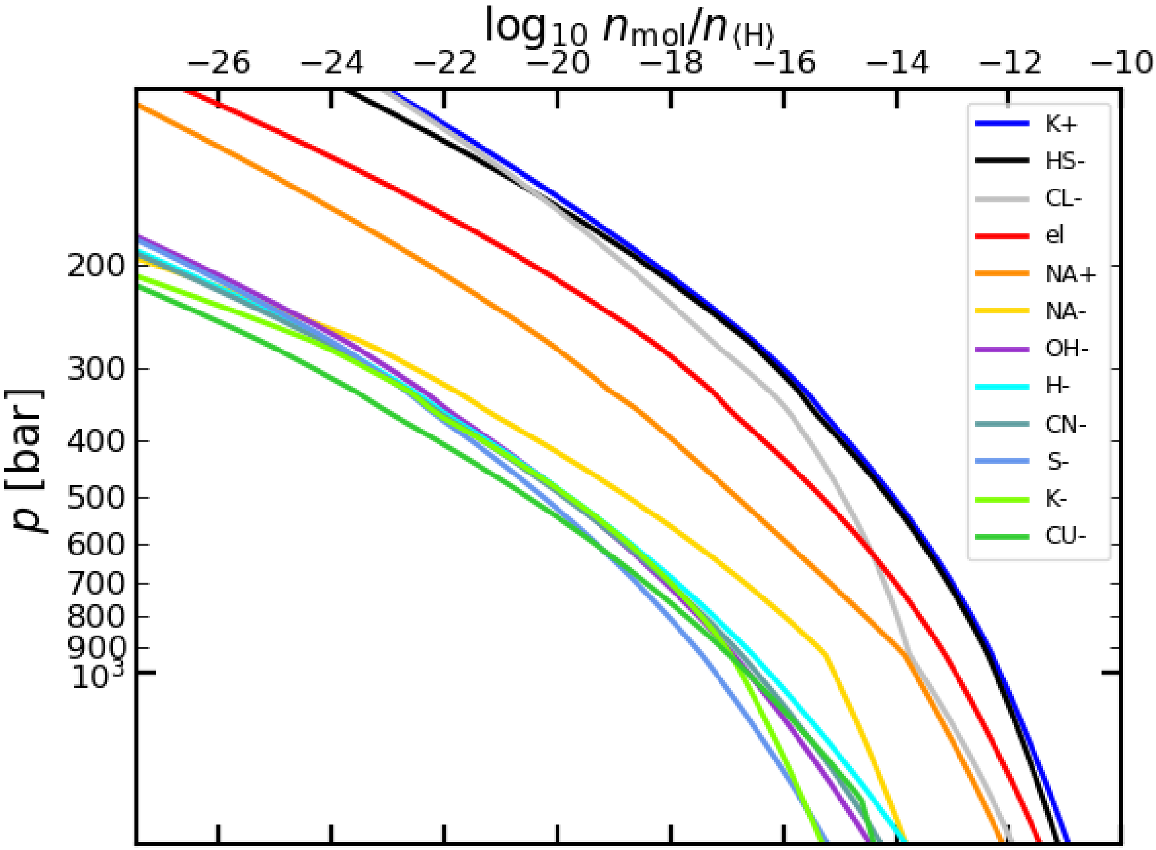

Figure 3.9: Charge carrier concentrations for Jupiter's deep atmosphere with observed C, N, P, S abundances (GPMS) and 5 x solar oxygen

It shows a sharp transition between 200-300 bar where NaCl clouds are expected to be thicker than KCl. Despite cloud formation at such depths, Na ions increase monotonically throughout the temperature transition through various alkali cloud layers. The dominant charge carriers between 300 - 1000 bar are found to be Na^+ and HS^- (Fig. 3.14). The concentration of Na^+ overcomes HS^- beyond 1000 bar, and it is balanced by the upheaval of the free electron concentration.

In the second case, we fix the K abundance and study the variation in charge carrier concentrations owing to the change in [Na/H] (Fig. 3.13). The dominant charge carriers are found to be K^+ and Cl^- between 200 - 1000 bar. Sharp transitions are observed in Na^+ and K^+ between 100 - 400 bar owing to the formation of alkali salt clouds. Beyond 1000 bar, HS^- overshadows Cl^- to

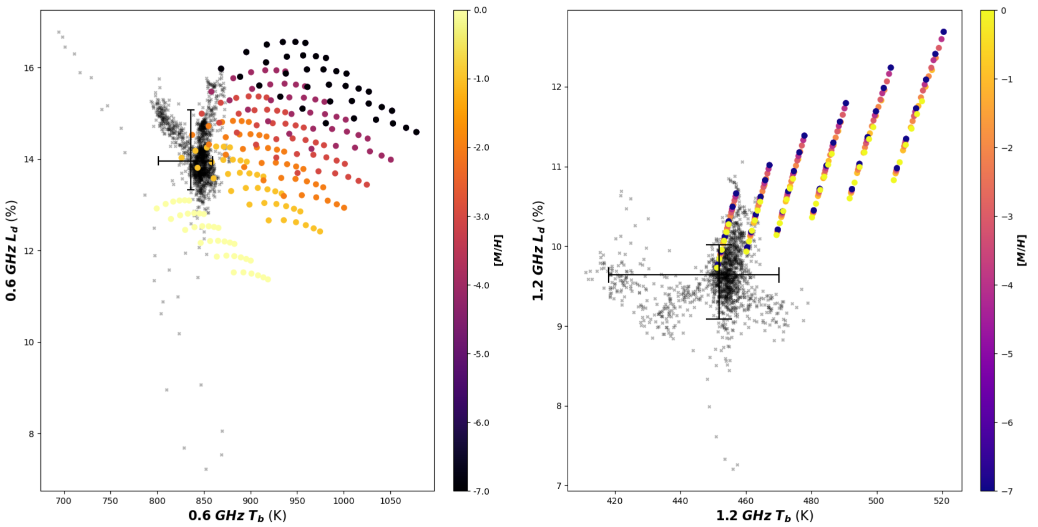

Figure 3.10: Limb darkening and brightness temperature comparison of MWR observations and forward model results at 600 MHz and 1.2 GHz for alkali metal [M/H] 0 to -7 at different ammonia vapor concentration profiles and opacities. Electron concentrations are adopted from GGChem simulations of oxygen abundance equal to 0.5 x solar.

be the dominant anions as free electron concentrations increase rapidly to catch up with Cl^- (Fig. 3.15). At [Na/H] = -4, charge carrier concentrations are larger than in the former case, i.e. [K/H] = -4 ([Na/H] = 0.48). This effect can be largely attributed to the lower ionization energy.

Microwave radiative transfer simulations of T_b and L_d for both cases do not affect MWR observations at 1.2 GHz. At 0.6 GHz frequency channel, simulation results are found to closely overlap one another, exhibiting lower sensitivity to changes in only one of the alkali species (Fig. 3.16 - 3.19). Further, the projections from thermochemical equilibrium charge carrier concentrations do not provide a strong match with MWR observations, especially in the case of depletion of only Na. In the case where [Na/H] = 0.48 and K is depleted, a marginal match can be found for [K/H] -2, but the fit is worse than for both elements being 0.1 × solar. We repeat the simulations by keeping one of the elements (Na or K) at a fixed solar abundance. However, the case of alkali metal enrichment does not provide a satisfactory match with MWR data.

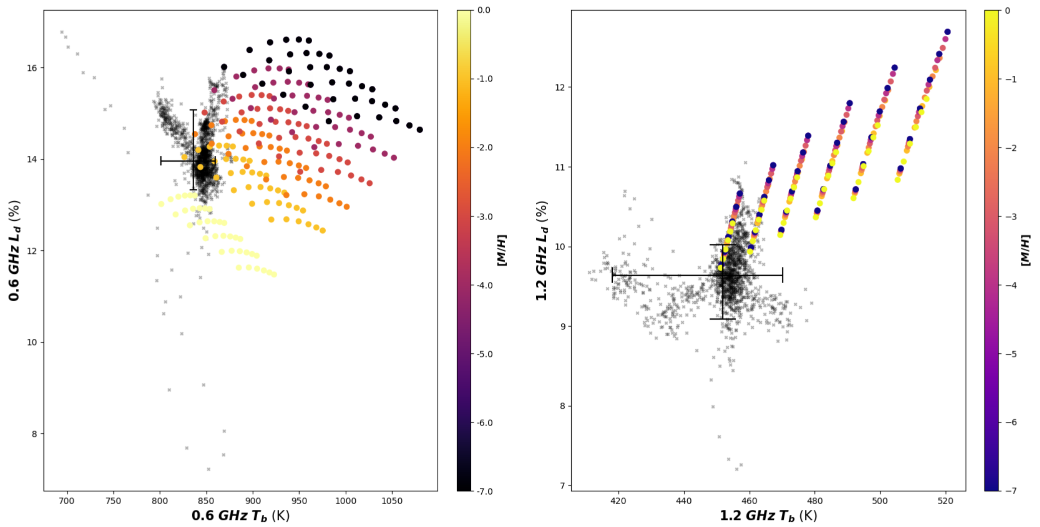

Figure 3.11: Limb darkening and brightness temperature comparison of MWR observations and forward model results at 600 MHz and 1.2 GHz for alkali metal [M/H] 0 to -7 at different ammonia vapor concentration profiles and opacities. Electron concentrations are adopted from GGChem simulations of oxygen abundance equal to 5 x solar.

The depletion of either Na or K predicts the formation of NH_4Cl clouds in Jupiter. However, the abundance of Cl has been not confirmed at Jupiter or Saturn owing to challenges in the observation. Showman et al., (2001) [248] showed that atmospheric chlorine is depleted by reactions with NH_3 in the troposphere below the water cloud. It does not allow Cl to reach shallower levels in any detectable amounts traceable from spectroscopy. Even a value of [M/H] = -1 for alkali metals would not allow mass transport from a deeper Cl inventory to reach the NH_3 cloud. GGChem solves the system of reactions point by point throughout the atmosphere. This approach excludes the upwelling transport of chemicals from deeper levels, and the prediction of NH_4Cl clouds could be attributed to the methodology and lack of information associated with Cl at deeper levels. However, the analysis does not shed light on the chemical transport of Cl in Jupiter.

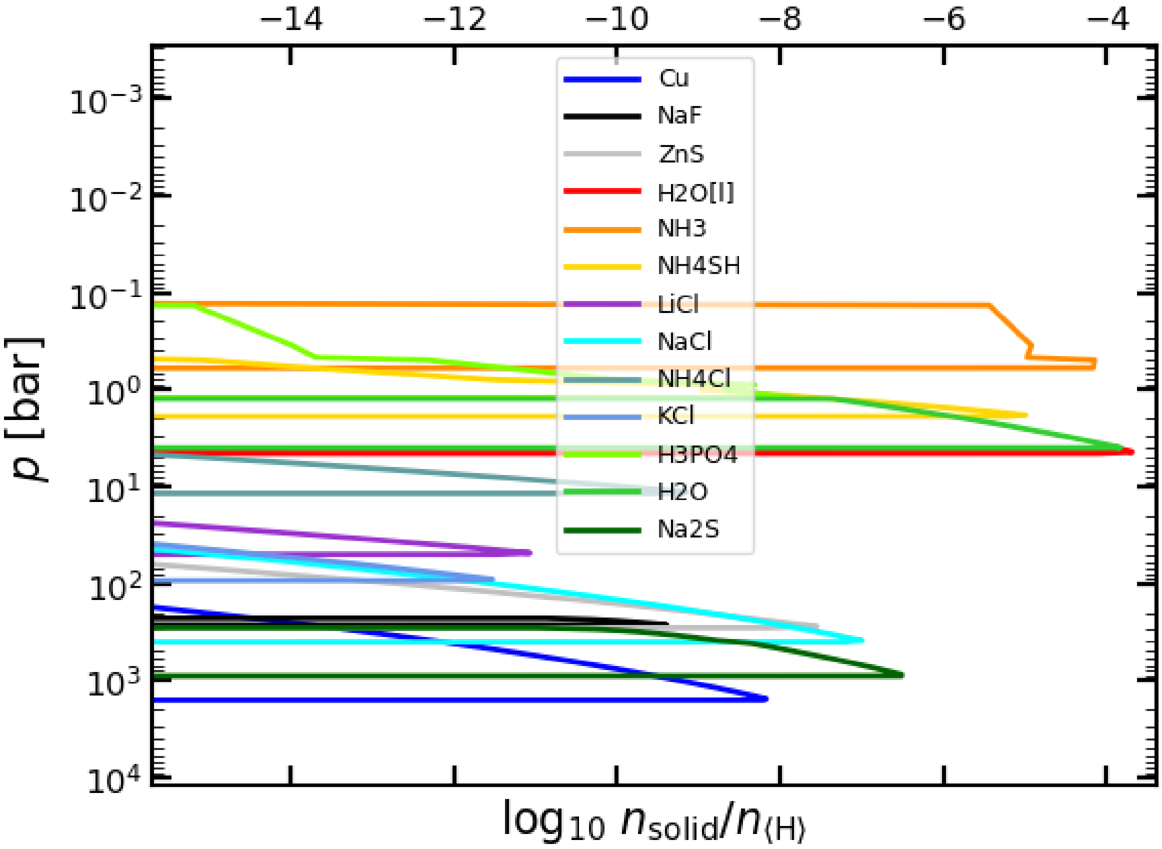

Figure 3.12: Modeled cloud decks for Jupiter's deep atmosphere with observed C, N, P, S abundances (GPMS) and [K/H] = -4 at Na abundance set to 3 x solar

3.3.4 Effects of alkali and silicate cloud formation

We simulate an extreme case of convective transport by not removing the atmospheric condensates according to their saturation vapor pressures (Fig. 3.20). This is analogous to a strong convective plume rising from deeper levels. GGChem simulations show the total gas-phase inventories of all participating elements. All condensable species have a constant mixing ratio between the lifting condensation level and their extinction levels. The charge carrier concentrations monotonically increase with temperature. The concentrations vary with similar values to those calculated with other assumptions (Fig. 3.21).

The radiative transfer simulations do not show any significant deviation from the standard case

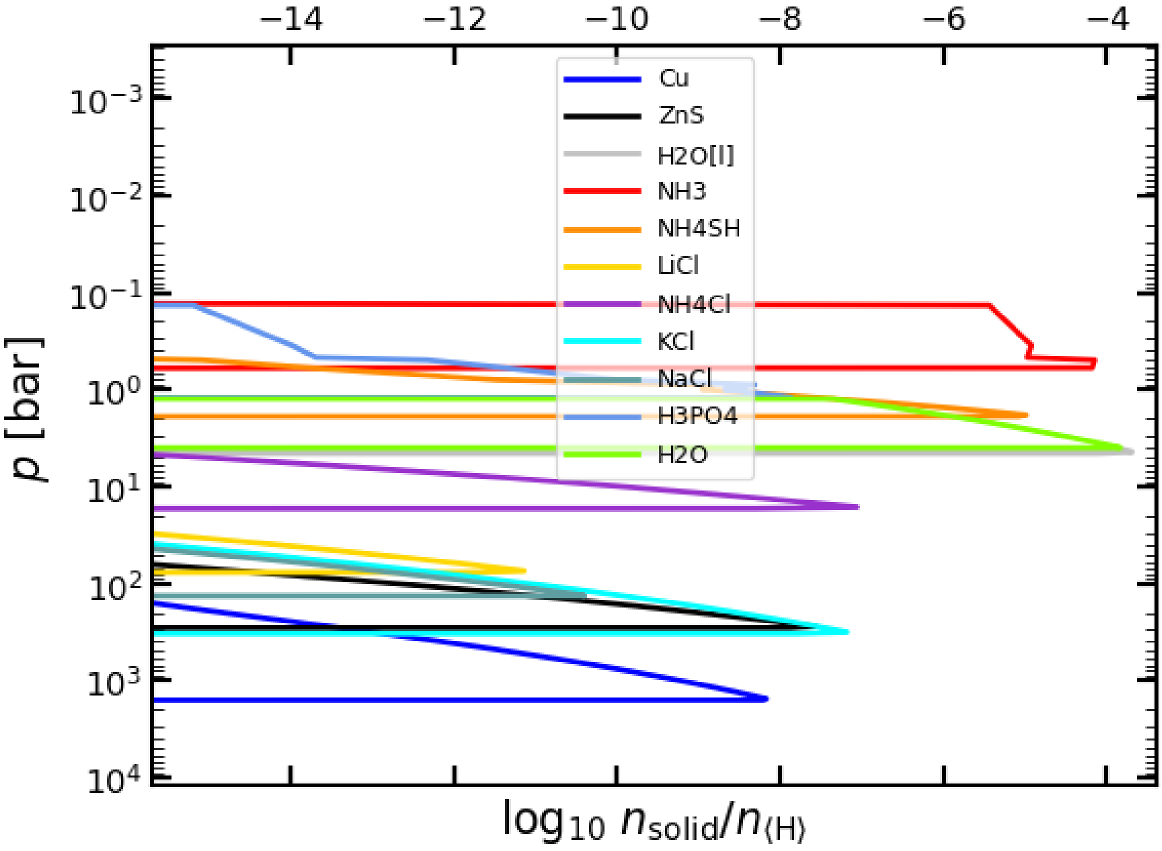

Figure 3.13: Modeled cloud decks for Jupiter's deep atmosphere with observed C, N, P, S abundances (GPMS) and [Na/H] = -4 at K abundance set to 3 x solar

of alkali metal thermal ionization. A metallicity value, [M/H] = -1 is still required to explain the MWR observations in the 0.6 GHz channel (Fig. 3.22). The similarity can be attributed to two causes. Firstly, the thermal ionization is expected to be higher below the lifting condensation level of condensable species. Therefore, the availability of condensates does not contribute to the microwave opacity. Secondly, the siliceous species are expected to condense much deeper than 1000 bar and MWR is expected to be insensitive to such species (Fig. 3.23).

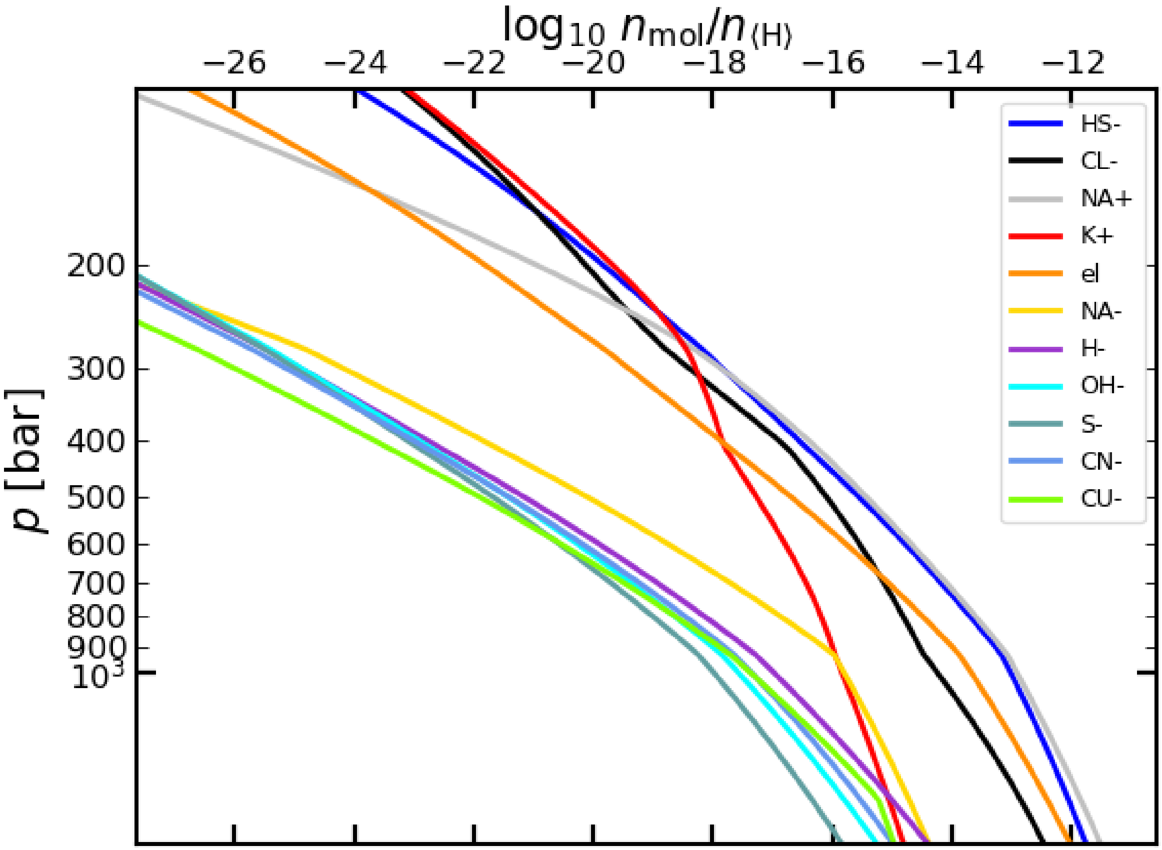

Figure 3.14: Charge carrier concentrations for Jupiter's deep atmosphere with observed C, N, P, S abundances (GPMS) and [K/H] = -4 at Na abundance set to 3 x solar

3.4 Discussion

A comprehensive modeling of neutral-ion thermochemistry provides key insights into the cloud formation and thermal ionization processes in Jupiter's atmosphere. At high temperatures, corresponding to pressures exceeding 300 bar, HCl and H_2S decompose and acquire free electrons to form anions. The formation of Cl^- and SH^- reduces the free electron concentration by an order of magnitude (Fig. 3.24 - 3.27). It reduces the overall microwave opacity of the deep atmosphere. A comparison between MWR observations and radiative transfer simulations reveals Na and K to be $\sim$ 0.1 x solar below the alkali salt clouds. An elevated amount of alkali metals relative to that previously calculated is required for an equivalent opacity as MWR, T_d and L_d are directly

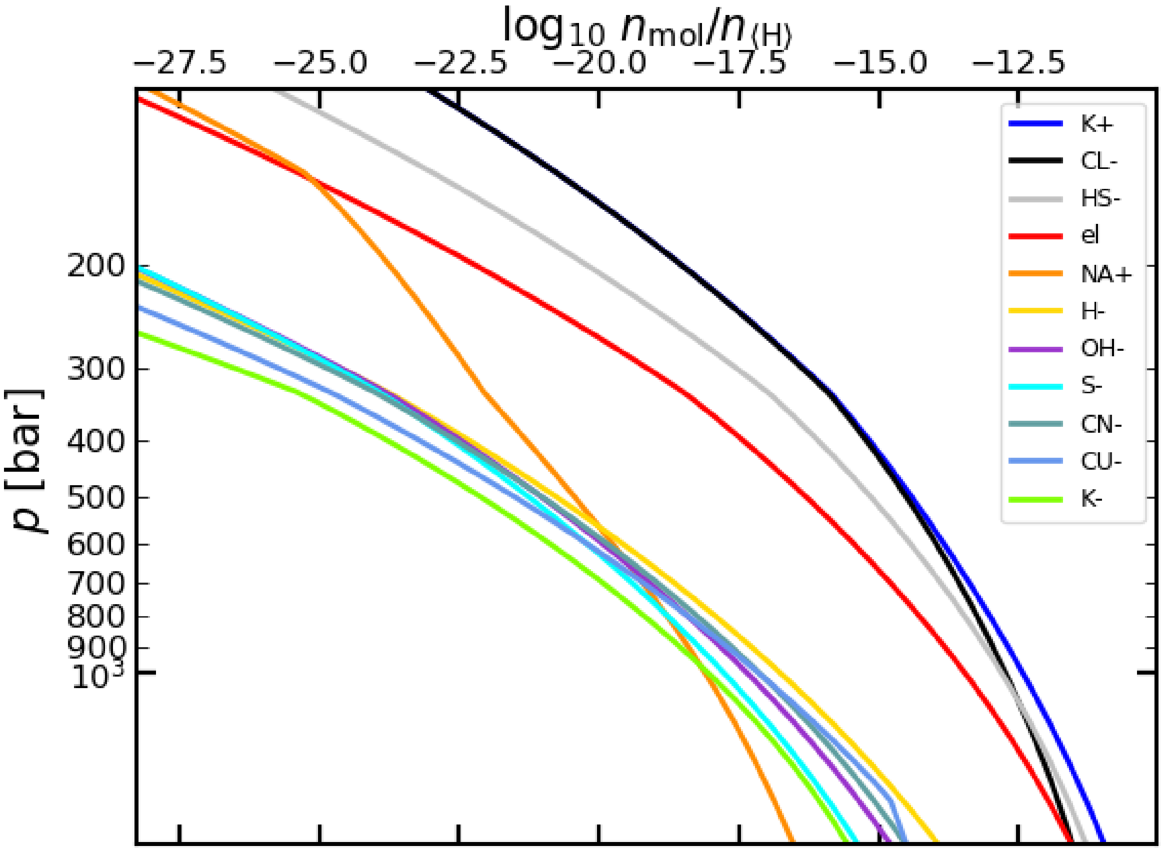

Figure 3.15: Charge carrier concentrations for Jupiter's deep atmosphere with observed C, N, P, S abundances (GPMS) and [Na/H] = -4 at K abundance set to 3 x solar

sensitive to free electron concentration.

We conduct sensitivity analysis to the heavy element inventory of Jupiter's deep atmosphere. Equilibrium chemistry associated with high-temperature thermal ionization is not sensitive to changes in water abundance between 0.5 to 5 x solar. The enrichment of either Na or K does not seem likely due to the mismatch of microwave radiative transfer simulations with MWR data. The enrichment of alkali metals affects the chlorine above 100 bar.

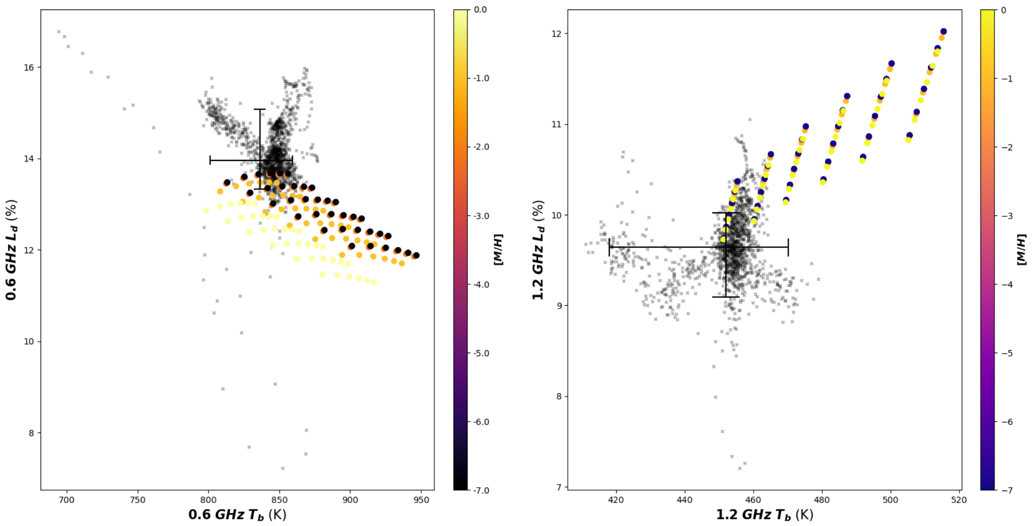

Figure 3.16: Limb darkening and brightness temperature comparison of MWR observations and forward model results at 600 MHz and 1.2 GHz for [K/H] 0 to -7 keeping Na at fixed abundance (3 x solar).

3.5 Disequilibrium Chemistry in Jupiter's Atmosphere

While the calculations above show equilibrium concentrations of all gas-phase species and condensates, the gas-phase dissociation and electron attachment processes can be expected to be rapid. The thermal decomposition of H_2S has a time scale between 0.2 to 2 seconds at high-temperature conditions (above 1073.15 K) [153]. Thus, at pressures corresponding to 800 bar and above, partial decomposition takes place within a few seconds. Decomposition of HCl in the presence of atomic hydrogen is rapid even at lower temperatures [76]. As such, it's likely both anions will be present; however, either one is thermodynamically favored over free electrons. While an additional anion species not included in the chemistry model may be even more favorable, this would only further deplete the free electrons. Therefore, at temperatures corresponding to alkali vapor ionization, the chemical processes are largely expected to achieve equilibrium faster than convective and diffusive time scales.

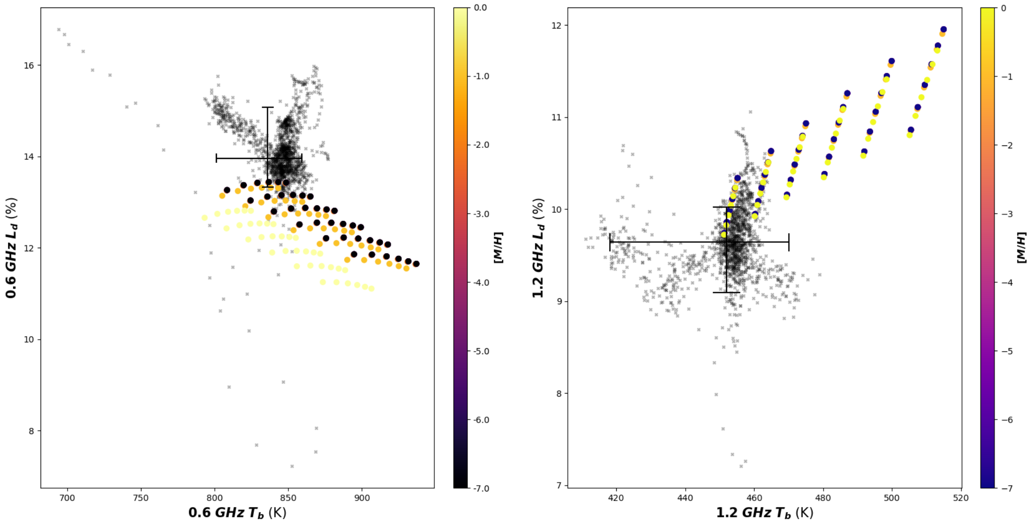

Figure 3.17: Limb darkening and brightness temperature comparison of MWR observations and forward model results at 600 MHz and 1.2 GHz for [Na/H] 0 to -7 keeping K at fixed abundance (3 x solar).

3.6 Alkali metals: An exoplanetary perspective

The elements Na and K have strong absorption lines between 5000-8000 Å [9, 10, 285]. These absorption lines have been able to identify and detect the presence of alkali elements in exoplanetary atmospheres. However, their abundances show a wide range of variability in different types of atmospheres in the presence of other clouds. There is no major consensus on the trends of their abundance in terms of the planetary size or mass. Welbanks et al., (2019) [285] provide a summary of all detections through 2019.

A possible indication of the low metallicity of the alkali metals in a hot Jupiter exoplanet was first proposed by [90] as one plausible explanation for the high albedo of Kepler-7b. They derived an alkali metal abundance 10–100 times lower than the solar value. Since then, the abundance of alkali metals has been derived for several other giant exoplanets, with abundances ranging from $\sim$ 100 times below solar to $\sim$ 100 times above solar (Fig. 3.28), although the uncertainties are

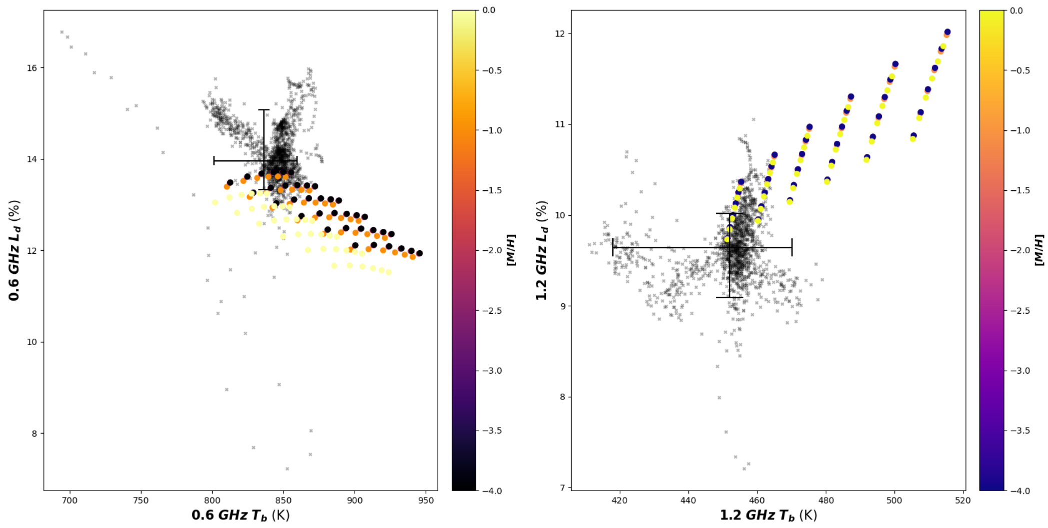

Figure 3.18: Limb darkening and brightness temperature comparison of MWR observations and forward model results at 600 MHz and 1.2 GHz for [K/H] 0 to -7 keeping Na at fixed abundance (solar)

large. Recent observations of two hot Jupiters or Saturns with clear or mostly clear atmospheres were made. The alkali metal abundance for one such hot Jupiter (HAT-P-1b) is found to be sub-solar [70], while it was found to be solar to greatly super-solar for the other (WASP-96b) [212]. Considering the relatively small sample size of hot Jupiters with clear atmospheres, it is premature to make a meaningful comparison between their alkali metal abundance and the metallicity in Jupiter presented in this chapter.

The orbit and temperature structure of hot Jupiters are significantly different from Jupiter. This class of objects does not have a solar system analog. In the case of hot Jupiters, alkali metals undergo thermal ionization to provide ions driving drag force and ohmic dissipation processes influencing atmospheric dynamics [225]. Mean zonal winds in Jupiter extend to thousands of kilometers into the atmosphere, and they are expected to be quenched in the high electron conductivity regime deeper than 100 - 1 kbar [71]. Planetary formation models have recently hinted at connecting the enrichment of alkali metals in hot Jupiter with planetary migration inward of the

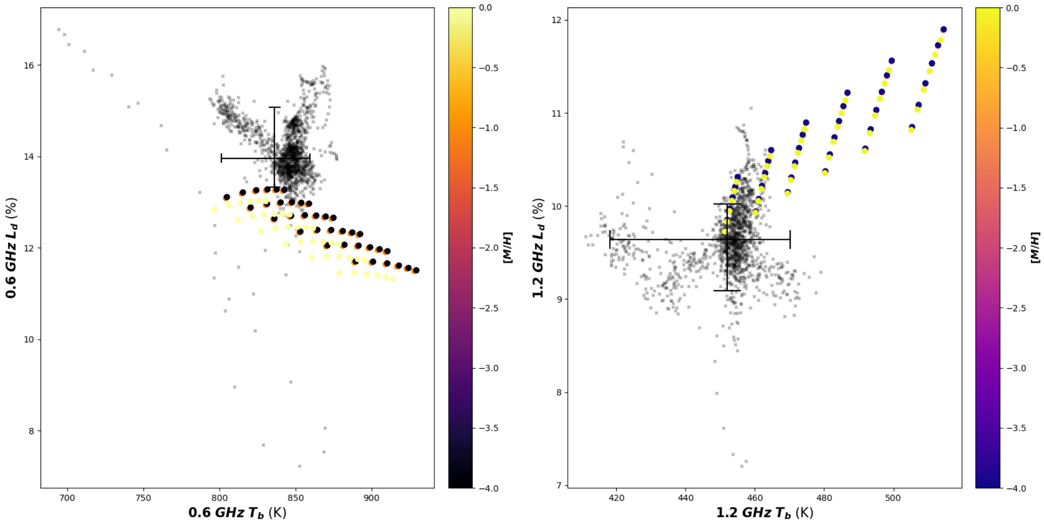

Figure 3.19: Limb darkening and brightness temperature comparison of MWR observations and forward model results at 600 MHz and 1.2 GHz for [Na/H] 0 to -7 keeping K at fixed abundance (solar)

water ice line [133]. The relative inventory of refractory elements and volatiles can also probe into the formation processes of hot Jupiters [177]. Irrespective of differences, it can be concluded that atmospheric composition measurements may not be representative of global abundances in gas giants and exoplanets. A new calculation of Rosseland mean opacity shows that both Na and K abundances have to less than 10^{-3} x solar value to form a radiative zone at 1 - 10 kbar pressure levels [251]. Therefore, Juno MWR constraints on alkali metal abundance disprove the existence of such a deep radiative layer in Jupiter.

3.7 Conclusion

Juno MWR observations of Jupiter's atmosphere previously indicated Na and K abundances to range between [M/H] = -2 to -5. Alkali metals could be then taken as a representative for other heavy element abundances at higher pressures. However, metallic elements react with atmospheric sulphur, oxygen, and halogens to form layers of rock clouds below the water cloud. We run

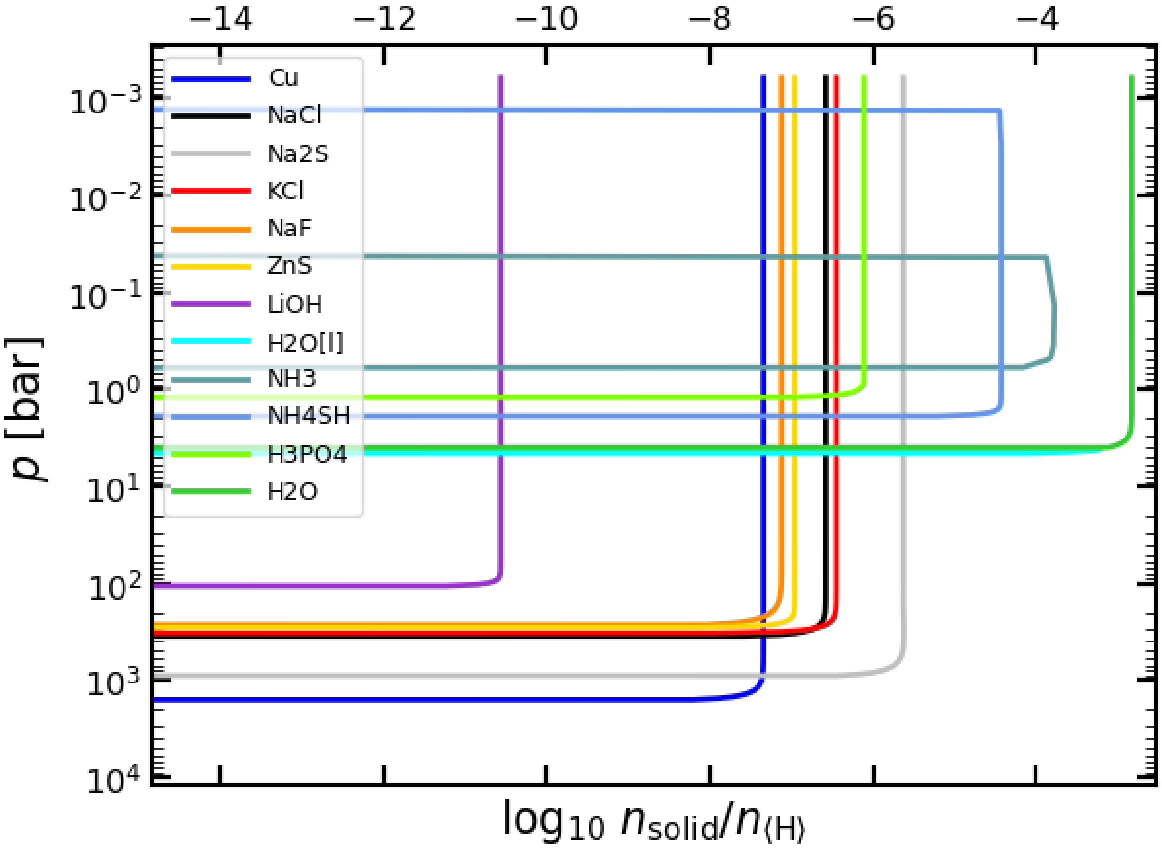

Figure 3.20: Modeled cloud decks for Jupiter's deep atmosphere with observed C, N, P, S abundances (GPMS) and alkali metals set to 3 x solar abundance. Supersaturated vapors and gases are not removed from the system as an extreme case of convective action

full-scale simulations of chemical equilibrium using GGChem, a Newton-Raphson solver for atmospheric chemical equilibrium. We derive a formulation of Gibbs-free energy based on theory and laboratory data.

Equilibrium concentrations of gas-phase species, ions, and condensates are estimated for each point in Jupiter's atmosphere with pressure ranging from 0.1 to 10 kbar. High-temperature charge carrier concentrations reveal Cl^- and SH^- to be dominant negative charges, exceeding local electron concentrations by a factor of 10. They form due to H_2S and HCl dissociation followed by electron capture. The anions are relatively transparent to microwave frequency and act as a sink

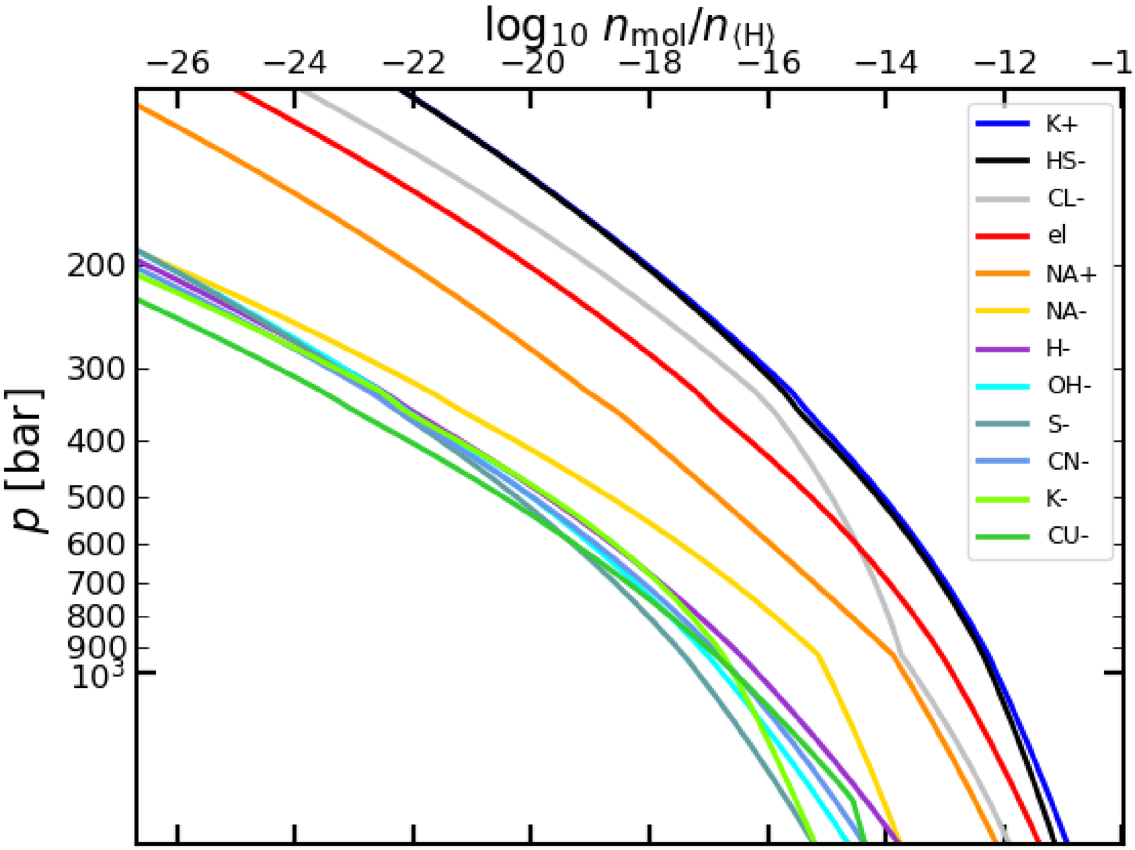

Figure 3.21: Charge carrier concentrations for Jupiter's deep atmosphere with observed C, N, P, S abundances (GPMS) and alkali metals set to 3 x solar abundance. Supersaturated vapors and gases are not removed from the system as an extreme case of convective action

of free electrons. We simulate the electron concentrations for a range of metallicities between [M/H] = 0 to -7. Electron concentration profiles are fed as input into a HARP microwave radiative transfer code. A comparison between MWR and RT calculations of brightness temperature and limb darkening reveals alkali metals to have an elevated abundance compared to previous calculations, i.e. [M/H] = -1.

Sensitivity tests check the effect of deep oxygen abundance, silicate cloud formation, and enrichment in sodium or potassium abundances on these results. The deep oxygen abundance has no visible effect on alkali metal salt clouds and charge carrier concentrations. Alkali-silicate melts

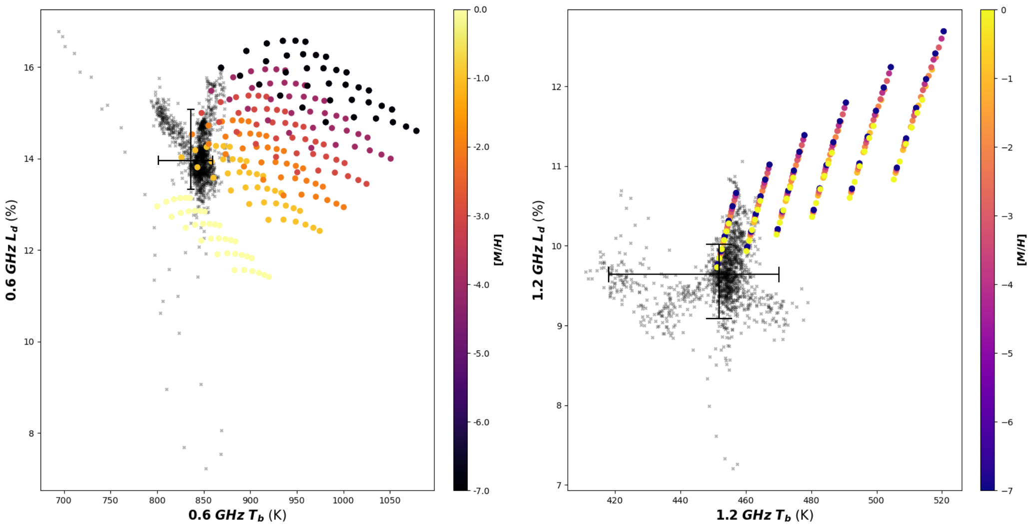

Figure 3.22: Limb darkening and brightness temperature comparison of MWR observations and forward model results at 600 MHz and 1.2 GHz for Jupiter's atmosphere for strong convective activity

may exist at pressure levels deeper than those sensitive to MWR operating frequencies. They could provide an additional source of alkali metal sequestration. A detailed knowledge of gas phase dissolution in metallic compounds will help analyze the role of silicate clouds. Assuming either sodium or potassium to be enriched relative to the other is not favored as an explanation for atmospheric microwave thermal emission, although a relative enrichment of sodium and stronger depletion of potassium cannot be excluded. In sum, a detailed analysis of Jupiter's deep atmospheric chemistry can be combined with Juno MWR observations to show an abundance of sodium and potassium near [M/H] = -1 at pressure levels of roughly 1 kilobar.

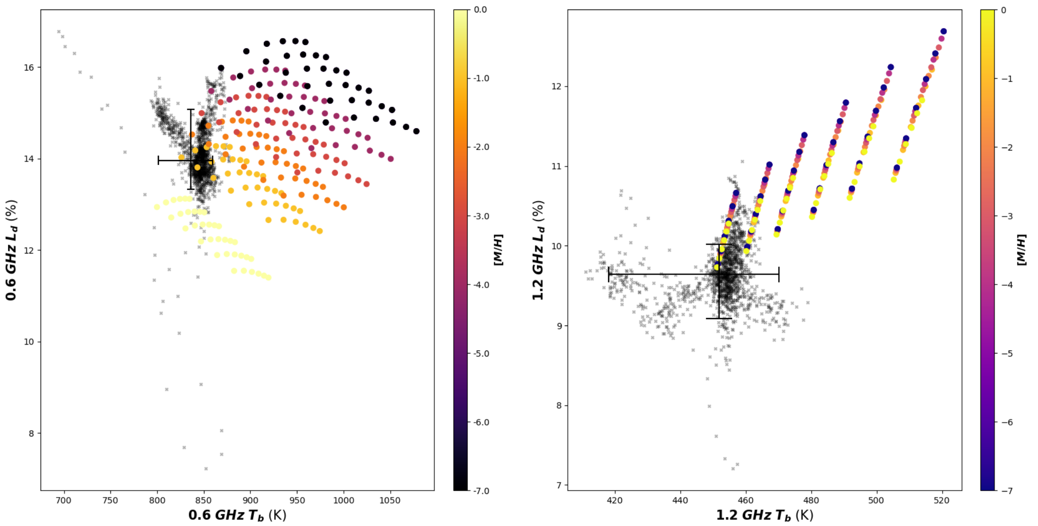

Figure 3.23: Limb darkening and brightness temperature comparison of MWR observations and forward model results at 600 MHz and 1.2 GHz for Jupiter's atmosphere for strong convective activity in the presence of siliceous species

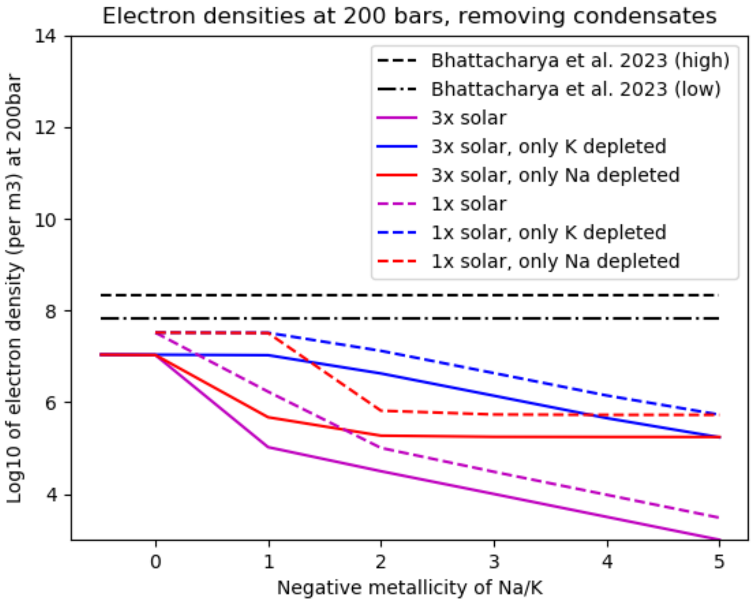

Figure 3.24: Modeled free electron densities at a given pressure level, compared to two of the best-fit profiles of Bhattacharya et al. (2023) [39] at 200 bar

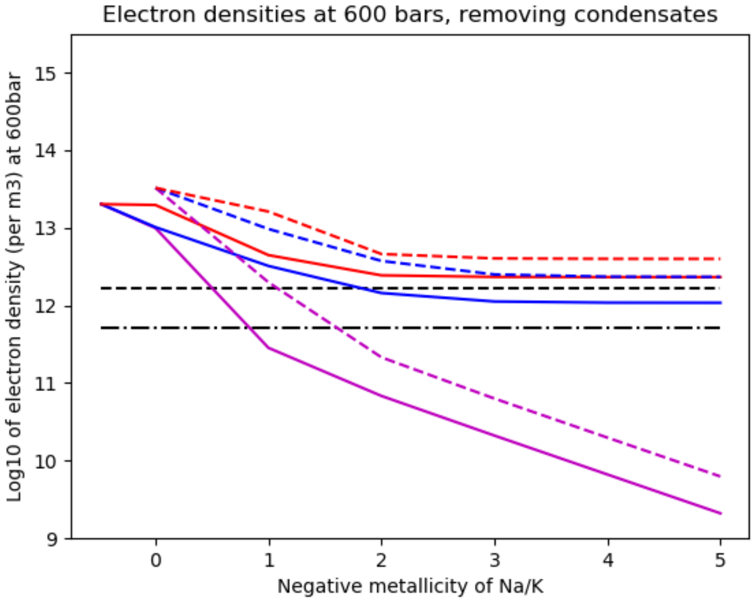

Figure 3.25: Modeled free electron densities at a given pressure level, compared to two of the best-fit profiles of Bhattacharya et al. (2023) [39] at 600 bar

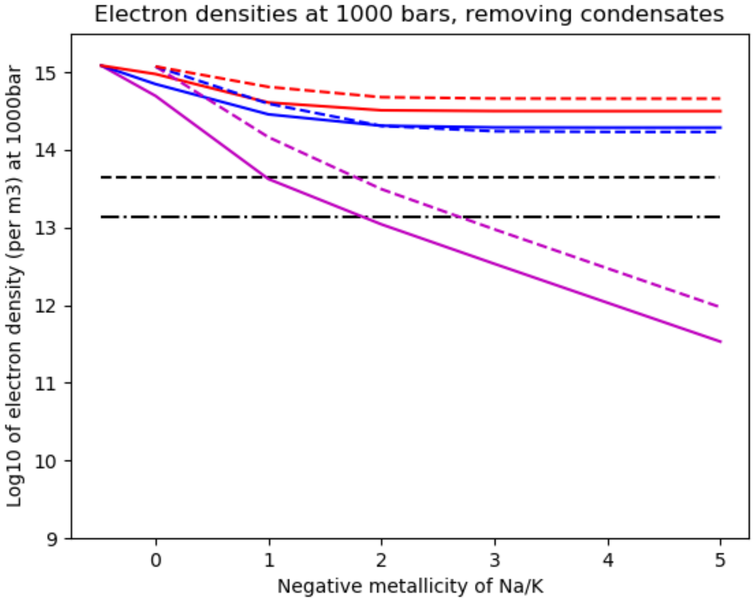

Figure 3.26: Modeled free electron densities at a given pressure level, compared to two of the best-fit profiles of Bhattacharya et al. (2023) [39] at 1 kbar

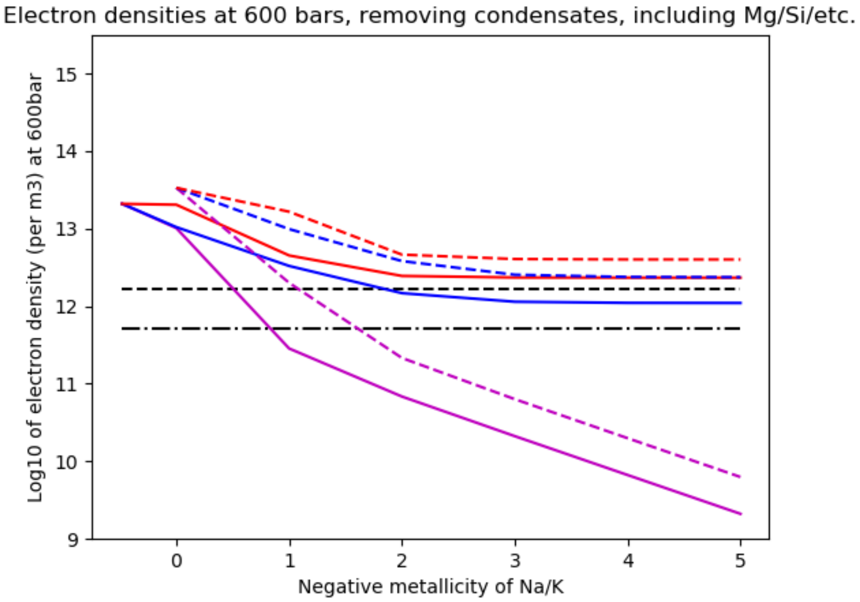

Figure 3.27: Modeled free electron densities at a given pressure level, compared to two of the best-fit profiles of Bhattacharya et al. (2023) [39] with case of deep-condensing elements included at 600 bar

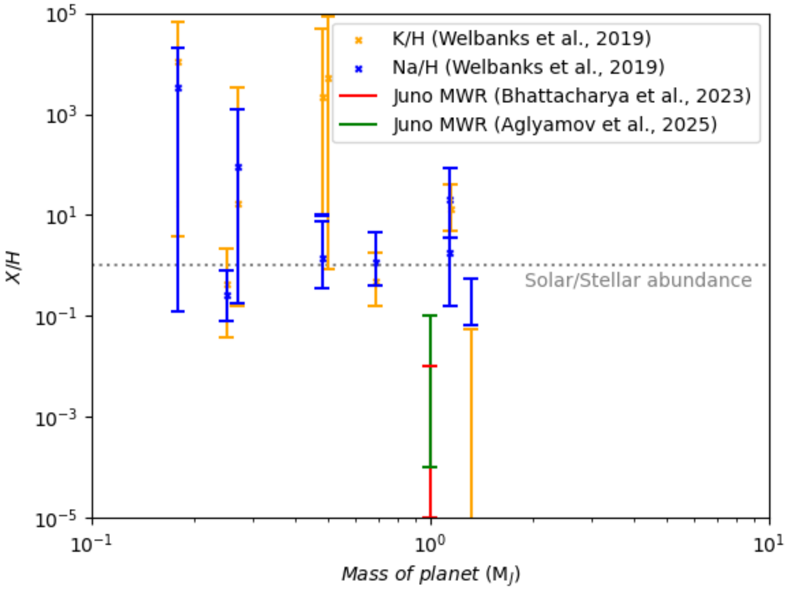

Figure 3.28: Comparison of exoplanet Na and K metallicities with Juno MWR inferred alkali metal abundance in Jupiter's atmosphere $\sim$ 100 bar - 1 kbar

CHAPTER 4

Juno Microwave Radiometer Observations of High-Energy Electron Precipitation Events

4.1 Introduction

Juno Microwave Radiometer passes over Jupiter's Northern Aurora showing regions of antenna temperature much colder than deep thermal emission. They are prominent features at the lowest frequency channels, i.e., 0.6 GHz and 1.2 GHz. Hodges et al., (2020) [140] analyzed the MWR data to show these features to be correlated with main auroral UV emissions. A plasma reflection theory was put forward to explain the reduction in antenna temperatures. It requires high electron concentration in the auroral ionosphere that reflects a proportion of Cosmic Microwave Background Radiation (CMBR) to reduce the observed antenna temperature significantly. Plasma reflection-based inversion of MWR temperatures estimated electron densities $\sim 10^9$ cm^{-3}. The electron concentrations are found to be 100 times higher than steady-state predictions from theoretical models of energetic/plasma particle precipitation. Furthermore, the inversion of T_b to determine electron density did not provide much information about the ionospheric structure and sources of ionization. The Jovian ionosphere is influenced by various ionization processes due to solar EUV photons, electron, and ion precipitation as evident by the presence of multiple electron density layers found during radio occultation experiments [193].

Since JOI in 2016, MWR has collected antenna temperature data over the North Pole during the perijove passes. The previous literature dated 2020 focuses on reporting the MWR observations of the Jovian aurora for the first 21 orbits. Since 2020, Juno has completed more than 60 orbits, far into its extended mission phase. Thus, there is a strong scientific desire to analyze the MWR data through the extended mission phase as the Juno spacecraft line of apsides precesses provides a detailed analysis of the antenna temperatures and their variability. In this chapter, antenna temperature variations over spin and orbit changes are studied about the effect of electron precipitation. The sensitivity of atmospheric plasma opacity to electron precipitation is simulated with inputs from Juno in-situ electron flux up to energies of 10 MeV.

Electron precipitation intensities at energies up to 10 MeV inferred from the Jupiter Energetic-Particle Detector Instrument (JEDI) [186] and Ultraviolet Spectrograph (UVS) [115, 144] instruments are used as a Northern Hemisphere case study to understand the energy deposition and ionization processes in the lower stratosphere, and subsequently used to estimate the microwave and ultraviolet opacity and emission from the auroral region. A new auroral energy deposition model that combines a continuous slowing down approximation (CSDA) of energetic particles [216] with discrete energy loss modeling at electron energies below 10 keV [276] was used to determine the ionization and thermal heating of the atmosphere. The ion production, chemical reactions, and thermal dissipation resulting from the auroral energy deposition were integrated into a time-dependent model of Jovian atmospheric chemical kinetics, that corresponds to the energetic electron precipitation. Then, the model is used to calculate the microwave absorption and to assess the impact of locally generated ionospheric layers on the transmission of microwaves in the high-latitude atmosphere. The generally elevated electron densities throughout the high latitude region result in increased absorption of microwaves with dramatic transient changes in antenna temperature that vary over a timescale of less than 10-30 s in localized regions associated with a large energy flux of electrons.

4.2 Multi-spectral observations of Jupiter's polar aurorae

Planetary aurorae result from energetic electron or ion impingement into the gaseous envelope of a planet. The particles are accelerated by plasma and wave processes that in the case of magnetized planets result from interactions with the solar wind or from internal shears in the magnetospheric plasma of the planet. In many cases these processes lead to the redistribution of momentum and energy within the system via field-aligned currents, consequently accelerating charged particles to very high energies. As the energetic particles interact with the gaseous envelope of the planet, they dissipate their energy through ionization; production of x-rays, ultraviolet, and visible (nonthermal) emissions; molecular dissociation and resulting chemistry; and through heating of the atmospheric envelope that results in atmospheric/ionospheric transport and increased infrared emission.

The high latitude aurora at Jupiter's North Pole is largely divided into three sections [122]:

- Satellite flux tube footprints: These emission features are observed at the polar footprints of plasma flux tubes originating from the motion of Jovian satellites. The moons Io, Ganymede, and Europa exhibit the strongest footprint features, with Io's contribution being the most dominant feature in the UV emission spectrum.
- Main auroral emission: It consists of the main auroral oval titled w.r.t. Jupiter's pole. This feature co-rotates with the planetary magnetic field and appears as a static feature in the System III corotating coordinate system.
- Poleward auroral emission: These emission features lie poleward of the main auroral oval. They are highly transient emission sources corresponding to a complex magnetic field topology of open and closed field line features.

The polar region inside the main auroral oval can also be classified into active, swirl, and dark regions. The active region consists of two bright transient polar flares and a permanent arc-like feature. It has a sub-corrotational nature, and it is confined between noon to post-noon solar local time sector. The swirl region is characterized by a region of patchy, transient features that occasionally form a clockwise swirl motion. Lastly, the dark region is a sub-corotating crescent-shaped region occurring on the dawn side. It is almost devoid of any auroral emission. Field-aligned currents in this region are expected to be downward-directed (upward-moving electrons).

4.2.1 Pre-Juno Observations

Radio and microwave frequencies have been useful tools to probe Jupiter's auroral emission and inner magnetospheric interactions. Jupiter's magnetic field was first detected by Earth-based measurements of nonthermal radio emissions at the Carnegie xx. [59]. It hinted at the presence of ultra-relativistic electrons in its space environment. Emissions between 10-40 MHz were detected and consequently attributed to cyclotron emissions from electrons. Radio wave emissions with low-frequency components in 10 kHz to several MHz were detected during flyby of Voyager 1 and Voyager 2 emissions: hectometric emission (HOM, 200 kHz - 1 MHz), broadband kilometric emission (bKOM, 10 kHz - 1 MHz) and narrowband kilometric emission (nKOM, 100-200 kHz) [65, 162, 295]. The discovery of Jovian decametric emission (DAM) modulations with the orbital position of Io provided strong evidence for electromagnetic interactions between Jupiter's inner magnetosphere and its inner satellites [41]. Further observations from Ulysses, Galileo, and Cassini instruments led to the discovery of quasi-periodic radio bursts (QP, period $\sim$ 15-40 minutes) [179], and characterized the population of non-equilibrium charged particles at high-latitude Jovian plasma.

Likewise, radio occultation conducted during Pioneer 10 flyby provided the first measurements of Jupiter's ionospheric electron density profiles. Later, Voyager missions and the Galileo orbiter collectively provided an extensive survey of ionospheric electron density profiles. It was primarily focused on the low and mid-latitude ionosphere, with a few auroral radio occultation experiments conducted by Galileo at 68^o and 76^o N latitudes. The microwave frequencies at GHz frequency are sensitive to Jupiter's synchrotron radiation [45]. Relativistic electrons in Jupiter emit nonthermal emissions at microwave frequencies, exhibiting a strong variability with solar wind pressure. Both radio wave and microwave emissions have been useful in understanding the effects of solar wind on magnetospheric structure [44, 130].

Electron precipitation into the hydrogen envelope of the gas giant atmosphere causes the excitation of hydrogen Lyman band, Werner band, and Lyman Alpha emissions. First discovered by Voyager 1 UVS instrument [54], it has followed with subsequent investigations by Voyager 2 [238, 55], International Ultraviolet Explorer (IUE) [276], Galileo UVS [7], Hopkins Ultraviolet Telescope (HUT) [8] and Hubble Space Telescope (HST) [74]. UV emission spectra can be directly connected to the amount of electron precipitation using a UV color ratio (CR), defined as the ratio of UV emission intensities between 155-162 nm to that of 123-130 nm. It differentiates the electron energy by taking into account UV absorption contribution from Jovian hydrocarbon species [294].

$$CR = \frac{I(155nm - 162nm)}{I(123nm - 130nm)} \tag{4.1}$$

The morphology of UV aurora emissions maps the nature of magnetic field topology at the Northern and Southern hemispheres. These emissions can be magnetically mapped to sources within the Jovian magnetosphere, with footprints of inner satellites like Io, Ganymede, and Europa contributing to localized charged particle precipitation [75, 121]. Some UV emission events poleward to MAE have been mapped at distances beyond $\sim$ 100 R_J, providing evidence for plasmoid ejection at the magnetotail [123]. As UV emissions are caused by collisional excitation, they have very short decay times and vary rapidly. Auroral emission mapping shows that the MAE features are fixed regarding Jupiter's rotation frame, unlike Earth's aurora.

The precipitation of heavy ions of carbon, oxygen, and sulphur undergoes charge exchange and ionization that emit at X-ray wavelengths. These emissions have been monitored over many decades by the Chandra X-ray Observatory [116, 51], XMM Newton Telescope [52, 99] and Röntgen satellite (ROSAT) [275]. In both the Northern and Southern hemispheres, X-ray auroral hotspots were found to have periodic pulsations at periodicities of 9, 12, 40-45 min. Recent studies show pulsations to be bi-modal, likely due to the expansion and compression of the Jovian magnetosphere in response to the solar wind [99].

Ionization of molecular hydrogen in the aurora and its interaction with molecular hydrogen neutrals leads to the formation of H_3^+. H_3^+ emits in an infrared emission at 2–5 μm band that occurs 450-1050 km above the 1 bar level [95]. It is considered a tracer to probe the high-altitude region, and its response to atmospheric energy deposition at altitudes above the methane homopause. Measurement of H_3^+ emissions provides the column depth and ionospheric temperature that can be attributed to both external (solar EUV, particle precipitation) and internal sources (gravity waves). Near the CH_4 homopause, H_3^+ ions are consumed by reaction with methane. Electron precipitation at energies $\geq$ 100 MeV penetrates the CH_4 homopause leading to neutral heating. The primary hydrocarbons i.e. CH_4, C_2H_2, C_2H_6, and CH_3 show up at 1 μbar level, leading a polar brightening in both the hemispheres [63, 158, 62, 253]. These hotspots are observed within the main auroral oval and have been attributed to high-energy charged particle precipitation.

4.2.2 Juno Observations

Being a polar orbiter with a perijove around the North Pole, Juno provides an extensive radial survey of energetic charged particles in Jupiter's inner magnetosphere. The JEDI electron flux data over multiple Juno perijoves revealed the presence of a broadband electron flux, highlighting plasma turbulence and stochastic processes to play a role in charged particle acceleration

[184, 190]. Ions of S, O, and Na with energies greater than 10 MeV were detected to be precipitating over the polar cap in the Northern and Southern hemispheres [131]. Precipitation of these energetic ions is a source for X-ray auroral emissions at the Jovian poles [81]. Several cases of high-energy electron flux with peak energy equivalent to 100 keV were measured at both hemispheres. Electrons have a higher penetration power relative to ions with similar energies. Thus, precipitation of MeV electrons leads to atmospheric heating and ionization much deeper into the stratospheric region. Regions of bidirectional electron beams have been inferred from JEDI data, with a strong upward acceleration of electrons [189]. Additionally, the Juno star trackers: Advanced Stellar Compass (ASC) [91] and Stellar Reference Unit (SRU) are also sensitive to high-energy relativistic ions and electrons. The magnetometer instrument onboard Juno conducts pole-to-pole measurements of Jupiter's magnetic field. The magnetic field vectors have been analyzed over the first 9 orbits to provide a high-order spherical harmonics model of Jupiter's internal magnetic field [78]. Connerney et al., (2022) updated the model to include magnetic field data from the first 33 Juno orbits [79]. These measurements provide improvements in understanding magnetic field anomalies, and tracing of charged particle transport through magnetic field line vectors.

The Juno UVS emission and CR maps characterized the auroral emission poleward to MAE. Auroral UV emissions amount to 1000 kR and the upper bound of UV CR is found to be 20. Magnetically mapping the UVS emissions to JEDI in-situ electron flux hints at charged particle acceleration between spacecraft and TOA. Benmahi et al., (2024) showed a correlation between UV CR and characteristic energy corresponding to electron energy kappa distribution [33]. Thus, CR maps can be interpreted to infer TOA electron flux over the auroral region. UVS emission spectra also probe the overall Pedersen conductivity due to steady-state concentrations of H_3^+, and hydrocarbon ions; estimating the conductances to range between 0.1 to several mhos. The Jovian InfraRed Auroral Mapper (JIRAM) instrument measurements associated with thermospheric H_3^+ emissions show a large variability between 600-1400 K within a Jovian day [3]. Spatial locations of auroral oval inferred from JIRAM data show a match with Earth-based observations of MAE, and statistical model derived from HST Space Telescope Imaging Spectrograph (STIS) [122]. Concurrent observations of JIRAM and UVS during PJ 1 pointed at the precipitation of high-energy electrons, and H_3^+ loss due to interaction with CH_4 in Jupiter's atmosphere [112]. It hints at the formation of hydrocarbon ions in Jupiter's auroral regions.

4.3 Juno Microwave Radiometer observations

The measurements from the Juno mission [140, 214] have demonstrated that the aurora via its generation of a local plasma enhancement (ionosphere) is associated with the apparent cold spots in the microwave emission. These cold spots in MWR antenna temperatures are correlated with UVS measurements at the Northern Aurora. Figure 4.1 describes a case of cold spot during PJ 5 which can be seen to be associated with UV auroral emissions. These phenomena are observed as a local decrease in brightness temperatures at low frequencies (0.6 – 1.2 GHz) within the observation window of the Juno Microwave Radiometer. As a result of the latter, the process affects the high-altitude distribution of the planet's microwave radiation by absorbing and redistributing the atmospheric microwave thermal emission at high latitudes, effectively acting like an opaque medium.

In Chapter 2 we briefly mentioned the association of Jupiter's aurora with the MWR observations. When the Juno spacecraft passes over the poles, the low-frequency channels i.e. channels 1-4 observe regions colder than the nominal atmospheric thermal emission [140]. The existence of this absorption is most apparent in the correlation when overlaying a map of the microwave radiation onto the auroral oval observed by the Juno UltraViolet Spectrograph (UVS) [140], which serves as an excellent proxy of the boundaries of Jupiter's auroral and polar cap particle precipitation regions. In the Northern Hemisphere, Juno provides a more spatially resolved measurement of polar thermal radiation. It has been particularly designed to identify and resolve thermal emissions

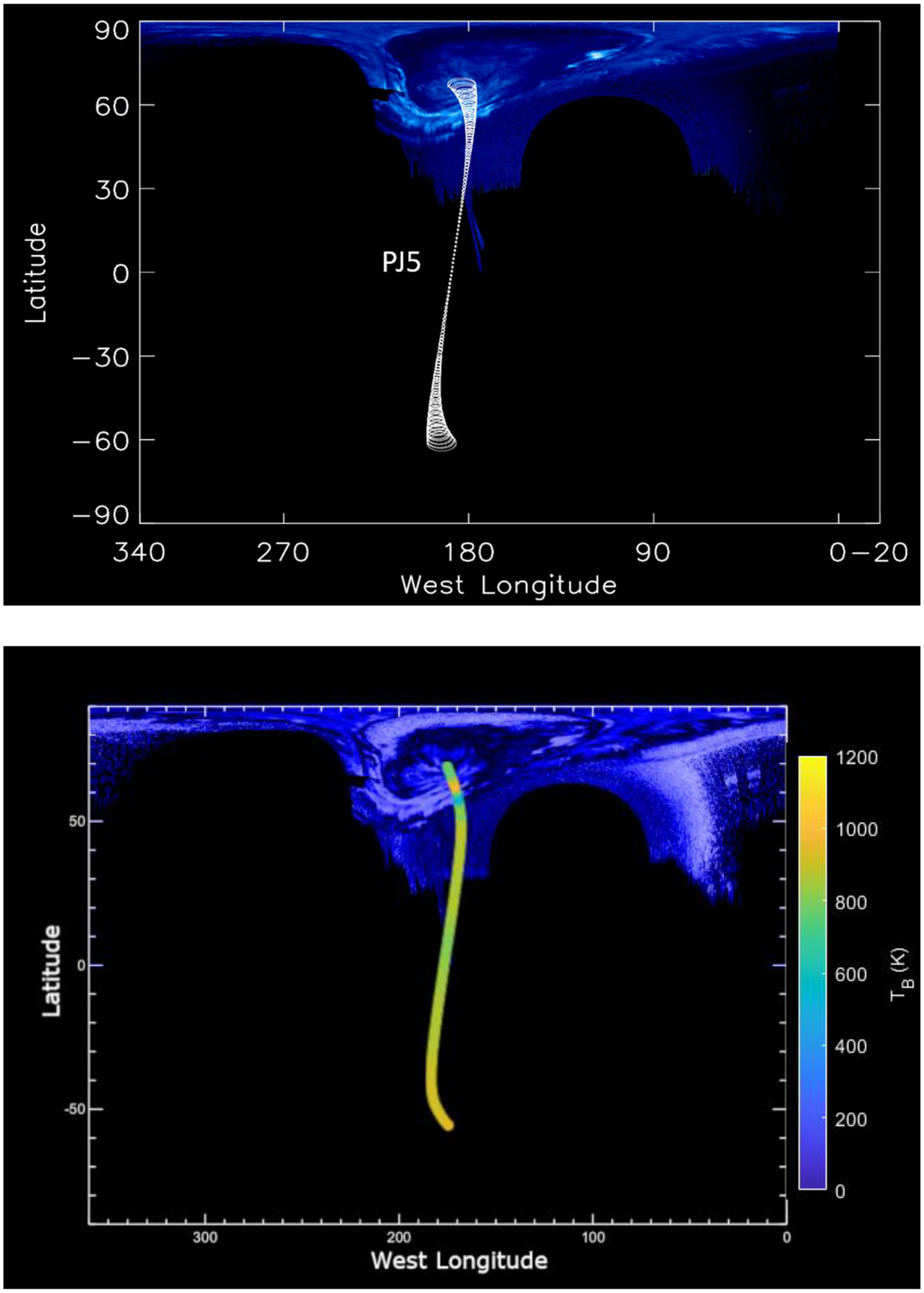

Figure 4.1: Juno MWR channel 1 (0.6 GHz) antenna footprint (top figure) and antenna temperatures (bottom figure) overlaid on the Juno UVS data during PJ 5 (blue color)

from polar vortices at high atmospheric pressures not observable in visible or infrared wavelengths.

Juno perijove (PJ) observations provide a direct measurement of antenna temperature at microwave frequencies. The antenna temperatures at high latitudes exhibit cold features at 0.6, 1.2, and 2.2 GHz channels over discrete auroral arcs [140] and within the polar cap. The relative differences between the cold spot brightness temperature and the background atmospheric temperature decrease at higher frequencies, but are more prominent at 0.6 and 1.2 GHz. For our study, we consider the antenna temperatures corresponding to PJ 1, 3-54 at 0.6 GHz and 1.2 GHz from 50 deg. N to the pole. We apply a cutoff filter for T_A such that temperatures below the cutoff value represent auroral cold spot regions. The cutoff T_A for the 0.6 GHz and 1.2 GHz are equal to 800 K and 450 K respectively. The cutoff latitude for data filtering is chosen to be 50 deg. N as cold spots have been observed between 50-90 deg. N [140].

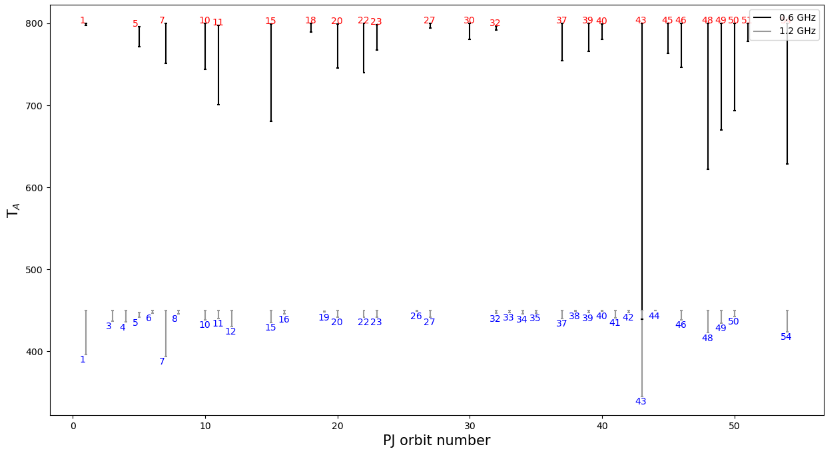

Figure 4.2: T_A corresponding to low-frequency channels filtered for emission angle less than 10 deg., and T_A magnitude less than the respective cut-off for PJ 1-54. Near-nadir values of T_A exhibit a large range with lower limits in ranges $\sim 450 - 750$ K (0.6 GHz), and $350 - 415$ K (1.2 GHz). Large dips in the T_A can be observed in both channels during multiple PJ orbits. A small range of T_A can also be attributed to atmospheric variations in both channels. Orbits with a large range in T_A magnitudes appear to be positively attributed to energetic precipitation events.

Figure 4.2 shows a range of T_A magnitudes for each PJ where T_A is expected to be less than the cut-off value. We set cut-off values for the 0.6 GHz channel, and the 1.2 GHz channel equal to 800 K, and 450 K respectively based on the probability distribution of T_A from atmospheric thermal radiation. It can be seen that regions of cold T_A have been observed over multiple orbits. [140]

provides a detailed analysis of these cold regions during Juno's first 21 orbits. It represents the variation over various latitudes and footprint sizes. During the mission, the perijove (i.e., line of apsides) of Juno continuously precesses northward, providing increased resolution of the northern high latitudes (Fig. 4.3). Therefore, the MWR footprint over the North Pole varies over each perijove. Radiometer resolution is limited by footprint length scale, and any variations in T_A can be partially attributed to the observation geometry, and distance from the nadir viewing altitude.

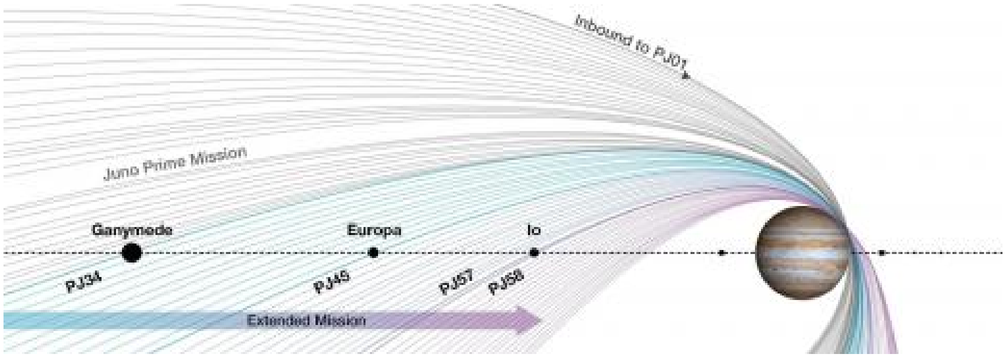

Figure 4.3: Illustration of Juno orbit trajectories from Juno Prime Mission to the extended mission phase including a flyby of inner Jovian moons. The perijove continuously approaches towards the North Pole, providing a fine antenna beam size during the later orbits.

The effective variation in cold spot antenna temperatures cannot be solely attributed to changes in MWR footprint over different orbits. We highlight the MWR observations corresponding to two distinct orbital geometries i.e., PJ 15 and PJ 22. These observations represent the changes in MWR observation geometry and polar projection of antenna footprints. Footprint size decreases relative to the auroral oval in later PJ orbits as we go from PJ 15 to PJ 22 (Fig. 4.4, 4.7).

This phenomenon has been identified in other perijove orbits, including PJ 05, 10, 11, 16, 22, 26, 27, 28, 30, 32, 37, 40, 46 and 54. Here we present a case study of PJ 37 where the MWR antenna temperatures identify rapid change within consecutive spacecraft spins (Fig. 4.8 and 4.9). Four cases are presented where the feature is particularly prominent in both channels i.e. PJ 10, PJ 37, PJ 46, and PJ 54 (Fig. 4.10 - 4.13). In the figures given below, the time series of antenna

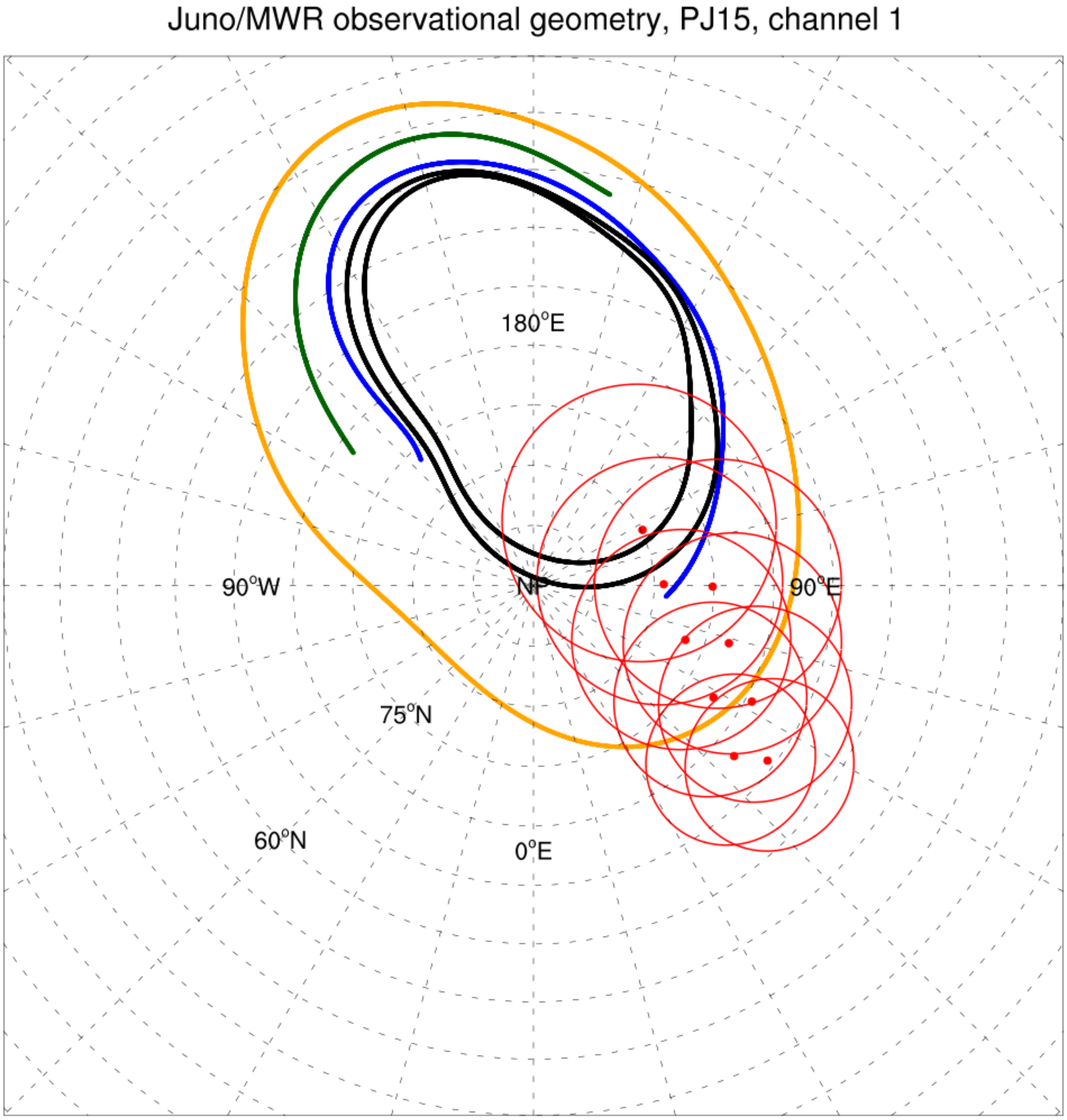

Figure 4.4: Polar projections of MWR channel 1 antenna footprints corresponding to PJ 15 as a function of spin number. The footprint size of the MWR antenna beam changes relative to the size of the auroral oval (black), and the footprints of Io (orange), Europa (green), and Ganymede (blue). The plotted footprints represent a sample of actual footprints throughout the mission. As the mission progresses, the altitude of the observation changes due to the northward precession of the perijove of Juno's orbit. The footprints indicate a large degree of overlap between consecutive spins.

temperatures for the first two MWR channels show rapid changes in bore sight temperature within 30 seconds for a given channel. In many cases, the temperatures appear to be consistently

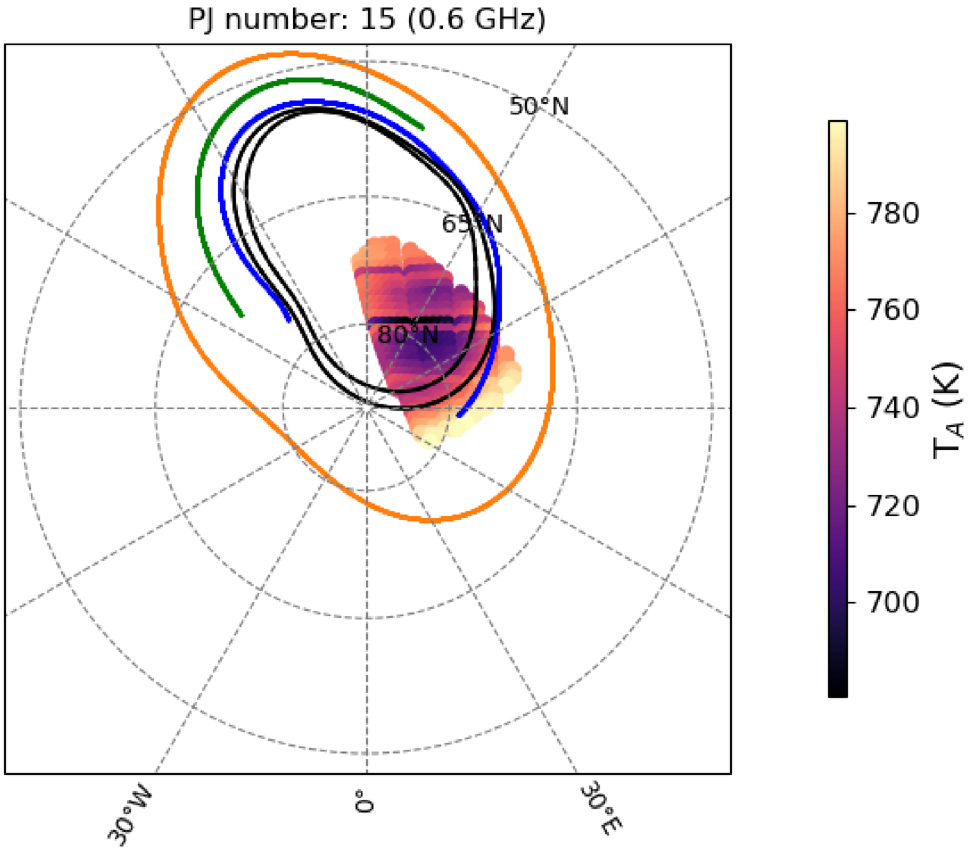

Figure 4.5: Polar projections of MWR channel 1 antenna footprints corresponding to PJ 15 as a function of spin number. The footprint size of the MWR antenna beam changes relative to the size of the auroral oval (black), and the footprints of Io (orange), Europa (green), and Ganymede (blue). The plotted footprints represent a sample of actual footprints throughout the mission. As the mission progresses, the altitude of the observation changes due to the northward precession of the perijove of Juno's orbit. The footprints indicate a large degree of overlap between consecutive spins.

changing in both channels, however the magnitude of variation differs between the two. T_A is expected to change within a spin period ($\sim$ 30 s). However, there is a 120-degree along-spin

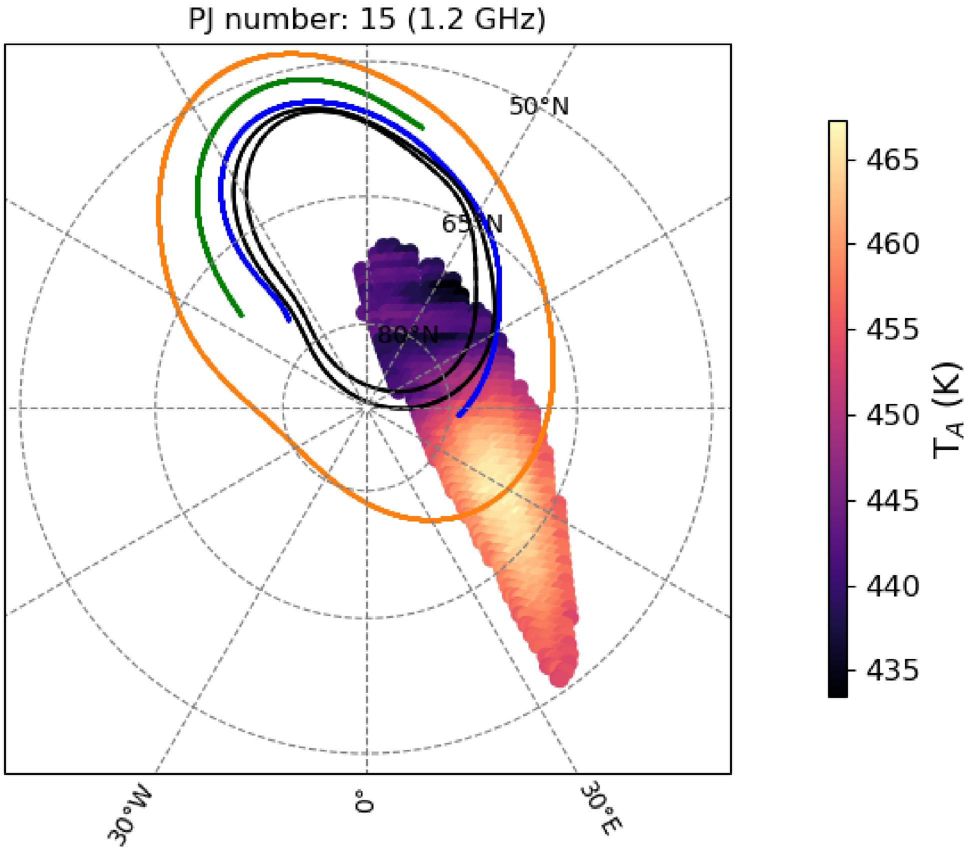

Figure 4.6: Polar projections of MWR antenna temperatures (1.2 GHz) corresponding to PJ 15. Consecutive spins observe the same region of the atmosphere due to the overlapping footprints. Similar to the 0.6 GHz channel, the 1.2 GHz channel exhibits cold T$_A$ magnitudes ranging between 450 - 435 K. A small degree of variation is observed over consecutive spins along the PJ track. The cold regions at 1.2 GHz are bounded by the Io footprint and spatial variations of polar auroral emissions.

separation between the 0.6 GHz antenna boresight and the 1.2 GHz boresight, resulting in a 10-second delay between observations of the same location. As the stripes of high and low T$_A$

Juno/MWR observational geometry, PJ22, channel 1

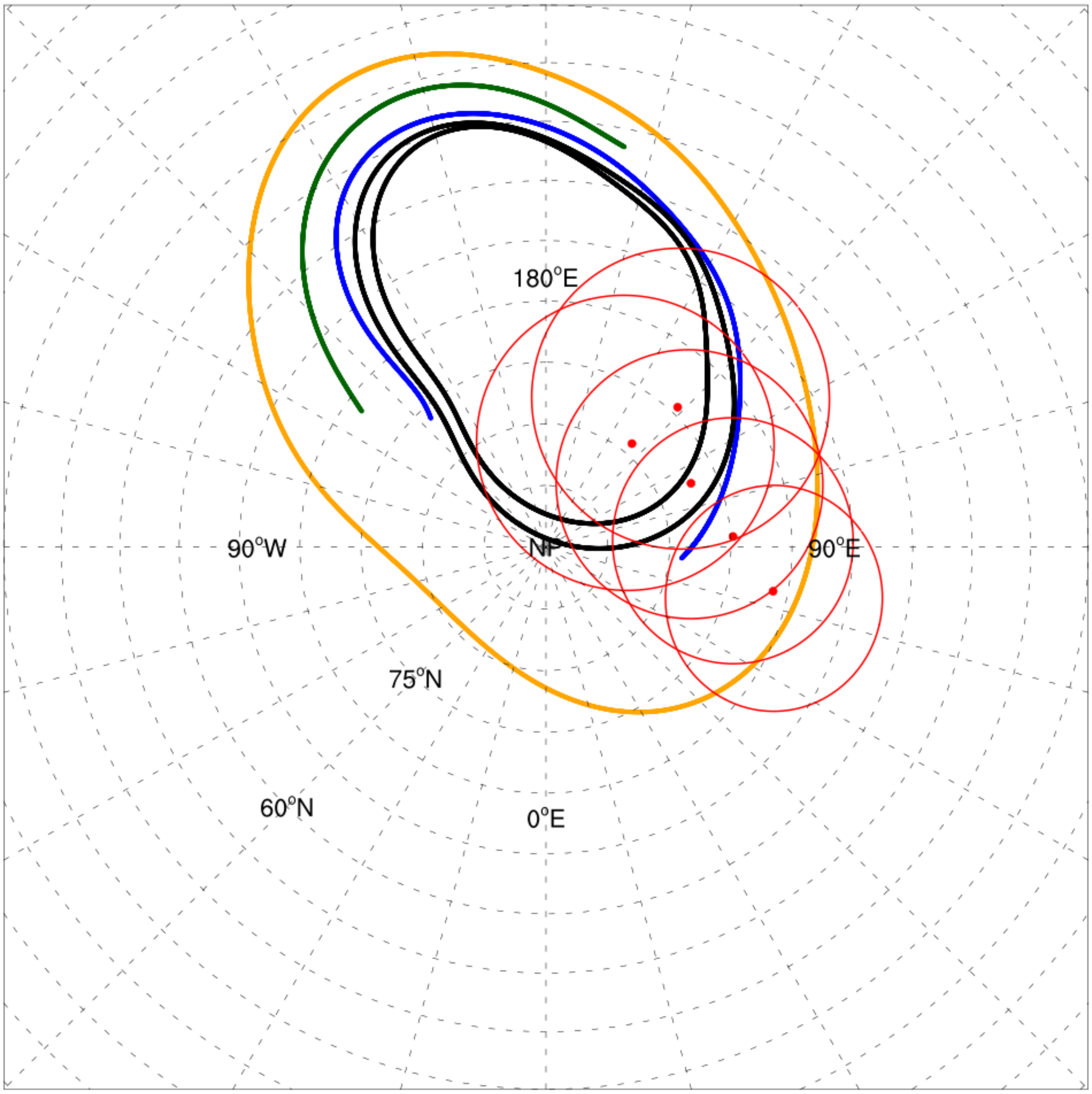

Figure 4.7: Polar projections of MWR channel 1 antenna footprints corresponding to PJ 22. The footprint size of the MWR antenna beam changes relative to the size of the auroral oval (black), and the footprints of Io (orange), Europa (green), and Ganymede (blue). The plotted footprints represent a sample of actual footprints throughout the mission. As the mission progresses, the altitude of the observation changes due to the northward precession of the perijove of Juno's orbit. The footprints show a large degree of overlap between consecutive spins. Both PJ 15 and PJ 22 represent cases of large channel 1 antenna beam footprint relative to the main oval.

regions do not show any spatial correlation between 0.6 and 1.2 GHz channels, the source function of the electrons absorbing the microwave emission can be expected to vary much faster ($\sim$ 10 s).

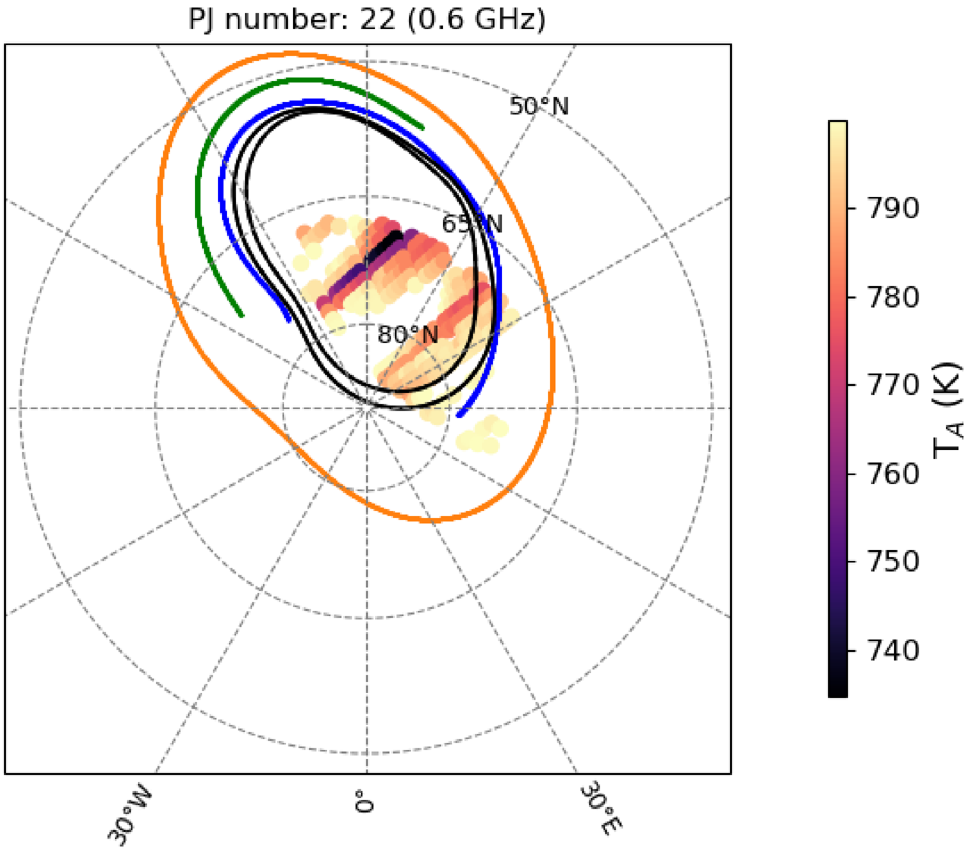

Figure 4.8: Polar projections of MWR antenna temperatures (0.6 GHz) corresponding to PJ 22. Consecutive spins observe the same region of the atmosphere due to the overlapping footprints. As in the case of PJ 15, a large degree of variation is observed in 0.6 GHz T_A values within the MAE.

These regions of cold T_A are contained primarily within the main auroral emission (MAE) and footprints of primary satellites: Io, Ganymede, and Europa. They are situated either poleward or in regions adjacent to the Io footprint. However, the morphology of cold regions can differ from

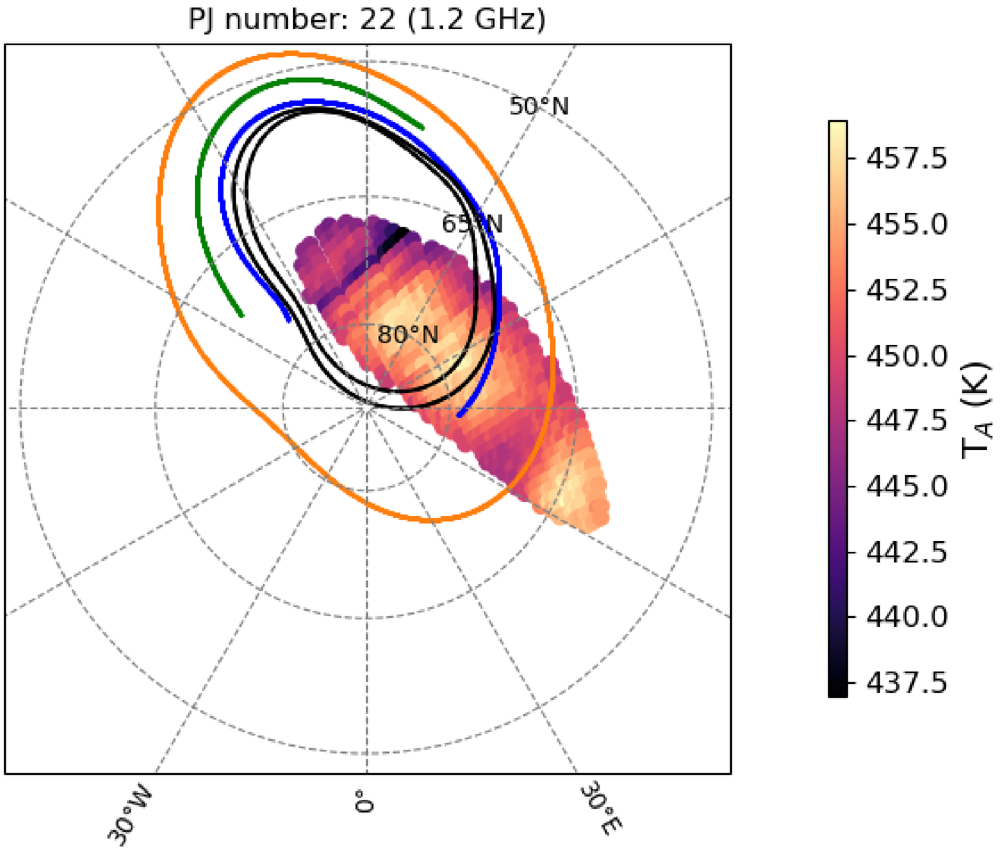

Figure 4.9: Polar projections of MWR antenna temperatures (1.2 GHz) corresponding to PJ 22. Consecutive spins observe the same region of the atmosphere due to the overlapping footprints. Thus, rapid changes in antenna temperatures are associated with temporal changes in the ionospheric medium. A little portion of 1.2 GHz T_A values outside the MAE show a small decrease, attributed to large antenna beam size.

one orbit to another. Bonfond et al., (2017) [47] provides the mean position of MAE and satellite footprints over the North Pole. The footprint and MAE coordinates are publicly available in the supplementary data section of the referenced paper.

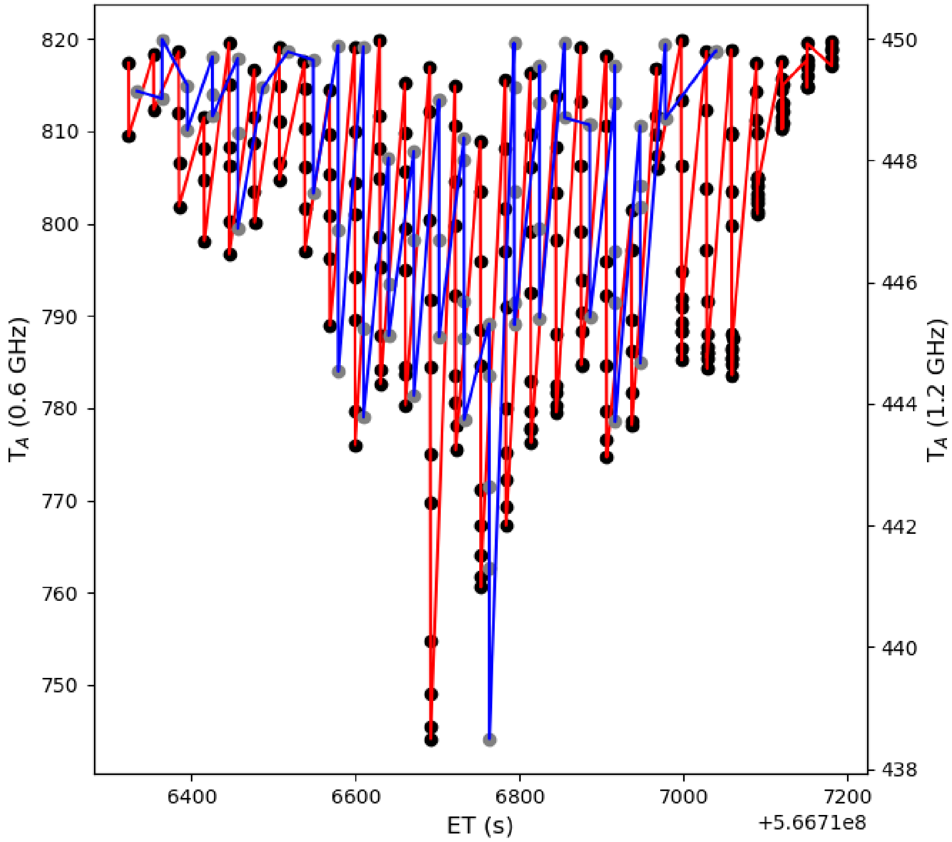

Figure 4.10: Time series data of 0.6 GHz (blue) and 1.2 GHz (red) channel bore sight antenna temperatures (PJ 10) within 15 deg. emission angles.

4.4 Electron Precipitation: Atmospheric Heating and Ionization

4.4.1 Background

Early works on electron precipitation at Jupiter and Saturn focus on low-energy monoenergetic electron beams and their degradation due to collisional processes with H_2 and He. In a real atmo-

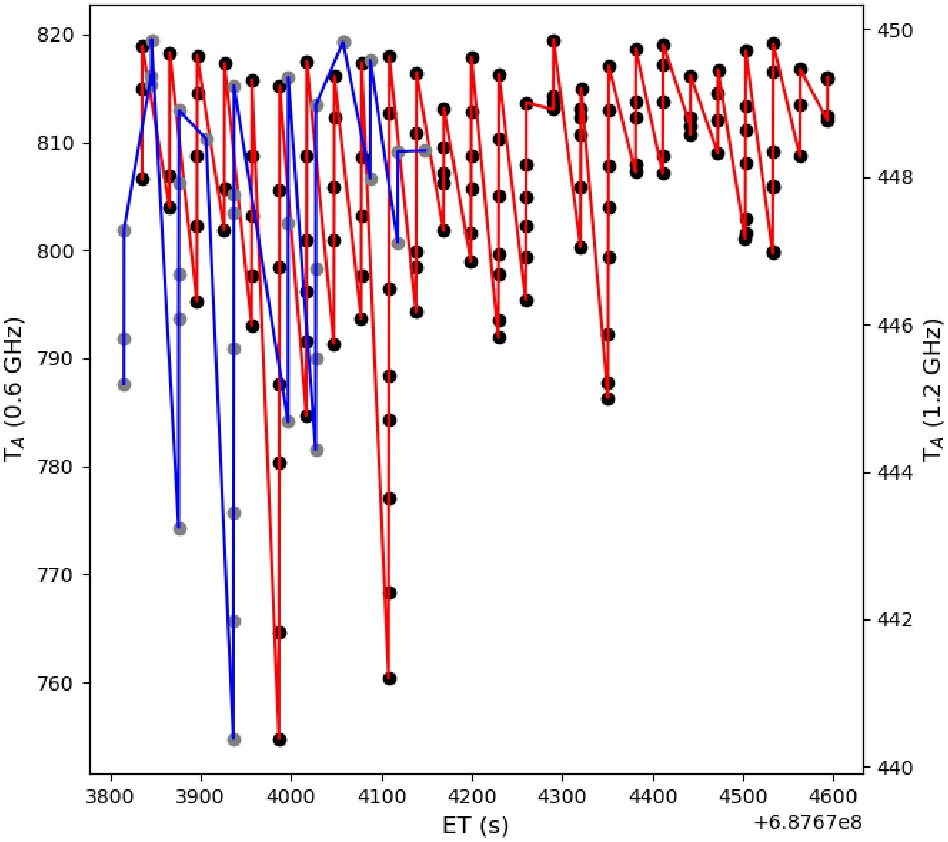

Figure 4.11: Time series data of 0.6 GHz (blue) and 1.2 GHz (red) channel bore sight antenna temperatures (PJ 37) within 15 deg. emission angles.

sphere, a complex energy distribution of energetic electrons and ions beam into the atmosphere, causing neutral heating and excitation processes. Hot electrons collide with H_2 to ionize the atmosphere and form H$^+$ and H_3^+ ions. Secondary electrons undergo subsequent collisions to distribute the electron energy into deeper levels of the upper atmosphere. One-dimensional models of electron transport and energy deposition have been crucial to the understanding of Jovian ionospheric composition and thermal structure. Waite et al. 1983, adopted a Saturn ionosphere two-stream model of electron transport for Jupiter to estimate electron density, and UV emission rate [276]. It was extended by Grodent to couple electron transport with a heat conduction model. Egert et al., (2017) adopted the Global Ionosphere Thermosphere Model (GITM) for a

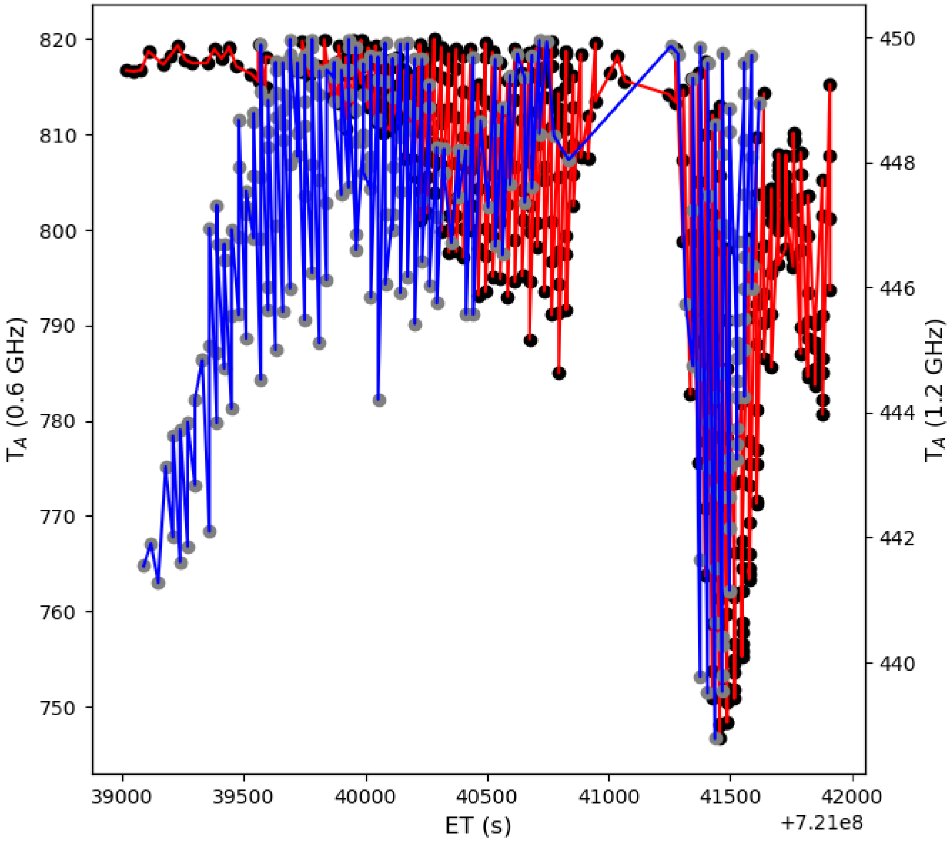

Figure 4.12: Time series data of 0.6 GHz (blue) and 1.2 GHz (red) channel bore sight antenna temperatures (PJ 46) within 15 deg. emission angles.

one-dimensional auroral ionosphere model [101]. It simulated electron precipitation up to 100 keV electrons.

Continuous slowing down approximation models based on particle interactions have been applied to Jupiter's atmosphere with 100 keV energies [257]. The model provides an accurate distribution of energy deposition, and secondary electrons without the complexity of simulating transport for each energy bin. These models have a wide application, from cosmic ray ionization of molecular clouds to particle precipitation in terrestrial atmospheres. In recent years, particle interaction codes based on Monte Carlo methods have been adopted for planetary applications. In

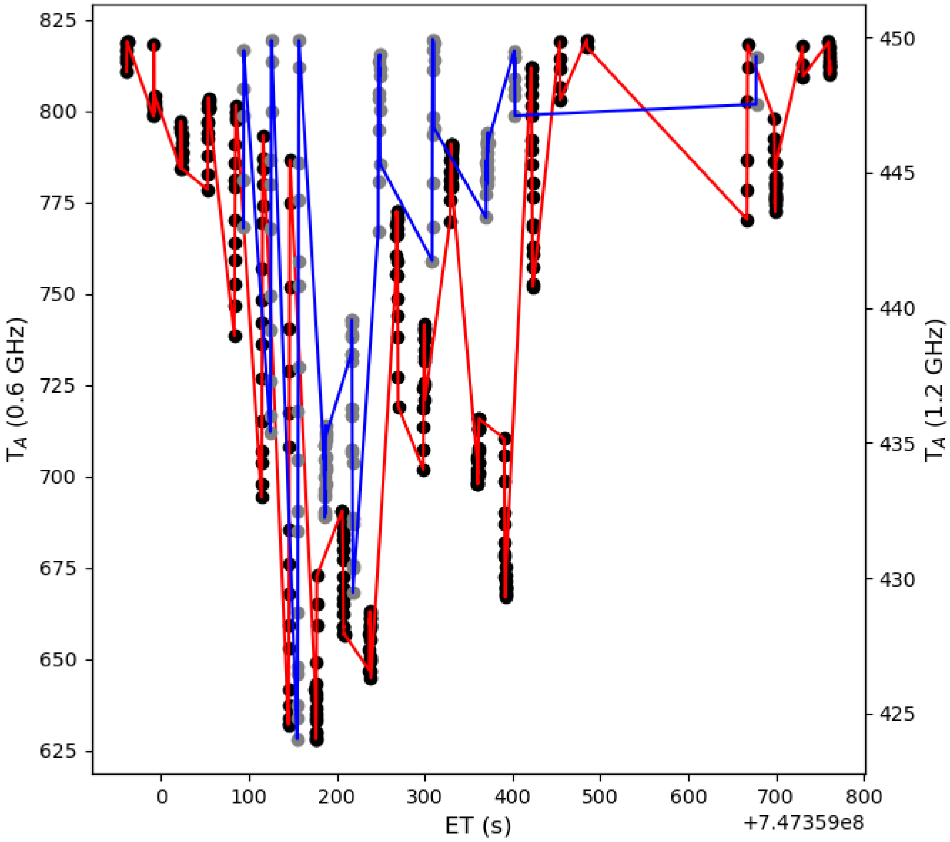

Figure 4.13: Time series data of 0.6 GHz (blue) and 1.2 GHz (red) channel bore sight antenna temperatures (PJ 54) within 15 deg. emission angles.

particular, GEANT4, a particle physics code developed at the European Organization for Nuclear Research (CERN), has been adapted for planetary environments (planetocosmics) [92]. In its recent forms, it has been used to simulate the effects of solar energetic particles, and galactic cosmic rays on terrestrial planets and Titan.

The spatial complexity and importance of auroral processes that lead to heating, ionization, and dissociation over a large high-latitude surface area cannot be understood without the use of global circulation models that bear on the associated atmospheric transport. Several global circulation models (GCM) of Jupiter's upper atmosphere have been developed over the years: Jovian Ionosphere Model (JIM) [2], Jupiter Thermosphere General Circulation Model (JTGCM) [50]. Additionally, some one-dimensional magnetospheric models are coupled with two-dimensional GCMs. The GCMs provide system-level constraints on vertical and horizontal winds at mid-latitudes and polar regions, effectively simulating the transport of hydrocarbons in the thermosphere and stratosphere. In addition, Juno's fields and particle measurements have changed the paradigm on particle acceleration processes in Jupiter's aurora with both classical Earth inverted V and broadband energy acceleration taking place. Most notably the degree of acceleration extends the anticipated energy range to energies exceeding 10 MeV, almost an order of magnitude larger than pre-Juno expectations.

4.4.2 Hybrid Electron Precipitation Model

To deal with the highly extended energy range of auroral acceleration we developed an electron precipitation model of the Jovian upper atmosphere using the CSDA approach. In the model, energy loss is expressed as a differential of local column density of H_2 equal to the loss function. The energy loss function of electrons in H_2 is a sum of various loss processes like Coulomb interactions, inelastic collisions, ionization, bremsstrahlung, synchrotron emission, and inverse Compton scattering (Fig. 4.14). Atmospheric energy deposition and ionization due to collisional interactions with neutral species are simulated for a pure H_2 atmosphere. We apply CSDA to compute electron energy loss at an average 45^o pitch angle using the loss function of H_2-e^- interactions provided in [216].

$$L_k(E_k) = -\frac{dE_k}{dN(H_2)} \tag{4.2}$$

$$N(H_2) = \int n(H_2)\, dl \tag{4.3}$$

Here, $L_k(E_k)$ is the total electron loss function, dE_k is the amount of differential energy loss corresponding to penetration of $dN(H_2)$ hydrogen column depth, and $n(H_2)$ is total H_2 number density. The effects due to other constituents such as He or CH_4 will be secondary to H_2.

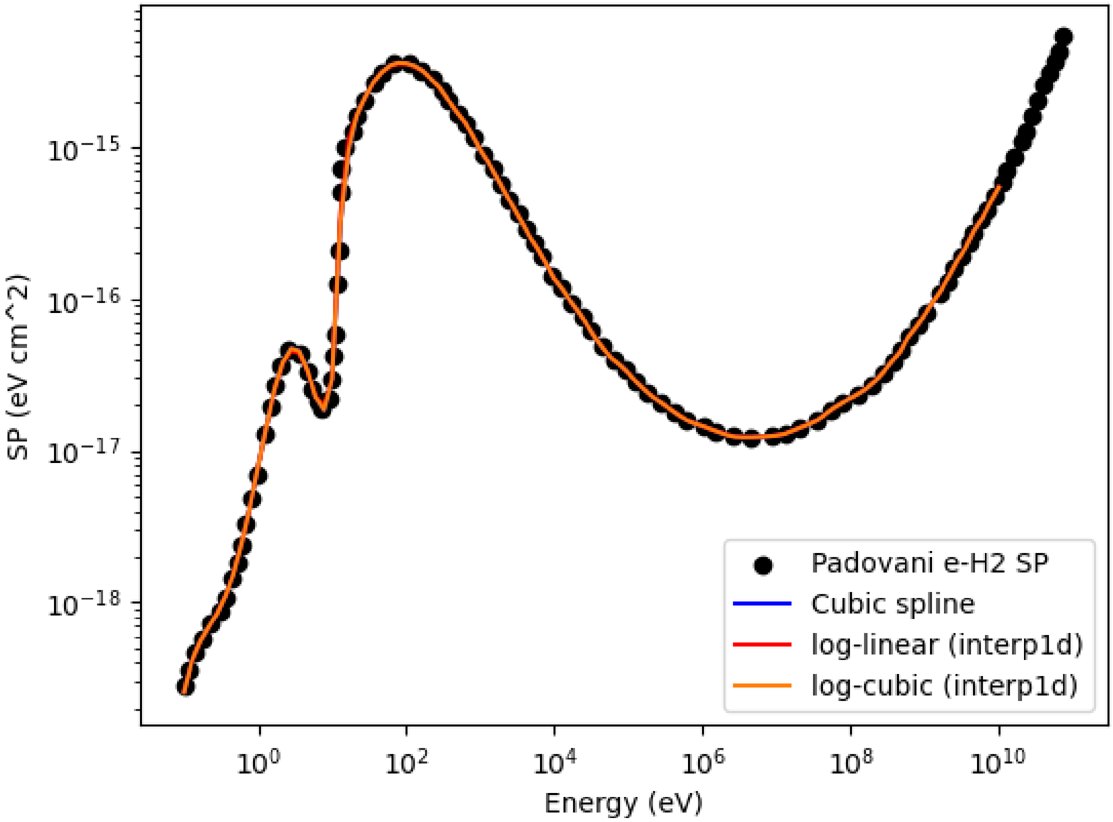

Figure 4.14: Fitting curves to total electron stopping power of hydrogen molecule at different electron energies [216]

A high-latitude model of Jupiter's thermosphere and stratosphere from [206] is adopted for the simulations. We apply the results of two-stream electron transport modeling assuming primary electrons $\sim$ 10 keV. The energy partitioning is used to calculate rates for electron impact ionization, and direct excitation ($\nu_1 - \nu_3$) assuming ion-pair production of 39.38 eV per ion pair produced. The direct electron impact excitation of H_2 has a branching ratio of 1 : 0.1: 0.007. Table 4.1 provides a summary of all energy partition values used in this work.

Table 4.1: Summary of energy partitioning of total energy deposition associated with electron precipitation in Jupiter's atmosphere

Process	Energy partitioning value (percent)
Neutral heating	11.06
Electron heating	1.65
H_2^+ production (reaction E_1)	38.91
H^+ production (reaction E_2)	6.09
UV emission	18
Total H_2 direct excitation	8.31

4.4.3 Chemical Kinetics of Jupiter's Auroral Ionosphere

We developed a one-dimensional chemical kinetics code for planetary atmospheres, Comprehensive Coupled Chemistry Model (C^3M). It solves the reaction-diffusion equations for a set of coupled reactions for electrons, ions, and neutrals. It has been developed based on Athena++ [265], a magnetohydrodynamics code for astrophysical applications, and Cantera [118], a C++-based chemistry code used for combustion and chemical engineering applications. The code is publicly available on GitHub.

$$\frac{\partial q_i}{\partial t} = -\frac{\partial \phi_i}{\partial z} + R_i \tag{4.4}$$

$$\phi_i = -(K+D)Q\frac{\partial x_i}{\partial z} + Dq_i(\frac{1}{H_0} - \frac{1}{H_i} - \frac{1}{P_e}\frac{\partial P_e}{\partial z} - \frac{\alpha_i}{T}\frac{\partial T}{\partial z}) \tag{4.5}$$

Here, q_i is the number density of species i, ϕ_i is the flux of species i through a given point in the atmosphere, Q is the total number density, R_i is the net production rate i.e., the sum of all chemical source, and sinks. K is the eddy diffusion coefficient, D_i is the molecular/ambipolar diffusion coefficient, and x refers to the mole fraction of a given chemical species i. H_0 is the average well-mixed atmospheric scale height, and H_i is the scale height corresponding to a given atomic or molecular species. For ions, ambipolar diffusion has been taken into account with an additional term due to the electron pressure gradient. P_e is electron pressure, and it is relevant to ambipolar diffusion in ions [209]. α_i refers to thermal diffusion coefficient. Thermal diffusion is important for H, and He, and it is set to zero for all other species [161]. A fixed mixing ratio of H_2, He, CH_4, C_2H_2, C_2H_4, and C_2H_6 are assumed at the lower boundary following number densities provided by Moses and Poppe (2017) [206]. We also maintain a zero flux boundary condition at the upper boundary, as atmospheric constituents are too heavy to escape and the upper boundary is expected to be at photochemical equilibrium (Table 4.2).

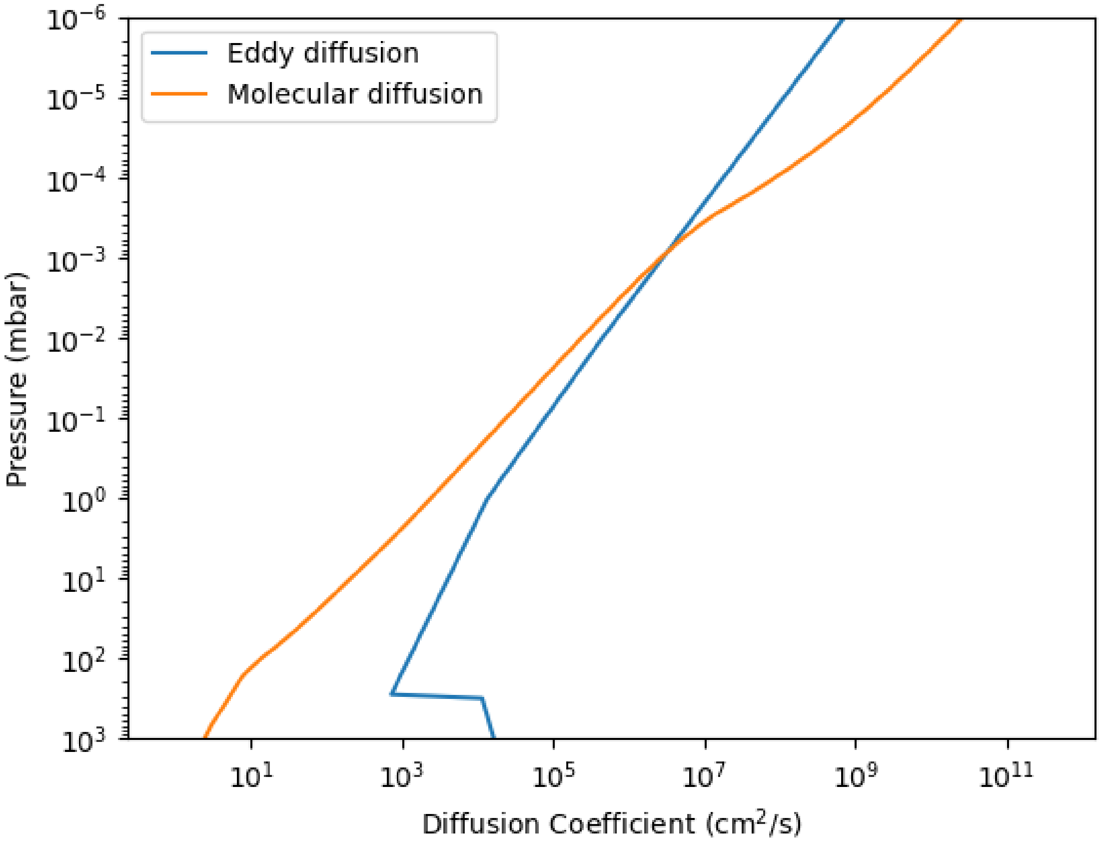

Figure 4.15: Eddy and molecular diffusion profiles adopted for Jupiter's atmospheric chemical kinetics model. Eddy diffusion is adopted from early models of Jupiter's stratosphere [204, 206], while the molecular diffusion is calculated based on binary diffusion provided in Nakamura et al., (2022) [209]

Table 4.2: List of important boundary conditions for Jupiter's atmospheric chemistry model

Species	**Boundary condition (Bottom)**	**Boundary condition (Top)**
H_2	$X_{H_2} = 0.86$	$\Phi_{H_2} = 0$
He	$X_{He} = 0.135$	$\Phi_{He} = 0$
CH_4	$X_{CH_4} = 0.0018$	$\Phi_{CH_4} = 0$
C_2H_2	$X_{C_2H_2} = 3.450 \text{ x } 10^{-12}$	$\Phi_{C_2H_2} = 0$
C_2H_4	$X_{C_2H_4} = 5.805 \text{ x } 10^{-13}$	$\Phi_{C_2H_4} = 0$
C_2H_6	$X_{C_2H_6} = 1.025 \text{ x } 10^{-9}$	$\Phi_{C_2H_6} = 0$
H_3^+	$X_{H_3^+} = 0$	$\Phi_{H_3^+} = 0$
H^+	$X_{H^+} = 0$	$\Phi_{H^+} = 0$
e^-	$X_{e^-} = 0$	$\Phi_{e^-} = 0$

C^3M uses a semi-implicit scheme for evolving the system to the final state. The scheme is first-order implicit in the time domain [165], and uses an explicit second-order finite difference scheme [143] for diffusion. Therefore, the stability is controlled by the total diffusion coefficient expressed as the sum of molecular, and eddy diffusion. Eddy diffusion in our model is based on knowledge of stratospheric photochemistry [204, 206], and molecular diffusion is expressed in terms of binary collision frequency with H_2 [209] (Fig. 4.15).

4.4.4 Reaction Mechanism

Charged particle precipitation into high-latitude ionosphere initiates a chain of reaction leading up to the formation of C_2 hydrocarbons [252, 288]. These products act as precursors for the production of complex hydrocarbons like Benzene and other polycyclic aromatic hydrocarbons (PAH). Between the 0.1 to 1 mbar pressure range, these complex hydrocarbons undergo nucleation and sedimentation [108]. Their role in heterogeneous chemistry has been proposed in the context of recent HCN and CO column density observations by ALMA [67]. Electron precipitation governs a system of coupled ion-neutral and neutral reactions affecting the local chemistry of hydrocarbons and nitrogen species. As the microwave opacity of the Jovian ionosphere is dependent on local electron and ion concentrations, we restrict our reaction mechanism to simulate the chemical cycling of ions and electrons in the upper atmosphere.

The primary chemical reactions corresponding to Jupiter's ionosphere consist of photochemical, electron impact processes coupled with ion-neutral reactions. We solve the system of reactions relevant to electron impact process, and ion-neutral reactions for the following species: H_2, H_2^+, H^+, H, e^-, H_3^+, CH_4, CH_3^+, CH_4^+, CH_5^+, He, CH_3, CH_2, He^+, CH_2^+, CH^+, HeH^+, CH, C_2H_6, C_2H_5, C_2H_4, C_2H_3, C_2H_2, C_4H_6, C, C_4H_5, C_3H_6, C_2, C_2H, $H_2(\nu_1)$, $H_2(\nu_2)$, $H_2(\nu_3)$, $H_2(\nu_4)$, $H_2(\nu_5)$, $H_2(\nu_6)$, $H_2(\nu_7)$, $H_2(\nu_8)$, and $C_2H_5^+$. All reaction pathways, and corresponding rate expressions, are provided in Appendix C.

Molecular hydrogen undergoes secondary electron impact ionization through the E_1 and E_2 pathways. H_2^+ reacts with H_2 to produce H_3^+ (reaction C_1). H_3^+ undergoes destruction through two pathways: (i) dissociative recombination with electrons (C_3), and (ii) proton exchange with hydrocarbons below CH_4 homopause (C_9). We mainly focus on the reaction with CH_4 due to its higher abundance, and it leads to the formation of CH_5^+ ions. Similarly, H_2^+ reacts with CH_4 to produce CH_3^+, CH_4^+ and CH_5^+ ions (C_{11}—C_{13}). CH_5^+ reacts with other constituent hydrocarbon species like C_2H_4 and C_2H_6 to produce $C_2H_5^+$ ions (C_{29} and C_{30}). In our model, we restrict ourselves to CH_5^+ and $C_2H_5^+$ ions due to uncertainties in reaction rates associated with longer chain hydrocarbon ions. The CH_5^+ and $C_2H_5^+$ ions recycle back to constituent hydrocarbons through dissociative recombination with electrons (C_{18}—C_{21} and C_{32}—C_{38}). For molecular ions, the dissociative recombination rates are high and thereby, they are expected to be short-lived species. As high-energy electrons penetrate below the CH_4 homopause, their interactions with molecular hydrogen will produce hydrocarbon ions. Figure 4.16 shows a schematic of important ion-neutral reactions within the chemical kinetics reaction network.

Collisions with secondary electrons also cause vibrational excitation processes in molecular hydrogen (V_1). A significant proportion of total energy deposition is partitioned into direct excitation

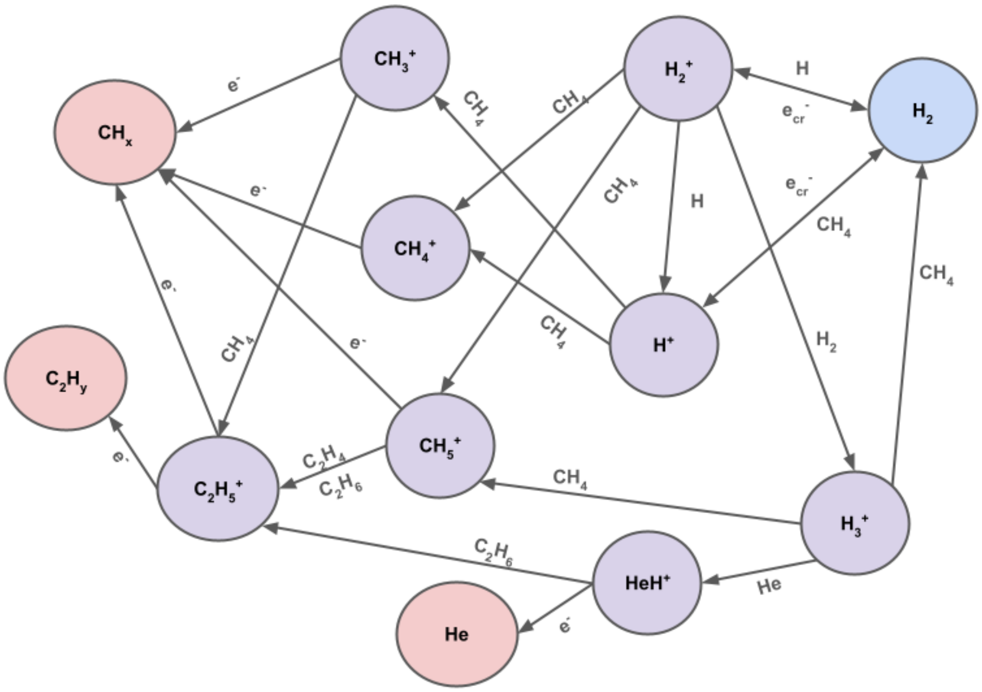

Figure 4.16: A schematic diagram showing the reaction mechanism for forming important hydrogen and hydrocarbon cations in the model Jupiter atmosphere. Electron impact ionization, dissociative recombination, and interaction with major atmospheric constituents like H_2, He, CH_4, C_2H_6 and C_2H_4 drives the cycling of the ions into atmospheric neutrals.

reactions. These excitation processes lead to the production of excited states of H_2 in Jupiter's auroral ionosphere. Interactions between other excited states also cause transitions between them (V_7—V_8). Additionally, collisions with atomic hydrogen (V_5), protons (V_3), and dissociative recombination of H_3^+ (V_4) also produces vibrationally excited states of H_2. We apply the rate formulations based on previous literature on the treatment of molecular hydrogen vibrational excitation [276, 80]. They are largely derived from theoretical models of H_2 vibrational states and laboratory experiments on H_2 excitation [23, 119, 42, 250].

4.4.5 Microwave Opacity Model

Microwave absorption processes at centimeter wavelengths have been shown in the case of the Earth to occur at locations with both low and high values of neutral density [291]. In the case of low neutral density regimes, ionospheric plasma exhibits absorption of high-frequency radio waves [230]. Similar processes have been observed on the Martian night side that exhibit a high electron density due to precipitation of solar energetic particles (SEP) [135]. In Jupiter's ionospheric medium, large amounts of energy are deposited at lower altitudes resulting from the decreased stopping power of high energy electrons in H_2, which produces significant transient ionization to affect the propagation of the interior microwave radiation in the high-density regime, whereas the explanation that [140] had put forward earlier had modeled relatively lower neutral densities of the Jovian ionosphere at higher altitudes normally associated with solar photons and/or low energy (10 keV) precipitating electrons.

The presence of free electrons in a strongly collisional medium is analogous to those observed in Earth's aurora [182], where high electron-ion/neutral collision frequencies of a similar nature to the Jovian atmosphere coupled with high electron density generate the opacity that could explain the auroral cold spot phenomenon [230]. Utilizing the Appleton-Lassen (derived from Appleton-Hartree) equations by [137] and [230], microwave absorption due to electrons in a highly collisional medium can be expressed as:

$$A = \int \alpha(z)\, dl, \tag{4.6}$$

Where A is the attenuation in dB, z represents the altitude above 1 bar atmospheric pressure, l is the microwave absorption path which equals z if the path is vertical, and $\alpha(z)$ is the absorptivity at the altitude z expressed in dB/km, which can be calculated as:

$$\alpha(z) = 4.6 \times 10^{-5} \frac{N_e(z)\nu_e(z)}{\nu_e^2(z) + \omega^2}, \tag{4.7}$$

where $N_e(z)$ is the altitude-dependent electron density per cubic meter. ν_e(z) is the combined electron-ion and electron-neutral collision frequency dependent on altitude, and ω is the microwave's angular frequency. We take into account interactions with H_2 [222], He [25] and CH_4

[259] to estimate total collision frequency.

In our plasma microwave opacity model, we assume that the ionosphere consists of multiple isothermal plasma layers characterized by elevated electron densities owing to electron precipitation. The relation between attenuation and brightness temperature is expressed as:

$$
\begin{aligned}
t_1 &= 10^{-A/10} && (4.8) \\
T_B &= t_1 \times T_b + (1 - t_1) \times T_e && (4.9)
\end{aligned}
$$

Where A is the attenuation in dB, t_1 is the transmissivity within the absorbing layer, T_B is the attenuated auroral brightness temperature emitted from the absorptive layer, T_b is the auroral brightness temperature from the layer below with the global average atmospheric brightness temperature as the T_b below the lowest absorbing layer, T_e is the ionospheric electron temperature.

4.5 Extreme Electron Precipitation

As the Juno spacecraft increased its coverage of in-situ measurements within the Jovian magnetosphere, several transient events with highly energetic electrons and ions and large energy fluxes ($\geq$ 1 W m^{-2}) began to emerge [185, 188, 46]. Electrons with energies 100 keV - 1 MeV have been detected by the JEDI instrument near Jupiter's polar auroras [188, 73]. Spacecraft passes over the northern aurora and polar cap have identified several events associated with a high flux of downward precipitation electrons. Table 4.3 summarizes the peak energy, intensity, and timescale associated with the high-energy electron flux events.

Analytical expressions of the particle energy distribution provide information about their

Table 4.3: High-energy electron flux events reported from JEDI observations

PJ	**Radius (R_j)**	**Time (s)**	**Peak energy**	**Peak flux (1/cm^2 s sr keV)**	**Reference**
1	1.5	1	Broadband event	10^6	[187]
5	1.3	1.5	Broadband event	10^6	[100]
7	1.64	5	300 keV	Between 10^6 - 10^7	[184]
10	2.21	20	500-700 keV	10^6	[184]

deviation from the equilibrium state, and the charged particle acceleration process. Juno JEDI and JADE sensors provide an extensive survey of electron energy distributions over the aurorae, including cases of enhanced electron flux detected over multiple polar passes. Juno has detected a higher proportion of broadband electron distribution relative to the inverted V-type distribution. Kappa electron distribution has been applied to investigate the effects of electron precipitation on auroral UV emissions [33].

$$\begin{aligned} f_k(E,<E>) &= Q_0 \frac{4\kappa(\kappa-1)}{\pi(\kappa-2)^2} \frac{E}{<E>} \frac{<E>^{\kappa-1}}{(\frac{2E}{\kappa-2}+<E>)^{\kappa+1}} && (4.10) \\ <E> &= 2E_0 \frac{\kappa}{\kappa-2} && (4.11) \end{aligned}$$

Where Q_0 is total energy flux, and ¡E¿ is a function of energy maximum E_0. A kappa value equal to 2.5 was inferred from JEDI electron fluxes during the first 20 orbits of Juno [237].

4.5.1 Heating and Ionization Processes

We consider an extreme case of a charged particle precipitation event detected by JEDI during PJ 7 [188]. We further note from Figure 4.1 that there is a cold spot phenomenon observed during PJ 7. During this event, the MWR instrument observed a significant decrease in antenna temperature, and a strong downward flux of precipitating electrons was measured near the same time on 11th

July 2017 at 01:14:38 UTC. JEDI-integrated electron energy intensity is converted into differential intensity for the electron energy bins ranging from 32 KeV to 1 MeV. For electrons $\geq$ 1 MeV, UVS omnidirectional background count rates are converted to extend the electron energy distribution to 10 MeV as per the method described in Zhu et al., (2021)[299]. Electrons at energies greater than 1 MeV are expected to penetrate the stratosphere to much deeper pressure levels and cause a high degree of ionization below the methane homopause.

Two intermediate cases are generated by linearly scaling the JEDI-UVS intensities throughout the energy bins (Fig. 4.17). JEDI electron flux measurements from PJ 1, PJ 5, and PJ 10 show high-energy electron intensities can rise to magnitudes corresponding to PJ 7 and associated down-scaled energy spectra. The PJ 7 electron flux is much higher than kappa distributions for various cases of mean electron energy between 10 - 100 keV (Fig. 4.18). Further, our analysis sheds light on the role of high-energy electrons from JEDI electron range up to 10 MeV.

The total energy deposition due to electron precipitation during the PJ7 event is validated against planetocosmics. Specifically, we use the implementation previously used by [213] to model particle precipitation at Venus, which has been recently adapted for Jupiter. For both the CSDA approach and Planetocosmics, we choose the standard model from [206] for computing the total energy deposition during the PJ7 event. planetocosmics statistically generates a population of electrons from the input electron intensity spectrum. The loss processes and secondary electrons are tracked by interpolating the coarse atmospheric grid into cm scale fine resolution. Running Monte Carlo simulations takes a longer computation time but ensures highly accurate distribution of energy loss processes.

Energy deposition for the JEDI-UVS composite peaks in-between 0.1-1 mbar pressure level corresponding to altitudes between 150, and 250 km above a 1 bar level (Fig. 4.19). Both CSDA and Planetocosmics show agreement at higher energy bins corresponding to the peak in total

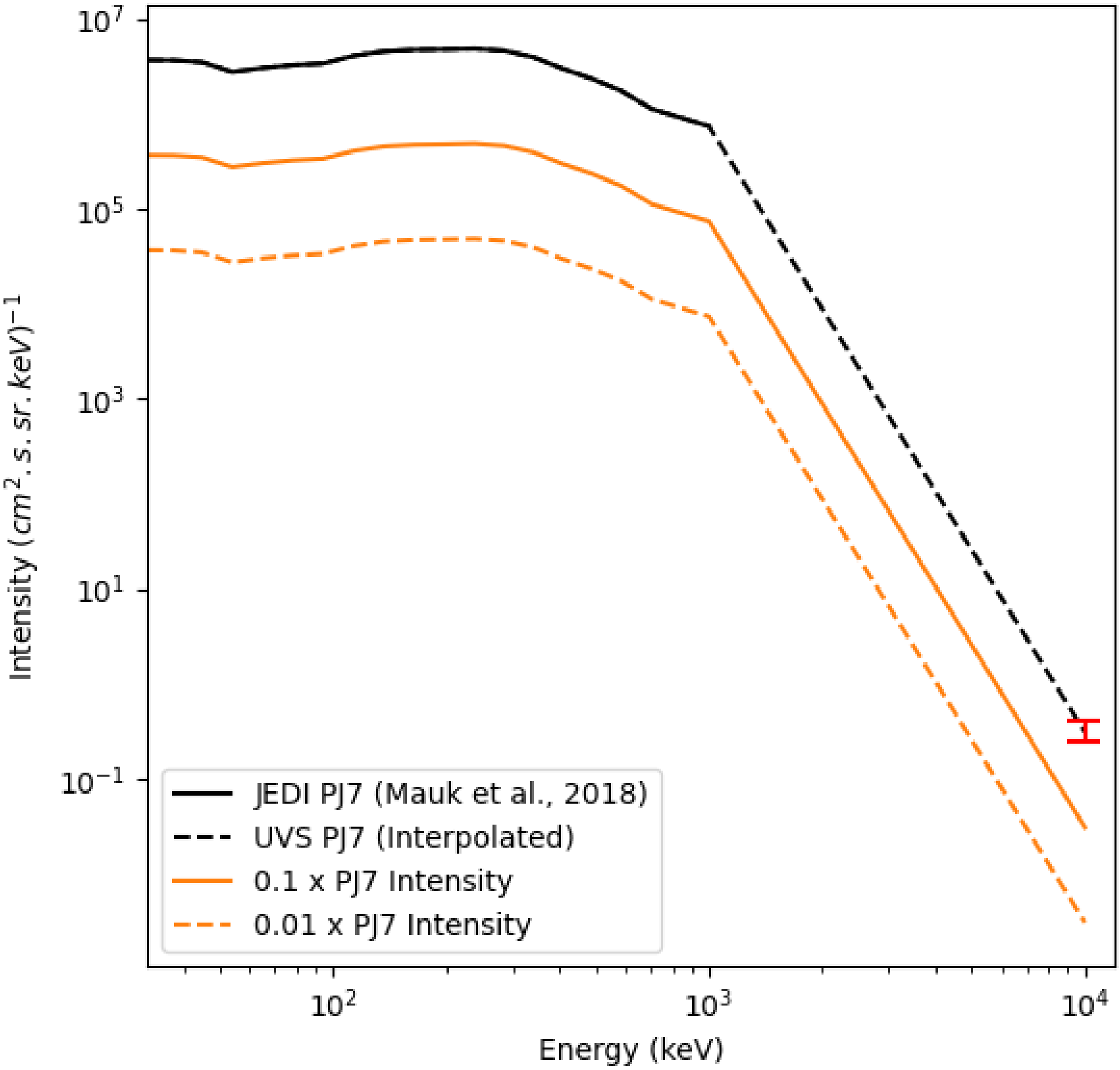

Figure 4.17: Intensity of downward directed electrons as inferred from JEDI and UVS composite data. The red bar indicates the uncertainty bounds for the 10 MeV energy intensity required to match the UVS background rate for integrated flux between 6-10 MeV. The 10 MeV intensity is interpolated with JEDI data to match the UVS background corresponding to 11th July 2017 at 01:14:38 UTC.

energy deposition amounting to 5 x 10^{-5} W/m^3. Compared to previous models, we expect electron density layers at lower altitudes below the CH_4 homopause.

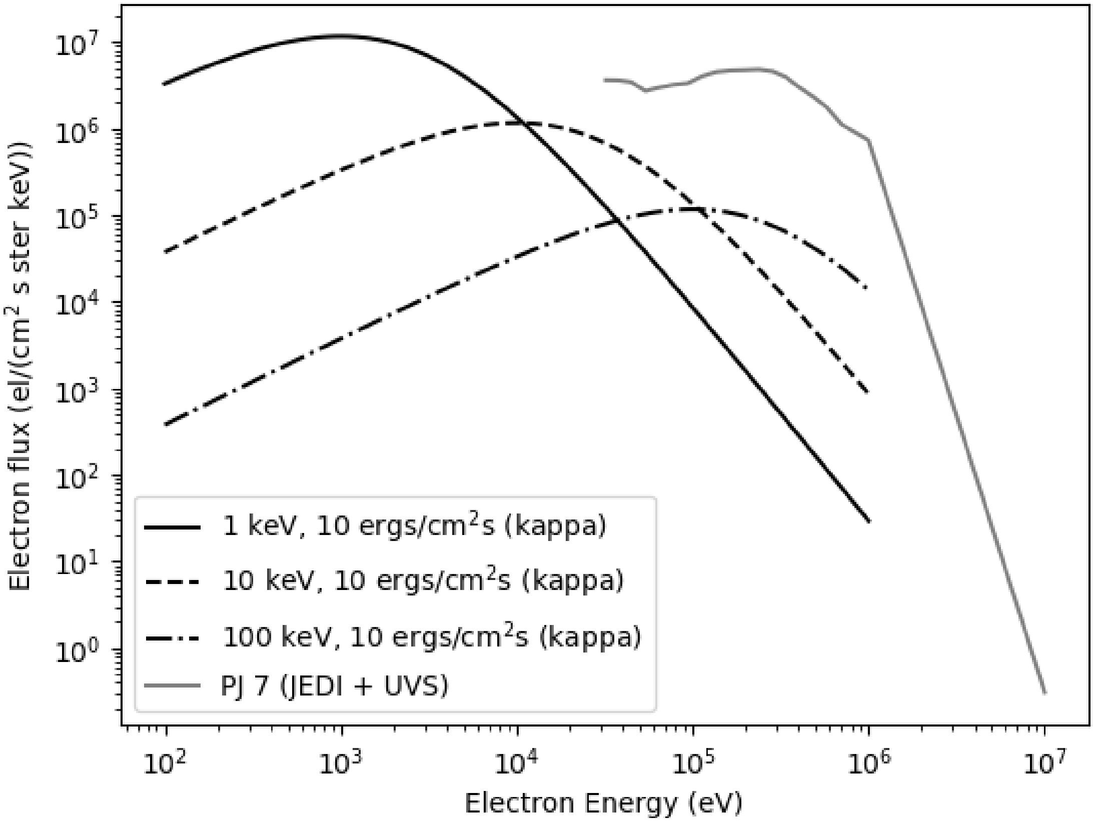

Figure 4.18: Electron flux intensities corresponding to electron energies between 32 keV - 10 MeV. The PJ 7 JEDI and UVS inferred electron fluxes provide a larger contribution compared to cases of kappa distribution [33].

The atmospheric model of Jupiter adopted from [206] has photochemical equilibrium concentrations of hydrogen, helium, and neutral hydrocarbons. Electron precipitation and recombination processes are short-time scale processes relative to Jovian photochemistry. Therefore, we consider reactions relevant to auroral electron precipitation initiated by electron impact ionization and vibrational excitation [80].

As we apply an explicit diffusion scheme, the numerical stability is limited by the Courant–Friedrichs–Lewy (CFL) condition. We limit the timescale to one-tenth of the minimum dynamical timescale governed by eddy diffusion [204]. The system of coupled reactions becomes

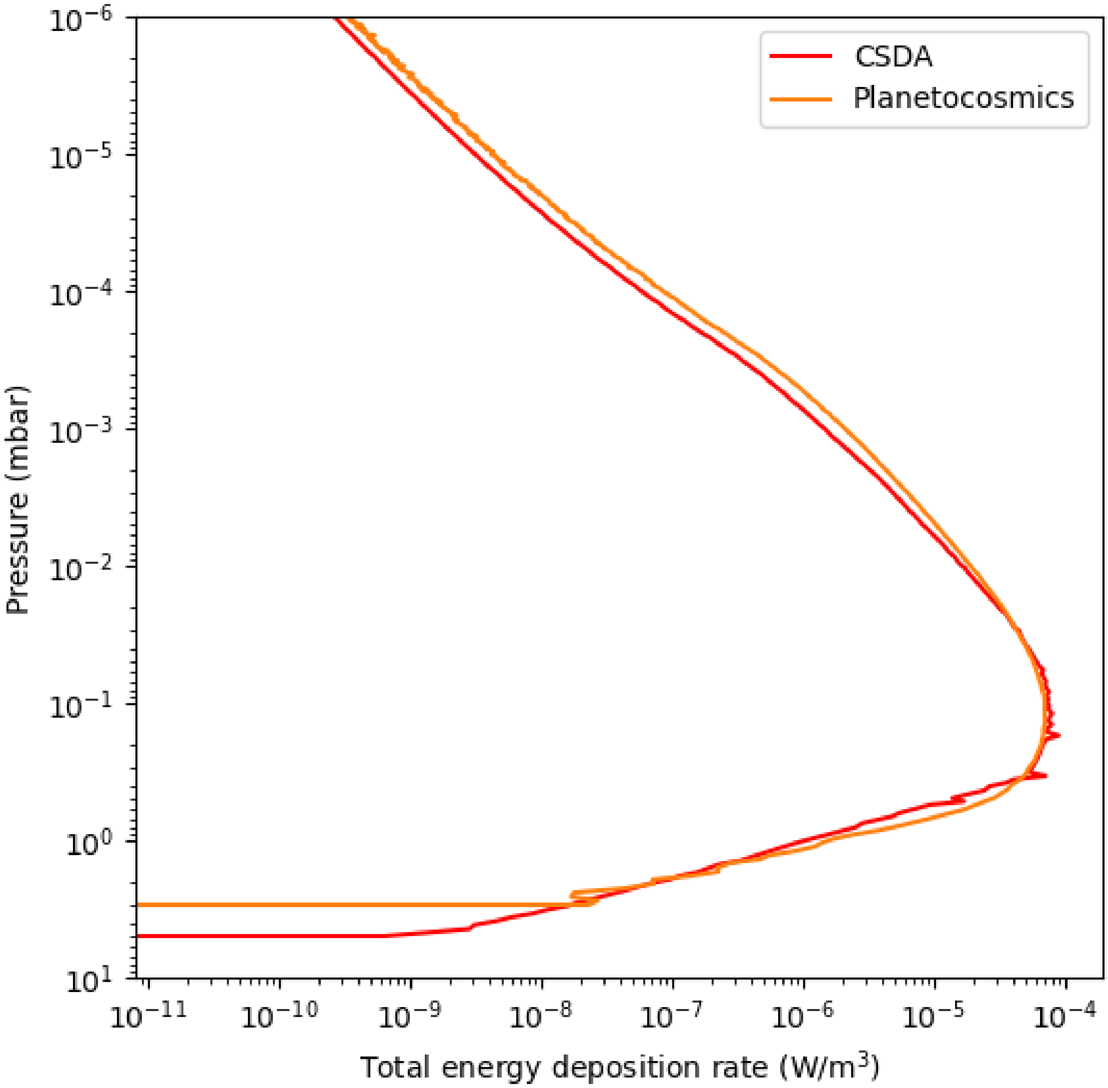

Figure 4.19: Energy deposition rates computed by CSDA and Planetocosmics for high intensity downward precipitating electrons during PJ 7.

a numerically stiff system due to orders of magnitude differences in reaction timescale. Therefore, we start at a small time step dt = 10^{-10} s and gradually increase it to $\sim 10^{-4}$ s for a stable, and accurate numerical solution. The narrow auroral arcs are 100 km long and drift at a speed $\sim$ 1 km/s [1]. Thus, the timescale for electron precipitation can be estimated to be $\sim$ 100 s.

We solve the system of coupled chemical kinetic equations to estimate electron and ion

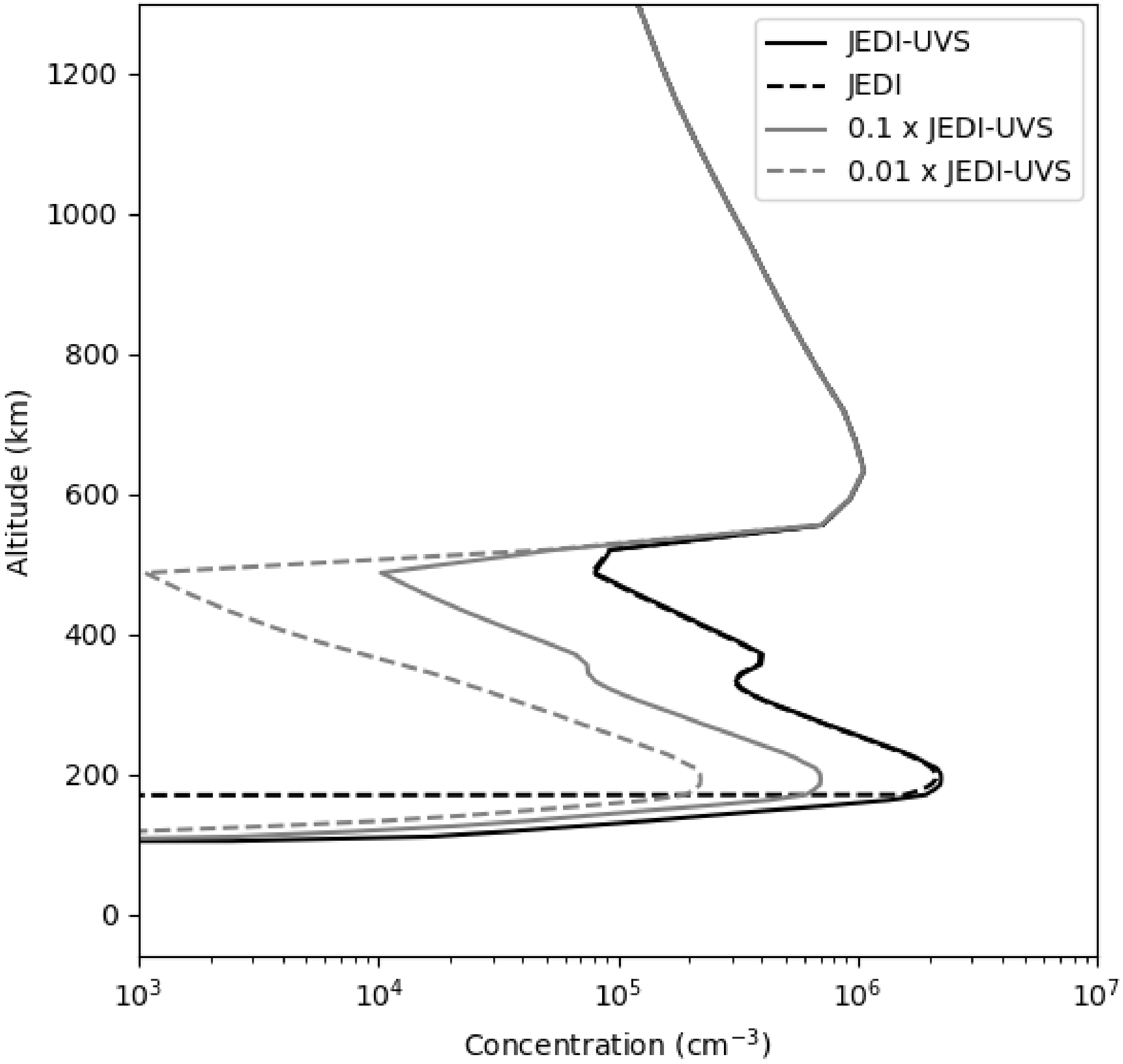

Figure 4.20: Auroral ionospheric electron concentration (cm^{-3}) in Jupiter's upper atmosphere, corresponding to four cases of PJ 7 event for a duration of 100 s. Photoionization peaks at 600 km, and eventually extincts $\sim$ 500 km. As we consider electron sources between 32 keV - 10 MeV energies, the effect of lower energy electrons is not considered. Thus, 500 km appears as a cutoff level for the transition to electron impact ionization regime. The contribution of low-energy electrons is insignificant, as microwave opacity is dependent on atmospheric neutral density.

concentrations corresponding to four cases of electron precipitation. JEDI and JEDI-UVS electron spectra distinguish the effects of electrons from 1-10 MeV. Two intermediate cases are generated

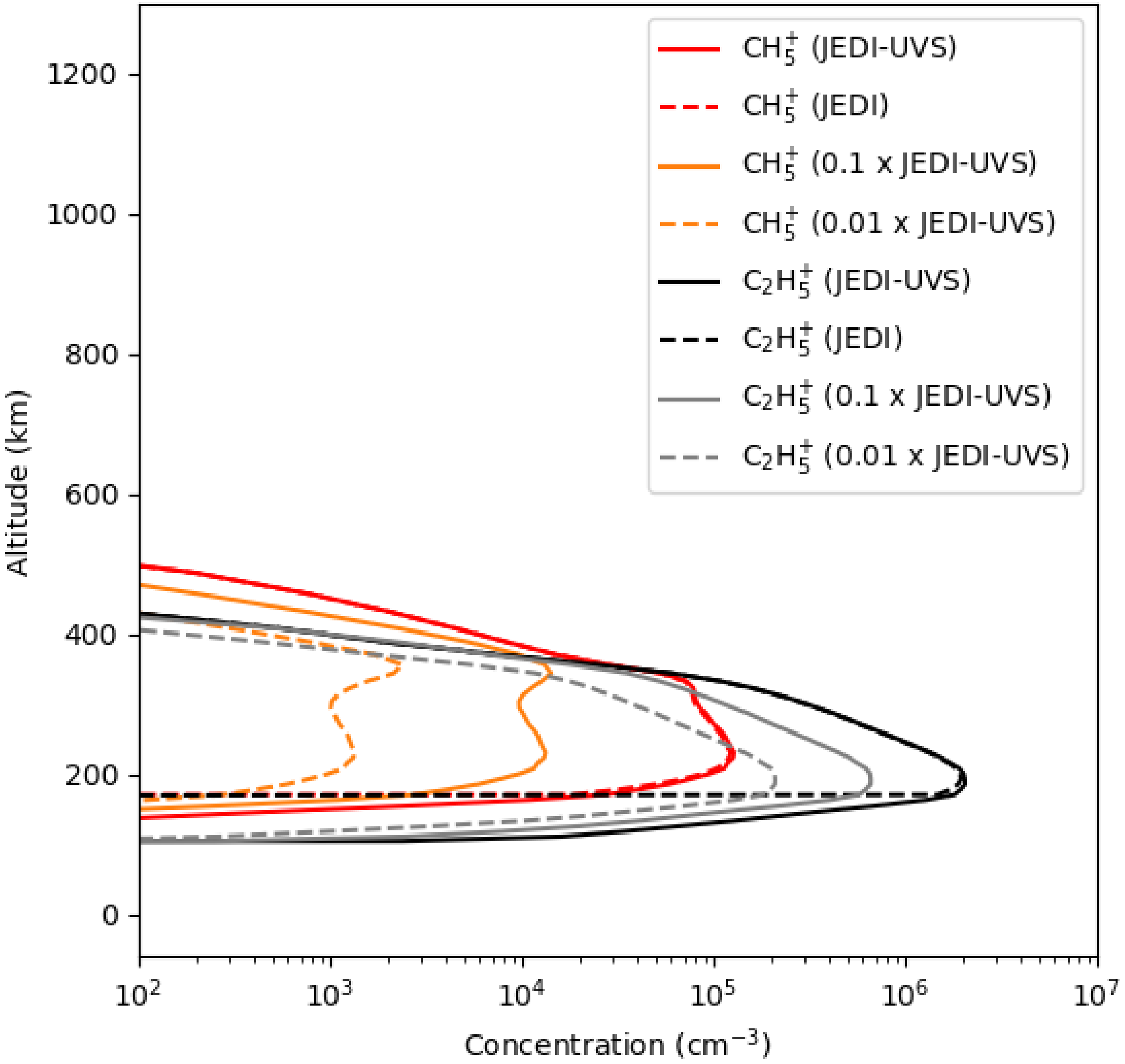

Figure 4.21: Auroral hydrocarbon ion concentrations (CH_5^+ and $C_2H_5^+$) due to high-energy electron precipitation, corresponding to four cases of PJ 7 event for a duration of 100 s.

by linearly scaling the JEDI-UVS intensities throughout the energy bins. Electron densities build up to $\sim 10^5$–10^6 cm^{-3} within 100 s (Fig. 4.20). This rapid increase in ionization also contributes to the formation of higher hydrocarbon ions like CH_5^+, and $C_2H_5^+$ that serve as the dominant positive ions below the CH_4 homopause (Fig. 4.21). The chemical pathways and numerical model leading up to the formation of CH_5^+, $C_2H_5^+$ and heavier hydrocarbon ions by photoionization was

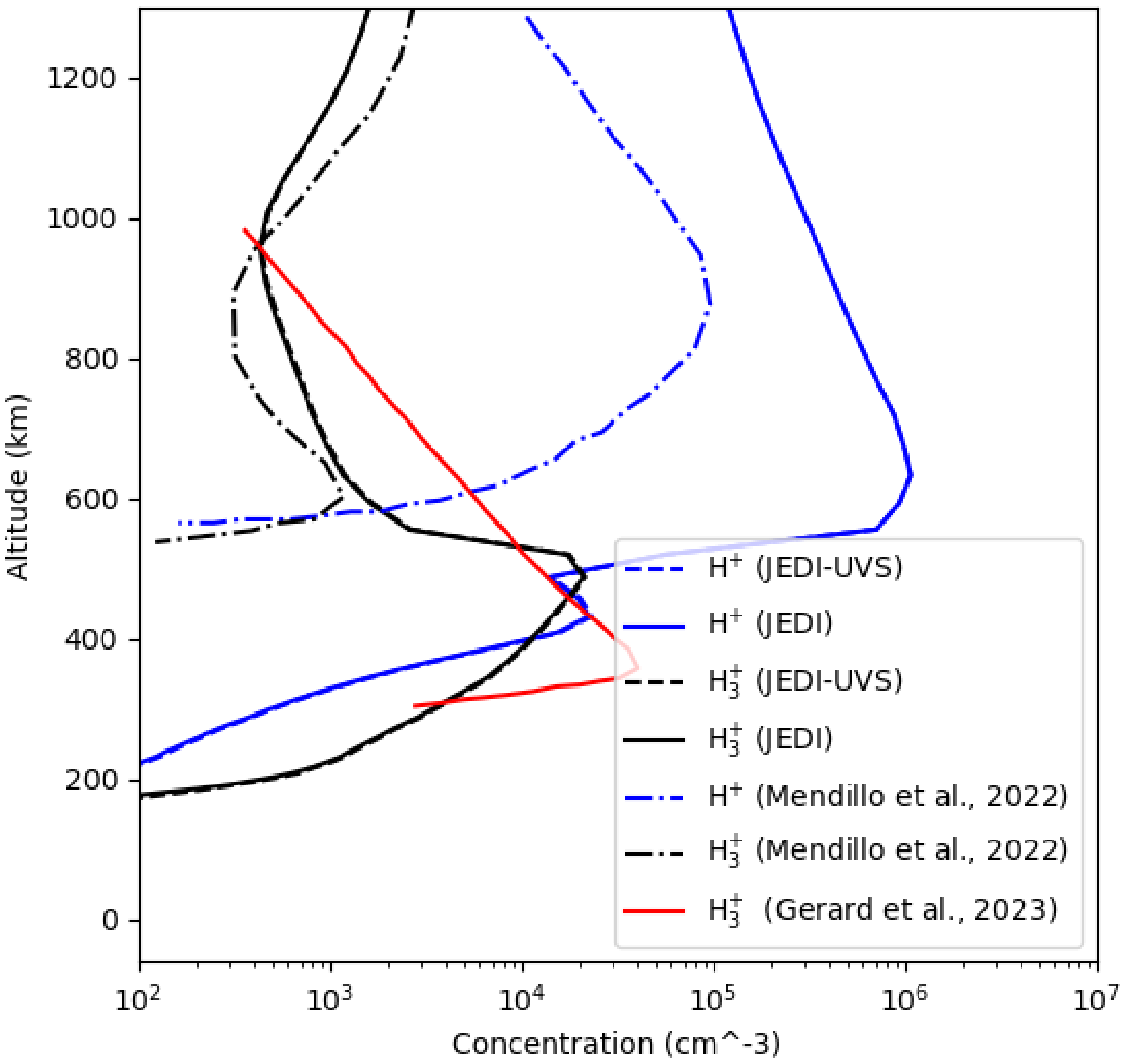

Figure 4.22: Hydrogen ion concentrations (H^+ and H_3^+) in Jupiter's upper atmosphere corresponding to four cases of PJ 7 event for a duration of 100 s. Photochemical simulations of low latitude ionospheric concentration and FUV inferred H_3^+ concentration are provided to draw a comparison with predictions for extreme electron precipitation.

developed previously [17, 21, 159]. This paper shows that energetic particle precipitation similarly results in the production of hydrocarbon ions at auroral latitudes. These ions and more complex hydrocarbon ions become dominant charge carriers below the CH_4 homopause [98, 253].

Penetration depth in the atmosphere is proportional to electron energy, therefore the extended-spectrum from UVS background counts contributes to additional ionization. Energetic electron layers are present much deeper compared to Galileo radio occultation derived ionospheric electron densities (Fig. 4.20) [193]. This effect is also exhibited by hydrogen ions, and we expect H_3^+ to dominate over H^+ below 400 km (Fig. 4.22). H_3^+ concentration is found to exist below 400 km, like the PJ 1 simulations of UV emission [111].

4.5.2 Microwave Opacity and Antenna Temperatures

4.5.3 Sensitivity to electron energy

Previous literature on charged particle precipitation explores the effect of mono-energetic electron beams to quantify the effects of electron energy and intensity of charged particle flux into the atmosphere. An energy flux between 1-10 ergs/cm^2.s is expected to provide strong UV emission in Lyman and Werner bands. These cases explore the sensitivity of atmospheric heating and ionization to electron energy values. We run cases of mono-energetic electron beams to understand the sensitivity of microwave opacity to primary electron energies (Fig. 4.23). Four cases of mono-energetic beams: 100 keV, 300 keV, 500 keV, and 1000 keV with a constant energy flux at 10 ergs/cm^2.s are simulated for secondary electron impact ionization for 100 s. Microwave absorptivity for electron density profiles is calculated based on the Appleton-Lassen theory described before. The microwave absorptivity shows a monotonic increase with electron beam energy due to an increase in penetration depth and resulting higher electron neutral collision rate. The absorptivity profile at 1 MeV is 100 times larger than the 100 keV mono-energetic beam (Fig. 4.24-4.27). The local opacity peak above 500 km lies in the photochemical regime, orders of magnitude smaller than microwave opacity in the electron impact ionization regime. Therefore, the ionospheric microwave opacity is sensitive to high-energy electrons ($\geq$ 500 keV).

The column-integrated microwave attenuation and auroral brightness temperature for the four

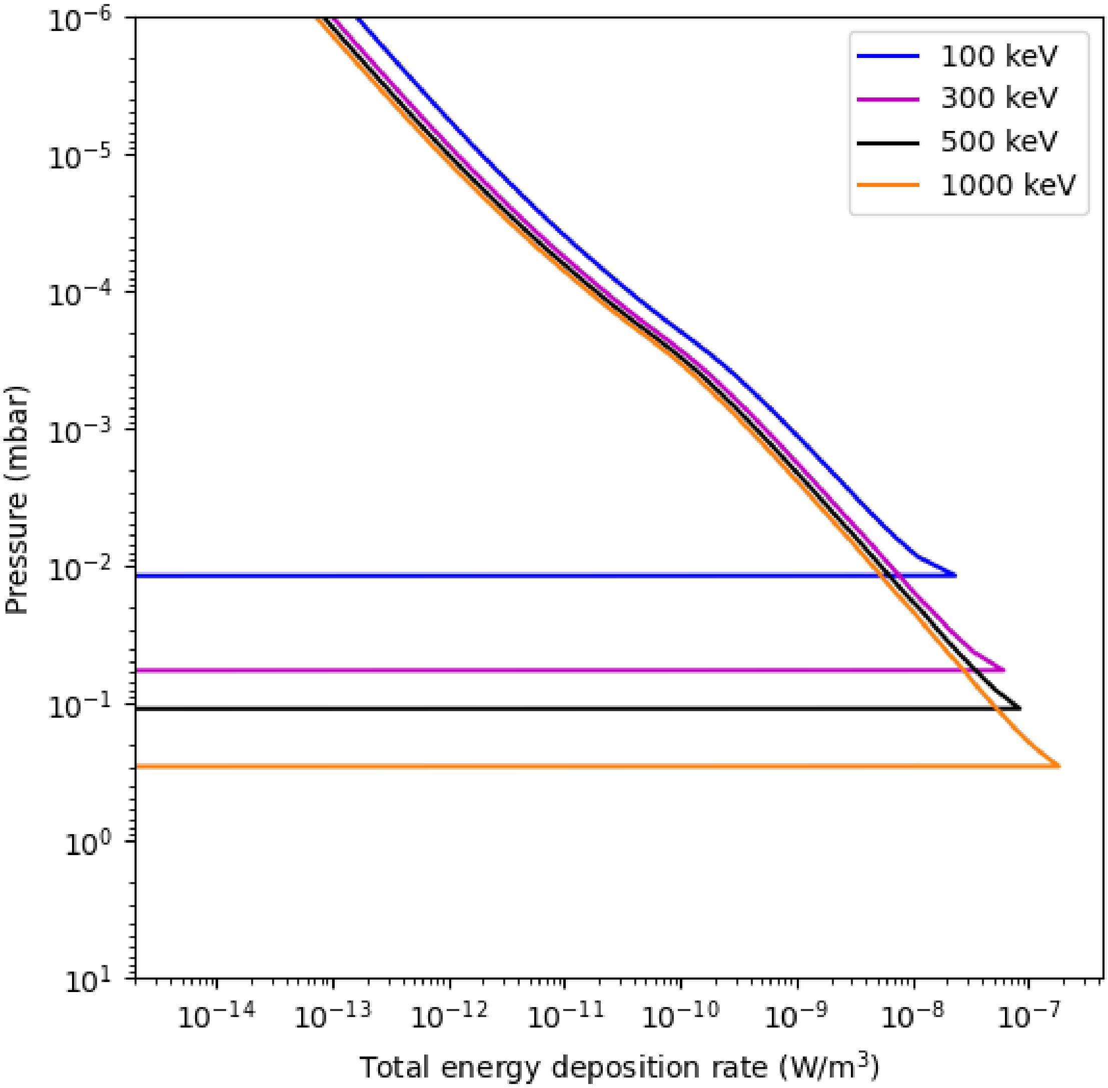

Figure 4.23: Energy deposition rates computed by CSDA for various mono-energetic electron beams

cases are summarized in Table 4.4. These cases represent the nadir view of Jovian electron precipitation. The monoenergetic beam can result in 0.6 GHz T$_A$ values 733.18 to 835.66 K. It matches well within the expect range of MWR observations during the first 54 Juno orbits. Figure 4.28 shows the expected microwave auroral temperature for the first four MWR channels (0.6 - 5.2 GHz) including a case of the photochemically generated ionosphere. Sensitivity to electron ener-

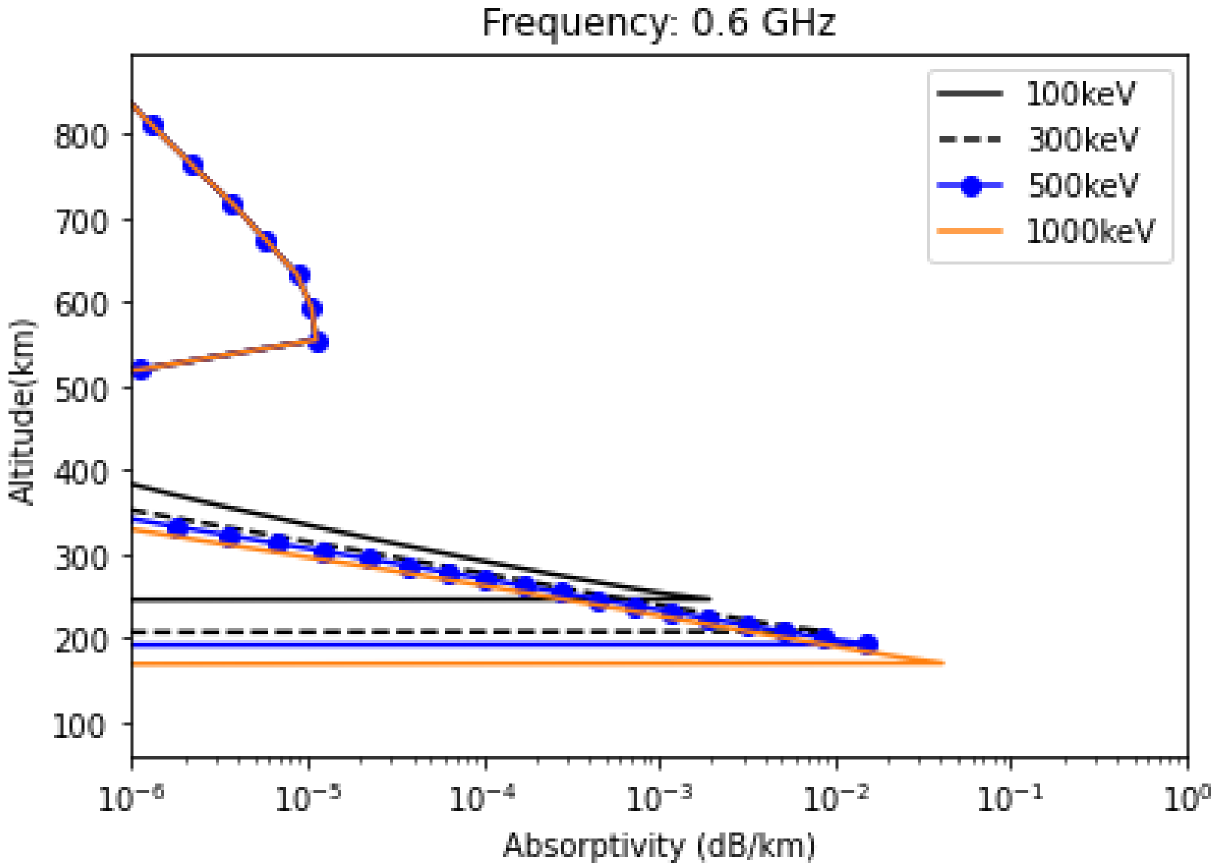

Figure 4.24: Microwave absorptivity (dB/km) for photochemically generated ionosphere, and four cases of mono-energetic electron beam at the four lowest frequency MWR channels at 0.6 GHz.

gies decreases with the frequency of microwave radiation. At 0.6 GHz frequency, electron energies greater than 100 keV amount anywhere between 10 to 100 K reduction in T_A. For the other three frequencies, there is no significant contrast between the photochemical and electric precipitation T_A.

4.5.3.1 Sensitivity to electron flux intensity

The interaction of free electrons with neutrals acts as a strongly collisional medium opaque to atmospheric microwave thermal emission from deeper levels. The brightness temperature observed by the Juno MWR instrument over these cold spots should be attributed to local electron temperature, and microwave absorption in the medium. Ionospheric electrons contribute to a

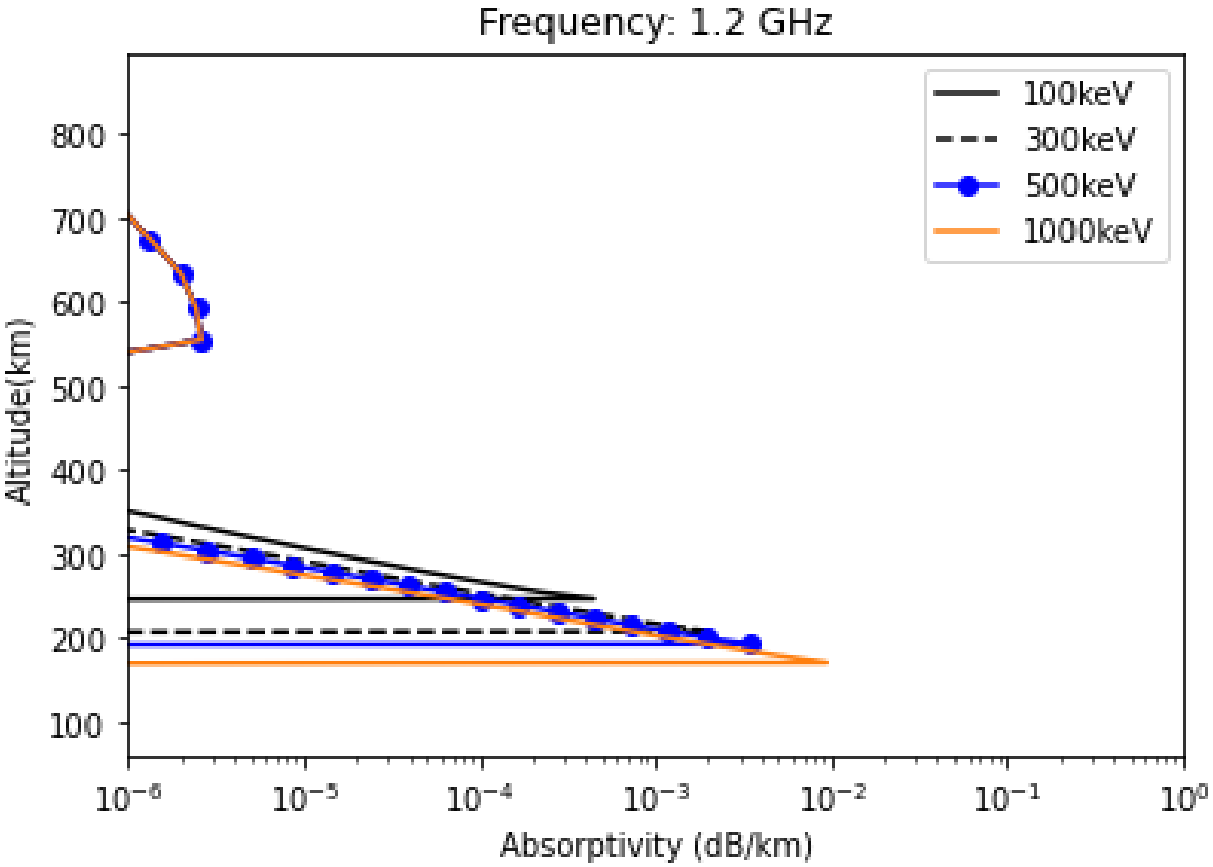

Figure 4.25: Microwave absorptivity (dB/km) for photochemically generated ionosphere, and four cases of mono-energetic electron beam at the four lowest frequency MWR channels at 1.25 GHz

wide range of microwave absorptivities for MWR (0.6 – 5.2 GHz). The intensity and energy of high-energy electrons affect the amount of microwave attenuation. This can be seen in the lower attenuation from cases where JEDI and UVS electron intensity is scaled by 0.1 and 0.01 to simulate intermediate particle precipitation events (Fig. 4.29-4.32).

Due to their greater sensitivity to electron precipitation, the substantially higher attenuation in lower frequency channels (0.6 GHz and 1.2 GHz) results in much lower brightness temperatures. At higher frequencies, the gap between electron temperature and physical temperature of the deep atmosphere decreases owing to absorption by NH_3, and H_2O vapors at shallow levels [151]. In addition, the magnitude of plasma is also expected to decrease with frequency, as shown in

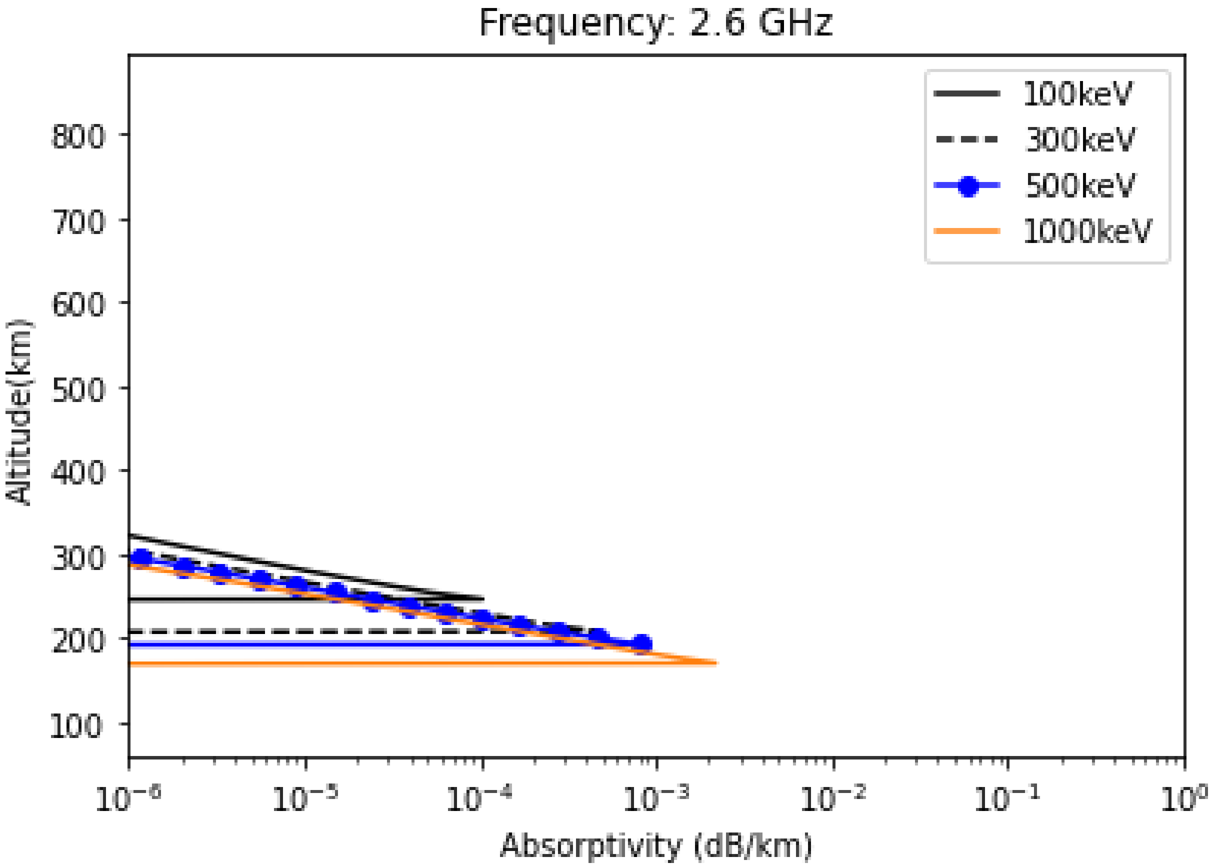

Figure 4.26: Microwave absorptivity (dB/km) for photochemically generated ionosphere, and four cases of mono-energetic electron beam at the four lowest frequency MWR channels at 2.6 GHz

Fig. 4.32-4.35. Thus, low-frequency channels i.e., 0.6 GHz, and 1.2 GHz are more sensitive to an electron precipitation-driven cold spot. For example, the attenuated brightness temperature (168.51 K) for JEDI and UVS condition in the 0.6 GHz channel is lower than the cold spot brightness temperature deconvolved from antenna temperature data from PJ7 [140]. This discrepancy could be potentially explained by the electron precipitation events being temporary and spatially limited to a size smaller than the MWR's 0.6 and 1.2 GHz channel footprint projection during the main phase orbits, resulting in the Juno MWR antenna receiving both the partially attenuated and unattenuated brightness temperature data within the cold spots.

Electron impact processes can lead to near-complete or complete absorption of thermal

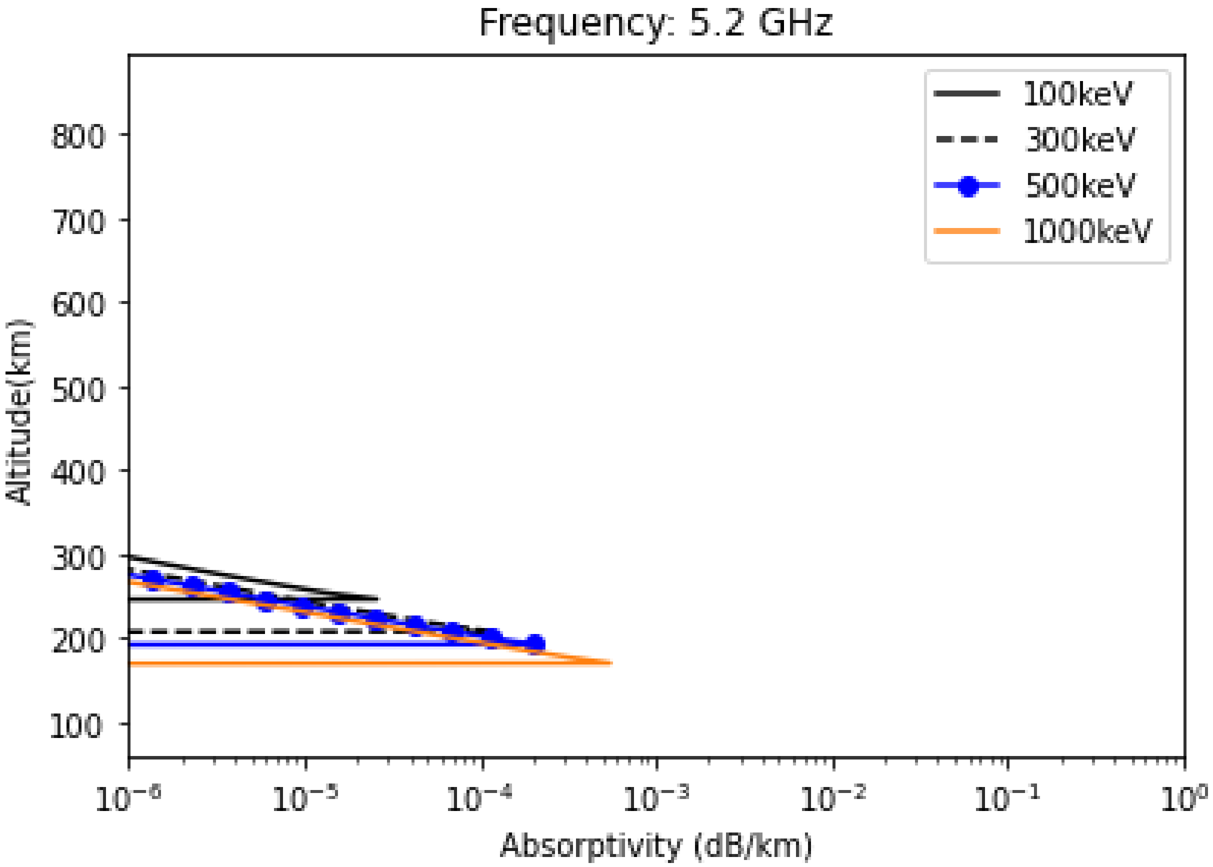

Figure 4.27: Microwave absorptivity (dB/km) for photochemically generated ionosphere, and four cases of mono-energetic electron beam at the four lowest frequency MWR channels at 5.2 GHz

radiation in the atmospheric region within the precipitating electron beam. A summary of total microwave attenuation caused by the four cases of electron precipitation events is provided in Table 4.3. Extreme electron precipitation events can lead to significant variations in 0.6 - 1.2 GHz T_A (Fig. 4.33). Thus, the first two MWR channels can distinguish between the thermal emission emanating from the aurora and the deep atmosphere.

4.5.4 MWR antenna coverage of auroral features

The effective antenna temperature can be expressed as a sum of contributions from the ionosphere and deep thermal emission averaged within the footprint of a given microwave channel. The

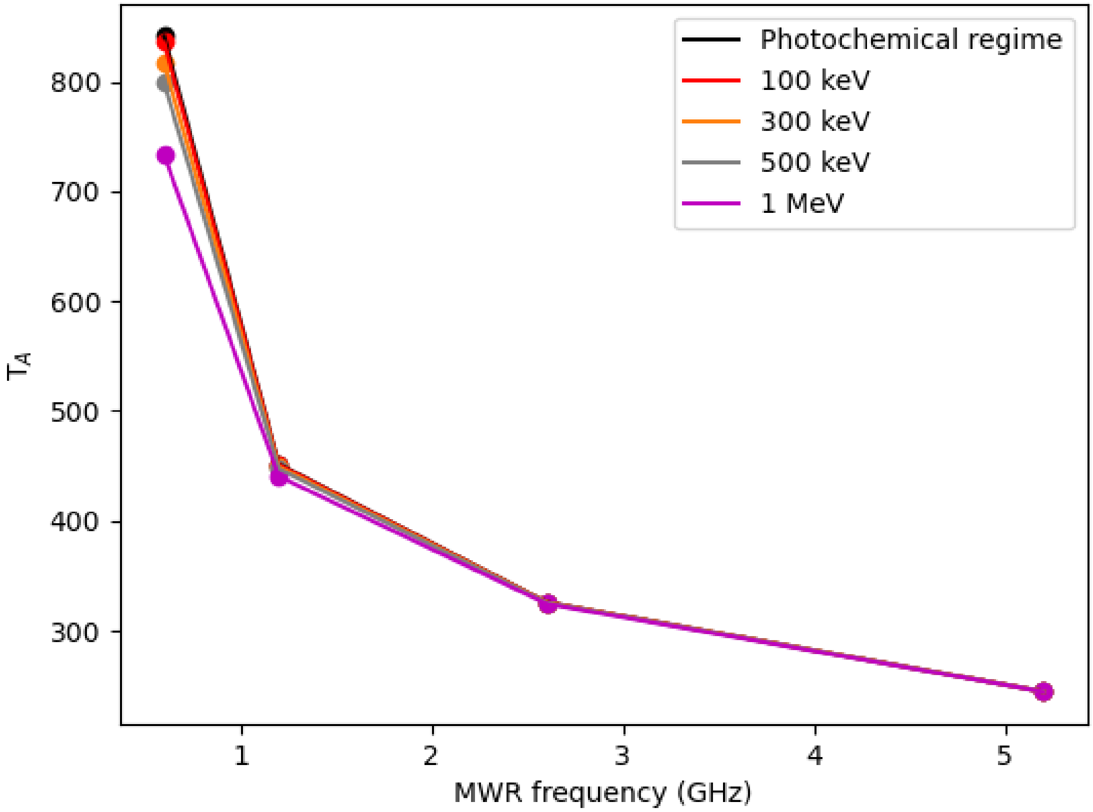

Figure 4.28: Auroral brightness temperature corresponding to first four MWR channels (0.6 - 5.2 GHz). Each curve represents the electron precipitation of a monoenergetic electron beam. Temperature decreases with electron energy, and the temperature variation relative to the photochemical regime converges at higher frequencies. Due to relatively less contrast in auroral temperatures, only 0.6 GHz and 1.2 GHz channels are largely sensitive to auroral cold spots.

variation in spatial scales associated with high-energy electron beams directly affects the contributions of the auroral ionosphere. Here we introduce the concept of fill factor, i.e., the ratio of projected electron beam area to that of MWR footprint. The fill factor determines the contribution of auroral electrons to the bore sight temperature. Based on the estimated antenna temperature (Table 4.3) from different cases of electron precipitation, we determine the possible fill factors required to explain the antenna temperatures for the first two frequency channels (0.6 and 1.2 GHz).

Table 4.4: Microwave Attenuation A and Attenuated Brightness Temperature T_B at nadir view of ionospheric medium subject to different cases of monoenergetic electron beam

Condition	100 keV beam	300 keV beam	500 keV beam	1000 keV beam
$A_{0.6GHz}$	0.037	0.16	0.284	0.76
$T_{B,0.6GHz}$	835.66	816.848	798.67	733.18
$A_{1.25GHz}$	0.0085	0.037	0.065	0.17
$T_{B,1.25GHz}$	451.11	449.24	447.39	440.38
$A_{2.6GHz}$	0.002	0.009	0.015	0.040
$T_{B,2.6GHz}$	325.84	325.59	325.36	324.43
$A_{5.2GHz}$	0.00049	0.0021	0.0038	0.010
$T_{B,5.2GHz}$	244.59	244.56	244.53	244.42

Table 4.5: Microwave Attenuation A and Attenuated Brightness Temperature T_B at nadir view of the ionospheric medium subject to electron precipitation at different intensities

Condition	JEDI and UVS	JEDI	JEDI and UVS electron intensity scaled by 0.1	JEDI and UVS scaled by 0.01	Photoelectrons
$A_{0.6GHz}$	25.66 dB	13.84 dB	7.90 dB	2.38 dB	0.0021 dB
$T_{B,0.6GHz}$	168.23 K	194.27 K	275.39 K	556.50 K	841.06 K
$A_{1.25GHz}$	5.93 dB	3.19 dB	1.82 dB	0.55 dB	0.00048 dB
$T_{B,1.25GHz}$	238.63 K	302.96 K	353.50 K	417.70 K	451.63 K
$A_{2.6GHz}$	1.37 dB	0.74 dB	0.42 dB	0.13 dB	0.00011 dB
$T_{B,2.6GHz}$	282.45 K	300.90 K	311.06 K	321.30 K	325.91 K
$A_{5.2GHz}$	0.34 dB	0.18 dB	0.11 dB	0.032 dB	2.79 x 10^{-5} dB
$T_{B,5.2GHz}$	238.59 K	241.32 K	242.70 K	244.03 K	244.60 K

$$T_{eff} = f \times T_B + (1 - f) \times T_{th}, \tag{4.12}$$

Here, T_{eff} is effective footprint averaged temperature, T_{th} is brightness temperature corresponding to atmospheric thermal emission and f is the fill factor. The analysis of the first two frequency channels reveals electron beams to cover $\sim$ 7 to 80 percent of the MWR footprint area (Fig. 4.34). We assume MWR channel footprint size $\sim$ 0.1 R_j for our calculations, consistent with MWR footprint geometry.

The electron beam scale from the JEDI in-situ field of view (FOV) is estimated from the orbital

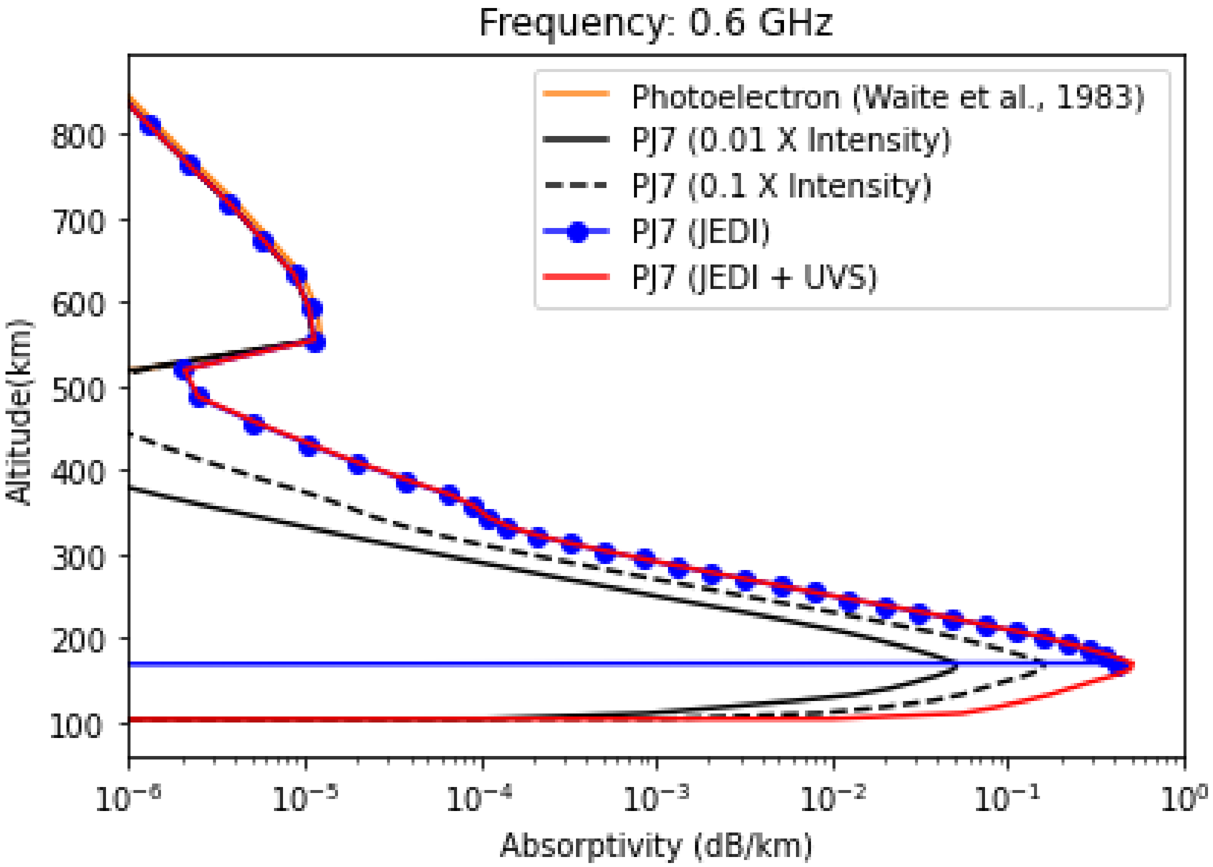

Figure 4.29: Microwave absorptivity (dB/km) for photochemically generated ionosphere, and four cases of PJ 7 precipitation event at 0.6 GHz. The photochemically-generated ionosphere doesn't contribute significant attenuation to atmospheric thermal radiation. However, energetic precipitation events such as the PJ7 event modeled herein can cause intermediate to near-complete absorption of microwave radiation with a decrease in the magnitude of attenuation with increasing microwave frequency. At altitudes below 100 km (4 mbar) and above 1200 km (0.1 nbar), microwave absorption from electrons becomes insignificant due to insufficient electron densities.

speed of Juno from the radial position of the spacecraft. Spacecraft passes over the northern aurora and polar cap have identified several events associated with a high flux of downward precipitation electrons. Orbital speed and event time scales determine the length scale of these downward-directed energetic electron flux events from JEDI FOV. It is compared against the MWR antenna footprint size to estimate fill factors. JEDI FOV-based fill factors are found to be much smaller than predictions from different cases of electron precipitation. This effect can be attributed to limited global scale coverage of electron precipitation over the North Pole, and rapid changes associated

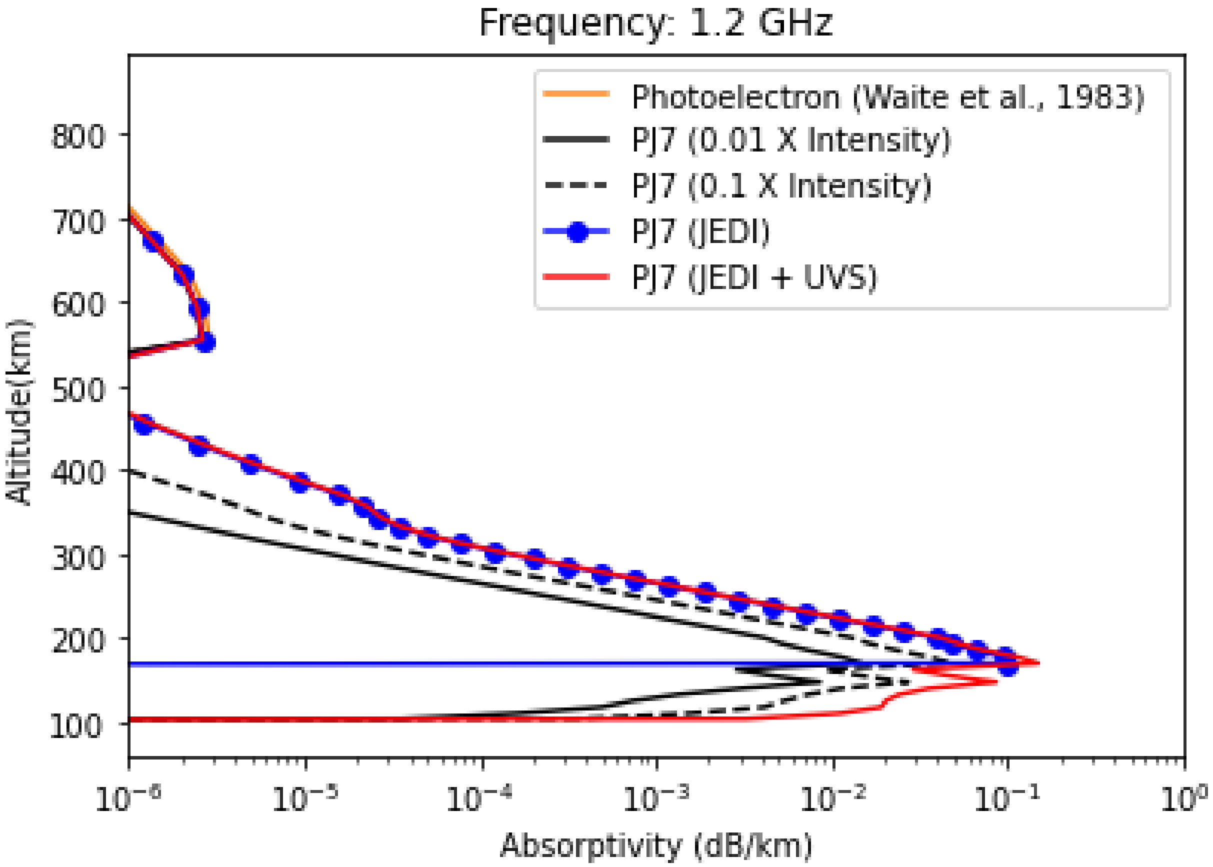

Figure 4.30: Microwave absorptivity (dB/km) for photochemically generated ionosphere, and four cases of PJ 7 precipitation event at 1.25 GHz. The photochemically-generated ionosphere doesn't contribute significant attenuation to atmospheric thermal radiation. However, energetic precipitation events such as the PJ7 event modeled herein can cause intermediate to near-complete absorption of microwave radiation with a decrease in the magnitude of attenuation with increasing microwave frequency. At altitudes below 100 km (4 mbar) and above 1200 km (0.1 nbar), microwave absorption from electrons becomes insignificant due to insufficient electron densities.

with electron beam intensities.

4.5.5 UV Emission Characteristics

During most of the polar passes, MWR antenna footprint size is large relative to satellite auroral footprints, and other UV emission features within the MAE. Boresight antenna temperatures represent an average of thermal radiation from deep atmospheres and regions with localized electron precipitation. On the other hand, UVS image data cubes have a fine spatial resolution

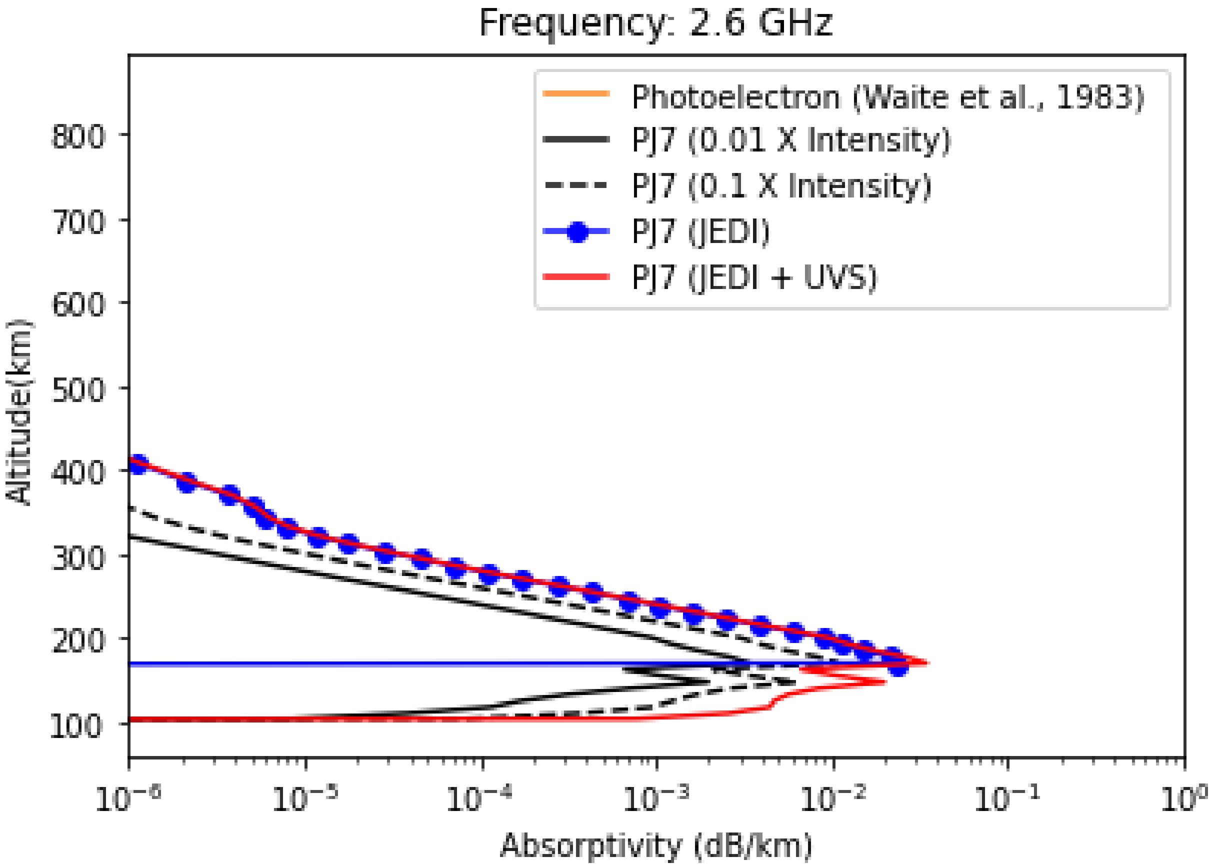

Figure 4.31: Microwave absorptivity (dB/km) for photochemically generated ionosphere, and four cases of PJ 7 precipitation event at 2.6 GHz. The photochemically-generated ionosphere doesn't contribute significant attenuation to atmospheric thermal radiation. However, energetic precipitation events such as the PJ 7 event modeled herein can cause intermediate to near-complete absorption of microwave radiation with a decrease in the magnitude of attenuation with increasing microwave frequency. At altitudes below 100 km (4 mbar) and above 1200 km (0.1 nbar), microwave absorption from electrons becomes insignificant due to insufficient electron densities.

to map color ratio and emissions over the MAE. Mapping the magnetic field trajectory of in-situ particle flux provides a direct comparison between JEDI and UVS observations. However, a direct comparison between MWR and UVS is not possible due to two reasons. Firstly, the 0.6 GHz measurements are difficult to deconvolve due to uncertainties in the spatial extent and intensity of auroral precipitation. Secondly, the UVS and MWR measurements have different observation angles that introduce additional uncertainties in a one-to-one comparison.

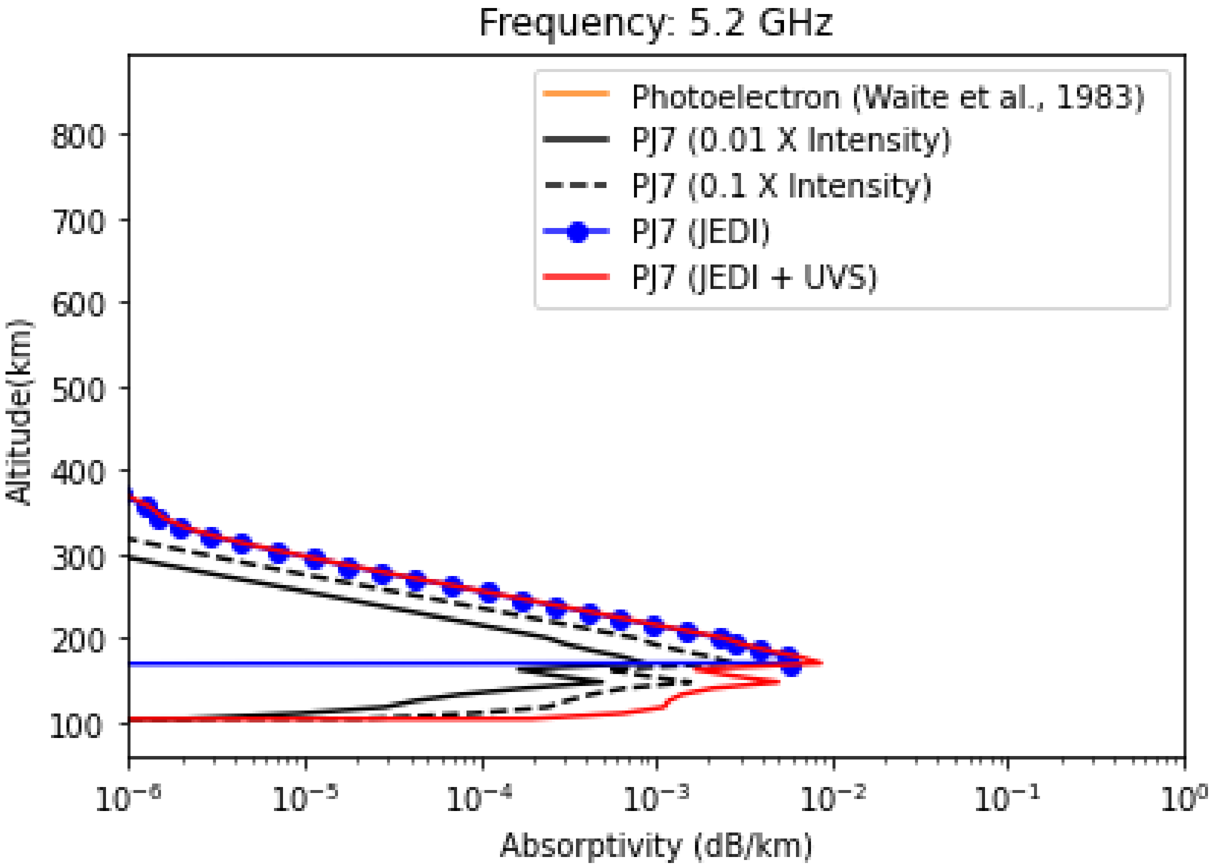

Figure 4.32: Microwave absorptivity (dB/km) for photochemically generated ionosphere, and four cases of PJ 7 precipitation event at 5.2 GHz. The photochemically-generated ionosphere doesn't contribute significant attenuation to atmospheric thermal radiation. However, energetic precipitation events such as the PJ7 event modeled herein can cause intermediate to near-complete absorption of microwave radiation with a decrease in the magnitude of attenuation with increasing microwave frequency. At altitudes below 100 km (4 mbar) and above 1200 km (0.1 nbar), microwave absorption from electrons becomes insignificant due to insufficient electron densities.

The second limitation can be overcome by searching for an MWR measurement with a small footprint size. We found two cases during PJ 50 and PJ 54 where MWR measures cold spots over the polar cap with footprints smaller relative to the auroral oval (Fig. 4.37, 4.41). The 0.6 GHz channel measurements at near nadir angles can be mapped over the Northern Aurora (Fig. 4.38, 4.42). UVS-derived color ratio maps (private communication with Dr. Thomas Greathouse) integrated over multiple Juno spins provide a comprehensive picture of high-energy particle precipitation (Fig. 4.35, 4.36, 4.39, 4.40). Based on the UV color ratio calculations, we observe

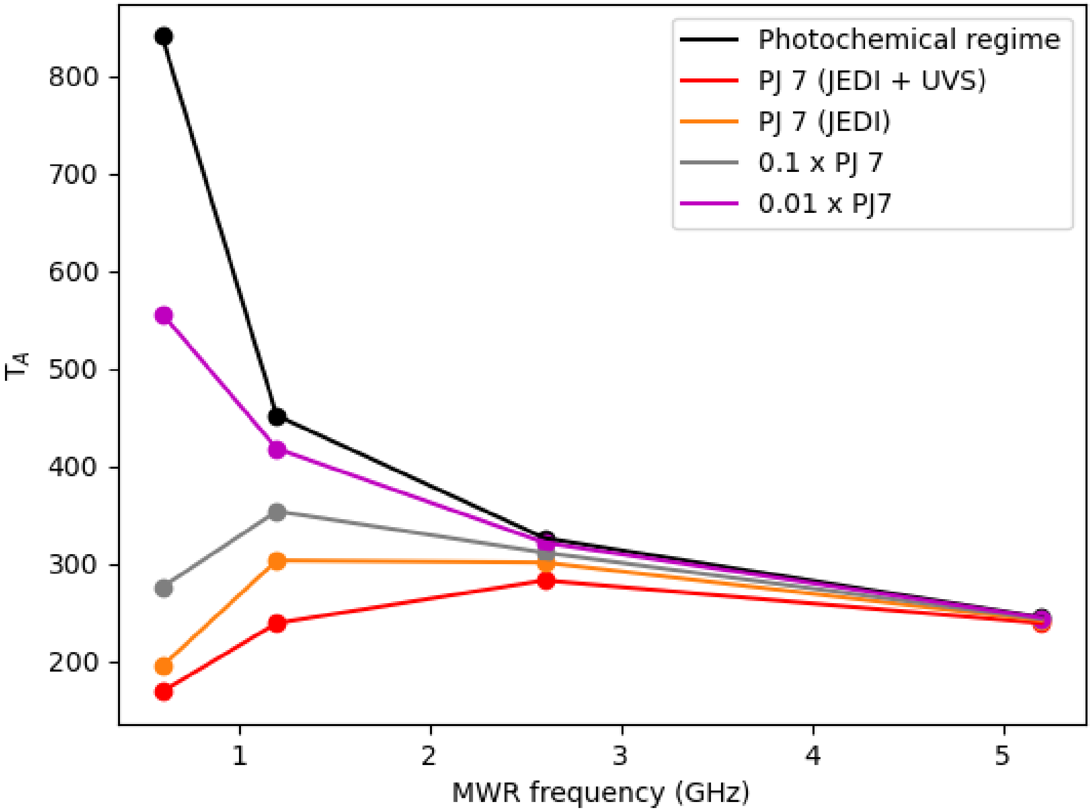

Figure 4.33: Projection of Juno MWR brightness temperatures corresponding to photochemical and electron impact ionization regime. PJ 7 and associated electron precipitation cases are compared with a purely photochemically generated ionosphere. The case of PJ 7 exhibits a strong reduction in atmospheric thermal emission, and the variation in temperature decreases with an increase in microwave frequency. A strong temperature contrast is observed in 0.6 GHz and 1.2 GHz relative to the photoelectron cases, posing a strong case for microwave opacity to probe atmospheric ionization.

that electron energy is proportional to the color ratio. Thus, a direct comparison between cold spot and high color ratio zones provides co-located observations of high-energy electron precipitation over the Northern Aurora.

The UVS data is filtered for Juno spins and timestamps corresponding to MWR 0.6 GHz cold spot measurements. Total UV emission and the corresponding UV color ratio are averaged for 15 consecutive spins to provide a map of auroral UV emission activity. In both cases of PJ 50 and PJ 54, we observe that regions of low antenna temperature can be spatially correlated with a high color ratio ranging between 15 – 20. Thus, microwave radiometry can be applied as a tool to understand atmospheric ionization, providing a complementary perspective on UV color ratio and electron precipitation.

About 18.29 percent of total energy deposition undergoes excitation of atomic and molecular hydrogen at Lyman and Werner bands [276]. As electrons higher than 100-200 keV penetrate below the methane homopause, the auroral UV emission undergoes atmospheric absorption due to H_2, He, CH_4 and C_2H_2. Estimating UV opacities for photoabsorption between 50 and 250 nm reveals sharp gradients in opacity. In case of PJ7 event, UV emission originating at 0.1 mbar level undergo complete absorption between 70-125 nm as $\tau \sim 10^3$–10^6 (Fig. 4.20). At 1 μbar pressure, less than 1 percent of total energy deposition may result in UV emissions as $\tau \sim$ 0.01–1 between 110–125 nm wavelengths. Therefore, we find that UV auroral emissions may underestimate the population of high-energy electrons during extreme precipitation events.

High-energy electron beams are quite ubiquitous, as inferred from the UVS color ratio [33] and statistical analysis of JEDI electron beams [237]. However, the penetration of secondary electrons to greater depths causes a large proportion of UV emissions to be absorbed by the atmospheric column above.

The partitioning of total energy deposition into UV Lyman and Werner band emission rates provides an estimate of the UV emission spectrum and corresponding CR values. We adopt laboratory measurements of H_2 UV emission spectrum (U(ν)) between 120 – 160 nm [**?**]. The relative intensities of the emission spectrum are normalized and the normalized intensities are used for generating UV emission spectra at each height grid through the atmospheric column. We simulate the UV radiative transfer throughout the atmospheric column to project top-of-atmosphere (TOA) UV emission in kR units. The volumetric production rate (J_{prod}) at each point is the geometric mean of the surrounding top and bottom grid points. It is integrated over each grid point integrated over the atmospheric column to provide TOA UV emission (I_ν).

$$I_\nu = \int_{base}^{TOA} J_{prod}(z,\nu) e^{-\tau(z,\nu)} dz \tag{4.13}$$

$$J_{prod}(z,\nu) = U(\nu)\phi_{UV} E(z) \tag{4.14}$$

Here, $\tau(z,\nu)$ is the total monochromatic opacity from each grid point to TOA. It is represented as the sum of H_2, He, CH_4 and C_2H_2 opacities, each consisting of UV absorption cross-section adopted from the Leiden photochemical database (Fig. 4.43), in its tabulated format provided in VULCAN - open-source chemical kinetics package [268, 138]. For H_2 and He, we add the Rayleigh scattering cross-section to the opacity. ϕ_{UV} is the percent of total energy (E) that goes into Lyman and Wener band emissions.

The κ distribution of electron energy shows a linear relationship between UV color ratio and characteristic energy (Fig. 4.44). Our crude UV emission model matches the trend in UV color ratio estimated by Benmahi et al., (2024) [33]. The color ratio values are systematically less compared to the literature values, however they show a match at high energies. The PJ 7 case of high-energy electron precipitation amounts to a color ratio between 17 to 20, matching with the upper bound of UVS color ratio observations over the auroral regions. The total UV emission for a 10 keV monoenergetic beam is found to match with literature values [276]. It is observed that the model predicts UV emission during the PJ 7 event to be a few times the maximum UV emission levels (Fig. 4.45). However, the cases of monoenergetic beam, and scaled values of PJ 7 intensities fall within the range of UVS measurements.

4.6 Conclusion

Electron precipitation has profound effects on Jupiter's auroral ionosphere. Juno energetic particle instruments have provided a comprehensive survey of energetic electrons beaming into the atmosphere. By using an electron precipitation event during PJ 7 representative of the newly discovered [188] extreme precipitation events, we have estimated consequences due to collisional interaction between precipitating electrons and neutral molecules. Electrons with energies larger than 100 keV will penetrate deeper than the methane homopause [101]. Electron impact ionization at deeper levels initiates a chain of reactions leading to the formation of short-lived hydrocarbon ions. It is established through modeling and simulation that a short-time-scale event ($\sim$ 100 seconds) can provide appreciable microwave absorption required to explain cold features inferred from MWR, while at the same time resulting in absorption of the ultraviolet H_2 band emissions that are generally used as a measure of the precipitating energetic particle flux (due to their depth of penetration into the atmospheric column) and thereby hiding the extent of the auroral energy input into the high-latitude atmosphere at Jupiter.

Table 4.6: A summary of factors responsible for variations in MWR antenna temperatures over Jupiter's northern aurora

Cause	Methodology	Conclusion
Variation in intensity and energy of downward directed electron flux	Calculate microwave absorptivity profile and brightness temperatures for different electron beam intensities and energy distributions	0.6 GHz channel auroral T_B vary between 168.23 - 556.50 K, 1.2 GHz channel auroral T_B vary between 238.63 - 302.96 K
Variation in spatial scales of downward directed electrons	Calculate fill factors based on MWR antenna temperatures and apriori knowledge of brightness temperature contributions from aurora and deep thermal emission	Fill factors range between 7 to 80 percent of MWR footprint area
Variation in MWR footprint size relative to aurora (fill factor)	Normalize antenna temperatures to square of radial distance to spacecraft expressed in R_j	Unnormalized 0.6 GHz channel T_A vary between 450 - 800 K Unnormalized 1.2 GHz channel T_A vary between 350 - 450 K T_A reaches below 100 K at certain regions, changes cannot be solely attributed to variation in MWR footprint

Total energy deposition corresponding to electron precipitation peaks between 0.1 to 1 mbar. It can be expected to be a contributor to local atmospheric heating, besides ionization processes evident from MWR and UVS observations. The NASA Infrared Telescope Facility (IRTF) Texas Echelon Cross Echelle Spectrograph (TEXES) measures mid-infrared emissions lines of Jupiter's aurora. Spectral inversion of mid-IR observations reveal local atmospheric heating $\sim$ 1 mbar pressure at the Northern Aurora [254, 255]. Sinclair et al., (2025) [256] provided an improvement in the estimation of CH_4 homopause levels both northward and equatorward of MAE. Auroral energy deposition may play a role in vertical transport of CH_4 leading to enhanced homopause altitude poleward to MAE. Recent James Webb Telescope (JWST) mid-IR observations infer the presence of two local temperature peaks at 0.01 and 1 mbar [229]. There is also a general elevation in CH_4 homopause altitude at the polar regions. Precipitation of high-energy electrons may contribute to the observed changes in auroral temperature and CH_4 upwelling. Both IRTF and JIRAM have detected local warming in hydrocarbon regions, which could be attributed to local temperature increases or enhancement in hydrocarbon concentration.

The sporadic nature of precipitation intensities can explain the temporal variations in the high-latitude auroral ionosphere. The hydrocarbon ions will undergo rapid dissociative recombination with ionospheric electrons. Recombination coefficients (α_r) for the major hydrocarbon ions are $\sim$ 5 x 10^{-7} cm^3/s in presence of local electron densities (N_e) in range of 10^5-10^6 cm^{-3}. A simple estimation of recombination timescale $\tau_r \sim \frac{1}{\alpha_r N_e} \sim$ 2-20 s. Larger electron densities will have even smaller recombination time scales, consistent with temporal variations observed within $\sim$ 10 s.

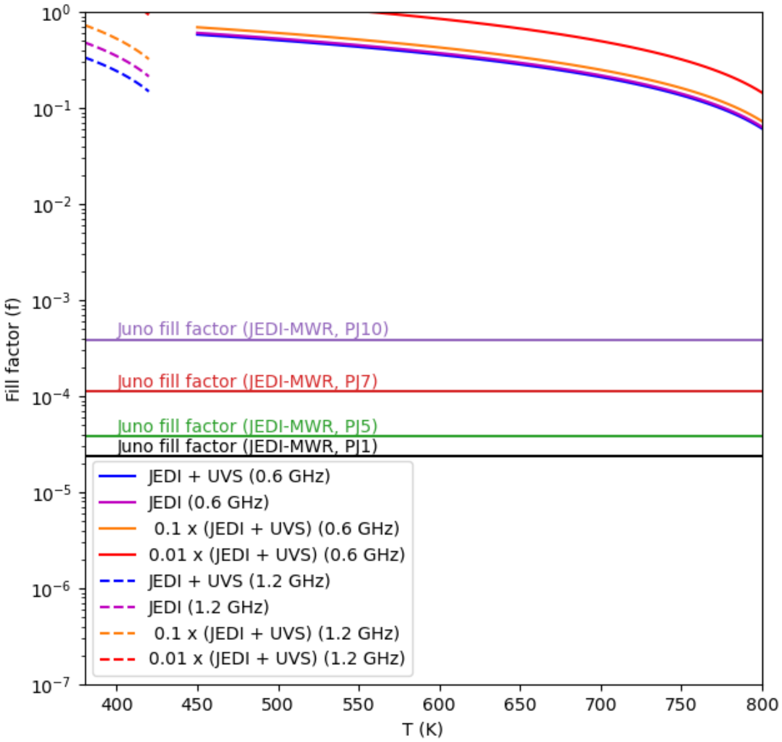

Figure 4.34: Fill factor inferred from MWR cold spot antenna temperatures for different cases of high-energy electron precipitation. MWR fill factors for 0.6 and 1.2 GHz frequency channels range between 7 and 80 assuming a MWR footprint size ~ 0.1 R$_j$. The JEDI in-situ precipitation region is found to be two orders of magnitude smaller than that inferred from model solutions. We identify fill factors corresponding to JEDI downward electron flux data over the North Pole collected during PJ1, PJ5, PJ7, and PJ10. Thus, cold spot antenna temperatures are found to be highly sensitive to electron beam spatial scales to the peak energy of the electrons and the energy flux of the electrons.

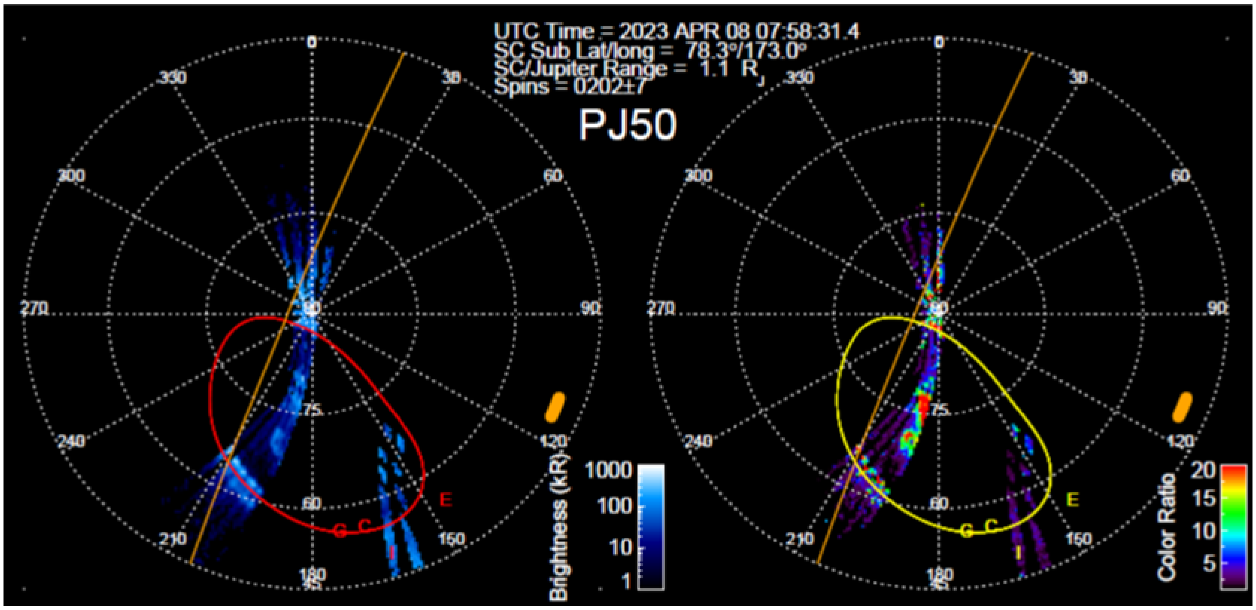

Figure 4.35: Polar projection of Juno UVS total UV emission and UV color ratio corresponding to Jupiter's Northern Aurora on 8th April 2023 (PJ 50) averaged over 15 consecutive Juno spins.

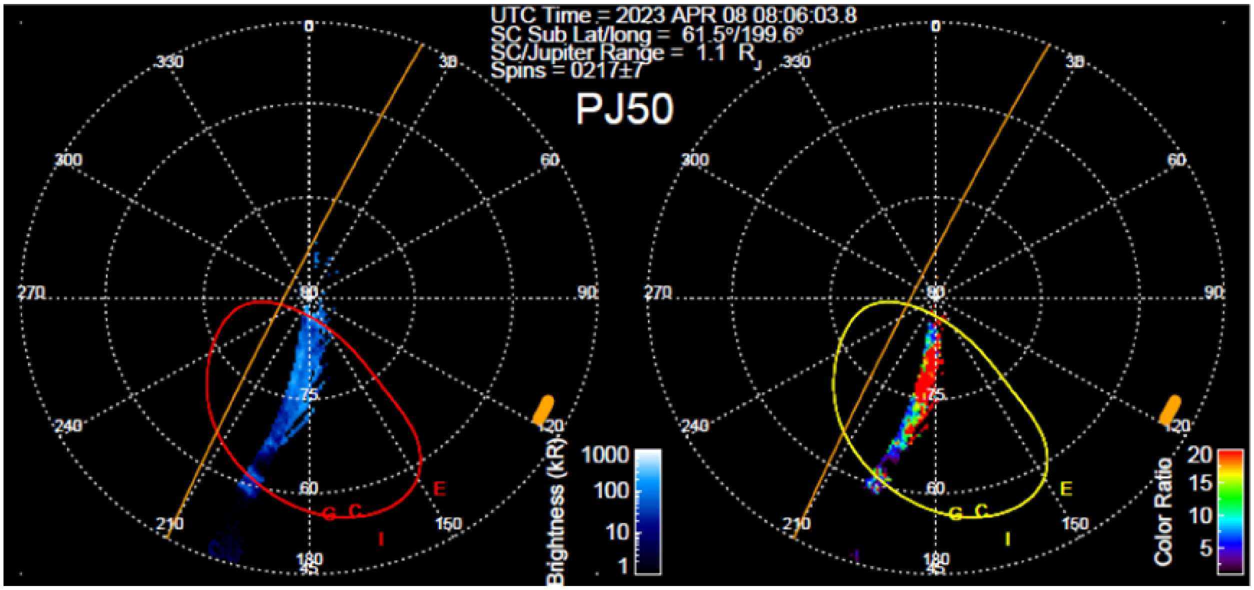

Figure 4.36: Polar projection of Juno UVS total UV emission and UV color ratio corresponding to Jupiter's Northern Aurora on 8th April 2023 (PJ 50) averaged over another set of 15 consecutive Juno spins.

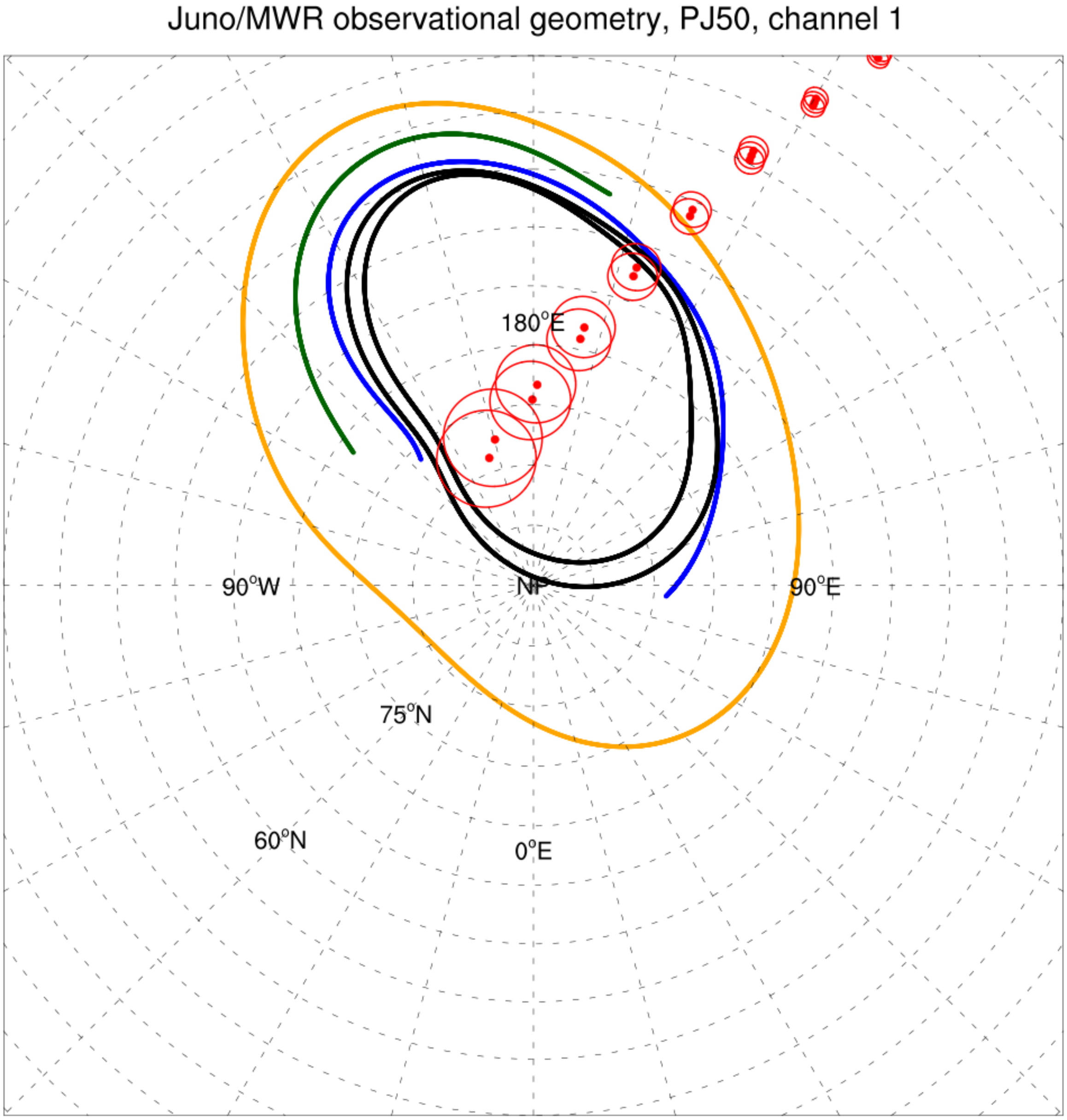

Figure 4.37: Polar projection of MWR 0.6 GHz channel footprint mapped relative to MAE, and satellite auroral footprints during PJ 50.

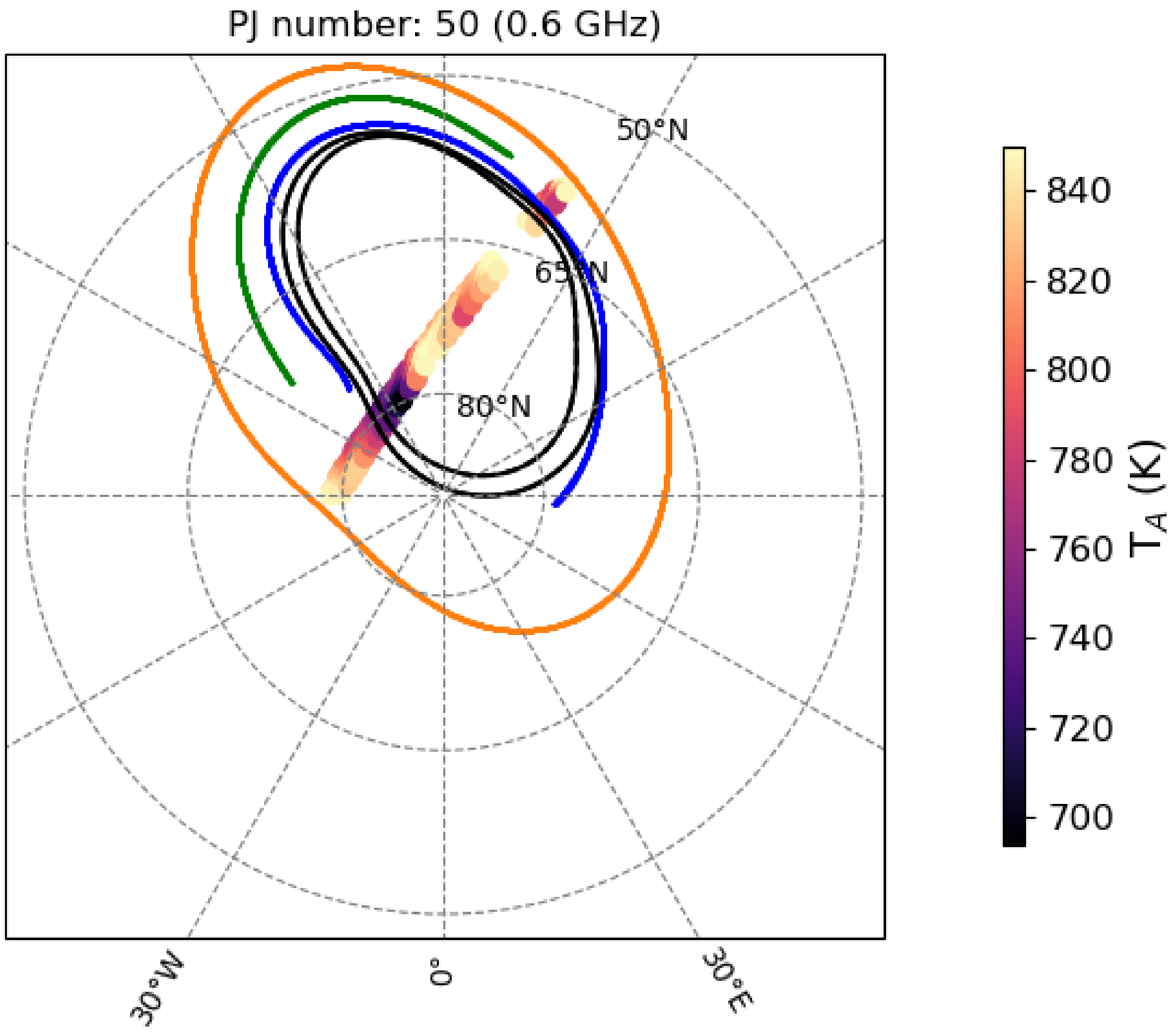

Figure 4.38: Polar projection of MWR 0.6 GHz channel nadir equivalent antenna temperatures during PJ 50. A large temperature variation is observed over the polar cap and MAE.

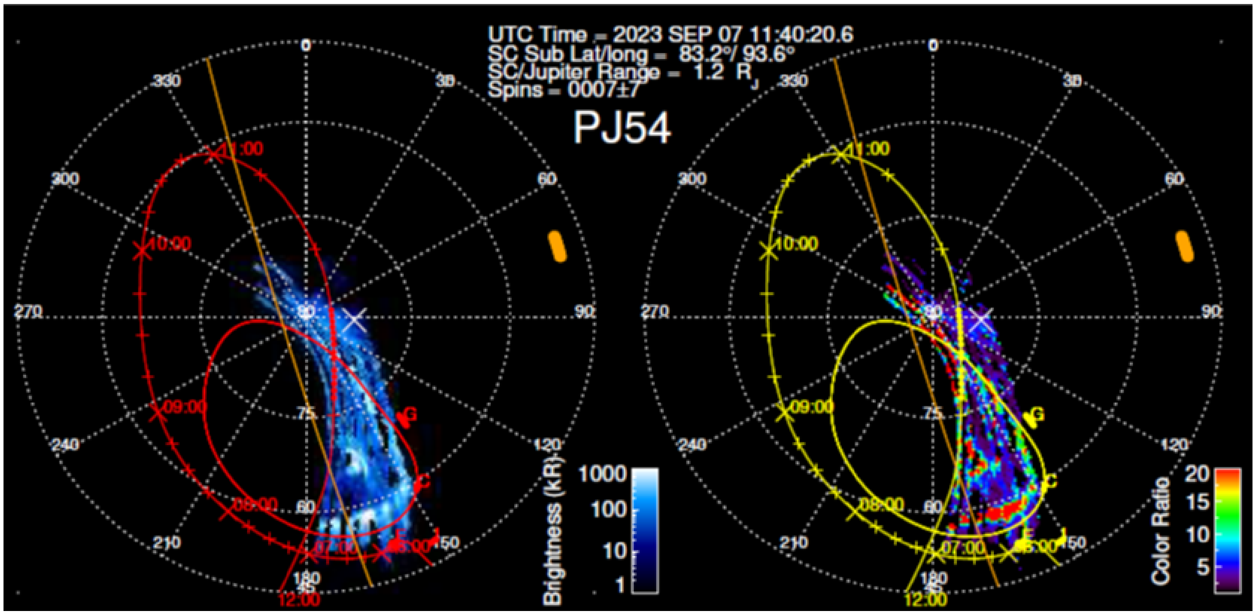

Figure 4.39: Polar projection of Juno UVS total UV emission and UV color ratio corresponding to Jupiter's Northern Aurora on 7th September 2023 (PJ 54) averaged over 15 consecutive Juno spins.

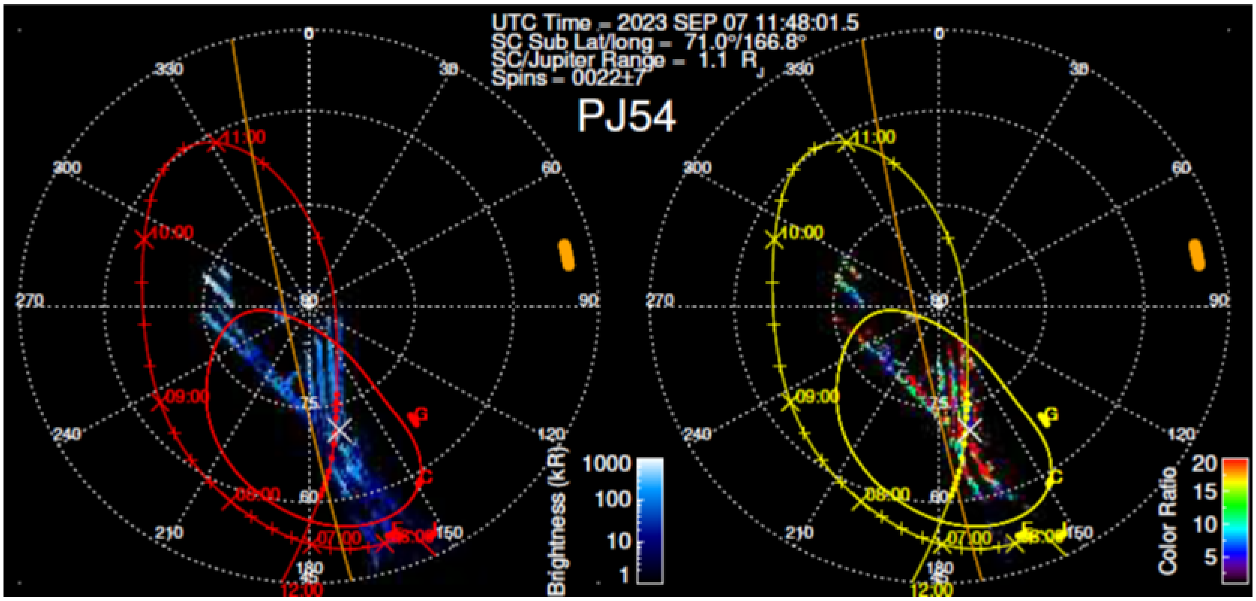

Figure 4.40: Polar projection of Juno UVS total UV emission and UV color ratio corresponding to Jupiter's Northern Aurora on 7th September 2023 (PJ 54) averaged over another set of 15 consecutive Juno spins.

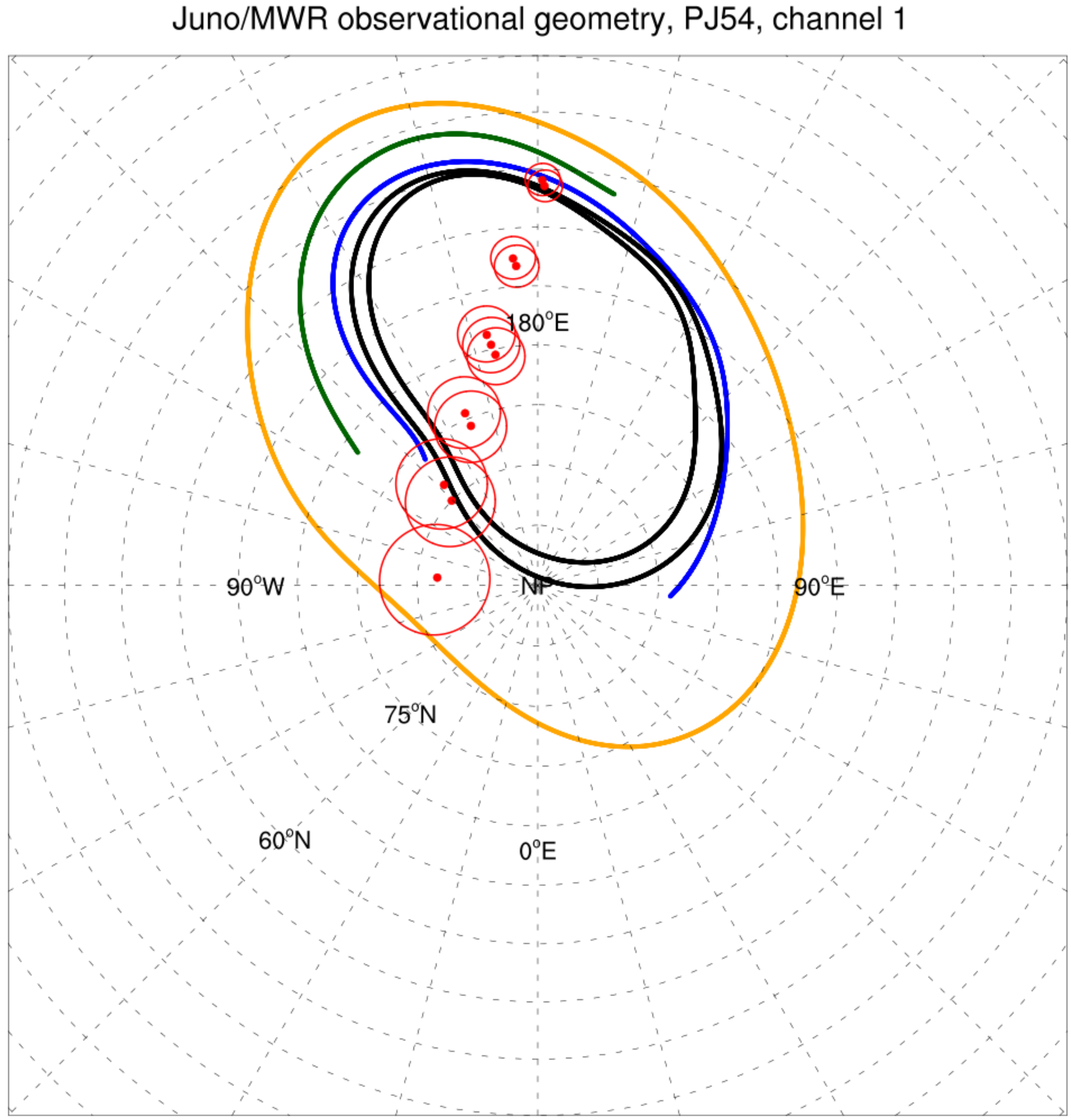

Figure 4.41: Polar projection of MWR 0.6 GHz channel footprint mapped relative to MAE, and satellite auroral footprints during PJ 54.

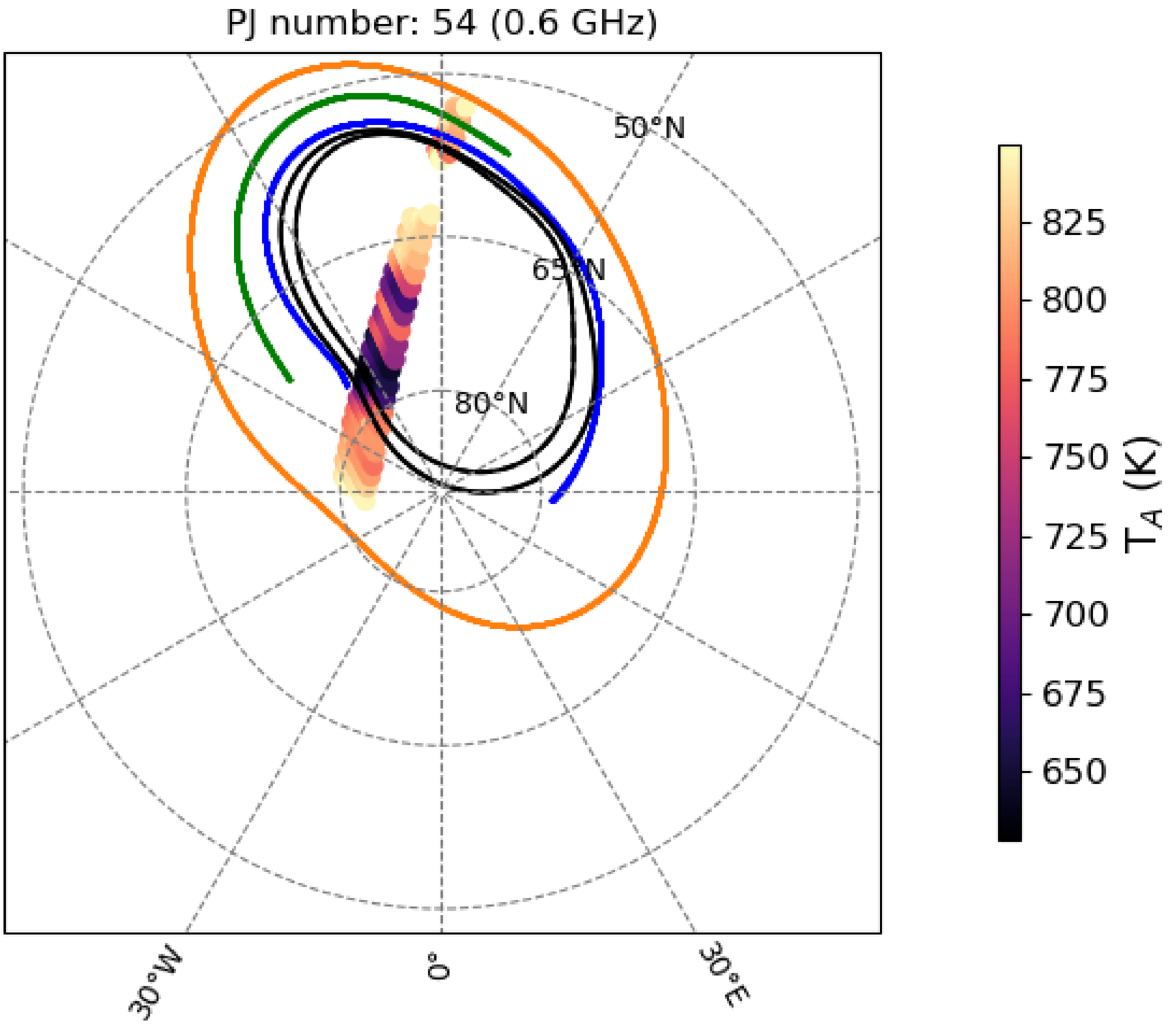

Figure 4.42: Polar projection of MWR 0.6 GHz channel nadir equivalent antenna temperatures during PJ 54. A large temperature variation is observed over the polar cap and MAE.

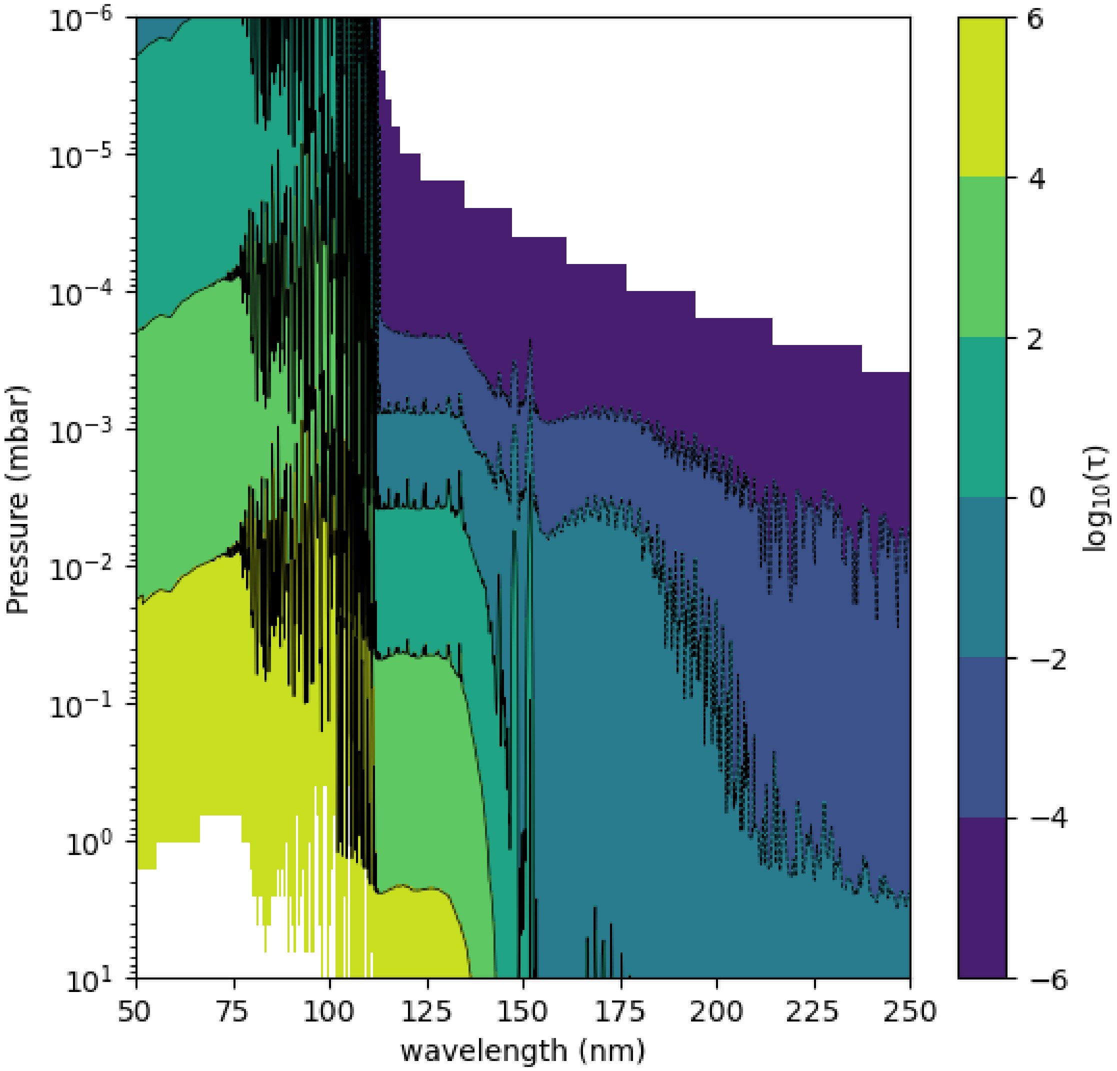

Figure 4.43: UV optical depth of Jupiter's atmosphere for UV wavelengths ranging between 50 - 250 nm. The opacity at short wavelengths increase rapidly due to CH_4 and C_2H_2 absorption.

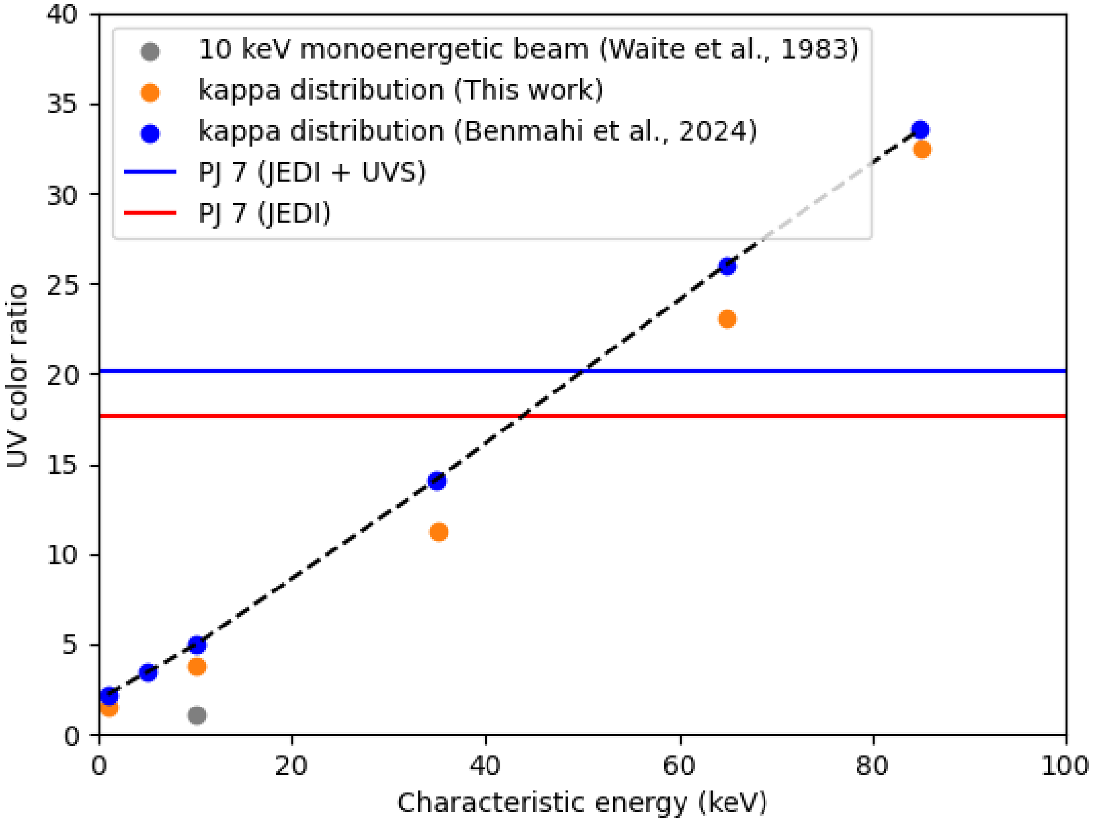

Figure 4.44: Comparison of UV color ratio for various cases of electron precipitation: (i) 10 keV monoenergetic beam [276], (ii) predicted UV color ratio of κ distribution from this work, (iii) Benmahi et al., (2024) estimations of UV color ratio for κ distribution, (iv) PJ 7: JEDI and UVS inferred electron flux, and (v) PJ 7: JEDI inferred electron flux. A linear relationship between UV color ratio and characteristic energy in κ distribution. JEDI and UVS electron flux measurements estimate UV color ratio within the range of UVS color ratio associated with auroral regions.

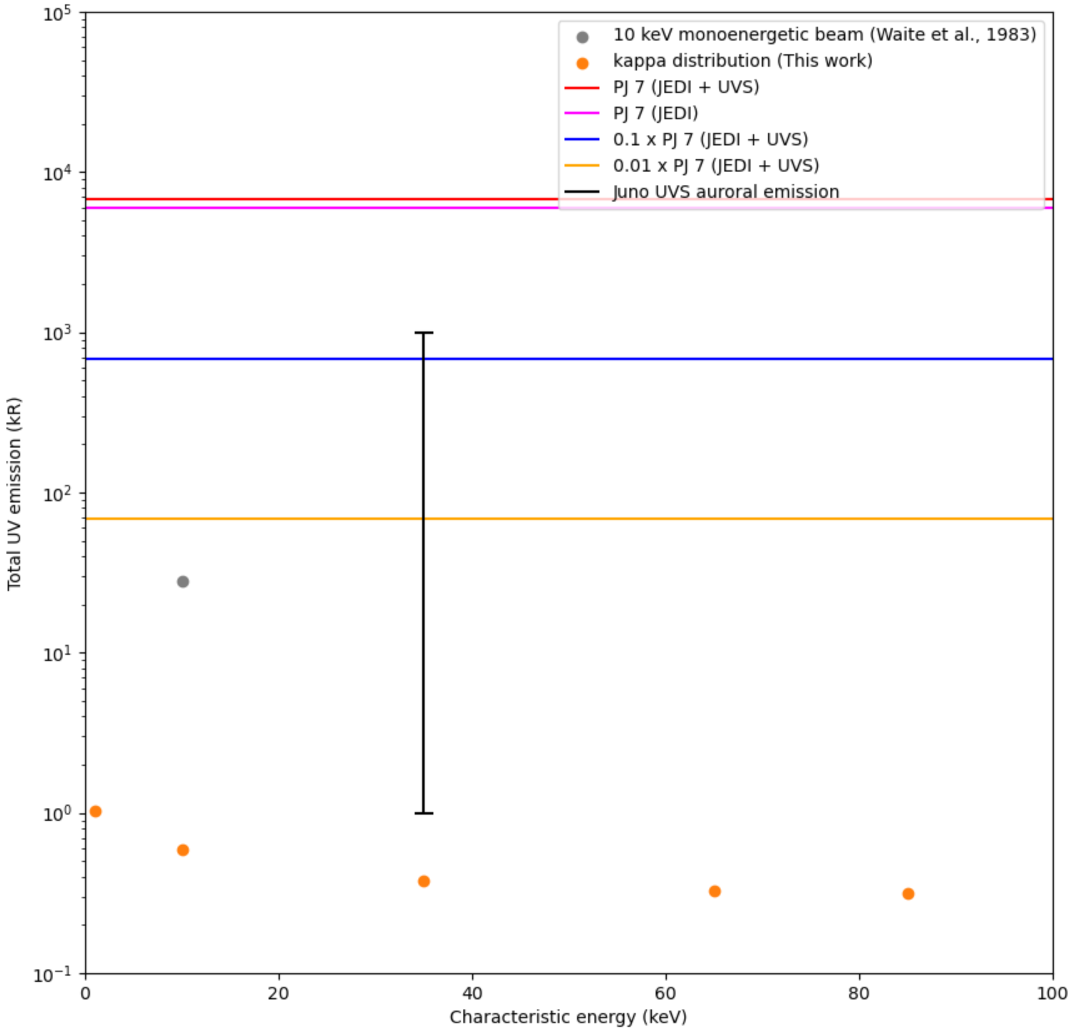

Figure 4.45: Comparison of total UV emission for various cases of electron precipitation: (i) 10 keV monoenergetic beam [276], (ii) κ electron energy distribution, (iii) PJ 7: JEDI and UVS, (iv) PJ 7: JEDI, (v) 0.1 x (JEDI + UVS), and (vi) 0.01 x (JEDI + UVS) inferred electron flux. The inclusion of electrons up to 10 MeV surpasses the UVS measurement range. However, the other cases are found to be within the range of total auroral emission. The κ distribution shows low emission due to a low amount of input energy flux i.e. 1 erg/cm^{2}s.

CHAPTER 5

Conclusion

5.1 Summary

The Juno Microwave Radiometer measurements have provided key insights into Jupiter's neutral atmosphere and polar aurora. Jupiter's atmosphere exhibits unique signatures at centimeter wavelengths. Signals at frequencies less than 5 GHz are generally not accessible from Earth-based radio telescopes due to the shrouding effect of Jupiter's synchrotron radiation in line-of-sight. The Juno spacecraft provides a unique window to probe Jupiter's deep thermal radiation and polar aurora at low-frequency microwave spectrum (0.6 – 1.2 GHz). Bypassing the inner radiation belts allows Juno to collect measurements of both thermal and nonthermal microwave radiation sources in the Jovian system.

5.2 Jupiter: Neutral Atmosphere

Passive microwave radiometry has been extensively applied to study water in the atmosphere, soil, and cryosphere. However, past missions did not carry this type of instrument to characterize the gas giant atmosphere. The MWR instrument onboard Juno probes the three-dimensional structure of Jupiter's atmosphere between the weather layer and deep atmosphere up to 1 kbar pressure. A priori knowledge of microwave absorbers, their concentration, and information about Jupiter's temperature structure complement the interpretation of data. It allows for the inversion of radiometer measurements to trace variations in atmospheric temperature and cloud-forming vapors, and map them to the dynamical structures of Jupiter.

Jupiter's microwave emission spectrum between 0.5 - 40 GHz is an important tool to derive atmospheric temperature and concentration of key cloud-forming volatiles like NH_3 and H_2O [88]. Weighting function at microwave frequencies probes between the cloud layers of NH_3, NH_4SH and H_2O. The cloud-forming process largely drives moist convective processes at Jupiter to control energy transport at shallow pressures. At pressures exceeding 100 bar, the abundances of refractory elements, volatiles, and alkali metals could sustain a radiative zone supporting non-adiabatic temperature gradients and convective inhibition.

A microwave radiative transfer model of Jupiter's atmosphere [169] is adapted to draw a comparison with MWR multi-wavelength brightness temperature and limb darkening. The brightness temperature and its angular dependence are largely contaminated by nonthermal emission sources from synchrotron and aurora. Thereby, the analysis is restricted to 40 deg. in both hemispheres. MWR data is processed for PJ 1-9, and PJ 12 to remove local temperature anomalies and normalize the brightness temperature for changes in Jupiter's gravity. The forward model adopts the T_{1bar} values based on Galileo Probe and Voyager Radio Science experiments.

At 0.6 GHz, brightness temperature data shows a uniform deviation from the forward model across the latitudes. This uniform deviation is attributed to an elevated amount of opacity source exclusive to pressures sensitive to the 0.6 GHz channel i.e. 100 bar-1 kbar. The latitudinal variation in NH_3 mixing ratio and its temperature-dependent microwave absorption coefficients do not solely contribute to the observed thermal radiation characteristics. Fegley and Lodders (1994) [105] provide thermochemical equilibrium-based predictions of alkali cloud formation and consequent thermal ionization of alkali vapors below the cloud base. Free electrons provide a significant contribution to the mean opacity of gas giants. The inclusion of alkali vapor ionization and free electron opacity source fits the 0.6 GHz measurements. Alkali metals are inferred to be depleted relative to their solar abundances by a factor of 10^2 to 10^5.

The presence of Na and K can elevate the mean opacity in the gas giant atmosphere. Burrows et al. 2000, [60] showed that alkali hydrides are a major source of opacity in hydrogen-helium atmospheres. The presence of halogens, oxygen, and silicates produces condensates storing Na and K within different layers of Jupiter's envelope. Na and K absorption lines have a clear signature in exoplanetary atmospheres, and their reactivity in exoplanetary atmospheres gives us to wide variety of exotic clouds. In particular, Na_2S and KCl are the two most stable clouds and store a large proportion of alkali metals above the cloud condensation level. Rensen et al., (2023) [227] applied a thermochemical model of coupled chemical reactions and phase change processes to predict the composition and density of alkali clouds at solar abundance. Under different conditions of alkali, and oxygen inventory, the model predicts decks of thin overlapping alkali halide and sulphide clouds, consistent with previous thermochemical models.

We extended the analysis of Jupiter's deep thermochemistry in the context of thermal ionization and MWR measurements. An ensemble of reactions involving ions, neutrals, and condensates are solved for steady-state concentrations of free electrons till 10 kbar pressure. Our simulations reveal HS^- and Cl^- as dominant charge carriers between 100 bar - 10 kbar pressure regimes, reducing free electrons to a tenth of thermal ionization magnitudes. Stable anions are formed from high-temperature dissociation and electron gain reactions of H_2S and HCl gases. The reduction in free electron concentration decreases the effective microwave opacity of the deep atmosphere, requiring an equivalent increase in Na and K metallicity. Microwave radiative transfer predictions based on thermochemical equilibrium free electron concentrations constrain [M/H] = -1 for equal proportions of Na and K mixtures.

The information about alkali metal abundance and the equilibrium concentrations of their products with other atmospheric constituents supply crucial information to calculate the mean opacity of Jupiter's atmosphere. Guillot et al., (1994a, 1994b) [125, 124] predict Jupiter's mean opacity and quantify its effect on the overall cooling and evolution of the planet. The presence of a radiative layer shows the age of Jupiter and Saturn to be Myr younger compared to a purely adiabatic atmosphere. Juno MWR constraints on alkali metal abundance provide a new baseline for comparative studies with exoplanet detections of Na and K [285]. Given the reactive nature of alkali metals, they may also be considered as a representative of other heavy elements in Jupiter's atmosphere. However, there is no concrete reason to support or refute this claim. The case for inhomogeneity and vertical gradients in Jupiter's atmosphere warrants a deeper look into the chemistry and dynamics of mean circulation processes at play.

5.3 Jupiter: Aurora

During the polar passes, 0.6 GHz and 1.2 GHz channels measure a strong decrease in antenna temperatures over Northern Aurora. MWR measurements show a large degree of variation, largely attributed to molecular ionization driven by electron precipitation in Jupiter's stratosphere. It can be independently confirmed from spatial correlation with Lyman and Werner band missions detected by Juno UVS. JEDI, UVS, and the star cameras provide complementary data to characterize electron energy distribution over the poles, revealing downward electron flux with energies greater than 1 MeV.

Hodges et al., (2020) [140] analyzed the first 21 orbits of Juno to put forward trends in microwave antenna temperatures of the Northern Aurora. These cold features show a large range of variation in temperatures over a wide range of latitudes between 50 deg. to the polar cap. The work attributed these features to plasma reflection originating from regions of high electron concentration. Antenna temperature inversion based on the plasma reflection theory required extremely high concentrations $\sim 10^9$ cm^{-3}. These predictions are found to contrast with electron precipitation models of Jupiter's upper atmosphere [276, 257, 101].

The theory of radio and microwave transmission through ionospheric medium predicts a strongly collisional plasma medium to exhibit absorption of electromagnetic radiation transmitted through the medium. The amount of absorption is dependent on the collision of free electrons with neutral molecules. This phenomenon has been observed in the form of radio wave absorption on Earth [182, 230] and SEP-induced radio absorption on Mars [135, 136]. Thus, high electron-neutral collisions coupled with electron precipitation over Jupiter's Northern Aurora can explain the formation of cold spots in microwave [137, 291].

A hybrid method of electron energy deposition for Jupiter's high-latitude ionosphere is developed using CSDA [216] and energy partitioning from two-stream electron transport from Waite et al., (1983) [276]. The total energy deposition rate is partitioned into neutral heating, electron impact ionization, and direct H_2 vibrational excitation processes. A one-dimensional time-dependent chemical kinetics model is developed to solve a system of coupled reactions involving ions, neutrals, and electrons. The extreme electron precipitation events lead to the production of ionospheric electron layers and hydrocarbon ions at 0.1 - 1 mbar pressures within 100 s. The intensity of electron precipitation events and their beam fill factor greatly influence the MWR antenna temperatures. The dissociative recombination loss pathway shows time scales in the range of 2-20 s in the presence of local electron densities $\sim 10^5$ - 10^6 el/cm^3 [17, 21]. Thus, extreme electron precipitation with a time-dependent electron flux can be associated with the rapid changes in auroral antenna temperatures.

The low-frequency channels at 0.6 GHz and 1.2 GHz exhibit strong signatures associated with the Northern Aurora. The antenna beam footprint shows a proportion of the beam overlaps with the main auroral oval and the polar cap at the cold spot antenna boresight points. The variation in antenna footprint size throughout the Juno mission causes variations in auroral antenna temperatures from one orbit to another. Multiple Juno orbits show the presence of rapidly changing antenna temperatures largely associated with the polar cap and main auroral oval. Temperatures change within tens to hundreds of Kelvin within consecutive spins associated with overlapping spatial regions. As these rapid changes appear at 0.6 GHz and 1.2 GHz channels, the antenna temperatures are expected to vary within 10-30 s. These rapid changes in antenna temperatures can be associated with short-term changes in the Jovian ionospheric plasma medium. Electron precipitation-driven ionization and dissociative recombination of molecular ions exhibit small time scales $\sim$ 10-100 s, causing rapid change in local electron and ion concentrations.

5.4 Limitations of the Study

Our current understanding of Jupiter's aurora is limited by several factors concerned with the analysis of Juno MWR data and the atmospheric models presented in Chapters 2-4. Firstly, the 0.6 GHz channel measurements at latitudes beyond 40 degrees become contaminated with sources of nonthermal radiation. As Juno progresses towards the later orbits, the synchrotron emission from inner radiation belts dominates thermal radiation. Due to extremely high synchrotron emission, signal-to-noise is very low, and thermal emission from deep atmosphere cannot be retrieved. Similarly, limb darkening is very sensitive to changes in atmospheric temperature and composition. The synchrotron radiation can vary with time, and it is highly dependent on viewing geometry due to its characteristic polarization. A thorough understanding of the radiation belt emission sources and their variation over each orbit is required to estimate uncertainties in Juno high-latitude atmospheric measurements.

Particle losses from inner radiation belts will lead to the precipitation of electrons, protons, and higher energy ions into the Jovian stratosphere. In Chapter 4, it has been shown that a monoenergetic beam corresponding to energies greater than 100 keV could contribute to a reduction in MWR antenna temperature by a few Kelvin. Moving forward, the MWR data should be reassessed to search for radiation belt particle precipitation events. From the perspective of probing neutral atmosphere, such temperature anomalies would require additional filtering. It could introduce small uncertainties in the calculation of the darkening of the limb at high latitudes. Irrespective of these localized ionization effects, the mean 0.6 GHz shows a deviation from Jupiter's microwave radiation, and it requires alkali vapor thermal ionization to fit the Juno data.

The chemical kinetic rates of formation and convective transport suggest the presence of several semi-metallic hydrides as disequilibrium species such as SiH_4 and GeH_4. They are strongly coupled with the deep atmospheric oxygen abundance. Our treatment of thermochemical equilibrium associated with alkali metals and refractory elements does not take into account the effects of vertical transport. It is limited by the lack of laboratory experiments to determine chemical kinetic rate coefficients at high temperatures. However, the assumption of equilibrium will provide a basis for comparison in the presence of adequate laboratory data.

Lastly, the precipitation of high-energy electrons in keV - MeV energies causes auroral UV emissions in addition to the formation of electron layers opaque to microwave. In particular, cold spot regions are expected to be correlated with regions of high UV color ratio. Juno MWR antenna footprint is much larger compared to the UVS image resolution, therefore it is not possible to draw strong comparisons between the two datasets for most Juno orbits. During PJ 50 and PJ 54, MWR cold spots show a strong spatial correlation with a high color ratio over the polar cap and MAE. It is also complicated by detector saturation as Juno perijove nears Jupiter's pole. The star sensors ACS, and SRU along with UVS are sensitive to MeV charged particles. However, the data from these sensors have not been studied collectively to map the variability in charged particle flux. We limit our analysis to the extreme downward electron flux detected by the JEDI instrument.

5.5 Future Work

This body of work covers a range of topics closely tied to the energetics of Jupiter's deep atmosphere and magnetosphere-ionosphere coupling. The measurement of thermal and nonthermal radiation and the quantification of their sources provide a unique lens to understand Jupiter as a system. The measurement of sub-solar alkali metals and auroral cold spots have shared synergies with Earth and space-borne instrumentation to study the gas giant atmosphere and its space environment.

The analysis of MWR atmospheric measurements was restricted to mid-latitude due to contamination from synchrotron and aurora. Our analysis hints that atmospheric abundances of heavy elements are not representative of global abundance. However, the influence of temperature and dynamics on the distribution of alkali metals remains an open question. During the later orbits, MWR antenna footprints reduce in size relative to MAE. It ensures a higher proportion of low emission angle measurements to be free from cold spot emission. The 0.6 GHz measurements beyond PJ 12 should be analyzed to retrieve brightness temperature and limb darkening data. In addition, the MWR channels 2-6 and updated T_{1bar} based on Juno radio occultation will aid in the interpretation of deep atmospheric temperature and alkali metal abundance.

Mid-IR emission spectra measurements of the polar atmosphere show brightening due to CH_4 and H_3^+ emissions. Auroral electron and ion precipitation contribute to the heating and production of complex hydrocarbon species. A local brightening of the hydrocarbon region is observed over the auroral regions. It is characterized by local temperature maxima $\sim$ 1 mbar and an elevated level of CH_4 homopause. This phenomenon is attributed to auroral heating driving vertical transport of CH_4 at high latitudes. Our analysis of high-energy electron precipitation shows peak energy deposition at 0.1 - 1 mbar. Thus, high-energy electrons can penetrate the lower stratosphere to provide strong neutral heating. The effects of electron and ion precipitation on CH_4 transport and atmospheric dynamics warrants the usage of global circulation models of Jovian ionosphere and thermosphere.

The PJ 7 event has been used as a prototype to understand the effects of high-energy electron precipitation [188]. Previous literature from JEDI reports many high-energy electron flux events in Jupiter's space environment. The search for downward high-energy electron flux, its time-dependent variations, and mapping w.r.t. auroral features can help interpret the MWR observations over the North Pole. Especially, there is additional particle acceleration occurring between the Juno spacecraft and the polar aurora. Hydrocarbon chemistry models of Jupiter and Saturn suggest that electron impact ionization can drive the formation of benzene and the formation of aerosols. Similar mechanisms have been proposed at Titan [83]. The production of these hazes and aerosols controls the radiative budget of the polar atmosphere. Cavalie et al., (2023) measured local depletion in HCN column density attributed to auroral chemistry [67]. With the aid of one-dimensional electron precipitation models, the effects of electron precipitation on C-H-N-O can be concretely quantified.

Juno will conduct radio occultation experiments northward of the MAE during its extended mission phase. These ionospheric electron density profiles will characterize the auroral ionosphere, and search for signatures of precipitation events. The time-dependent simulations of charged particle precipitation can be applied to provide an interpretation of ionospheric electron densities in the auroral regions.

Our analysis benefits the analysis of sub-millimeter and IR emission measurements of the Jovian aurora. These atmospheric models can also be applied to other planets to support the JWST solar system observations of Uranus and Neptune. The observations will support the development of space missions to investigate the ice giant space environment. The Understanding of auroral emissions at these planets widens our knowledge of the planet's magnetosphere-ionosphere-atmosphere coupling.

APPENDIX A

Appendix 1

The numerical modeling of atmospheric microwave radiative transfer is important to correctly interpret the Juno MWR data associated with multi-frequency brightness temperature and their emission angle dependence. In infrared and visible spectroscopy, line absorption models and line broadening parameterizations are important to understand the interactions of electromagnetic radiation through the transmission medium. HITRAN [228], GEISA [150] and HITEMP [234] are important databases containing information about line absorption associated chemical species significant for planetary atmospheres e.g. CO_2, O_3, CH_4, H_2O, N_2, etc.

However, simulating the microwave absorption of Jupiter's atmosphere is tricky due to its extreme environment. Jupiter's atmosphere is mostly made up of H_2 and He as its main constituents. The depths at which MWR probes Jupiter correspond to a large range of temperatures between 500 to 1000 K. The contributions of H_2 and He are exhibited through the collision-induced absorption (CIA) process. We adopt the publicly available CIA model from the HITRAN database to simulate CIA from two sources: H_2-H_2 and H_2-He collisions. To assist the interpretation of MWR data laboratory experiments were conducted to measure the absorption coefficients of cloud-forming vapors like NH_3 and H_2O subject to Jupiter's chemical and temperature environments.

A series of experiments have been conducted to measure the line broadening and shape features associated with microwave frequencies $\sim$ 1-10 GHz. In Chapter 2 we adopt the method described in Bellotti et al., (2016) [32] to simulate the line absorption of NH_3 and H_2O vapors. The total

NH_3 absorptivity (α, in dB/km) can be expressed as the sum of inversion (α_{inv}), rotational (α_{rot}) and roto-vibrational transitions (α_{v_2}).

$$\alpha = 434294.5(\alpha_{rot} + \alpha_{v_2} + \alpha_{inv}) \tag{A.1}$$

The rotational and roto-vibrational transitions contribute largely at millimeter wavelengths corresponding to Jovian atmosphere pressure above 1 bar. Devaraj et al., (2014) [93] model is adopted to simulate the two contributing sources. The inversion line opacity model from Bellotti et al., (2016) [32] is added to calculate the total NH_3 opacity. In the case of water vapor, the absorptivity is a sum of individual resonant lines and the water vapor continuum. The microwave opacity model provided by Karpociwz and Steffes (2011) [154] is updated with a new formulation of water vapor continuum absorptivity. Empirical constants are added to fit high-temperature experiment data. Water vapor continuum is due to self-continuum [233] and dependent on foreign gas influence i.e. H_2 and He.

The Microwave Radiative Transfer code (HARP) uses saturation vapor pressure curves to correct for cloud condensation processes associated with NH_3, H_2O, NaCl, and KCl. NH_3 and H_2O form liquid and ice clouds in gas giant atmospheres. We calculate the liquid and ice cloud saturation vapor pressures based on the model provided by Briggs and Sackett (1989) [53] which has been applied to study radio observations of gas giants. The general expression is provided below:

$$log(P) = \frac{a_1}{T} + a_2 + a_3 log(T) + a_4 T + a_5 T^2 \tag{A.2}$$

Here a_i with i = 1 to 5 are constants, P is expressed in dyne/cm^2 and T is atmospheric temperature in K. We place 195 K and 273.16 K as the transition temperatures from liquid to ice formation. The ice and liquid saturation vapor pressure constants for NH_3 and H_2O are given in Table A.1.

Table A.1: Empirical Saturation Vapor Constants for NH_3 and H_2O

Coefficient	**NH_3 over NH_3 ice [155]**	**NH_3 over liquid NH_3 [282]**	**H_2O over H_2O ice [281]**	**H_2O over liquid H_2O [282, 53]**
a_1	-4122	-4409.3512	-5631.1206	-2313.0338
a_2	41.67871	76.864252	-8.363602	-164.03307
a_3	-1.81630	-8.4598340	8.2312	38.053682
a_4	0	5.51029 x 10^{-3}	-3.861449 x 10^{-2}	-1.3844344 x 10^{-1}
a_5	0	6.80463 x 10^{-6}	2.77494 x 10^{-5}	7.4465367 x 10^{-5}

APPENDIX B

Appendix 2

B.1 Thermochemical data

The k_p data associated with all molecular and ions in thermochemical equilibrium simulations can be expressed as a function of temperature. GGChem uses certain standard formats for expressing k_p as an empirical function of temperature, based on laboratory data from standard chemical databases. Here we describe some of the important formats.

B.1.1 Tsuji format

Tsuji et al., (1973) [269] described the k_p as an internal fit of the independent variable $\theta = 5040/T$.

$$log_{10} k_p^{Tsu} = -a_0 - a_1\theta - a_2\theta^2 - a_3\theta^3 - a_4\theta^4 \tag{B.1}$$

B.1.2 Gail and Sedlmayr format

Gail and Sedlmayr (1986) [109] provided an alternate fit as a function of θ It was used in the old form of GGChem.

$$log k_p^{GS} = a_0 + a_1\theta + a_2\theta^2 + a_3\theta^3 + a_4\theta^4 \tag{B.2}$$

B.1.3 Sharp and Huebner format

Sharp and Huebner (1990) [246] directly fitted the Gibbs free energy to provide a new expression of k_p values. It is expressed in terms of a standard pressure p^0 = 1 atm and R_{cal} = 1.987 cal mol^{-1} K^{-1}

$$logk_p^{SH} = (1-n)logp^0 - \frac{a_0/T + a_1 + a_2T + a_3T^2 + a_4T^3}{R_{cal}T} \tag{B.3}$$

B.1.4 Stock format

Stock (2008) [287] gave another expression for k_p as a function of temperature T.

$$logk_p^{SH} = (1-n)logp^0 + \frac{a_0}{T} + a_1logT + a_2 + a_3T + a_4T^2 \tag{B.4}$$

B.2 Saturation curves

Some important saturation vapor pressure expressions corresponding to important clouds are listed below. They are expressed in terms of total pressure (P_{tot}), and metallicities of different elemental species constituting each compound. In other cases, Iron metallicity ([Fe/H]) has been used as a proxy for elemental abundances.

B.2.1 Ammonia

NH_3 condensation curve [176]:

$$\frac{10^4}{T_{cond}} = 68.02 - 6.19[Fe/H] - 6.31logP_{tot} \tag{B.5}$$

B.2.2 Water

H_2O condensation curve [176]:

$$\frac{10^4}{T_{cond}} = 38.84 - 3.93[Fe/H] - 3.83 log P_{tot} - 0.2[Fe/H] log P_{tot} \tag{B.6}$$

B.2.3 Ammonia Hydrogensulphide

NH_4SH condensation curve [176]:

$$\frac{10^4}{T_{cond}} = 48.94 - 4.27[Fe/H] - 4.15 log P_{tot} \tag{B.7}$$

B.2.4 Zinc Sulphide

ZnS condensation curve [274]:

$$\frac{10^4}{T_{cond}} = 12.52 - 0.63(log P_T + [Zn/H] + [S/H]) \tag{B.8}$$

B.2.5 Manganese Sulphide

MnS condensation curve [274]:

$$\frac{10^4}{T_{cond}} = 7.45 - 0.42(log P_T + [Mn/H] + [S/H]) \tag{B.9}$$

B.2.6 Magnesium Silicate - I

$MgSiO_3$ condensation curve [273]:

$$\frac{10^4}{T_{cond}} = 6.26 - 0.35 log P_T - 0.7[Fe/H] \tag{B.10}$$

B.2.7 Magnesium Silicate - II

Mg_2SiO_4 condensation curve [273]:

$$\frac{10^4}{T_{cond}} = 5.89 - 0.37 log P_T - 0.73[Fe/H] \tag{B.11}$$

APPENDIX C

Appendix 3

The list of chemical reactions corresponding to Jupiter's ionosphere can be grouped into several categories. Each category has a corresponding rate expression based on theory or laboratory experiments.

C.1 Photochemical reactions

In Jupiter's ionosphere, primary species that undergo photodissociation or photoionization are H_2, He, CH_4, C_2H_2, C_2H_4 and C_2H_6. The photochemical cross-sections and branching ratios have been adopted from the Leiden astrochemistry database [138]. It has been organized in its latest form in Tsai et al., (2017) [268]. For time-dependent simulations of ionospheric chemistry, we do not add the photochemical reactions to explicitly model contributions from high-energy electron precipitation. List of key photoionization and photodissociation reactions are given in Table C.1

C.2 Electron impact processes

During electron precipitation, electrons collide with atmospheric neutrals and a part of their energy goes into neutral ionization. In a gas giant atmosphere, electron impact ionization of molecular hydrogen is the dominant process. It has two pathways to form either H_2^+ or H^+ ions. The ionization rate per unit hydrogen molecule density is computed from the total energy deposition rate. We apply the yield factor corresponding to hydrogen ionization from Waite et al., (1983) [276]. The

Table C.1: List of photodissociation and photoionization reactions

Index	**Equation**
P_1	$H_2 \rightarrow H_2^+ + e^-$
P_2	$He \rightarrow He^+ + e^-$
P_3	$H_2 \rightarrow 2\ H$
P_4	$H_2 \rightarrow H^+ + H + e^-$
P_5	$CH_4 \rightarrow CH_3 + H$
P_6	$CH_4 \rightarrow CH_2 + 2\ H$
P_7	$CH_4 \rightarrow CH_2 + H_2$
P_8	$CH_4 \rightarrow CH + H_2 + H$
P_9	$C_2H_2 \rightarrow C_2H + H$
P_{10}	$C_2H_4 \rightarrow C_2H_2 + H_2$
P_{11}	$C_2H_4 \rightarrow C_2H_2 + 2\ H$
P_{12}	$C_2H_6 \rightarrow C_2H_4 + H_2$
P_{13}	$C_2H_6 \rightarrow C_2H_4 + 2\ H$
P_{14}	$C_2H_6 \rightarrow C_2H_2 + 2\ H_2$
P_{15}	$C_2H_6 \rightarrow 2\ CH_3$

energy deposition rate profiles from CSDA are converted into H_2 ionization rate (Table C.2). These rates are applied to the chemical kinetics solver, C^3M to predict the electron concentration during short-time scale events.

Table C.2: List of electron impact processes

Index	**Equation**
E_1	$H_2 + e^-_{cr} \rightarrow H_2^+ + e^- + e^-_{cr}$
E_2	$H_2 + e^-_{cr} \rightarrow H^+ + H + e^- + e^-_{cr}$

C.3 Bimolecular reactions

The bimolecular reaction rate expressions are generally expressed as Arrhenius rate expressions. The following table (Table C.3) provides a list of bimolecular reactions and their corresponding rate expression coefficients.

Table C.3: List of important bimolecular reactions

Index	**Equation**	**k**	**Rate expression**
C_1	$H + CH \rightarrow C + H_2$	a = 1.4×10^{-11}, b = 0.0, E_a = 0.0	[31]
C_2	$H + {}^1CH_2 \rightarrow CH + H_2$	a = 2.0×10^{-10}, b = 0.0, E_a = 0.0	[57]
C_2	$H + {}^3CH_2 \rightarrow CH + H_2$	a = 2.66×10^{-10}, b = 0.0, E_a = 0.0	[64]
C_3	$H + CH_3 \rightarrow {}^1CH_2 + H_2$	a = 1.0×10^{-10}, b = 0.0, E_a = 7600.0	[218]
C_4	$H + CH_4 \rightarrow CH_3 + H_2$	a = 3.73×10^{-20}, b = 3.0, E_a = 4406.0	[218]
C_5	$H + C_2H_3 \rightarrow C_2H_2 + H_2$	a = 2.0×10^{-11}, b = 0.0, E_a = 0.0	[28]
C_6	$H + C_2H_4 \rightarrow C_2H_3 + H_2$	a = 9.0×10^{-10}, b = 0.0, E_a = 7500.0	[218]
C_7	$H + C_2H_6 \rightarrow C_2H_5 + H_2$	a = 2.35×10^{-15}, b = -1.5, E_a = 3725.0	[29]
C_8	$H_2 + CH \rightarrow {}^3CH_2 + H$	a = 3.1×10^{-10}, b = 0.0, E_a = 1650.0	[57]
C_9	$H_2 + {}^1CH_2 \rightarrow CH_3 + H$	a = 9.24×10^{-11}, b = 0.0, E_a = 0.0	[293]
C_{10}	$H_2 + {}^1CH_2 \rightarrow {}^3CH_2 + H_2$	a = 1.26×10^{-11}, b = 0.0, E_a = 0.0	[293]
C_{11}	$H_2 + CH_3 \rightarrow CH_4 + H$	a = 1.14×10^{-20}, b = 2.74, E_a = 4740.0	[29, 218]
C_{12}	$H_2 + C_2H_3 \rightarrow C_2H_4 + H$	a = 5.0×10^{-20}, b = 2.63, E_a = 4298.0	[104]
C_9	$CH + CH_4 \rightarrow C_2H_4 + H$	a = 3.96×10^{-8}, b = -1.04, E_a = 36.1	[64]
C_{13}	$CH + C_2H_4 \rightarrow C_2H_2 + CH_3$	a = 2.23×10^{-10}, b = 0.0, E_a = -173.0	[35]
C_{14}	$CH + C_2H_6 \rightarrow C_2H_4 + CH_3$	a = 1.9×10^{-8}, b = -0.859, E_a = 53.2	[64]
C_{15}	$2\ {}^3CH_2 \rightarrow C_2H_2 + H_2$	a = 2.0×10^{-11}, b = 0.0, E_a = 400.0	[29]

Continued on next page

Index	Equation	k	Rate expression
C_{16}	$2\ ^3CH_2 \rightarrow C_2H_2 + 2\ H$	$a = 1.8\times10^{-11}$, $b = 0.0$, $E_a = 400.0$	[29]
C_{17}	$^3CH_2 + C_2H_3 \rightarrow C_2H_2 + CH_3$	$a = 8.0\times10^{-11}$, $b = 0.0$, $E_a = 0.0$	[205]
C_{18}	$^1CH_2 + CH_4 \rightarrow CH_4 + {}^3CH_2$	$a = 1.2\times10^{-11}$, $b = 0.0$, $E_a = 0.0$	[43]
C_{19}	$^1CH_2 + CH_4 \rightarrow 2\ CH_3$	$a = 5.9\times10^{-11}$, $b = 0.0$, $E_a = 0.0$	[43]
C_{20}	$2\ CH_3 \rightarrow C_2H_5 + H$	$a = 5.0\times10^{-11}$, $b = 0.0$, $E_a = 6800.0$	[29, 218]
C_{21}	$CH_3 + C_2H_3 \rightarrow C_2H_2 + CH_4$	$a = 3.4\times10^{-11}$, $b = 0.0$, $E_a = 0.0$	[103]
C_{22}	$CH_3 + C_2H_4 \rightarrow C_2H_3 + CH_4$	$a = 6.9\times10^{-11}$, $b = 0.0$, $E_a = 5600.0$	[29, 218]
C_{23}	$CH_3 + C_2H_6 \rightarrow C_2H_5 + CH_4$	$a = 2.45\times10^{-31}$, $b = 6.0$, $E_a = 3043.0$	[29, 218]
C_{24}	$C_2H_5 + H \rightarrow 2\ CH_3$	$a = 1.25\times10^{-10}$, $b = 0.0$, $E_a = 0.0$	[203]
C_{25}	$C_2H_5 + H \rightarrow C_2H_4 + H_2$	$a = 3.0\times10^{-12}$, $b = 0.0$, $E_a = 0.0$	[203]

C.4 Three-body reactions

The three-body reactions in the reaction network largely come from Egert et al., (2017) [101] originally compiled from multiple sources. These reactions can be dependent on background pressure and the total rate can be a contribution of their low-pressure (k_0) and high-pressure (k_∞) rate expressions given by the following equation [172].

$$k(T,[M]) = \frac{k_0[M]}{1+\frac{k_0[M]}{k_\infty}} \tag{C.1}$$

Here, k is the forward reaction rate. The rate approaches k_0 [M] in the low-pressure limit, and it approaches k_∞ in the high-pressure limit. Each reaction rate has been expressed in a temperature-dependent Arrhenius rate format:

$$k = A(\frac{T}{T_0})^b e^{\frac{-E_a}{T}} \tag{C.2}$$

where A is pre-exponential factor, T_0 is a reference temperature, b is the temperature exponent, and E_a is the activation energy of the reaction. For all the tables given below, E_a is expressed in Kelvin and the rate coefficient k is expressed in c.g.s. units. The list of three-body reactions are stored in Table C.4.

Table C.4: List of three-body reactions

Index	**Equation**	**k$_0$**	**k$_\infty$**	**Rate expression**
T_1	H + CH_3 (+ M) → CH_4 (+ M)	a = 5.8×10^{-29}, b = 0.0, E_a = -355.0	a = 2.37×10^{-12}, b = 0.0, E_a = -523.0	[11]
T_2	H + $^3CH_2$ (+ M) → CH_3 (+ M)	a = 5.8×10^{-30}, b = 0.0, E_a = -355.0	a = 2.37×10^{-12}, b = 0.0, E_a = -523.0	[114]
T_3	H + C_2H_2 (+ M) → C_2H_3 (+ M)	a = 2.6×10^{-31}, b = 0.0, E_a = 0.0	a = 3.8×10^{-11}, b = 0.0, E_a = 1374.0	[232]
T_4	H + C_2H_3 (+ M) → C_2H_2 + H_2 (+ M)	a = 1.49×10^{-27}, b = 0.0, E_a = 0.0	a = 1.55×10^{-10}, b = 0.0, E_a = 0.0	[231]
T_5	H + C_2H_4 (+ M) → C_2H_5 (+ M)	a = 2.15×10^{-29}, b = 0.0, E_a = 349.0	a = 4.95×10^{-11}, b = 0.0, E_a = 1051.0	[232]

Continued on next page

Index	**Equation**	**k$_0$**	**k$_\infty$**	**Rate expression**
T_6	H_2 + CH (+ M) $\rightarrow$ CH_3 (+ M)	a = 4.7×10^{-26}, T_0 = 1, b = -1.6, E_a = 0.0	a = 2.5×10^{-10}, T_0 = 1 , b = -0.08, E_a = 0.0	[57]
T_7	H_2 + CH + M $\rightarrow$ $^1CH_2$ + H + M	a = 2.38×10^{-11},T_0 = 1, b = 0.0, E_a = 1760.0	-	[293]
T_8	H_2 + C_2H_3 + M $\rightarrow$ C_2H_4 + H + M	a = 5.0×10^{-20},T_0 = 1, b = 2.63, E_a = 4298.0	-	[231]
T_9	CH + CH_4 + M $\rightarrow$ C_2H_4 + H + M	a = 2.5×10^{-11}, b = 0.0, E_a = 200.0	-	[293]
T_{10}	2 CH_3 (+ M) $\rightarrow$ C_2H_6 (+ M)	a = 2.22×10^{-16}, T_0 = 1, b = -3.75, E_a = 494.0	a = 3.78×10^{-9}, T_0 = 1, b = -0.69, E_a = 88.0	[278]
T_{11}	CH_3 + C_2H_3 + M $\rightarrow$ C_3H_6 + M	a = 1.1×10^{-28}, T_0 = 1, b = 8.52, E_a = -1248.0	-	[114]
T_{12}	C + H_2 + M $\rightarrow$ $^3CH_2$	a = 7.0×10^{-32}, T_0 = 1, b = 0.0, E_a = 0.0	a = 2.06×10^{-11}, T_0 = 1 , b = 0.0, E_a = 57.0	[203]
T_{13}	2 C_2H_3 + M $\rightarrow$ C_2H_4 + C_2H_2 + M	a = 2.4×10^{-11}, b = 0.0, E_a = 0.0	-	[293]
T_{14}	2 H + M $\rightarrow$ H_2 + M	a = 2.7×10^{-31}, T_0 = 1, b = -0.6, E_a = 0.0	-	[29, 218]

C.5 Ion-neutral reactions

The volume of reactions involving ionic species and their interactions with neutrals and electrons are largely borrowed from existing literature on gas giant ionospheric chemistry. Table C.5 compiles the reactions and the corresponding rate coefficients. Generally, the rate expressions are a function of local electron temperature (T_e) within the Arrhenius rate form. We assume an equilibrium condition where T_e is equal to the neutral temperature (T).

Table C.5: List of ion-neutral and electron recombination reactions

Index	**Equation**	**k**	**Rate expression**
C_1	$H_2^+ + H_2 \rightarrow H_3^+ + H$	a = 1.72×10^{-9}, b = 0.0, E_a = 0.0	[198]
C_2	$H_2^+ + e^- \rightarrow 2\,H$	a = 2.25×10^{-6}, T_0 = 1, b = -0.4, E_a = 0.0	[199]
C_3	$H_3^+ + e^- \rightarrow H_2 + H$	a = 4.932×10^{-8}, T_0 = 300, b = -1.0, E_a = 0.0	[117, 192]
C_4	$H_3^+ + e^- \rightarrow 3\,H$	a = 8.768×10^{-8}, T_0 = 300, b = -1.0, E_a = 0.0	[117, 192]
C_5	$H_3^+ + He \rightarrow HeH^+ + H_2$	a = 3.0×10^{-12}, b = 0.0, E_a = 0.0	[15]
C_6	$H_2^+ + H \rightarrow H^+ + H_2$	a = 6.4×10^{-10}, b = 0.0, E_a = 0.0	[12]
C_7	$H^+ + CH_4 \rightarrow CH_3^+ + H_2$	a = 3.403×10^{-9}, b = 0.0, E_a = 0.0	[13]
C_8	$H^+ + CH_4 \rightarrow CH_4^+ + H$	a = 7.47×10^{-10}, b = 0.0, E_a = 0.0	[13]
C_9	$H_3^+ + CH_4 \rightarrow CH_5^+ + H_2$	a = 2.4×10^{-9}, b = 0.0, E_a = 0.0	[224]
C_{10}	$H^+ + e^- \rightarrow H$	a = 1.66×10^{-10}, T_0 = 1, b = -0.64, E_a = 0.0	[197]

Continued on next page

Index	**Equation**	**k**	**Rate expression**
C_{11}	$H_2^+ + CH_4 \rightarrow CH_5^+ + H$	a = 1.1×10^{-10}, b = 0.0, E_a = 0.0	[157]
C_{12}	$H_2^+ + CH_4 \rightarrow CH_4^+ + H_2$	a = 1.41×10^{-9}, b = 0.0, E_a = 0.0	[157]
C_{13}	$H_2^+ + CH_4 \rightarrow CH_3^+ + H + H_2$	a = 2.28×10^{-9}, b = 0.0, E_a = 0.0	[157]
C_{14}	$CH_4^+ + e^- \rightarrow CH_3 + H$	a = 6.09×10^{-8}, T_0 = 300, b = -0.53, E_a = 0.0	[247, 226]
C_{15}	$CH_4^+ + e^- \rightarrow CH_2 + 2\ H$	a = 1.247×10^{-7}, T_0 = 300, b = -0.53, E_a = 0.0	[247, 226]
C_{16}	$CH_4^+ + e^- \rightarrow CH_2 + H_2$	a = 2.61×10^{-8}, T_0 = 300, b = -0.53, E_a = 0.0	[247, 226]
C_{17}	$CH_4^+ + e^- \rightarrow CH + H_2 + H$	a = 7.25×10^{-8}, T_0 = 300, b = -0.53, E_a = 0.0	[247, 226]
C_{18}	$CH_4^+ + e^- \rightarrow C + 2\ H_2$	a = 5.8×10^{-9}, T_0 = 300, b = -0.53, E_a = 0.0	[247, 226]
C_{19}	$CH_5^+ + e^- \rightarrow CH_4 + H$	a = 1.45×10^{-8}, T_0 = 300, b = -0.46, E_a = 0.0	[245, 247]
C_{20}	$CH_5^+ + e^- \rightarrow CH_3 + H_2$	a = 1.45×10^{-8}, T_0 = 300, b = -0.46, E_a = 0.0	[245, 247]
C_{21}	$CH_5^+ + e^- \rightarrow CH_3 + 2\ H$	a = 2.03×10^{-7}, T_0 = 300, b = -0.46, E_a = 0.0	[245, 247]

Continued on next page

Index	Equation	k	Rate expression
C_{22}	$CH_5^+ + e^- \rightarrow CH_2 + H_2 + H$	a = 5.22×10^{-8}, T_0 = 300, b = -0.46, E_a = 0.0	[245, 247]
C_{23}	$CH_5^+ + e^- \rightarrow CH + 2\,H_2$	a = 8.7×10^{-9}, T_0 = 300, b = -0.46, E_a = 0.0	[245, 247]
C_{24}	$CH_3^+ + e^- \rightarrow CH_2 + H$	a = 1.28×10^{-7}, T_0 = 300, b = -0.53, E_a = 0.0	[247]
C_{25}	$CH_3^+ + e^- \rightarrow CH + H_2$	a = 4.48×10^{-8}, T_0 = 300, b = -0.53, E_a = 0.0	[247]
C_{26}	$CH_3^+ + e^- \rightarrow CH + H$	a = 5.12×10^{-8}, T_0 = 300, b = -0.53, E_a = 0.0	[247]
C_{27}	$CH_3^+ + e^- \rightarrow C + H_2 + H$	a = 9.6×10^{-8}, T_0 = 300, b = -0.53, E_a = 0.0	[247]
C_{28}	$He^+ + e^- \rightarrow He$	a = 1.77×10^{-10}, T_0 = 1, b = -0.65, E_a = 0.0	[197]
C_{29}	$HeH^+ + e^- \rightarrow He + H$	a = 3.06×10^{-7}, T_0 = 1.0, b = -0.6, E_a = 0.0	[292]
C_{30}	$HeH^+ + C_2H_6 \rightarrow C_2H_5^+ + He + H_2$	a = 2.1×10^{-9}, b = 0.0, E_a = 0.0	[180]
C_{31}	$CH_5^+ + C_2H_4 \rightarrow C_2H_5^+ + CH_4$	a = 1.5×10^{-9}, b = 0.0, E_a = 0.0	[106]
C_{32}	$CH_5^+ + C_2H_6 \rightarrow C_2H_5^+ + CH_4 + H_2$	a = 1.215×10^{-9}, b = 0.0, E_a = 0.0	[13]

Continued on next page

Index	**Equation**	**k**	**Rate expression**
C_{33}	$CH_3^+ + CH_4 \rightarrow C_2H_5^+ + H_2$	a = 1.1×10^{-9}, b = 0.0, E_a = 0.0	[14]
C_{34}	$C_2H_5^+ + e^- \rightarrow C_2H_4 + H$	a = 7.2×10^{-8}, T_0 = 300, b = -0.5, E_a = 0.0	[163, 226]
C_{35}	$C_2H_5^+ + e^- \rightarrow C_2H_3 + H_2$	a = 3.6×10^{-8}, T_0 = 300, b = -0.5, E_a = 0.0	[163, 226]
C_{36}	$C_2H_5^+ + e^- \rightarrow C_2H_3 + 2\ H$	a = 2.82×10^{-7}, T_0 = 300, b = -0.5, E_a = 0.0	[163, 226]
C_{37}	$C_2H_5^+ + e^- \rightarrow C_2H_2 + H_2 + H$	a = 7.2×10^{-8}, T_0 = 300, b = -0.5, E_a = 0.0	[163, 226]
C_{38}	$C_2H_5^+ + e^- \rightarrow C_2H_2 + 3\ H$	a = 3.6×10^{-8}, T_0 = 300, b = -0.5, E_a = 0.0	[163, 226]
C_{39}	$C_2H_5^+ + e^- \rightarrow CH_4 + CH$	a = 1.2×10^{-8}, T_0 = 300, b = -0.53, E_a = 0.0	[163, 226]
C_{40}	$C_2H_5^+ + e^- \rightarrow CH_3 + CH_2$	a = 9.0×10^{-8}, T_0 = 300, b = -0.5, E_a = 0.0	[163, 226]

C.6 Hydrogen vibrational excitation

The vibrational states of molecular hydrogen (ν = 1-8) using a system of reactions based on collisional excitation and electron impact dissociative recombination. Reaction rates corresponding to the following set of reactions (Table C.6) are derived from a combination of theory and laboratory experiments.

Table C.6: List of hydrogen vibrational excitation reactions

Index	**Equation**	**Rate expression**
V_1	H_2 + e^-_{cr} $\rightarrow$ $H_2(\nu)$ + e^-_{cr}	[276, 101]
V_2	2 H + H_2 $\rightarrow$ $H_2(\nu)$ + H_2	[80]
V_3	H^+ + $H_2(\nu)$ $\rightarrow$ H_2^+ + H	[145, 101]
V_4	H_3^+ + e^- $\rightarrow$ $H_2(\nu)$ + H	[80, 107]
V_5	$H_2(\nu)$ + H $\rightarrow$ $H_2(\nu - 1)$ + H	[61, 80]
V_6	H^+ + $H_2(\nu)$ $\rightarrow$ H^+ + $H_2(\nu - 1)$	[101]
V_7	H_2 + $H_2(\nu)$ $\leftrightarrow$ H_2 + $H_2(\nu - 1)$	[23, 250]
V_8	$H_2(\nu)$ + H_2(w) $\leftrightarrow$ $H_2(\nu - 1)$ + H_2(w+1)	[42, 119]

BIBLIOGRAPHY

[1] N Achilleos, S Miller, R Prangé, G Millward, and MK Dougherty. A dynamical model of jupiter's auroral electrojet. *New Journal of Physics*, 3(1):303, 2001.

[2] N Achilleos, S Miller, J Tennyson, AD Aylward, I Mueller-Wodarg, and D Rees. Jim: A time-dependent, three-dimensional model of jupiter's thermosphere and ionosphere. *Journal of Geophysical Research: Planets*, 103(E9):20089–20112, 1998.

[3] Alberto Adriani, Alessandro Mura, ML Moriconi, BM Dinelli, F Fabiano, Francesca Altieri, G Sindoni, SJ Bolton, JEP Connerney, SK Atreya, et al. Preliminary jiram results from juno polar observations: 2. analysis of the jupiter southern h3+ emissions and comparison with the north aurora. *Geophysical Research Letters*, 44(10):4633–4640, 2017.

[4] Virgil Adumitroaie, Steven M Levin, Daniel Santos Costa, Samuel Gulkis, and Michael A Janssen. Towards a fast background radiation subtraction technique for the juno mission. In *2016 IEEE Aerospace Conference*, pages 1–11. IEEE, 2016.

[5] Yury S Aglyamov, Sushil K Atreya, Ananyo Bhattacharya, Cheng Li, Steven Levin, Scott J Bolton, and Michael H Wong. Alkali metal depletion in the deep jovian atmosphere: The role of anions. *Icarus*, 425:116334, 2025.

[6] Yury S Aglyamov, Jonathan Lunine, Heidi N Becker, Tristan Guillot, Seran G Gibbard, Sushil Atreya, Scott J Bolton, Steven Levin, Shannon T Brown, and Michael H Wong. Lightning generation in moist convective clouds and constraints on the water abundance in jupiter. *Journal of Geophysical Research: Planets*, 126(2):e2020JE006504, 2021.

[7] Joseph Ajello, Donald Shemansky, Wayne Pryor, Kent Tobiska, Charles Hord, Stuart Stephens, Ian Stewart, John Clarke, Karen Simmons, William McClintock, et al. Galileo orbiter ultraviolet observations of jupiter aurora. *Journal of Geophysical Research: Planets*, 103(E9):20125–20148, 1998.

[8] Joseph M Ajello, Donald E Shemansky, Wayne R Pryor, A Ian Stewart, Karen E Simmons, Tariq Majeed, J Hunter Waite, G Randy Gladstone, and Denis Grodent. Spectroscopic evidence for high-altitude aurora at jupiter from galileo extreme ultraviolet spectrometer and hopkins ultraviolet telescope observations. *Icarus*, 152(1):151–171, 2001.

[9] Nicole F Allard, Fernand Spiegelman, and JF Kielkopf. K–h2 line shapes for the spectra of cool brown dwarfs. *Astronomy & Astrophysics*, 589:A21, 2016.

[10] Nicole F Allard, Fernand Spiegelman, Thierry Leininger, and P Molliere. New study of the line profiles of sodium perturbed by h2. *Astronomy & Astrophysics*, 628:A120, 2019.

[11] Mark Allen, Yuk L Yung, and G Randall Gladstone. The relative abundance of ethane to acetylene in the jovian stratosphere. *Icarus*, 100(2):527–533, 1992.

[12] V Anicich, WT Huntress, et al. An ion cyclotron resonance study of reactions of ions with hydrogen atomsa. *The Journal of Chemical Physics*, 70(6):2877–2881, 1979.

[13] Vincent G Anicich. Evaluated bimolecular ion-molecule gas phase kinetics of positive ions for use in modeling planetary atmospheres, cometary comae, and interstellar clouds. *Journal of Physical and Chemical Reference Data*, 22(6):1469–1569, 1993.

[14] Vincent G Anicich, Paul Wilson, and Murray J McEwan. Termolecular ion-molecule reactions in titan's atmosphere. iv. a search made at up to 1 micron in pure hydrocarbons. *Journal of the American Society for Mass Spectrometry*, 14(8):900–915, 2003.

[15] VINCENZO Aquilanti, ANDREA Galli, ANNA Giardini-Guidoni, and GIAN GUALBERTO Volpi. Ion—molecule reactions in hydrogen—rare-gas mixtures. *The Journal of Chemical Physics*, 43(6):1969–1973, 1965.

[16] Martin Asplund, Nicolas Grevesse, A Jacques Sauval, and Pat Scott. The chemical composition of the sun. *Annual review of astronomy and astrophysics*, 47:481–522, 2009.

[17] SK Atreya and TM Donahue. Ionospheric models of saturn, uranus, and neptune. *Icarus*, 24(3):358–362, 1975.

[18] SK Atreya and PN Romani. Photochemistry and clouds of jupiter, saturn and uranus. *Recent advances in planetary meteorology*, 17:68, 1985.

[19] SK Atreya, MH Wong, TC Owen, PR Mahaffy, HB Niemann, I De Pater, P Drossart, and Th Encrenaz. A comparison of the atmospheres of jupiter and saturn: deep atmospheric composition, cloud structure, vertical mixing, and origin. *Planetary and Space Science*, 47(10-11):1243–1262, 1999.

[20] Sushil K Atreya, Aurélien Crida, Tristan Guillot, Jonathan I Lunine, Nikku Madhusudhan, and Olivier Mousis. The origin and evolution of saturn, with exoplanet perspective, in "saturn in the 21st century", (eds. baines k. h. et al.), pp. 5-43, 2019.

[21] Sushil K Atreya and Thomas M Donahue. The role of hydrocarbons in the lonospheres of the outer planets. *Icarus*, 25(2):335–338, 1975.

[22] Sushil K Atreya, Mark H Hofstadter, Joong Hyun In, Olivier Mousis, Kim Reh, and Michael H Wong. Deep atmosphere composition, structure, origin, and exploration, with particular focus on critical in situ science at the icy giants. *Space Science Reviews*, 216:1–31, 2020.

[23] M-M Audibert, C Joffrin, and J Ducuing. Vibrational relaxation in hydrogen-rare-gases mixtures. *Chemical Physics Letters*, 19(1):26–28, 1973.

[24] Fran Bagenal and Vincent Dols. The space environment of io and europa. *Journal of Geophysical Research: Space Physics*, 125(5):e2019JA027485, 2020.

[25] Peter Banks. Collision frequencies and energy transfer electrons. *Planetary and Space Science*, 14(11):1085–1103, 1966.

[26] FT Barath, AH Barrett, J Copeland, DE Jones, and AE Lilley. Mariner ii: Preliminary reports on measurements of venus: Microwave radiometers. *Science*, 139(3558):908–909, 1963.

[27] Stephen S Barshay and John S Lewis. Chemical structure of the deep atmosphere of jupiter. *Icarus*, 33(3):593–611, 1978.

[28] D Baulch, J Cobos, A Cox, P Frank, G Hayman, Th Just, T Murrells, J Pilling, J Troe, R Walker, et al. Summary table of evaluated kinetic data for combustion modelling: Supplement 1. *Combustion and Flame 98 (1994), pp. 59-79*, 1994.

[29] DL Baulch, CJal Cobos, RA Cox, C Esser, P Frank, Th Just, JA Kerr, MJ Pilling, J Troe, RW Walker, et al. Evaluated kinetic data for combustion modelling. 1992.

[30] Heidi N Becker, James W Alexander, Sushil K Atreya, Scott J Bolton, Martin J Brennan, Shannon T Brown, Alexandre Guillaume, Tristan Guillot, Andrew P Ingersoll, Steven M Levin, et al. Small lightning flashes from shallow electrical storms on jupiter. *Nature*, 584(7819):55–58, 2020.

[31] KH Becker, B Engelhardt, P Wiesen, and KD Bayes. Rate constants for ch (x 2π) reactions at low total pressures. *Chemical physics letters*, 154(4):342–348, 1989.

[32] Amadeo Bellotti, Paul G Steffes, and Garrett Chinsomboom. Laboratory measurements of the 5–20 cm wavelength opacity of ammonia, water vapor, and methane under simulated conditions for the deep jovian atmosphere. *Icarus*, 280:255–267, 2016.

[33] B Benmahi, B Bonfond, B Benne, D Grodent, V Hue, GR Gladstone, G Gronoff, J Lilensten, G Sicorello, LA Head, et al. Energy mapping of jupiter's auroral electrons from juno/uvs data using a new h2 uv emission model. *Astronomy & Astrophysics*, 685:A26, 2024.

[34] Steven Berline and Clark Bricker. The law of mass action. *Journal of Chemical Education*, 46(8):499, 1969.

[35] Michael R Berman, JW Fleming, AB Harvey, and Ming-Chang Lin. Temterature dependence of the reactions of ch radicals with unsaturated hydrocarbons. *Chemical physics*, 73(1-2):27–33, 1982.

[36] Bruno Bézard, Emmanuel Lellouch, Darrell Strobel, Jean-Pierre Maillard, and Pierre Drossart. Carbon monoxide on jupiter: Evidence for both internal and external sources. *Icarus*, 159(1):95–111, 2002.

[37] Anil Bhardwaj, CH Ishwara-Chandra, N Udaya Shankar, Hiroaki Misawa, Kota Imai, Yoshizumi Miyoshi, Fuminori Tsuchiya, Tetsuro Kondo, and Akira Morioka. Gmrt observations of jupiter's synchrotron radio emission at 610 mhz. In *The Low-Frequency Radio Universe*, volume 407, page 369, 2009.

[38] Ananyo Bhattacharya, Cheng Li, Sushil K Atreya, Paul G Steffes, Steven M Levin, Scott J Bolton, Tristan Guillot, Pranika Gupta, Andrew P Ingersoll, Jonathan I Lunine, et al. Harp radiation package for planetary atmospheres. *Zenodo*, 2023.

[39] Ananyo Bhattacharya, Cheng Li, Sushil K Atreya, Paul G Steffes, Steven M Levin, Scott J Bolton, Tristan Guillot, Pranika Gupta, Andrew P Ingersoll, Jonathan I Lunine, et al. Highly depleted alkali metals in jupiter's deep atmosphere. *The Astrophysical Journal Letters*, 952(2):L27, 2023.

[40] Ananyo Bhattacharya, J Hunter Waite, Steven M Levin, Fabiano A Oyafuso, Paul G Steffes, Yue Lu, G Randall Gladstone, Joshua Kammer, Tom A Nordheim, Chris Paranicas, et al. Jupiter's auroral ionosphere: Juno microwave radiometer observations of energetic electron precipitation events. *Authorea Preprints*, 2024.

[41] EK Bigg. Influence of the satellite i o on jupiter's decametric emission. *Nature*, 203(4949):1008–1010, 1964.

[42] Gert Due Billing and Edward R Fisher. Vv and vt rate coefficients in h2 by a quantum-classical model. *Chemical Physics*, 18(1-2):225–232, 1976.

[43] Thomas Böhland, Friedrich Temps, and H Gg Wagner. The contributions of intersystem crossing and reaction in the removal of ch2 (ã1a1) by hydrocarbons studied with the lmr. *Berichte der Bunsengesellschaft für physikalische Chemie*, 89(9):1013–1018, 1985.

[44] SJ Bolton, S Gulkis, MJ Klein, I De Pater, and TJ Thompson. Correlation studies between solar wind parameters and the decimetric radio emission from jupiter. *Journal of Geophysical Research: Space Physics*, 94(A1):121–128, 1989.

[45] SJ Bolton, M Janssen, R Thorne, S Levin, M Klein, S Gulkis, T Bastian, R Sault, C Elachi, M Hofstadter, et al. Ultra-relativistic electrons in jupiter's radiation belts. *Nature*, 415(6875):987–991, 2002.

[46] Bertrand Bonfond, GR Gladstone, Denis Grodent, J-C Gérard, TK Greathouse, V Hue, JA Kammer, MH Versteeg, MW Davis, HN Becker, et al. Bar code events in the juno-uvs data: Signature 10 mev electron microbursts at jupiter. *Geophysical Research Letters*, 45(22):12–108, 2018.

[47] Bertrand Bonfond, J Saur, Denis Grodent, SV Badman, D Bisikalo, V Shematovich, J-C Gérard, and Aikaterini Radioti. The tails of the satellite auroral footprints at jupiter. *Journal of Geophysical Research: Space Physics*, 122(8):7985–7996, 2017.

[48] Alan P Boss. Giant planet formation by gravitational instability. *Science*, 276(5320):1836–1839, 1997.

[49] Alan P Boss. Gas giant protoplanet formation: Disk instability models with thermodynamics and radiative transfer. *The Astrophysical Journal*, 563(1):367, 2001.

[50] SW Bougher, JH Waite Jr, Tariq Majeed, and G Randy Gladstone. Jupiter thermospheric general circulation model (jtgcm): Global structure and dynamics driven by auroral and joule heating. *Journal of Geophysical Research: Planets*, 110(E4), 2005.

[51] G Branduardi-Raymont, Ronald F Elsner, M Galand, Denis Grodent, TE Cravens, P Ford, GR Gladstone, and JH Waite Jr. Spectral morphology of the x-ray emission from jupiter's aurorae. *Journal of Geophysical Research: Space Physics*, 113(A2), 2008.

[52] Graziella Branduardi-Raymont, A Bhardwaj, RF Elsner, GR Gladstone, G Ramsay, P Rodriguez, Roberto Soria, JH Waite, and TE Cravens. A study of jupiter's aurorae with xmm-newton. *Astronomy & Astrophysics*, 463(2):761–774, 2007.

[53] Franklin H Briggs and Penny D Sackett. Radio observations of saturn as a probe of its atmosphere and cloud structure. *Icarus*, 80(1):77–103, 1989.

[54] AL Broadfoot, MJS Belton, PZ Takacs, BR Sandel, DE Shemansky, JB Holberg, JM Ajello, SK Atreya, TM Donahue, HW Moos, et al. Extreme ultraviolet observations from voyager 1 encounter with jupiter. *Science*, 204(4396):979–982, 1979.

[55] AL Broadfoot, BR Sandel, DE Shemansky, JC McConnell, GR Smith, JB Holberg, SK Atreya, TM Donahue, DF Strobel, and JL Bertaux. Overview of the voyager ultraviolet spectrometry results through jupiter encounter. *Journal of Geophysical Research: Space Physics*, 86(A10):8259–8284, 1981.

[56] Shannon Brown, Michael Janssen, Virgil Adumitroaie, Sushil Atreya, Scott Bolton, Samuel Gulkis, Andrew Ingersoll, Steven Levin, Cheng Li, Liming Li, et al. Prevalent lightning sferics at 600 megahertz near jupiter's poles. *Nature*, 558(7708):87–90, 2018.

[57] Richard A Brownsword, André Canosa, Bertrand R Rowe, Ian R Sims, Ian WM Smith, David WA Stewart, Andrew C Symonds, and Daniel Travers. Kinetics over a wide range of temperature (13–744 k): Rate constants for the reactions of ch (ν= 0) with h2 and d2 and for the removal of ch (ν= 1) by h2 and d2. *The Journal of chemical physics*, 106(18):7662–7677, 1997.

[58] Alexander Burcat and Branko Ruscic. Third millenium ideal gas and condensed phase thermochemical database for combustion (with update from active thermochemical tables). Technical report, Argonne National Lab.(ANL), Argonne, IL (United States), 2005.

[59] Bernard F Burke and Kenneth L Franklin. Observations of a variable radio source associated with the planet jupiter. *Journal of Geophysical Research*, 60(2):213–217, 1955.

[60] Adam Burrows, MS Marley, and CM Sharp. The near-infrared and optical spectra of methane dwarfs and brown dwarfs. *The Astrophysical Journal*, 531(1):438, 2000.

[61] M Cacciatore, M Capitelli, and M Dilonardo. A joint vibro-electronic mechanism in the dissociation of molecular hydrogen in nonequilibrium plasmas. *Chemical Physics*, 34(2):193–204, 1978.

[62] John Caldwell, Rangasayi Halthore, Glenn Orton, and Jay Bergstralh. Infrared polar brightenings on jupiter: Iv. spatial properties of methane emission. *Icarus*, 74(2):331–339, 1988.

[63] John Caldwell, AT Tokunaga, and FC Gillett. Possible infrared aurorae on jupiter. *Icarus*, 44(3):667–675, 1980.

[64] André Canosa, Ian R Sims, Daniel Travers, Ian WM Smith, and BR Rowe. Reactions of the methylidine radical with ch_4_, c_2_h_2_, c_2_h_4_, c_2_h_6_, and but-1-ene studied between 23 and 295k with a cresu apparatus. *Astronomy and Astrophysics, v. 323, p. 644-651*, 323:644–651, 1997.

[65] TD Carr, MD Desch, and JK Alexander. Physics of the jovian magnetosphere, ed. *AJ Dessler, Cambridge University Press, Cambridge*, pages 226–284, 1983.

[66] T Cavalié, J Lunine, and O Mousis. A subsolar oxygen abundance or a radiative region deep in jupiter revealed by thermochemical modelling. *Nature Astronomy*, pages 1–6, 2023.

[67] T Cavalié, L Rezac, R Moreno, E Lellouch, T Fouchet, Bilal Benmahi, TK Greathouse, JA Sinclair, V Hue, P Hartogh, et al. Evidence for auroral influence on jupiter's nitrogen and oxygen chemistry revealed by alma. *Nature Astronomy*, 7(9):1048–1055, 2023.

[68] Malcolm W Chase. Nist-janaf thermochemical tables 4th ed. *J. of Physical and Chemical Reffernce Data*, pages 1529–1564, 1998.

[69] MW Chase Jr, JL Curnutt, JR Downey Jr, RA McDonald, AN Syverud, and EA Valenzuela. Janaf thermochemical tables, 1982 supplement. *Journal of Physical and Chemical Reference Data*, 11(3):695–940, 1982.

[70] Guo Chen, Hongchi Wang, Roy van Boekel, and Enric Pallé. Detection of na and k in the atmosphere of the hot jupiter hat-p-1b with p200/dbsp. *The Astronomical Journal*, 164(5):173, 2022.

[71] Ulrich R Christensen and Paula N Wulff. Quenching of zonal winds in jupiter's interior. *Proceedings of the National Academy of Sciences*, 121(25):e2402859121, 2024.

[72] Jessie L Christiansen. Five thousand exoplanets at the nasa exoplanet archive. *Nature Astronomy*, 6(5):516–519, 2022.

[73] G Clark, Chihiro Tao, BH Mauk, J Nichols, J Saur, EJ Bunce, F Allegrini, R Gladstone, F Bagenal, S Bolton, et al. Precipitating electron energy flux and characteristic energies in jupiter's main auroral region as measured by juno/jedi. *Journal of Geophysical Research: Space Physics*, 123(9):7554–7567, 2018.

[74] John T Clarke, Gilda E Ballester, John Trauger, Robin Evans, J EP Connerney, Karl Stapelfeldt, David Crisp, Paul D Feldman, Christopher J Burrows, Stefano Casertano, et al. Far-ultraviolet imaging of jupiter's aurora and the io "footprint". *Science*, 274(5286):404–409, 1996.

[75] John T Clarke, Denis Grodent, Stan WH Cowley, Emma J Bunce, Philippe Zarka, John EP Connerney, and Takehiko Satoh. Jupiter's aurora. *Jupiter: The planet, satellites and magnetosphere*, 1:639–670, 2004.

[76] MAA Clyne and DH Stedman. Reactions of atomic hydrogen with hydrogen chloride and nitrosyl chloride. *Transactions of the Faraday Society*, 62:2164–2174, 1966.

[77] Andreas Colliander, Mohammad Mousavi, Shawn Marshall, Samira Samimi, John S Kimball, Julie Z Miller, Joel Johnson, and Mariko Burgin. Ice sheet surface and subsurface melt water discrimination using multi-frequency microwave radiometry. *Geophysical Research Letters*, 49(4):e2021GL096599, 2022.

[78] JEP Connerney, S Kotsiaros, RJ Oliversen, JR Espley, John Leif Joergensen, PS Joergensen, José MG Merayo, Matija Herceg, J Bloxham, KM Moore, et al. A new model of jupiter's magnetic field from juno's first nine orbits. *Geophysical Research Letters*, 45(6):2590–2596, 2018.

[79] JEP Connerney, S Timmins, RJ Oliversen, JR Espley, JL Joergensen, S Kotsiaros, PS Joergensen, JMG Merayo, M Herceg, J Bloxham, et al. A new model of jupiter's magnetic field at the completion of juno's prime mission. *Journal of Geophysical Research: Planets*, 127(2):e2021JE007055, 2022.

[80] TE Cravens. Vibrationally excited molecular hydrogen in the upper atmosphere of jupiter. *Journal of Geophysical Research: Space Physics*, 92(A10):11083–11100, 1987.

[81] TE Cravens, E Howell, JH Waite Jr, and GR Gladstone. Auroral oxygen precipitation at jupiter. *Journal of Geophysical Research: Space Physics*, 100(A9):17153–17161, 1995.

[82] Ashley Gerard Davies. Volcanism on io: Estimation of eruption parameters from galileo nims data. *Journal of Geophysical Research: Planets*, 108(E9), 2003.

[83] Virginie de La Haye, JH Waite Jr, TE Cravens, IP Robertson, and Sébastien Lebonnois. Coupled ion and neutral rotating model of titan's upper atmosphere. *Icarus*, 197(1):110–136, 2008.

[84] Imke De Pater. The significance of microwave observations for the planets. *Physics Reports*, 200(1):1–50, 1991.

[85] Imke de Pater and David E Dunn. Vla observations of jupiter's synchrotron radiation at 15 and 22 ghz. *Icarus*, 163(2):449–455, 2003.

[86] Imke de Pater and RJ Sault. An intercomparison of three-dimensional reconstruction techniques using data and models of jupiter's synchrotron radiation. *Journal of Geophysical Research: Planets*, 103(E9):19973–19984, 1998.

[87] Imke De Pater, RJ Sault, Bryan Butler, David DeBoer, and Michael H Wong. Peering through jupiter's clouds with radio spectral imaging. *Science*, 352(6290):1198–1201, 2016.

[88] Imke de Pater, RJ Sault, Michael H Wong, Leigh N Fletcher, David DeBoer, and Bryan Butler. Jupiter's ammonia distribution derived from vla maps at 3–37 ghz. *Icarus*, 322:168–191, 2019.

[89] PA Delamere, RJ Wilson, S Wing, AR Smith, B Mino, C Spitler, P Damiano, K Sorathia, A Sciola, J Caggiano, et al. Signatures of open magnetic flux in jupiter's dawnside magnetotail. *AGU Advances*, 5(2):e2023AV001111, 2024.

[90] Brice-Olivier Demory, Sara Seager, Nikku Madhusudhan, Hans Kjeldsen, Jørgen Christensen-Dalsgaard, Michaël Gillon, Jason F Rowe, William F Welsh, Elisabeth R Adams, Andrea Dupree, et al. The high albedo of the hot jupiter kepler-7 b. *The Astrophysical Journal Letters*, 735(1):L12, 2011.

[91] Troelz Denver, Julia Sushkova, John L Jørgensen, Leonardo Ghizoni, Matija Herceg, Christina Toldbo, Mathias Benn, Peter S Jørgensen, René Fléron, JEP Connerney, et al. The juno asc as an energetic particle counter. *Space Science Reviews*, 220(8):1–18, 2024.

[92] Laurent Desorgher, ERWIN O Flückiger, and Maria Gurtner. The planetocosmics geant4 application. In *36th COSPAR Scientific Assembly*, volume 36, page 2361, 2006.

[93] Kiruthika Devaraj, Paul G Steffes, and Danny Duong. The centimeter-wavelength opacity of ammonia under deep jovian conditions. *Icarus*, 241:165–179, 2014.

[94] Robert H Dicke, Robert Beringer, Robert L Kyhl, and AB Vane. Atmospheric absorption measurements with a microwave radiometer. *Physical Review*, 70(5-6):340, 1946.

[95] BM Dinelli, Alberto Adriani, Alessandro Mura, FRANCESCA Altieri, Alessandra Migliorini, and ML Moriconi. Juno/jiram's view of jupiter's h3+ emissions. *Philosophical transactions of the Royal Society A*, 377(2154):20180406, 2019.

[96] Timothy E Dowling and Andrew P Ingersoll. Jupiter's great red spot as a shallow water system. *Journal of Atmospheric Sciences*, 46(21):3256–3278, 1989.

[97] P Drossart, Th Encrenaz, V Kunde, R Hanel, and M Combes. An estimate of the ph3, ch3d, and geh4 abundances on jupiter from the voyager iris data at 4.5 μm. *Icarus*, 49(3):416–426, 1982.

[98] Pierre Drossart, Bruno Bézard, Sushil K Atreya, James Bishop, JH Waite Jr, and D Boice. Thermal profiles in the auroral regions of jupiter. *Journal of Geophysical Research: Planets*, 98(E10):18803–18811, 1993.

[99] WR Dunn, G Branduardi-Raymont, LC Ray, CM Jackman, RP Kraft, RF Elsner, IJ Rae, Zhonghua Yao, MF Vogt, GH Jones, et al. The independent pulsations of jupiter's northern and southern x-ray auroras. *Nature Astronomy*, 1(11):758–764, 2017.

[100] RW Ebert, TK Greathouse, G Clark, F Allegrini, F Bagenal, SJ Bolton, JEP Connerney, GR Gladstone, M Imai, V Hue, et al. Comparing electron energetics and uv brightness in jupiter's northern polar region during juno perijove 5. *Geophysical Research Letters*, 46(1):19–27, 2019.

[101] Austin Egert, J Hunter Waite Jr, and Jared Bell. Applications of the jupiter global ionosphere-thermosphere model: A case study of auroral electron energy deposition. *Journal of Geophysical Research: Space Physics*, 122(2):2210–2236, 2017.

[102] Charles Elachi, MD Allison, L Borgarelli, P Encrenaz, E Im, Michael A Janssen, WTK Johnson, Randolph L Kirk, Ralph D Lorenz, Jonathan I Lunine, et al. Radar: the cassini titan radar mapper. *The Cassini-Huygens Mission: Orbiter Remote Sensing Investigations*, pages 71–110, 2004.

[103] A Fahr, A Laufer, R Klein, and W Braun. Reaction rate determinations of vinyl radical reactions with vinyl, methyl, and hydrogen atoms. *The Journal of Physical Chemistry*, 95(8):3218–3224, 1991.

[104] Askar Fahr and Allan H Laufer. Deuterium isotope effect in vinyl radical combination/disproportionation reactions. *The Journal of Physical Chemistry*, 99(1):262–264, 1995.

[105] Bruce Fegley Jr and Katharina Lodders. Chemical models of the deep atmospheres of jupiter and saturn. *Icarus*, 110(1):117–154, 1994.

[106] A Fiaux, DL Smith, and JH Futrell. Reaction of ch5+ with c2h2, c2h4, c3h6 and c-c3h6. *International Journal of Mass Spectrometry and Ion Physics*, 15(1):9–21, 1974.

[107] AI Florescu-Mitchell and James Brian Alexander Mitchell. Dissociative recombination. *Physics reports*, 430(5-6):277–374, 2006.

[108] A James Friedson, Ah-San Wong, and Yuk L Yung. Models for polar haze formation in jupiter's stratosphere. *Icarus*, 158(2):389–400, 2002.

[109] H-P Gail and E Sedlmayr. The primary condensation process for dust around late m-type stars. *Astronomy and Astrophysics (ISSN 0004-6361), vol. 166, no. 1-2, Sept. 1986, p. 225-236.*, 166:225–236, 1986.

[110] Huazhi Ge, Cheng Li, Xi Zhang, and Dongwook Lee. A global nonhydrostatic atmospheric model with a mass-and energy-conserving vertically implicit correction (vic) scheme. *The Astrophysical Journal*, 898(2):130, 2020.

[111] J-C Gérard, Leonardos Gkouvelis, Bertrand Bonfond, GR Gladstone, A Mura, A Adriani, Denis Grodent, V Hue, and TK Greathouse. H3+ cooling in the jovian aurora: Juno remote sensing observations and modeling. *Icarus*, 389:115261, 2023.

[112] J-C Gérard, Alessandro Mura, Bertrand Bonfond, GR Gladstone, A Adriani, V Hue, BM Dinelli, TK Greathouse, Denis Grodent, FRANCESCA Altieri, et al. Concurrent ultraviolet and infrared observations of the north jovian aurora during juno's first perijove. *Icarus*, 312:145–156, 2018.

[113] PJ Gierasch, AP Ingersoll, D Banfield, SP Ewald, P Helfenstein, A Simon-Miller, A Vasavada, HH Breneman, DA Senske, Galileo Imaging Team, et al. Observation of moist convection in jupiter's atmosphere. *Nature*, 403(6770):628–630, 2000.

[114] G Randall Gladstone, Mark Allen, and YL Yung. Hydrocarbon photochemistry in the upper atmosphere of jupiter. *Icarus*, 119(1):1–52, 1996.

[115] G Randall Gladstone, Steven C Persyn, John S Eterno, Brandon C Walther, David C Slater, Michael W Davis, Maarten H Versteeg, Kristian B Persson, Michael K Young, Gregory J Dirks, et al. The ultraviolet spectrograph on nasa's juno mission. *Space Science Reviews*, 213:447–473, 2017.

[116] GR Gladstone, JH Waite Jr, Denis Grodent, WS Lewis, FJ Crary, Ronald F Elsner, MC Weisskopf, T Majeed, J-M Jahn, A Bhardwaj, et al. A pulsating auroral x-ray hot spot on jupiter. *Nature*, 415(6875):1000–1003, 2002.

[117] J Glosik, R Plasil, A Pysanenko, O Novotnỳ, P Hlavenka, P Macko, and G Bánó. Recombination studies in a he-ar-h2 plasma. In *Journal of Physics: Conference Series*, volume 4, page 104. IOP Publishing, 2005.

[118] David G. Goodwin, Harry K. Moffat, Ingmar Schoegl, Raymond L. Speth, and Bryan W. Weber. Cantera: An object-oriented software toolkit for chemical kinetics, thermodynamics, and transport processes. `https://www.cantera.org`, 2024. Version 3.0.0.

[119] BF Gordiets, Sh S Mamedov, and LA Shelepin. Vibrational kinetics of anharmonic oscillators under essentially nonequilibrium conditions. *Zhurnal Eksperimentalnoi i Teoreticheskoi Fiziki*, 67:1287–1300, 1974.

[120] Olivier Grasset, MK Dougherty, A Coustenis, EJ Bunce, C Erd, D Titov, M Blanc, A Coates, P Drossart, LN Fletcher, et al. Jupiter icy moons explorer (juice): An esa mission to orbit ganymede and to characterise the jupiter system. *Planetary and Space Science*, 78:1–21, 2013.

[121] Denis Grodent. A brief review of ultraviolet auroral emissions on giant planets. *Space Science Reviews*, 187:23–50, 2015.

[122] Denis Grodent, JT Clarke, J Kim, JH Waite Jr, and SWH Cowley. Jupiter's main auroral oval observed with hst-stis. *Journal of Geophysical Research: Space Physics*, 108(A11), 2003.

[123] Denis Grodent, J-C Gérard, JT Clarke, GR Gladstone, and JH Waite Jr. A possible auroral signature of a magnetotail reconnection process on jupiter. *Journal of Geophysical Research: Space Physics*, 109(A5), 2004.

[124] T Guillot, G Chabrier, P Morel, and D Gautier. Nonadiabatic models of jupiter and saturn. *Icarus*, 112(2):354–367, 1994.

[125] T Guillot, D Gautier, G Chabrier, and B Mosser. Are the giant planets fully convective? *Icarus*, 112(2):337–353, 1994.

[126] To Guillot, G Chabrier, D Gautier, and P Morel. Effect of radiative transport on the evolution of jupiter and saturn. *Astrophysical Journal v. 450, p. 463*, 450:463, 1995.

[127] Tristan Guillot, David J Stevenson, William B Hubbard, and Didier Saumon. The interior of jupiter, in "jupiter: The planet, satellites and magnetosphere", (eds. bagenal f. et al.), 2004.

[128] Pranika Gupta, Sushil K Atreya, Paul G Steffes, Leigh N Fletcher, Tristan Guillot, Michael D Allison, Scott J Bolton, Ravit Helled, Steven Levin, Cheng Li, et al. Jupiter's temperature structure: A reassessment of the voyager radio occultation measurements. *The Planetary Science Journal*, 3(7):159, 2022.

[129] DA Gurnett, RR Shaw, RR Anderson, WS Kurth, and FL Scarf. Whistlers observed by voyager 1: Detection of lightning on jupiter. *Geophysical Research Letters*, 6(6):511–514, 1979.

[130] Donald A Gurnett, William S Kurth, George B Hospodarsky, AM Persoon, Philippe Zarka, Alain Lecacheux, SJ Bolton, MD Desch, William M Farrell, Michael L Kaiser, et al. Control of jupiter's radio emission and aurorae by the solar wind. *Nature*, 415(6875):985–987, 2002.

[131] DK Haggerty, BH Mauk, CP Paranicas, G Clark, P Kollmann, AM Rymer, SJ Bolton, JEP Connerney, and SM Levin. Juno/jedi observations of 0.01 to¿ 10 mev energetic ions in the jovian auroral regions: Anticipating a source for polar x-ray emission. *Geophysical Research Letters*, 44(13):6476–6482, 2017.

[132] S Han, Go Murakami, Hajime Kita, Fuminori Tsuchiya, Chihiro Tao, Hiroaki Misawa, Atsushi Yamazaki, and Masato Nakamura. Investigating solar wind-driven electric field influence on long-term dynamics of jovian synchrotron radiation. *Journal of Geophysical Research: Space Physics*, 123(11):9508–9516, 2018.

[133] Tom O Hands and Ravit Helled. Super stellar abundances of alkali metals suggest significant migration for hot jupiters. *Monthly Notices of the Royal Astronomical Society*, 509(1):894–902, 2022.

[134] Thomas R Hanley, Paul G Steffes, and Bryan M Karpowicz. A new model of the hydrogen and helium-broadened microwave opacity of ammonia based on extensive laboratory measurements. *Icarus*, 202(1):316–335, 2009.

[135] Y Harada, Y Nakamura, B Sánchez-Cano, M Lester, N Terada, and François Leblanc. Radio absorption in the nightside ionosphere of mars during solar energetic particle events. *Space Weather*, 21(12):e2023SW003755, 2023.

[136] Y Harada, B Sánchez-Cano, M Lester, and A Ippolito. Short-wave fadeout on mars: Radio absorption in the dayside martian ionosphere enhanced by solar flares. *Icarus*, page 116342, 2024.

[137] JK Hargreaves. Auroral absorption of hf radio waves in the ionosphere: A review of results from the first decade of riometry. *Proceedings of the IEEE*, 57(8):1348–1373, 1969.

[138] AN Heays, van Bosman, AD, and EF Van Dishoeck. Photodissociation and photoionisation of atoms and molecules of astrophysical interest. *Astronomy & Astrophysics*, 602:A105, 2017.

[139] Robert A Helliwell. *Whistlers and related ionospheric phenomena*. Courier Corporation, 2014.

[140] Amoree Hodges, Paul Steffes, Amadeo Bellotti, J Hunter Waite, Shannon Brown, Fabiano Oyafuso, Glenn Orton, John Arballo, G Randall Gladstone, Steven Levin, et al. Observations and electron density retrievals of jupiter's discrete auroral arcs using the juno microwave radiometer. *Journal of Geophysical Research: Planets*, 125(9):e2019JE006293, 2020.

[141] SJ Houston, TE Cravens, DR Schultz, H Gharibnejad, WR Dunn, DK Haggerty, AM Rymer, BH Mauk, and N Ozak. Jovian auroral ion precipitation: X-ray production from oxygen and sulfur precipitation. *Journal of Geophysical Research: Space Physics*, 125(2):e2019JA027007, 2020.

[142] S Howard, T Guillot, M Bazot, Y Miguel, DJ Stevenson, E Galanti, Y Kaspi, WB Hubbard, B Militzer, R Helled, et al. Jupiter's interior from juno: Equation-of-state uncertainties and dilute core extent. *Astronomy & Astrophysics*, 672:A33, 2023.

[143] Renyu Hu, Sara Seager, and William Bains. Photochemistry in terrestrial exoplanet atmospheres. i. photochemistry model and benchmark cases. *The Astrophysical Journal*, 761(2):166, 2012.

[144] Vincent Hue, G Randall Gladstone, Thomas K Greathouse, Joshua A Kammer, Michael W Davis, Bertrand Bonfond, Maarten H Versteeg, Denis C Grodent, Jean-Claude Gérard, Scott J Bolton, et al. In-flight characterization and calibration of the juno-ultraviolet spectrograph (juno-uvs). *The Astronomical Journal*, 157(2):90, 2019.

[145] David L Huestis, Stephen W Bougher, Jane L Fox, Marina Galand, Robert E Johnson, Julianne I Moses, and Juliet C Pickering. Cross sections and reaction rates for comparative planetary aeronomy. *Comparative Aeronomy*, pages 63–105, 2008.

[146] Ali Hyder. *The Interplay of Moist Convective and Diffusive Transport in the Jovian Atmosphere*. PhD thesis, New Mexico State University, 2024.

[147] Andrew P Ingersoll, Virgil Adumitroaie, Michael D Allison, Sushil Atreya, Amadeo A Bellotti, Scott J Bolton, Shannon T Brown, Samuel Gulkis, Michael A Janssen, Steven M Levin, et al. Implications of the ammonia distribution on jupiter from 1 to 100 bars as measured by the juno microwave radiometer. *Geophysical Research Letters*, 44(15):7676–7685, 2017.

[148] AP Ingersoll, PJ Gierasch, D Banfield, AR Vasavada, fnm Galileo Imaging Team, et al. Moist convection as an energy source for the large-scale motions in jupiter's atmosphere. *Nature*, 403(6770):630–632, 2000.

[149] Patrick GJ Irwin. Cloud structure and composition of jupiter's atmosphere. *Surveys in geophysics*, 20(6):505–535, 1999.

[150] Nicole Jacquinet-Husson, NA Scott, Alain Chédin, L Crépeau, Raymond Armante, V Capelle, J Orphal, Athena Coustenis, C Boonne, N Poulet-Crovisier, et al. The geisa spectroscopic database: Current and future archive for earth and planetary atmosphere studies. *Journal of Quantitative Spectroscopy and Radiative Transfer*, 109(6):1043–1059, 2008.

[151] MA Janssen, JE Oswald, ST Brown, S Gulkis, SM Levin, SJ Bolton, MD Allison, SK Atreya, D Gautier, AP Ingersoll, et al. Mwr: Microwave radiometer for the juno mission to jupiter. *Space Science Reviews*, 213:139–185, 2017.

[152] Joel T Johnson, Kenneth C Jezek, Giovanni Macelloni, Marco Brogioni, Leung Tsang, Emmanuel P Dinnat, Jeffrey P Walker, Nan Ye, Sidharth Misra, Jeffrey R Piepmeier, et al. Microwave radiometry at frequencies from 500 to 1400 mhz: An emerging technology for earth observations. *IEEE Journal of Selected Topics in Applied Earth Observations and Remote Sensing*, 14:4894–4914, 2021.

[153] Kunal Karan, Anil K Mehrotra, and Leo A Behie. On reaction kinetics for the thermal decomposition of hydrogen sulfide. *AIChE journal*, 45(2):383–389, 1999.

[154] Bryan M Karpowicz and Paul G Steffes. In search of water vapor on jupiter: Laboratory measurements of the microwave properties of water vapor under simulated jovian conditions. *Icarus*, 212(1):210–223, 2011.

[155] Ernst Karwat. Der dampfdruck des festen chlorwasserstoffs, methans und ammoniaks. *Zeitschrift für Physikalische Chemie*, 112(1):486–490, 1924.

[156] Toneo Kawanishi, Toshihiro Sezai, Yasuyuki Ito, Keiji Imaoka, Toshiaki Takeshima, Yoshio Ishido, Akira Shibata, Masaharu Miura, Hiroyuki Inahata, and Roy W Spencer. The advanced microwave scanning radiometer for the earth observing system (amsr-e), nasda's contribution to the eos for global energy and water cycle studies. *IEEE Transactions on Geoscience and Remote Sensing*, 41(2):184–194, 2003.

[157] JK Kim and WT Huntress Jr. Ion cyclotron resonance studies on the reaction of h2+ and d2+ ions with various simple molecules and hydrocarbons. *The Journal of Chemical Physics*, 62(7):2820–2825, 1975.

[158] Sang J Kim, John Caldwell, AR Rivolo, R Wagener, and Glenn S Orton. Infrared polar brightening on jupiter: Iii. spectrometry from the voyager 1 iris experiment. *Icarus*, 64(2):233–248, 1985.

[159] YH Kim and Jane L Fox. The chemistry of hydrocarbon ions in the jovian ionosphere. *Icarus*, 112(2):310–325, 1994.

[160] H Kita, H Misawa, A Bhardwaj, F Tsuchiya, G Murakami, C Tao, T Kimura, K Yoshioka, A Yamazaki, Y Kasaba, et al. Short-term variation in the dawn–dusk asymmetry of the jovian radiation belt obtained from gmrt and hisaki exceed observations. *The Astrophysical Journal Letters*, 872(2):L24, 2019.

[161] Vladimir A Krasnopolsky. *Spectroscopy and photochemistry of planetary atmospheres and ionospheres: Mars, Venus, Titan, Triton and Pluto*, volume 23. Cambridge University Press, 2019.

[162] HP Ladreiter, P Zarka, and A Lecacheux. Direction finding study of jovian hectometric and broadband kilometric radio emissions: Evidence for their auroral origin. *Planetary and Space Science*, 42(11):919–931, 1994.

[163] L Lehfaoui, C Rebrion-Rowe, S Laubé, JBA Mitchell, and BR Rowe. The dissociative recombination of hydrocarbon ions. i. light alkanes. *The Journal of chemical physics*, 106(13):5406–5412, 1997.

[164] Cheng Li, Michael Allison, Sushil Atreya, Shawn Brueshaber, Leigh N Fletcher, Tristan Guillot, Liming Li, Jonathan Lunine, Yamila Miguel, Glenn Orton, et al. Super-adiabatic temperature gradient at jupiter's equatorial zone and implications for the water abundance. *Icarus*, 414:116028, 2024.

[165] Cheng Li and Xi Chen. Simulating nonhydrostatic atmospheres on planets (snap): Formulation, validation, and application to the jovian atmosphere. *The Astrophysical Journal Supplement Series*, 240(2):37, 2019.

[166] Cheng Li, Imke de Pater, Chris Moeckel, RJ Sault, Bryan Butler, David deBoer, and Zhimeng Zhang. Long-lasting, deep effect of saturn's giant storms. *Science Advances*, 9(32):eadg9419, 2023.

[167] Cheng Li, Andrew Ingersoll, Scott Bolton, Steven Levin, Michael Janssen, Sushil Atreya, Jonathan Lunine, Paul Steffes, Shannon Brown, Tristan Guillot, et al. The water abundance in jupiter's equatorial zone. *Nature Astronomy*, 4(6):609–616, 2020.

[168] Cheng Li, Andrew Ingersoll, Michael Janssen, Steven Levin, Scott Bolton, Virgil Adumitroaie, Michael Allison, John Arballo, Amadeo Bellotti, Shannon Brown, et al. The distribution of ammonia on jupiter from a preliminary inversion of juno microwave radiometer data. *Geophysical Research Letters*, 44(11):5317–5325, 2017.

[169] Cheng Li, Tianhao Le, Xi Zhang, and Yuk L Yung. A high-performance atmospheric radiation package: With applications to the radiative energy budgets of giant planets. *Journal of Quantitative Spectroscopy and Radiative Transfer*, 217:353–362, 2018.

[170] Liming Li, X Jiang, RA West, PJ Gierasch, S Perez-Hoyos, A Sanchez-Lavega, LN Fletcher, JJ Fortney, B Knowles, CC Porco, et al. Less absorbed solar energy and more internal heat for jupiter. *Nature Communications*, 9(1):3709, 2018.

[171] Gunnar F Lindal, GE Wood, GS Levy, JD Anderson, DN Sweetnam, HB Hotz, BJ Buckles, DP Holmes, PE Doms, VR Eshleman, et al. The atmosphere of jupiter: An analysis of the voyager radio occultation measurements. *Journal of Geophysical Research: Space Physics*, 86(A10):8721–8727, 1981.

[172] Frederick A Lindemann, Svante Arrhenius, Irving Langmuir, NR Dhar, J Perrin, and WC McC Lewis. Discussion on "the radiation theory of chemical action". *Transactions of the Faraday Society*, 17:598–606, 1922.

[173] Jack J Lissauer. Planet formation. *In: Annual review of astronomy and astrophysics. Vol. 31 (A94-12726 02-90), p. 129-174.*, 31:129–174, 1993.

[174] Junjun Liu, Peter M. Goldreich, and David J. Stevenson. Constraints on deep-seated zonal winds inside jupiter and saturn. *Icarus*, 196(2):653–664, 2008. Mars Polar Science IV.

[175] Junjun Liu, Peter M Goldreich, and David J Stevenson. Constraints on deep-seated zonal winds inside jupiter and saturn. *icarus*, 196(2):653–664, 2008.

[176] Katharina Lodders and Bruce Fegley Jr. Atmospheric chemistry in giant planets, brown dwarfs, and low-mass dwarf stars: I. carbon, nitrogen, and oxygen. *Icarus*, 155(2):393–424, 2002.

[177] Joshua D Lothringer, Zafar Rustamkulov, David K Sing, Neale P Gibson, Jamie Wilson, and Kevin C Schlaufman. A new window into planet formation and migration: refractory-to-volatile elemental ratios in ultra-hot jupiters. *The Astrophysical Journal*, 914(1):12, 2021.

[178] Jonathan I Lunine, Angioletta Coradini, Daniel Gautier, Tobias C Owen, and Guenther Wuchterl. The origin of jupiter. *Jupiter. The planet, satellites and magnetosphere*, 1:19–34, 2004.

[179] RJ MacDowall, ML Kaiser, MD Desch, WM Farrell, RA Hess, and RG Stone. Quasiperiodic jovian radio bursts: Observations from the ulysses radio and plasma wave experiment. *Planetary and Space Science*, 41(11-12):1059–1072, 1993.

[180] GI Mackay, HI Schiff, and DK Bohme. A room-temperature study of the kinetics and energetics for the protonation of ethane. *Canadian Journal of Chemistry*, 59(12):1771–1778, 1981.

[181] PR Mahaffy, HB Niemann, A Alpert, SK Atreya, J Demick, TM Donahue, DN Harpold, and TC Owen. Noble gas abundance and isotope ratios in the atmosphere of jupiter from the galileo probe mass spectrometer. *Journal of Geophysical Research: Planets*, 105(E6):15061–15071, 2000.

[182] AJ Mannucci, BT Tsurutani, O Verkhoglyadova, A Komjathy, and X Pi. Use of radio occultation to probe the high latitude ionosphere. *Atmospheric Measurement Techniques Discussions*, 8(2):2093–2121, 2015.

[183] Klara Matuszewska, Thangasamy Velusamy, Virgil Adumitroaie, John Arballo, Ryan Dorcey, Sooman Han, Ethan Klopping, Nancy Kreuser-Jenkins, Steven Levin, and Daniel Santos-Costa. Variability of jupiter's synchrotron radiation: Goldstone apple valley radio telescope (gavrt) observations-ii. *Publications of the Astronomical Society of the Pacific*, 134(1038):084401, 2022.

[184] Barry H Mauk, G Clark, G Randall Gladstone, Stavros Kotsiaros, Alberto Adriani, Frederic Allegrini, Fran Bagenal, Scott J Bolton, Bertrand Bonfond, John EP Connerney, et al. Energetic particles and acceleration regions over jupiter's polar cap and main aurora: A broad overview. *Journal of Geophysical Research: Space Physics*, 125(3):e2019JA027699, 2020.

[185] Barry H Mauk, DK Haggerty, C Paranicas, G Clark, P Kollmann, AM Rymer, SJ Bolton, SM Levin, A Adriani, F Allegrini, et al. Discrete and broadband electron acceleration in jupiter's powerful aurora. *Nature*, 549(7670):66–69, 2017.

[186] BH Mauk, DK Haggerty, SE Jaskulek, CE Schlemm, LE Brown, SA Cooper, RS Gurnee, CM Hammock, JR Hayes, GC Ho, et al. The jupiter energetic particle detector instrument (jedi) investigation for the juno mission. *Space Science Reviews*, 213:289–346, 2017.

[187] BH Mauk, DK Haggerty, C Paranicas, G Clark, P Kollmann, AM Rymer, DG Mitchell, SJ Bolton, SM Levin, A Adriani, et al. Juno observations of energetic charged particles over jupiter's polar regions: Analysis of monodirectional and bidirectional electron beams. *Geophysical Research Letters*, 44(10):4410–4418, 2017.

[188] BH Mauk, DK Haggerty, C Paranicas, G Clark, P Kollmann, AM Rymer, JM Peachey, SJ Bolton, SM Levin, A Adriani, et al. Diverse electron and ion acceleration characteristics observed over jupiter's main aurora. *Geophysical Research Letters*, 45(3):1277–1285, 2018.

[189] BH Mauk, Q Ma, HN Becker, JL Jørgensen, T Denver, JEP Connerney, F Allegrini, F Bagenal, SJ Bolton, G Clark, et al. Upward, mev-class electron beams over jupiter's main aurora. *Geophysical Research Letters*, 51(24):e2024GL108799, 2024.

[190] BH Mauk, JR Szalay, Frederic Allegrini, Fran Bagenal, SJ Bolton, George Clark, JEP Connerney, GR Gladstone, DK Haggerty, P Kollmann, et al. How bi-modal are jupiter's main aurora zones? *Journal of Geophysical Research: Space Physics*, 128(4):e2022JA031237, 2023.

[191] Michel Mayor and Didier Queloz. A jupiter-mass companion to a solar-type star. *nature*, 378(6555):355–359, 1995.

[192] BJ McCall, AJ Huneycutt, RJ Saykally, N Djuric, GH Dunn, J Semaniak, O Novotny, A Al-Khalili, A Ehlerding, F Hellberg, et al. Dissociative recombination of rotationally cold h 3+. *Physical Review A—Atomic, Molecular, and Optical Physics*, 70(5):052716, 2004.

[193] Michael Mendillo, Clara Narvaez, Luke Moore, and Paul Withers. Jupiter's enigmatic ionosphere: Electron density profiles from the pioneer, voyager, and galileo radio occultation experiments. *Journal of Geophysical Research: Planets*, 127(3):e2021JE007169, 2022.

[194] Y Miguel, M Bazot, T Guillot, S Howard, E Galanti, Y Kaspi, WB Hubbard, B Militzer, R Helled, SK Atreya, et al. Jupiter's inhomogeneous envelope. *Astronomy and Astrophysics-A&A*, 662, 2022.

[195] Burkhard Militzer and William B Hubbard. Study of jupiter's interior: Comparison of 2, 3, 4, 5, and 6 layer models. *Icarus*, 411:115955, 2024.

[196] Burkhard Militzer, William B Hubbard, Sean Wahl, Jonathan I Lunine, Eli Galanti, Yohai Kaspi, Yamila Miguel, Tristan Guillot, Kimberly M Moore, Marzia Parisi, et al. Juno spacecraft measurements of jupiter's gravity imply a dilute core. *The planetary science journal*, 3(8):185, 2022.

[197] TJ Millar, PRA Farquhar, and K Willacy. The umist database for astrochemistry 1995. *Astronomy and Astrophysics Supplement Series*, 121(1):139–185, 1997.

[198] Thomas Marshall Miller, JT Moseley, DW Martin, and EW McDaniel. Reactions of h+ in h 2 and d+ in d 2; mobilities of hydrogen and alkali ions in h 2 and d 2 gases. *Physical Review*, 173(1):115, 1968.

[199] JBA Mitchell. The dissociation recombination of molecules. *Phys. Rep.*, 186:216–248, 1990.

[200] Leonid M Mitnik, Maia L Mitnik, and Elizaveta V Zabolotskikh. Microwave sensing of the atmosphere-ocean system with adeos-ii amsr and aqua amsr-e. *Journal of The Remote Sensing Society of Japan*, 29(1):156–166, 2009.

[201] Chris Moeckel, Imke de Pater, and David DeBoer. Ammonia abundance derived from juno mwr and vla observations of jupiter. *The Planetary Science Journal*, 4(2):25, 2023.

[202] Caroline V Morley, Jonathan J Fortney, Mark S Marley, Channon Visscher, Didier Saumon, and SK Leggett. Neglected clouds in t and y dwarf atmospheres. *The Astrophysical Journal*, 756(2):172, 2012.

[203] Julianne I Moses, Bruno Bézard, Emmanuel Lellouch, G Randall Gladstone, Helmut Feuchtgruber, and Mark Allen. Photochemistry of saturn's atmosphere: I. hydrocarbon chemistry and comparisons with iso observations. *Icarus*, 143(2):244–298, 2000.

[204] Julianne I Moses, Thierry Fouchet, Bruno Bézard, G Randall Gladstone, Emmanuel Lellouch, and Helmut Feuchtgruber. Photochemistry and diffusion in jupiter's stratosphere: Constraints from iso observations and comparisons with other giant planets. *Journal of Geophysical Research: Planets*, 110(E8), 2005.

[205] Julianne I Moses, Thierry Fouchet, Roger V Yelle, Andrew J Friedson, Glenn S Orton, Bruno Bézard, Pierre Drossart, G Randall Gladstone, Theodor Kostiuk, and Timothy A Livengood. The stratosphere of jupiter. *Jupiter: Planet, Satellites and Magnetosphere*, pages 129–157, 2004.

[206] Julianne I Moses and Andrew R Poppe. Dust ablation on the giant planets: consequences for stratospheric photochemistry. *Icarus*, 297:33–58, 2017.

[207] Julianne I Moses, Mikhail Yu Zolotov, and Bruce Fegley Jr. Photochemistry of a volcanically driven atmosphere on io: Sulfur and oxygen species from a pele-type eruption. *Icarus*, 156(1):76–106, 2002.

[208] Mohammad Mousavi, Andreas Colliander, Julie Z Miller, Dara Entekhabi, Joel T Johnson, Christopher A Shuman, John S Kimball, and Zoe R Courville. Evaluation of surface melt on the greenland ice sheet using smap l-band microwave radiometry. *IEEE Journal of Selected Topics in Applied Earth Observations and Remote Sensing*, 14:11439–11449, 2021.

[209] Yuki Nakamura, Koichiro Terada, Chihiro Tao, Naoki Terada, Yasumasa Kasaba, François Leblanc, Hajime Kita, Aoi Nakamizo, Akimasa Yoshikawa, Shinichi Ohtani, et al. Effect of meteoric ions on ionospheric conductance at jupiter. *Journal of Geophysical Research: Space Physics*, 127(3):e2022JA030312, 2022.

[210] Hasso B Niemann, Sushil K Atreya, George R Carignan, Thomas M Donahue, John A Haberman, Dan N Harpold, Richard E Hartle, Donald M Hunten, Wayne T Kasprzak, Paul R Mahaffy, et al. The galileo probe mass spectrometer: Composition of jupiter's atmosphere. *Science*, 272(5263):846–849, 1996.

[211] HB Niemann, SK Atreya, GR Carignan, TM Donahue, JA Haberman, DN Harpold, RE Hartle, DM Hunten, WT Kasprzak, PR Mahaffy, et al. The composition of the jovian atmosphere as determined by the galileo probe mass spectrometer. *Journal of Geophysical Research: Planets*, 103(E10):22831–22845, 1998.

[212] Nikolay K Nikolov, David K Sing, Jessica J Spake, Barry Smalley, Jayesh M Goyal, Thomas Mikal-Evans, Hannah R Wakeford, Zafar Rustamkulov, Drake Deming, Jonathan J Fortney, et al. Solar-to-supersolar sodium and oxygen absolute abundances for a 'hot saturn'orbiting a metal-rich star. *Monthly Notices of the Royal Astronomical Society*, 515(2):3037–3058, 2022.

[213] TA Nordheim, LR Dartnell, L Desorgher, Andrew J Coates, and Geraint H Jones. Ionization of the venusian atmosphere from solar and galactic cosmic rays. *Icarus*, 245:80–86, 2015.

[214] Fabiano A Oyafuso, Steven Levin, Jack Hunter Waite, Paul Steffes, and Scott Bolton. Analysis of the effect of jupiter's northern aurora on juno microwave radiometer observations. In *EGU General Assembly Conference Abstracts*, pages EGU–10437, 2023.

[215] J O'Donoghue, Luke Moore, Tanapat Bhakyapaibul, H Melin, Tom Stallard, JEP Connerney, and C Tao. Global upper-atmospheric heating on jupiter by the polar aurorae. *Nature*, 596(7870):54–57, 2021.

[216] Marco Padovani, Daniele Galli, and Alfred E Glassgold. Cosmic-ray ionization of molecular clouds. *Astronomy & Astrophysics*, 501(2):619–631, 2009.

[217] Robert T Pappalardo, Bonnie J Buratti, Haje Korth, David A Senske, Diana L Blaney, Donald D Blankenship, James L Burch, Philip R Christensen, Sascha Kempf, Margaret G Kivelson, et al. Science overview of the europa clipper mission. *Space Science Reviews*, 220(4):1–58, 2024.

[218] JJ Perry, YH Kim, Jane L Fox, and HS Porter. Chemistry of the jovian auroral ionosphere. *Journal of Geophysical Research: Planets*, 104(E7):16541–16565, 1999.

[219] Gordon H Pettengill, Peter G Ford, and Robert J Wilt. Venus surface radiothermal emission as observed by magellan. *Journal of Geophysical Research: Planets*, 97(E8):13091–13102, 1992.

[220] Jeffrey R Piepmeier, Paolo Focardi, Kevin A Horgan, Joseph Knuble, Negar Ehsan, Jared Lucey, Clifford Brambora, Paula R Brown, Pamela J Hoffman, Richard T French, et al. Smap l-band microwave radiometer: Instrument design and first year on orbit. *IEEE Transactions on Geoscience and Remote Sensing*, 55(4):1954–1966, 2017.

[221] Jeffrey R Piepmeier, Liang Hong, and Fernando A Pellerano. Aquarius l-band microwave radiometer: 3 years of radiometric performance and systematic effects. *IEEE Journal of Selected Topics in Applied Earth Observations and Remote Sensing*, 8(12):5416–5423, 2015.

[222] Cecilia Pinto and Daniele Galli. Three-fluid plasmas in star formation-ii. momentum transfer rate coefficients. *Astronomy & Astrophysics*, 484(1):17–28, 2008.

[223] James B Pollack, Olenka Hubickyj, Peter Bodenheimer, Jack J Lissauer, Morris Podolak, and Yuval Greenzweig. Formation of the giant planets by concurrent accretion of solids and gas. *icarus*, 124(1):62–85, 1996.

[224] C Praxmarer, A Hansel, and W Lindinger. Interaction between the ion dipole and the ion-induced dipole in reactions of the polar ion arh+ 3. *The Journal of chemical physics*, 100(12):8884–8889, 1994.

[225] Emily Rauscher and Kristen Menou. Three-dimensional atmospheric circulation models of hd 189733b and hd 209458b with consistent magnetic drag and ohmic dissipation. *The Astrophysical Journal*, 764(1):103, 2013.

[226] D Reiter and RK Janev. Hydrocarbon collision cross sections for magnetic fusion: the methane, ethane and propane families. *Contributions to plasma physics*, 50(10):986–1013, 2010.

[227] Frank Rensen, Yamila Miguel, Mantas Zilinskas, Amy Louca, Peter Woitke, Christiane Helling, and Oliver Herbort. The deep atmospheric composition of jupiter from thermochemical calculations based on galileo and juno data. *Remote Sensing*, 15(3):841, 2023.

[228] Cyril Richard, Iouli E Gordon, Laurence S Rothman, Martin Abel, Lothar Frommhold, Magnus Gustafsson, J-M Hartmann, Christian Hermans, Walter J Lafferty, Glenn S Orton, et al. New section of the hitran database: Collision-induced absorption (cia). *Journal of Quantitative Spectroscopy and Radiative Transfer*, 113(11):1276–1285, 2012.

[229] Pablo Rodríguez-Ovalle, Thierry Fouchet, Sandrine Guerlet, Thibault Cavalié, Vincent Hue, Manuel López-Puertas, Emmanuel Lellouch, James A Sinclair, Imke de Pater, Leigh N Fletcher, et al. Temperature and composition disturbances in the southern auroral region of jupiter revealed by jwst/miri. *Journal of Geophysical Research: Planets*, 129(6):e2024JE008299, 2024.

[230] Alan EE Rogers, Judd D Bowman, Juha Vierinen, Raul Monsalve, and Thomas Mozdzen. Radiometric measurements of electron temperature and opacity of ionospheric perturbations. *Radio Science*, 50(2):130–137, 2015.

[231] Paul N Romani. Recent rate constant and product measurements of the reactions c2h3+ h2and c2h3+ h—importance for photochemical modeling of hydrocarbons on jupiter. *Icarus*, 122(2):233–241, 1996.

[232] Paul N Romani, James Bishop, Bruno Bézard, and Sushil Atreya. Methane photochemistry on neptune: Ethane and acetylene mixing ratios and haze production. *Icarus*, 106(2):442–463, 1993.

[233] Philip W Rosenkranz. Water vapor microwave continuum absorption: A comparison of measurements and models. *Radio Science*, 33(4):919–928, 1998.

[234] Laurence S Rothman, IE Gordon, RJ Barber, H Dothe, Robert R Gamache, A Goldman, VI Perevalov, SA Tashkun, and J Tennyson. Hitemp, the high-temperature molecular spectroscopic database. *Journal of Quantitative Spectroscopy and Radiative Transfer*, 111(15):2139–2150, 2010.

[235] Laurence S Rothman, Iouli E Gordon, Alain Barbe, D Chris Benner, Peter F Bernath, Manfred Birk, Vincent Boudon, Linda R Brown, Alain Campargue, J-P Champion, et al. The hitran 2008 molecular spectroscopic database. *Journal of Quantitative Spectroscopy and Radiative Transfer*, 110(9-10):533–572, 2009.

[236] Megh Nad Saha. Liii. ionization in the solar chromosphere. *The London, Edinburgh, and Dublin Philosophical Magazine and Journal of Science*, 40(238):472–488, 1920.

[237] A Salveter, J Saur, G Clark, and BH Mauk. Jovian auroral electron precipitation budget—a statistical analysis of diffuse, mono-energetic, and broadband auroral electron distributions. *Journal of Geophysical Research: Space Physics*, 127(8):e2021JA030224, 2022.

[238] BR Sandel, DE Shemansky, AL Broadfoot, JL Bertaux, JE Blamont, MJS Belton, JM Ajello, JB Holberg, SK Atreya, TM Donahue, et al. Extreme ultraviolet observations from voyager 2 encounter with jupiter. *Science*, 206(4421):962–966, 1979.

[239] D Santos-Costa, V Adumitroaie, A Ingersoll, S Gulkis, MA Janssen, SM Levin, F Oyafuso, S Brown, R Williamson, SJ Bolton, et al. First look at jupiter's synchrotron emission from juno's perspective. *Geophysical research letters*, 44(17):8676–8684, 2017.

[240] Daniel Santos-Costa and Scott J Bolton. Discussing the processes constraining the jovian synchrotron radio emission's features. *Planetary and Space Science*, 56(3-4):326–345, 2008.

[241] Yash Sarkango, Xianzhe Jia, and Gabor Toth. Global mhd simulations of the response of jupiter's magnetosphere and ionosphere to changes in the solar wind and imf. *Journal of Geophysical Research: Space Physics*, 124(7):5317–5341, 2019.

[242] Thomas Schmugge, P Gloersen, Tom Wilheit, and F Geiger. Remote sensing of soil moisture with microwave radiometers. *Journal of Geophysical Research*, 79(2):317–323, 1974.

[243] Martin Schwarzschild. *Structure and evolution of stars*, volume 2379. Princeton University Press, 2015.

[244] Alvin Seiff, Donn B Kirk, Tony CD Knight, Richard E Young, John D Mihalov, Leslie A Young, Frank S Milos, Gerald Schubert, Robert C Blanchard, and David Atkinson. Thermal structure of jupiter's atmosphere near the edge of a 5-μm hot spot in the north equatorial belt. *Journal of Geophysical Research: Planets*, 103(E10):22857–22889, 1998.

[245] J Semaniak, A Larson, A Le Padellec, C Stromholm, M Larsson, S Rosen, R Peverall, H Danared, N Djuric, GH Dunn, et al. Dissociative recombination and excitation of ch5+: Absolute cross sections and branching fractions. *The Astrophysical Journal*, 498(2):886–895, 1998.

[246] CM Sharp and WF Huebner. Molecular equilibrium with condensation. *Astrophysical Journal Supplement Series (ISSN 0067-0049), vol. 72, Feb. 1990, p. 417-431. Research supported by NASA, DOE, and Max-Planck-Institut für Physik und Astrophysik.*, 72:417–431, 1990.

[247] CH Sheehan and J-P St Maurice. Dissociative recombination of the methane family ions: rate coefficients and implications. *Advances in Space Research*, 33(2):216–220, 2004.

[248] Adam P Showman. Hydrogen halides on jupiter and saturn. *Icarus*, 152(1):140–150, 2001.

[249] Adam P Showman and Andrew P Ingersoll. Interpretation of galileo probe data and implications for jupiter's dry downdrafts. *Icarus*, 132(2):205–220, 1998.

[250] J Michael Shull and David J Hollenbach. H2 cooling, dissociation, and infrared emission in shocked molecular clouds. *Astrophysical Journal, Part 1, vol. 220, Mar. 1, 1978, p. 525-537.*, 220:525–537, 1978.

[251] Louis Siebenaler, Yamila Miguel, Sam de Regt, and Tristan Guillot. Conditions for radiative zones in the molecular hydrogen envelope of jupiter and saturn: The role of alkali metals. *arXiv preprint arXiv:2501.03756*, 2025.

[252] JA Sinclair, GS Orton, TK Greathouse, Leigh N Fletcher, JI Moses, V Hue, and PGJ Irwin. Jupiter's auroral-related stratospheric heating and chemistry ii: analysis of irtf-texes spectra measured in december 2014. *Icarus*, 300:305–326, 2018.

[253] JA Sinclair, GS Orton, TK Greathouse, LN Fletcher, JI Moses, V Hue, and PGJ Irwin. Jupiter's auroral-related stratospheric heating and chemistry i: analysis of voyager-iris and cassini-cirs spectra. *Icarus*, 292:182–207, 2017.

[254] James A Sinclair, Thomas K Greathouse, Rohini S Giles, Arrate Antuñano, Julianne I Moses, Thierry Fouchet, Bruno Bézard, Chihiro Tao, Javier Martín-Torres, George B Clark, et al. Spatial variations in the altitude of the ch4 homopause at jupiter's mid-to-high latitudes, as constrained from irtf-texes spectra. *The Planetary Science Journal*, 1(3):85, 2020.

[255] James A Sinclair, Thomas K Greathouse, Rohini S Giles, John Lacy, Julianne Moses, Vincent Hue, Denis Grodent, Bertrand Bonfond, Chihiro Tao, Thibault Cavalié, et al. A high spatial and spectral resolution study of jupiter's mid-infrared auroral emissions and their response to a solar wind compression. *The Planetary Science Journal*, 4(4):76, 2023.

[256] James A Sinclair, Thomas K Greathouse, Rohini S Giles, Matthew Richter, Maisie Rashman, Curtis de Witt, Julianne Moses, Vincent Hue, Pablo Rodríguez-Ovalle, Thierry Fouchet, et al. Improved constraints on the vertical profile of ch4 at jupiter's mid-to high latitudes, using irtf-texes and sofia-exes spectroscopy. *The Planetary Science Journal*, 6(1):15, 2025.

[257] RP Singhal, SC Chakravarty, A Bhardwaj, and B Prasad. Energetic electron precipitation in jupiter's upper atmosphere. *Journal of Geophysical Research: Planets*, 97(E11):18245–18256, 1992.

[258] William H Smyth and MC Wong. Impact of electron chemistry on the structure and composition of io's atmosphere. *Icarus*, 171(1):171–182, 2004.

[259] Mi-Young Song, Jung-Sik Yoon, Hyuck Cho, Yukikazu Itikawa, Grzegorz P Karwasz, Viatcheslav Kokoouline, Yoshiharu Nakamura, and Jonathan Tennyson. Cross sections for electron collisions with methane. *Journal of Physical and Chemical Reference Data*, 44(2), 2015.

[260] Knut Stamnes, Si-Chee Tsay, Warren Wiscombe, and Istvan Laszlo. Disort, a general-purpose fortran program for discrete-ordinate-method radiative transfer in scattering and emitting layered media: documentation of methodology. 2000.

[261] Paul G Steffes, Amadeo Bellotti, Pablo Cembellin, Steven M. Levin, and Scott J. Bolton. Laboratory measurements of the 15-46 cm wavelength opacity of water vapor under temperature conditions characteristic of the deep atmosphere of jupiter (submitted). *The Planetary Science Journal*, 2023.

[262] Bjorn Stevens. Atmospheric moist convection. *Annu. Rev. Earth Planet. Sci.*, 33(1):605–643, 2005.

[263] David J Stevenson. Jupiter's interior as revealed by juno. *Annual Review of Earth and Planetary Sciences*, 48(1):465–489, 2020.

[264] David John Stevenson. Formation of the giant planets. *Planetary and Space Science*, 30(8):755–764, 1982.

[265] James M Stone, Kengo Tomida, Christopher J White, and Kyle G Felker. The athena++ adaptive mesh refinement framework: design and magnetohydrodynamic solvers. *The Astrophysical Journal Supplement Series*, 249(1):4, 2020.

[266] Chihiro Tao, Sarah V Badman, and Masaki Fujimoto. Uv and ir auroral emission model for the outer planets: Jupiter and saturn comparison. *Icarus*, 213(2):581–592, 2011.

[267] FW Taylor, SK Atreya, Th Encrenaz, DM Hunten, PGJ Irwin, and TC Owen. The composition of the atmosphere of jupiter. *Jupiter: The planet, satellites and magnetosphere*, pages 59–78, 2004.

[268] Shang-Min Tsai, James R Lyons, Luc Grosheintz, Paul B Rimmer, Daniel Kitzmann, and Kevin Heng. Vulcan: an open-source, validated chemical kinetics python code for exoplanetary atmospheres. *The Astrophysical Journal Supplement Series*, 228(2):20, 2017.

[269] T Tsuji. Molecular abundances in stellar atmospheres. ii. *Astronomy and Astrophysics, Vol. 23, p. 411-431*, 23:411–431, 1973.

[270] GL Tyler, VR Eshleman, JD Anderson, GS Levy, GF Lindal, GE Wood, and TA Croft. Radio science investigations of the saturn system with voyager 1: Preliminary results. *Science*, 212(4491):201–206, 1981.

[271] Vytenis M Vasyliunas. Plasma distribution and flow. *Physics of the Jovian magnetosphere*, 1:395–453, 1983.

[272] T Velusamy, V Adumitroaie, J Arballo, SM Levin, PA Ries, R Dorcey, N Kreuser-Jenkins, J Leflang, David Jauncey, and S Horiuchi. Goldstone apple valley radio telescope monitoring flux density of jupiter's synchrotron radiation during the juno mission. *Publications of the Astronomical Society of the Pacific*, 132(1016):104402, 2020.

[273] Channon Visscher, Katharina Lodders, and Bruce Fegley. Atmospheric chemistry in giant planets, brown dwarfs, and low-mass dwarf stars. iii. iron, magnesium, and silicon. *The Astrophysical Journal*, 716(2):1060, 2010.

[274] Channon Visscher, Katharina Lodders, and Bruce Fegley Jr. Atmospheric chemistry in giant planets, brown dwarfs, and low-mass dwarf stars. ii. sulfur and phosphorus. *The Astrophysical Journal*, 648(2):1181, 2006.

[275] JH Waite Jr, F Bagenal, F Seward, C Na, GR Gladstone, TE Cravens, KC Hurley, JT Clarke, R Elsner, and SA Stern. Rosat observations of the jupiter aurora. *Journal of Geophysical Research: Space Physics*, 99(A8):14799–14809, 1994.

[276] JH Waite Jr, TE Cravens, J Kozyra, AF Nagy, SK Atreya, and RH Chen. Electron precipitation and related aeronomy of the jovian thermosphere and ionosphere. *Journal of Geophysical Research: Space Physics*, 88(A8):6143–6163, 1983.

[277] JH Waite Jr, Denis Grodent, BM Mauk, T Majeed, GR Gladstone, SJ Bolton, JT Clarke, J-C Gérard, WS Lewis, LM Trafton, et al. Multispectral observations of jupiter's aurora. *Advances in Space Research*, 26(10):1453–1475, 2000.

[278] Baoshan Wang, Hua Hou, Laurie M Yoder, James T Muckerman, and Christopher Fockenberg. Experimental and theoretical investigations on the methyl- methyl recombination reaction. *The Journal of Physical Chemistry A*, 107(51):11414–11426, 2003.

[279] Dong Wang, Peter J Gierasch, Jonathan I Lunine, and Olivier Mousis. New insights on jupiter's deep water abundance from disequilibrium species. *Icarus*, 250:154–164, 2015.

[280] Dong Wang, Jonathan I Lunine, and Olivier Mousis. Modeling the disequilibrium species for jupiter and saturn: Implications for juno and saturn entry probe. *Icarus*, 276:21–38, 2016.

[281] Edward W Washburn. The vapor pressure of ice and of water below the freezing point. *Monthly Weather Review*, 52(10):488–490, 1924.

[282] Edward Wight Washburn and Clarence Jay West. *International critical tables of numerical data, physics, chemistry and technology*, volume 3. National Academies, 1928.

[283] JW Waters, KF Kunzi, RL Pettyjohn, RKL Poon, and DH Staelin. Remote sensing of atmospheric temperature profiles with the nimbus 5 microwave spectrometer. *Journal of Atmospheric Sciences*, 32(10):1953–1969, 1975.

[284] SJ Weidenschilling and JS Lewis. Atmospheric and cloud structures of the jovian planets. *Icarus*, 20(4):465–476, 1973.

[285] Luis Welbanks, Nikku Madhusudhan, Nicole F Allard, Ivan Hubeny, Fernand Spiegelman, and Thierry Leininger. Mass–metallicity trends in transiting exoplanets from atmospheric abundances of h2o, na, and k. *The Astrophysical Journal*, 887(1):L20, 2019.

[286] Hugh F Wilson and Burkhard Militzer. Sequestration of noble gases in giant planet interiors. *Physical review letters*, 104(12):121101, 2010.

[287] Peter Woitke, Ch Helling, GH Hunter, JD Millard, GE Turner, M Worters, J Blecic, and JW Stock. Equilibrium chemistry down to 100 k-impact of silicates and phyllosilicates on the carbon to oxygen ratio. *Astronomy & Astrophysics*, 614:A1, 2018.

[288] Ah-San Wong, Anthony YT Lee, Yuk L Yung, and Joseph M Ajello. Jupiter: Aerosol chemistry in the polar atmosphere. *The Astrophysical Journal*, 534(2):L215, 2000.

[289] Michael H Wong, Gordon L Bjoraker, Charles Goullaud, Andrew W Stephens, Statia H Luszcz-Cook, Sushil K Atreya, Imke de Pater, and Shannon T Brown. Deep clouds on jupiter. *Remote Sensing*, 15(3):702, 2023.

[290] Michael H Wong, Paul R Mahaffy, Sushil K Atreya, Hasso B Niemann, and Tobias C Owen. Updated galileo probe mass spectrometer measurements of carbon, oxygen, nitrogen, and sulfur on jupiter. *Icarus*, 171(1):153–170, 2004.

[291] Wee Woo and JS DeGroot. Microwave absorption and plasma heating due to microwave breakdown in the atmosphere. *The Physics of Fluids*, 27(2):475–487, 1984.

[292] FB Yousif and JBA Mitchell. Recombination and excitation of heh+. *Physical Review A*, 40(8):4318, 1989.

[293] Yuk L Yung, Mark Allen, and Joseph P Pinto. Photochemistry of the atmosphere of titan-comparison between model and observations. *Astrophysical Journal Supplement Series (ISSN 0067-0049), vol. 55, July 1984, p. 465-506.*, 55:465–506, 1984.

[294] Yuk L Yung, G Randall Gladstone, Kar Man Chang, Joseph M Ajello, and SK Srivastava. H2 fluorescence spectrum from 1200 to 1700 a by electron impact-laboratory study and application to jovian aurora. *Astrophysical Journal, Part 2-Letters to the Editor, vol. 254, Mar. 15, 1982, p. L65-L69.*, 254:L65–L69, 1982.

[295] Philippe Zarka. Auroral radio emissions at the outer planets: Observations and theories. *Journal of Geophysical Research: Planets*, 103(E9):20159–20194, 1998.

[296] Binzheng Zhang, Peter A Delamere, Zhonghua Yao, Bertrand Bonfond, D Lin, Kareem A Sorathia, Oliver J Brambles, William Lotko, Jeff S Garretson, Viacheslav G Merkin, et al. How jupiter's unusual magnetospheric topology structures its aurora. *Science Advances*, 7(15):eabd1204, 2021.

[297] Z Zhang, AG Hayes, I de Pater, DE Dunn, MA Janssen, PD Nicholson, JN Cuzzi, BJ Butler, RJ Sault, and S Chatterjee. Vla multi-wavelength microwave observations of saturn's c and b rings. *Icarus*, 317:518–548, 2019.

[298] Z Zhang, AG Hayes, MA Janssen, PD Nicholson, JN Cuzzi, I de Pater, and DE Dunn. Exposure age of saturn's a and b rings, and the cassini division as suggested by their non-icy material content. *Icarus*, 294:14–42, 2017.

[299] BX Zhu, CD Lindstrom, I Jun, HB Garrett, P Kollmann, C Paranicas, BH Mauk, and GR Gladstone. Jupiter high-energy/high-latitude electron environment from juno's jedi and uvs science instrument background noise. *Nuclear Instruments and Methods in Physics Research Section A: Accelerators, Spectrometers, Detectors and Associated Equipment*, 1002:165244, 2021.